METHODS AND ANALYSIS OF MULTIPHASE FLOW AND INTERFACIAL PHENOMENA IN MEDICAL DEVICES

by

Javad Eshraghi

A Dissertation

Submitted to the Faculty of Purdue University

In Partial Fulfillment of the Requirements for the degree of

Doctor of Philosophy

School of Mechanical Engineering

West Lafayette, Indiana

May 2022

THE PURDUE UNIVERSITY GRADUATE SCHOOL

STATEMENT OF COMMITTEE APPROVAL

Dr. Pavlos P. Vlachos, Chair

School of Mechanical Engineering

Dr. Arezoo M. Ardekani

School of Mechanical Engineering

Dr. Sadegh Dabiri

School of Mechanical Engineering

Dr. Luis Solorio

Weldon School of Biomedical Engineering

Approved by:

Dr. Nicole L. Key

Dedicated to my mother and my father for their lifelong support and encouragement.

ACKNOWLEDGMENTS

I would like to thank my advisor Professor Pavlos P. Vlachos, for his guidance, mentorship, and support through my Ph.D. I was privileged to work with one of the well-known fluid mechanicians who taught me how to think outside the box, and I was held to such high standards that shaped me into a competent, independent researcher. I would also like to thank my committee members Professor Arezoo M. Ardekani, Professor Sadegh Dabiri, and Professor Luis Solorio, for their insights and support.

I was part of a multidisciplinary and collaborative research environment that helped establish several long-lasting and fruitful collaborations. I would like to thank Dr. Galen Shi, Dr. David S. Collins, and Dr. Jean-Christophe Veilleux from Eli Lilly and Company, Professor Mark A. Stremler from Virginia Tech, Professor Filippo Coletti from ETH, and of course, Professor Sunny Jung from Cornel and Professor Hector Gomez from Purdue University, who I probably learned the most from. Working with Dr. Sayantan Bhattacharya and Dr. Lalit Rajendran on the cavitation-air bubble interactions was delightful. Dr. Wenchao Yang from Queen's University was an indispensable part of developing the flowing soap film experimental setup. I would like to thank the School of Mechanical Engineering and Weldon School of Biomedical Engineering. I am also thankful to Eli Lilly and Company for their fruitful collaboration and support of my research.

I would like to thank my colleagues, collaborators, and fellow graduate students from the Vlachos research group, who were an essential part of my Ph.D. journey. I would also like to thank the undergraduate and graduate students I got the chance to mentor and learn by teaching.

I dedicate this dissertation to my family for their support and encouragement all around the globe. I would like to thank my parents for always being there. I would like to thank my sister, brother-in-law, and Aryanaz, my beloved niece, born a year into my Ph.D., and it is the hardest part of being away from family.

I hope this dissertation help to elucidate the effects of the air-/vapor-solution interface dynamics on the surrounding environment, specifically the biological environment.

TABLE OF CONTENTS

LIST OF TABLES

LIST OF FIGURES

ABSTRACT

Cavitation, liquid slosh, and splashes are ubiquitous in science and engineering. However, these phenomena are not fully understood. Yet to date, we do not understand when or why sometimes the splash seals, and other times does not. Regarding cavitation, a high temporal resolution method is needed to characterize this phenomenon. The low temporal resolution of experimental data suggests a model-based analysis of this problem. However, high-fidelity models are not always available, and even for these models, the sensitivity of the model outputs to the initial input parameters makes this method less reliable since some initial inputs are not experimentally measurable. As for sloshing, the air-liquid interface area and hydrodynamic stress for the liquid slosh inside a confined accelerating cylinder have not been experimentally measured due to the challenges for direct measurement.

This dissertation provides the first detailed analysis and physical explanations for the abovementioned phenomena. These have consequences for diverse applications such as biomedical, diving, sound propagation in oceans, ocean oxygenation, and energy harvesting.

First, we developed an analytical model to describe the trajectory and dynamics of the splash curtain in the water entry of hydrophobic spheres and validated it with a series of experiments. We elucidated the dynamics of splash curtain and discovered the existence of a critical dimensionless number that predicts the occurrence of the surface seal.

As for the cavitation modeling, we proposed a robust characterization tool based on a novel state observer-based data-assimilation technique to overcome the limitations in the existing methods. We fused time-resolved cavitation bubble diameter measurements with the governing model to yield enhanced Spatiotemporal prediction of the cavitation bubble dynamics in this new autonomous technique.

We then employed the data assimilation modeling to investigate the dynamics of a single air bubble exposed to an acoustic pressure field induced by a cavitation bubble using a unique combination of theory and experiment. We elucidated the effects of acoustic source intensity, the distance from the acoustic source, and air bubble size on the air bubble final oscillation regime. We also used data assimilation modeling to quantify cavitation intensity in autoinjector medical devices to assess the impact of cavitation on therapeutic protein.

Furthermore, a set of experiments by conducting simultaneous PIV and shadowgraphy were used to investigate the interfacial motion and hydrodynamic shear due to the acceleration/deceleration during the autoinjector insertion that might cause therapeutic protein aggregation.

1. INTRODUCTION

Water entry splashes, cavitation, and liquid slosh are intricate multiphase phenomena ubiquitous in science and engineering and are not fully understood yet despite a large amount of research.

A crown-like splash curtain is formed every time an object impacts the water surface. The water entry phenomenon is ubiquitously present in a wide range of applications, from the entrance of torpedoes into the water to divers jumping into pools at the Olympics, and a splash always accompanies it, a "surface curtain". This surface curtain may splash outwards, or dome over and close, referred to as a surface seal. The dynamics governing the splash curtain evolution and closure have been unexplored, and to date, we don't know why sometimes it the surface curtain seals and other times it does not. In chapter 2, we elucidate the dynamics of splash curtain and discover the existence of a critical dimensionless number that predicts the occurrence of a surface seal. In contrast to our current understanding which labels the projectile impact velocity as the main cause in the occurrence of surface seal, we show that this phenomenon is not fully defined with the impact velocity. We develop an analytical model to describe the trajectory and dynamics of the splash curtain in the water entry of hydrophobic spheres and validate it with a series of experiments. We reveal that the non-dimensionalized velocity of the airflow rushing into the cavity behind the sphere is the determinant factor in the splash curtain closure, enabling us to determine a critical dimensionless airflow velocity beyond which the surface seal occurs. This work represents the first detailed analysis of the splash curtain, providing the physical understanding of why the splash curtain sometimes seals and other times it does not.

Cavitation is ubiquitous in nature and engineering and governs processes from corrosion to propeller blades to drugs getting through the endothelial cells. Since the collapse of the cavitation bubble is so violent that it generates an intense shock wave and induces high shear stress to the surrounding liquid, we need a high temporal resolution method to characterize this moment. The low temporal resolution of experimental data suggests a model-based analysis of this problem. However, high-fidelity models are not always available, and even for these models, the sensitivity of the model outputs to the initial input parameters makes this method less reliable since some initial inputs are not experimentally measurable. Therefore, in chapter 3, we propose a robust characterization tool based on a novel state observer-based data-assimilation technique to

overcome these two challenges in the existing methods. In this new autonomous technique, we fuse time-resolved cavitation bubble diameter measurements with the governing model to yield enhanced Spatiotemporal prediction of the cavitation bubble dynamics.

In chapter 4, we employ the developed data assimilation method for modeling cavitation bubbles to explain fundamental cavitation bubble-air bubble interactions. The shape oscillation of an acoustically-excited gas bubble is not fully understood despite applications from biomedical to sound propagation in oceans. We present the first detailed investigation and characterization of air bubble oscillations due to a cavitation-induced acoustic field and quantify the energy needed to excite the growth of instabilities using a unique combination of theory and experiment. We show how the acoustic intensity and bubble size govern the bubble energy absorption and discover the relationship determining how the absorbed energy generates ripples on the bubble surface, their growth, and ultimate bubble breakup. This work will enable the physics community to explain fundamental bubble-bubble and cavitation-bubble interactions.

Chapter 5 and chapter 6 focus on the air-solution and vapor-solution interface dynamics in the biological environment and, in particular, investigate the impact of cavitation and liquid slosh phenomena in an autoinjector medical device on the therapeutic protein. Many recent works have demonstrated that the air-/vapor-liquid interface is the most detrimental reason for protein denaturation, while the hydrodynamic shear alone is rarely the leading cause of the damage for therapeutic proteins. Cavitation can happen during the drug administration using an autoinjector. Major competitors focus on developing the prefilled syringe and AIs by innovations in material and apparatus features. However, most of them might not be aware of a catastrophic phenomenon during drug injection, called cavitation collapse. Cavitation occurs in the syringe inside AI because of the container-drug relative displacement and the ensuing pressure drop at the bottom of the container. Our high-speed video imaging visualizations show severe cavitation in almost all tested spring-driven AIs on the market. Thus, it is crucial to assess the potential damage of cavitation collapse on drugs, silicone oil, syringe, and AI devices and investigate the effects of AI design parameters such as plunger position, rod length, syringe fill volume, and spring force on the risk of cavitation. Since there is no single non-invasive technique for characterization of the cavitation inside an AI, we will employ our developed non-invasive data assimilated-based method, introduced in chapter 3, to assess the severity of the cavitation in AIs with different configurations.

Thus, we will study the effects of drug viscosity, spring force, air gap size, and the fill volume of the syringe on the induced shear stress.

Interface motion and hydrodynamic shear induced by the liquid slosh during the insertion stage of autoinjector administration may damage the protein drug molecules. In chapter 6, a set of experiments are used to investigate the interfacial motion and hydrodynamic shear due to the acceleration and deceleration of syringes. The goal is to explore the role of fluid type, air gap size, and syringe acceleration on the interface dynamics caused by autoinjector activation. We use experimental methods to quantify the air-liquid interface motion and the hydrodynamic stress distributions in syringes during the insertion process of the AI. A simplified autoinjector platform submerged in water is built to record the syringe and liquid motion without the obstruction of view. The fluid in the syringe is seeded with micron-sized particles, and Particle Image Velocimetry (PIV) is employed to capture the motion of the particles to find the velocity field. Simultaneous shadowgraph visualization captures the air entrainment. Our in-house PIV and image processing algorithms are used to quantify the strain and shear fields and interfacial area in order to investigate the effects of various autoinjector design parameters and fluid types on liquid slosh.

The value of the flowing soap film as an experimental platform depends on its ability to approximate the two-dimensional Navier-Stokes equation. A variety of experimental techniques have been applied to characterize the soap film patterns, with the measured quantities being the thickness and the velocity of the soap film. Interferometry and Schlieren techniques are qualitative techniques to visualize the thickness variations and associated flow structures. Also, PIV is a common tool used to quantify the velocity of soap films. Despite the efforts for characterizing the soap film patterns, there remains a need for direct validation of soap film flows as a proxy for two-dimensional incompressible Newtonian flows. Chapter 7 addresses the connection between flow structures and soap film visualizations by developing a unique apparatus for conducting simultaneous and phase-locked experiments with interferometry and PIV. We develop a new methodology using BOS for measuring the relative thickness of soap films. Finally, we apply all three techniques (interferometry, PIV, and BOS) to characterize the soap film flow behind a circular cylinder and compare the wake patterns among the three techniques and with results in the literature for three-dimensional flows.

Overall, this dissertation involves a combination of multiphase flow, experimental fluid mechanics, and biomedical research disciplines and introduces novel methodologies and unique

experimental techniques to study multiphase flows, and provides insightful explanations of some ubiquitous phenomena in science and engineering.

2. ON FLOWING SOAP FILMS AS EXPERIMENTAL MODELS OF 2D NAVIER-STOKES FLOWS

2.1.Background

Flowing soap film systems typically consist of a (nearly) planar film with thickness $h = O(10\mu m)$ and free stream speed $U = O(1m/s)$. Local variations in flow speed, such as caused by a bluff body partially obstructing the flow, produce small variations in the local film thickness that correlate with pressure variations and can be used to identify flow structures such as coherent vortices. Inspired by Mysels et al. [1] and motivated by the observations of Couder et al. [2–4] in a stationary film, flowing soap films were first developed by Gharib and Derango [5] as a method of experimentally investigating fluid flows in a two-dimensional "tunnel". Gravity-driven films [6–8] are the most common implementation, and the system used in the study reported here is similar to the inclined designs introduced by Vorobieff and collaborators [8–10]. Flowing soap film systems have been used to investigate a variety of fluid mechanics phenomena such as two-dimensional turbulence [5,6,9–12] and the wake structures generated by a variety of embedded bodies, including cylinders [13,14], flapping foils [15], elastic loops [16], and flexible filaments [17–21].

A variety of experimental techniques have been applied to characterize soap film patterns, with typical measured quantities being the thickness and the velocity of the soap film. Interferometry is the most common approach to visualizing thickness variations and the associated flow structures [2]. When the soap film is illuminated with monochromatic light, the light waves reflected by the upper and lower boundaries of the soap film interfere, with the phase difference determined by the thickness of the film. Regions of constructive and destructive interference are characterized by bright and dark bands, respectively, and the arrangement of these bands gives a representation of the local film thickness [22,23]. Another qualitative approach, proposed by Auliel et al. [24], uses the Schlieren technique to visualize thickness gradients in the soap film

patterns based on light refraction at the air-soap film interface. In a quantitative approach, Vorobieff et al. [9] seeded the soap film with particles and measured the local thickness from the intensity of the scattered light. However, it was shown that this is not a precise measurement technique, with a 20% uncertainty reported in the calibration step.

Since film thickness is an important parameter in characterizing the soap film dynamics, it is desirable to provide quantitative thickness measurements with high accuracy, precision, and spatio-temporal resolution. In this work, we adapt the Background Oriented Schlieren (BOS) technique [25] for measuring the thickness field by utilizing the light refraction at the air-film interface. BOS is a quantitative variant of the Schlieren technique that is typically used to measure the density/refractive index gradients in fluid flows from the apparent distortion of a target dot pattern. In the case of soap films, the refractive index field is uniform everywhere and the distortion of the dot pattern is instead due to local thickness gradients. The details of the implementation are discussed in Sections 2.2.3.4 and 2.3.4.

For velocity measurements, digital particle image velocimetry (DPIV) is the most common method, and this technique has been applied in numerous soap film studies [8–10,12,13,17]. In this method, the soap film is seeded with micron- [17] or sub-micron-sized [8–10,12,13] particles that scatter light when illuminated. The images of the particles can then be tracked using computer vision algorithms to determine the local flow velocity [26,27]. The two-dimensional nature of a flowing soap film minimizes the out-of-plane motion of particles that is a common source of error in traditional DPIV experiments. We show that accurate measurements can be performed with micron-scale particles having diameters that are of the same order as the thickness of the film.

The value of the flowing soap film as an experimental platform depends on its ability to approximate the two-dimensional Navier-Stokes equation. One such condition is that the bulk fluid velocity in the film, U, be small relative to the Marangoni elastic wave speed, U_M, e.g. that the elastic Mach number, $M_e = U/U_M$, be small [3,28–30]; Auliel et al. [24] have demonstrated that in general, it is enough to have $M_e = O(10^{-1})$. While this condition is expected to be met for films with low soap concentration, small thickness, minimal thickness gradients, and low speeds, these predictions involve several assumptions about the film and the flow, and thus validation through experiments is an important step.

Several indirect validations of soap film systems as a proxy for two-dimensional incompressible Newtonian flows exist in the literature. Vorobieff et al. [9,31] showed a correlation

between vorticity and thickness fields in the flowing soap film using the Δ-criterion [32] to identify the flow structures. Vorobieff and Ecke [13] found that the Strouhal-Reynolds number relationship for a stationary circular cylinder in a soap film corresponds well to the two-dimensional relationship in a viscous fluid. Yang et al. [33] showed that the streamlines produced by steady flow over a backward-facing step correlate well with numerical simulations. Wu et al. [34] determined that the time-varying angle of separation from a stationary circular cylinder in a soap film agreed with results from a spectral numerical method simulation. Yang and Stremler [14] established experimental values of critical spacing between tandem cylinders and showed good agreement with two-dimensional simulations, in contrast to standard three-dimensional experiments. Despite this prior work, there remains a need for direct validation of using soap film flows as a proxy for two-dimensional incompressible Newtonian flows.

In this manuscript, we address the connection between flow structures and soap film visualizations by developing a unique apparatus for conducting simultaneous and phase-matched experiments with both interferometry and DPIV, and phase-matched experiments with BOS. We applied all three techniques (interferometry, DPIV, and BOS) to characterizing the wake structure behind a circular cylinder, and we compared the wake pattern characteristics with results from the literature for three-dimensional flows. The results show that the arrangement of vortices in our flowing soap film system correlated well among the techniques and with published results, in terms of streamwise spacing, spanwise spacing ratio, length of the formation region, and the vortex circulations. The results presented here verify the flowing soap film as an appropriate tool for investigating low Reynolds number two-dimensional flows.

2.2.Experimental setup

The aim of these experiments is to quantitatively explore the relationship between soap film patterns and flow structures. To do so, we identified the vortical structures in a circular cylinder wake using three methods: interferometry, time-resolved Digitial Particle Image Velocimetry (DPIV), and Background Oriented Schlieren (BOS). Four case studies were considered. In Case A, interferometry was used to identify wake patterns and locate vortex centers. In Case B, DPIV was used to quantify the velocity field, and from this field, the vortex structures were computed. In Case C we conducted interferometry and DPIV measurements simultaneously, giving the first direct comparison of these two methods. In Case D, we demonstrated the first use

of BOS to quantify the relative film thickness field and identify vortex centers, and we compared these results with those obtained using qualitative interferograms.

2.2.1. Soap film system

The experimental flow system is comprised of a gravity-driven flowing soap film apparatus (Figure 2.1) that can be tilted at an arbitrary angle with respect to the vertical. The soap film frame consists of three sections: expansion section, test section, and contraction section. Two $1\ mm$ diameter nylon wires are stretched from top to bottom to create a parallel channel (test section) with adjustable width ($W = 5\text{–}8\ cm$) and a length of $50\ cm$ (see Figure 2.1(b)). The expansion and contraction sections are approximately $35\ cm$ and $15\ cm$ long, respectively.

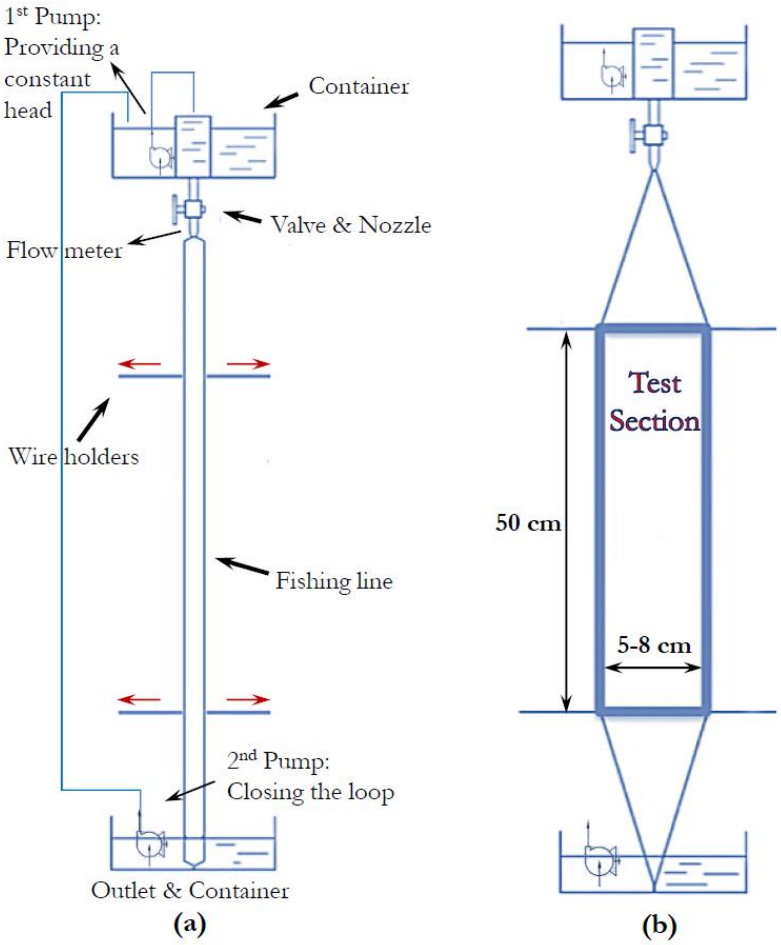

Figure 2.1. (a) Schematic of the soap film apparatus, (b) test section of our experimental setup.

As shown in Figure 2.1, the container at the top of the system consists of two concentric containers, one inside the other, and the soap solution is provided to the film from the center reservoir that is being maintained at a constant head. The head remains constant by the soap solution being pumped continuously from the outer container to the center container using a submersible pump (SmartPond FP500). By opening the valve below the container as seen in Figure 2.1, the soap solution runs from the top container to the outlet container along the fishing lines, and the flow rate is controlled with the same valve. The volumetric flow rate is measured with a turbine flow meter (OMEGA, FLR1007-D) with an accuracy of 1%. The soap solution constitutes 10% commercial soap (Dawn professional dish-washing detergent) in water. To create a flowing soap film, the fishing lines are then pulled apart and the rectangular test section is formed as shown in Figure 2.1(b).

The wakes investigated in this study were generated by placing a stationary carbon fiber cylinder with diameter $d = 1\ mm$ through the soap film, with the axis of the cylinder oriented at a 90° angle from the plane of the film. The center of the cylinder was placed at the spanwise center of the test section and a streamwise distance of $5\ cm$ from the test section entrance. The blockage ratio, $B = d/W$, for all tests was less than 3.5%, and thus blockage effects were considered negligible [35,36].

The stability of the flowing soap film comes from the concentration of soap molecules on its surface, which leads necessarily to an elastic behavior [37]. As the film thins locally, soap molecules are spread apart, causing the surface tension, σ, to increase locally, which in turn generates a restoring force aimed at returning the film to its original surface area, A. This effect gives rise to an elasticity $E_M = A(d\sigma/dA)$ for the film. The significance of these effects in a soap film flow are characterized by the elastic Mach number, $M_e = U/U_M$, where $U_M = \sqrt{2E_M/\rho h}$ is the Marangoni wave speed. We assumed $E_M \approx 22\ mN/m$ [37]. Based on mass conservation and the measured volumetric flow rate we estimated the average film thickness to be $\bar{h} \approx 5\ \mu m$ (see Section 2.2.2). We measured the density of the bulk solution using a Handheld Density Meter (Mettler Toledo, DensitoPro, $\pm 0.001 g/cm^3$) and found it to be $\rho = 1.001 \pm 0.001$ g/cm^3 (based on 5 measurements). Thus our system had $U_M \approx 3\ m/s$, giving $M_e < 0.5$ for all experiments (see Table 2.1). Therefore, any compressible-like effects caused by the film elasticity were assumed to have a negligible effect on the results reported here.

2.2.2. Determining Reynolds number

A direct calculation of the Reynolds number, $Re = \rho U d/\mu_f$, was accomplished by computing the effective dynamic viscosity of the soap film, μ_f, using a film thickness modification proposed by Couder and Basdevant [4] and further developed by [38,39]. In this approximation, the viscosity is estimated as

$$\mu_f = \mu_b + \frac{2\mu_S}{\bar{h}}, \qquad \text{Equation 2-1}$$

where μ_b is the viscosity of the interstitial bulk solution, μ_S is the viscosity of the two superficial surface layers, and $\bar{h}$ is the average film thickness. Using a hybrid rheometer (TA Instruments, HR-3), we determined $\mu_b = 1.59 \pm 0.14$ cP. We assumed $\mu_S = 10^{-3}$ cP [4]. The average film thickness was estimated using the measured volumetric flow rate of the soap solution and the measured velocity from DPIV by assuming a constant cross-section for the film, which gave $\bar{h} = 4.7 \pm 0.2\ \mu m$. Applying these values to Equation 2-1 gives the effective viscosity $\mu_f = 5.84 \pm 0.32$ cP. With $\rho = 1.001 \pm 0.001$ g/cm^3 we calculated the direct Reynolds number values shown in Table 2.1.

Owing to the challenges involved with determining an accurate value for the viscosity of a soap film [7], Gharib and Derango [5] proposed using the Strouhal number, $St = fd/U$, to indirectly estimate the value of Re based on the observed frequency of vortex shedding, f. Wen & Lin [40] and Roushan & Wu [41] have shown that the relationship between St and Re for a stationary cylinder in a soap film agrees with established three-dimensional results over a wide range of Re. We used this approach to validate the Re values determined using the direct method. The flow velocity and shedding frequency were obtained from the quantified velocity field using DPIV (see Section 2.2.3.2). We found the shedding frequency by computing the dominant frequency of the velocity fluctuations recorded by a representative "probe" point in the wake region, and from this frequency determined St. The corresponding value of Re was calculated using the $St - Re$ curve from [42], namely

$$St = 0.2731 + \frac{0.4821}{Re} - \frac{1.1129}{\sqrt{Re}}. \qquad \text{Equation 2-2}$$

Values of Re using this method are also shown in Table 2.1. Comparison of the two methods shows that the discrepancy in the calculated values of Re is less than 10%, with the error increasing with increasing Re. We take the representative *Re* value to be the average value from these two methods.

Table 2.1. Strouhal number, St; background flow speed, U; calculated elastic Mach number. M_e; and estimated Re for our study from direct calculations using Equation 2-1, using the $St - Re$ relationship [42] in Equation 2-2, and from averaging these results.

Nominal Re	St	$U\ (m/s)$	M_e	Re (1)	Re (2)	Mean Re
100	0.166 ± 0.0002	0.58 ± 0.01	0.17	99.3 ± 0.9	99.5 ± 0.4	99.4 ± 0.5
200	0.197 ± 0.0004	1.02 ± 0.01	0.31	187 ± 2	199 ± 2	193 ± 4
300	0.210 ± 0.0003	1.50 ± 0.02	0.45	279 ± 3	299 ± 3	289 ± 7

The carbon fiber cylinder was surrounded by a meniscus at the intersection with the soap film. Using an optical technique, the width of the meniscus was estimated to be approximately $m = 0.024 \pm 0.004\ mm$ in the present study. Couder and Basdevant [4] proposed using an effective diameter, equal to $d + 2m$, as the characteristic length for the cylinder. For our system, accounting for the meniscus would change the characteristic diameter by no more than approximately 3%. Furthermore, no significant meniscus effect was shown on the vortex-shedding characteristics in [5,13,40,43]. Thus, the physical cylinder diameter, d, was used as the characteristic length scale in all calculations.

2.2.3. Visualization systems

The configuration of the camera and light source for each of the four case studies is described below.

2.2.3.1.Case A: Soap film pattern visualization by interferometry

A $180\ W$ low-pressure sodium lamp (a monochromatic light source) with a wavelength of $589\ nm$ was used to illuminate the soap film. A high-speed 4-megapixel CMOS camera equipped with a 105 mm Nikon lens at an aperture setting of $f5.6$ (Phantom V2640, $Cam1$ in Figure 2.2) and the sodium lamp were placed on the same side of the soap film, as shown in Figure

2.2; the camera was oriented perpendicular to the plane of the soap film. We collected 5 sets of images at three values of Reynolds number, $Re \approx 100, 200, 300$. For each experimental run, we collected 12000 images at 6,000 Hz with a spatial resolution of 66.7 pixels per mm. The field of view of the images was $6d \times 20d$ (spanwise by streamwise). Due to the sodium lamp operating frequency ($60\ Hz$), a brightness variation was present in the images, so we applied the histogram equalization tool in MATLAB to increase the global contrast of images by matching each histogram with that of a reference image [44,45].

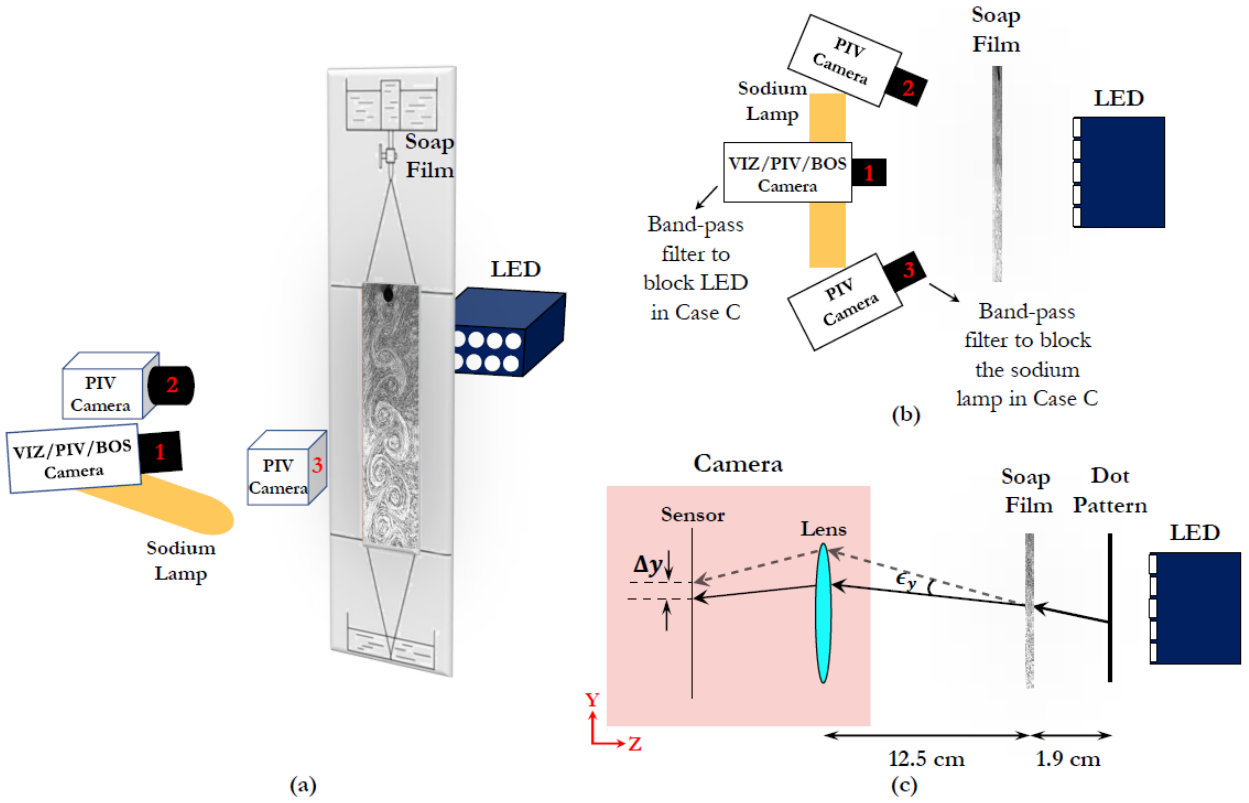

Figure 2.2. Configuration of the cameras and light sources: (a) 3D view, (b) top view. For Case A, B, and D, only the middle camera ($Cam1$) was used. For Case C, all three cameras were used: the two on the sides ($Cams2$ and 3) for stereo-DPIV and the middle one ($Cam1$) for the soap film pattern visualization. (c) Top view of the experimental layout for Case D.

2.2.3.2.Case B: Digital Particle Image Velocimetry (DPIV)

Time-resolved planar DPIV measurements were taken using 6 μm diameter hollow glass particles (mean diameter: 6 μm, size range: $10\% < 3\mu m$, $90\% < 9\ \mu m$, density: 1.00-1.05 g/cm^3, Potters Industries) as flow tracers. A 532 nm wavelength LED array (TSI PIV01807,

Multi-Element Array Illuminator) illuminated a $5\ mm$ by $10\ mm$ ($5d$ spanwise by $10d$ streamwise) area of the film in the wake of the cylinder. To capture the light scattered by the glass particles, a 4-megapixel CMOS high-speed camera (Phantom V2640, $Cam1$ in Figure 2.2) equipped with a 105 mm Nikon lens at an aperture setting of $f16$ was used to record 5 sets of images at $Re \approx 100$, 200, and 300. For each experimental run, we collected 21000 images at 10500 Hz with a spatial resolution of 70.4 pixels per mm. The field of view of the images was $5d \times 10d$. The arrangement of the camera and LED array is shown in Figure 2.2.

2.2.3.3.Case C: Simultaneous interferometry and DPIV

The configuration of the cameras and the light sources used for Case C is depicted in Figure 2.2. We used two 29-megapixel CCD cameras (Imperx B6640, $Cam2$ and $Cam3$ in Figure 2.2) equipped with two 105 mm Nikon lenses at an aperture setting of $f16$, and both light sources were active simultaneously. $Cam1$, equipped with a 105 mm Nikon lens at an aperture setting of $f5.6$, was used to capture the soap film patterns illuminated by the sodium lamp, while $Cam2$ and $Cam3$ were positioned in a stereo configuration to record particle images illuminated by the LED array for DPIV measurements. For a flowing soap film, the out-of-plane velocity component is negligible compared to in-plane velocity components. Thus, planar DPIV is the most suitable tool for characterizing the flow, as described in Section 2.2.3.2. However, since we conducted DPIV and interferometry measurements simultaneously for this case, and since the camera was placed perpendicular to the film plane for the soap film pattern visualization via interferometry, for the simultaneous DPIV measurements we employed two cameras in a stereo configuration.

$Cam2$ and $Cam3$ were calibrated using a single-level dot-matrix target with $0.5\ mm$ diameter dots spaced $1.0\ mm$ apart (FA131, Max Levy Autograph). The calibration target was placed at the location of the soap film when the soap solution was not flowing. The calibration target was translated from $-1.5\ mm$ to $+1.5\ mm$ in the out-of-plane direction, and calibration images of the target were acquired at $0.5\ mm$ increments. A polynomial (third order in the plane of the film and second order in the out-of-plane direction) was then fit to the detected dot positions [46]. A self-calibration step to correct for misalignment in the calibration procedure was also performed as described by Wieneke [47].

The LED and all three high-speed cameras were synchronized, and band-pass optical filters were applied to block the unwanted wavelengths in each camera. For $Cam1$ we used an $OD4$ band-pass filter with a Center Wavelength (CWL) of $589\ nm$ and Full Width-Half Max (FWHM) of $10\ nm$, so that $Cam1$ only captured light rays from the sodium lamp. For each experimental run, we collected 1000 interferometry images at 1 Hz with a spatial resolution of 57.6 pixels per mm. The field of view of the images was $10d \times 20d$. For $Cam2$ and $Cam3$, we applied two $OD4$ band-pass filters with a CWL of $532\ nm$ and FWHM of $10\ nm$ so that they only captured the green LED beams. We collected 1000 DPIV images from each camera with a spatial resolution of 69.3 pixels per mm (1000 frame-straddled pairs with an inter-frame interval of $70\ \mu s$) that were synchronized with the interferometry images at $1\ Hz$. The field of view of the images was $5d \times 9d$. For this case, we recorded 5 sets of data (interferometry and DPIV images) at $Re \approx 100$, 200, and 300.

2.2.3.4.Case D: Background-Oriented Schlieren (BOS)

A schematic of the BOS experimental setup is shown in Figure 2.2(c). A regular grid of transparent dots on a black background with diameters of $0.15\ mm$ and edge to edge spacing of $0.15\ mm$ was printed on a transparency, mounted on an acrylic plate, and back-illuminated using an LED to create a dot pattern consisting of bright dots on a dark background (see Figure 2.5(a)). A polycarbonate plate was used in front of the LED as a diffuser in order to obtain uniform illumination throughout the field of view. The dot pattern was placed 1.9 cm behind the soap film, and a Phantom V2640 camera ($Cam1$) equipped with a $105\ mm$ focal length lens at an aperture setting of $f32$ was placed $12.5\ cm$ away from the soap film. The effective magnification at the plane of the dot pattern was 13 μm/pixel (1:1) and the field of view was 7.5d spanwise by 10d streamwise. The resulting dot diameter on the image was 8 pixels. The dot pattern was imaged through the soap film at 600 Hz to provide adequate temporal resolution. Five sets of images were collected at $Re \approx 100, 200, 300$. In addition, 100 images of the pattern were recorded without the soap film present and averaged to provide a reference image. The reference image and the images with the soap film were processed using PIV-type cross-correlation algorithms to extract the displacement and relative thickness fields. To obtain the displacement field, every dot pattern imaged through the soap film was cross-correlated with the reference image. The PIV processing

and thickness integration methodologies are described in Section 2.3. The refractive index of the soap film was measured using a digital refractometer (Misco Palm Abbe, PA202) to be 1.3375; this data was needed to estimate the thickness field.

2.3.Post-processing methods

The main objective of the post-processing was to identify and quantify the center positions of coherent vortices in the soap film using interferograms, DPIV velocity fields, and BOS thickness fields. In Section 2.4 we compare the locations determined with these different methods and quantify any discrepancies. These vortex core locations and the corresponding circulations are then compared with the data for cylinder wake vortices observed in three-dimensional experiments as reported in the literature.

2.3.1. Case A: Soap film pattern visualization by interferometry

For the soap film images obtained using interferometry (Case A and Case C), circular shapes in the flow pattern are assumed to correspond with coherent vortices. These circular vortical shapes were identified using a modified Circle Hough Transform (CHT) [48–50]. The CHT aims to find circular patterns of a specified radius R within an image. The CHT is formulated as a convolution whose binary mask coefficients are set on the circle boundary and are zero elsewhere. This convolution is applied to an edge magnitude image (after suitable edge detection). For the CHT calculation, a separate circle filter is used for each radius of circle to be detected. For the interferograms in case A, we used the magnitude of image gradient to detect edges and defined the range of radius in the circle filter to be from $0.25d$ to $1.5d$. Figure 2.3(b) shows the application of this technique to a portion of the cylinder wake that also includes non-circular mid-wake vorticity. The geometric centers of the identified circles in the wake region are taken to be the vortex centers.

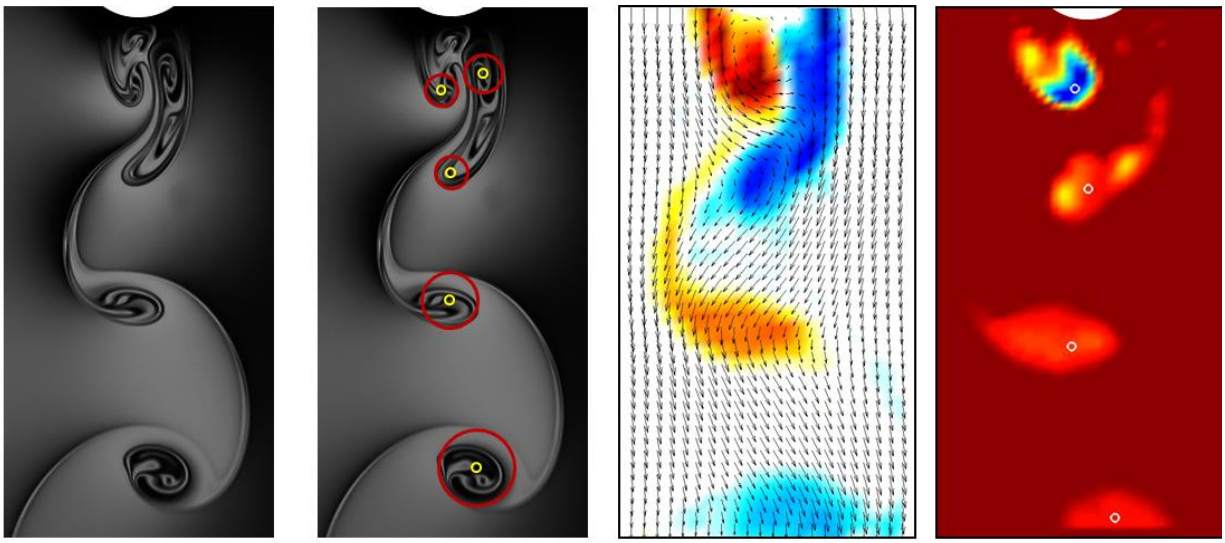

(a) (b) (c) (d)

Figure 2.3. (a) Interferogram in the wake of a stationary cylinder and (b) boundaries and vortex centers identified using a modified CHT technique; (c) velocity vector field obtained from DPIV processing with the calculated vorticity field, and (d) the λ_2 field and vortex centers (white circle) the DPIV data. FOV for all panels is approximately $3d \times 5.75d$.The example shown in (a,b) is similar to that in (c,d), but these are not phase-matched.

2.3.2. Case B: Digital Particle Image Velocimetry (DPIV)

For the DPIV images obtained in Case B (and also for Case C), our in-house DPIV processing software was employed to determine the velocity field in the cylinder wake. We used Robust Phase Correlation (RPC), which delivers improved accuracy and spatial resolution compared to conventional methods when processing images with a low signal-to-noise ratio. RPC builds upon our earlier work [51,52] and recent advancements [53–55] by incorporating a series of optimized filters to the Fourier-based cross-correlation. In this manuscript, the particle images were processed using RPC in a multi-grid window deformation framework with intermediate passes smoothed and validated using Universal Outlier Detection [52,54–56]. A total of four passes were used with the window resolution varied from 64×64 pixels on the first pass to 16×16 pixels on the last pass, and with a window overlap varied from 87.5% on the first pass to 50% on the last pass to provide a final grid spacing of 8×8 pixels corresponding to a spatial resolution of $0.11\ mm$.

Uncertainty in the velocity fields was quantified using a Moment of Correlation method as described in [57]. Uncertainty was computed using both the 1σ (68.5%) and 2σ (95%) confidence intervals. Detected outliers were not included in the uncertainty calculation. The estimated

uncertainty of the velocity components at each Re value for the 1σ and 2σ confidence intervals are presented in Table 2.2. The obtained velocity field was then denoised with a fully autonomous and objective mode-selection POD filtering method [58].

Table 2.2. Quantified uncertainty in the velocity components at each nominal Re value for the 1σ and 2σ confidence intervals.

Nominal Re	Case B DPIV		Case C Stereo DPIV	
	u $(1\sigma, 2\sigma)$	v $(1\sigma, 2\sigma)$	u $(1\sigma, 2\sigma)$	v $(1\sigma, 2\sigma)$
100	$0.08\ px, 0.21\ px$	$0.07\ px, 0.19\ px$	$0.11\ px, 0.24\ px$	$0.10\ px, 0.23\ px$
200	$0.07\ px, 0.20\ px$	$0.07\ px, 0.19\ px$	$0.11\ px, 0.24\ px$	$0.09\ px, 0.22\ px$
300	$0.07\ px, 0.17\ px$	$0.07\ px, 0.18\ px$	$0.09\ px, 0.23\ px$	$0.09\ px, 0.18\ px$

Vorticity, area, and circulation of the vortices in the wake region were computed. The vorticity field and the velocity gradient tensor were calculated from the denoised velocity field using a fourth-order central difference scheme [59]. The λ_2-criterion [60] with a 3.0% of the maximum value thresholding was applied to identify the vortical structures in the cylinder wake; related alternative choices include the Δ-criterion [32] (as used in [31]) and the Q-criterion [61]. In the λ_2 method, a vortical structure is defined as a connected region in which the $\lambda_2$value is negative. An example of the identified structures is presented in Figure 2.3(c,d). For an individual identified vortical structure, say vortex α, we used an area-weighted average of λ_2 to find the vortex center, $\boldsymbol{x}_\alpha$. An equivalent diameter for each vortex was computed using the area, $A_\alpha(t)$, identified by the λ_2 output. The time-dependent circulation of each vortical structure, $\Gamma_\alpha(t)$, was computed for this area using both the line integral of the velocity and the area integral of the vorticity, namely

$$\Gamma_\alpha(t) = \oint_{C_\alpha(t)} V.n\ dl = \int_{A_\alpha(t)} \omega.n\ dS, \qquad \text{Equation 2-3}$$

where $\boldsymbol{C}_\alpha(t)$ is the boundary curve for area $A_\alpha(t)$. Mathematically, these two integrals should produce the same value of circulation; however, discrepancies can occur because of experimental noise and approximation errors from the differentiation. For each individual vortex, these two

circulation values were thus averaged to determine the representative circulation, or vortex strength, as a function of time.

2.3.3. Case C: Simultaneous interferometry and DPIV

Post-processing for Case C was similar to that for Cases A and B, but with some modifications resulting from the interferometry and DPIV methods being used simultaneously. The DPIV analysis required seeding the soap solution with particles that contaminated the soap film pattern images, and the position of the cameras required the use of stereo DPIV, as described in Section 2.2.3.2.

As shown in Figure 2.4, particle-contaminated images differ from the interferometry images observed in Case A. To explain this difference, we consider the formation principle of soap film interference fringes. Soap film patterns result from the interference of light waves reflected from the back and front boundaries of the film (see Figure 2.4(a,b)). In the particle-contaminated soap film, at locations where particles are present between the two boundaries, the light beam is not reflected from the back boundary of the film and the light interference is corrupted (see Figure 2.4(c)). Therefore, no interference pattern is formed at these locations and, instead, images of the particles are captured. Throughout the remainder of the film, interference patterns are formed (see Figure 2.4(d)). To extract these interference fringe patterns from the noisy images, two additional processing steps were added: image contrast was enhanced, and the image was sharpened, as illustrated in Figure 2.4(d). These images were then post-processed using the same methods described in Section 2.3.1 to identify vortex centers.

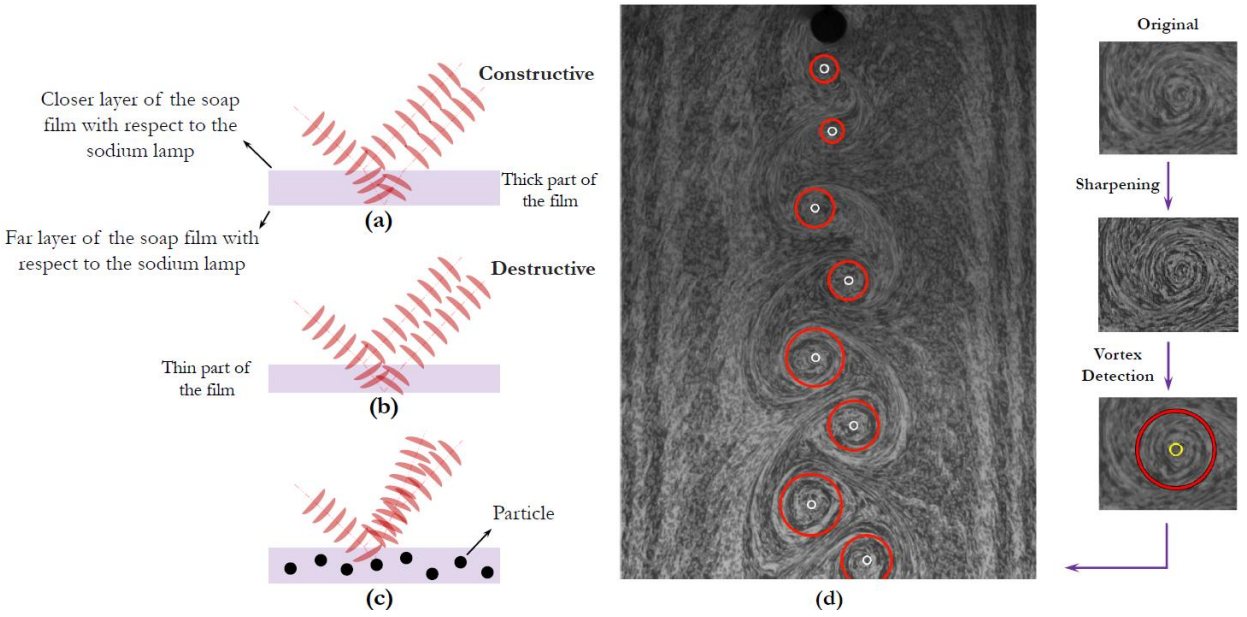

Figure 2.4. Constructive and destructive interference in the (a, b) absence and (c) presence of particles used for the DPIV measurements. The degree of constructive or destructive interference between the two light waves in the soap film depends on the wavelength of the light source, the thickness of the film layer, the angle of incidence of the original wave on the film, and the refractive index of the film [22,23]. (d) Identified circular objects in the soap film patterns in the presence of particles using the same methods as for Case A. FOV of the interferometry image is $10d \times 14d$.

Prior to processing the particle images captured by $Cam2$ and $Cam3$, the calibration step was performed as described in Section 2.2.3.3. The calibration provided a mapping between the two-dimensional object plane (the soap film) and each two-dimensional image plane from $Cam2$ and $Cam3$. DPIV processing parameters for Case C were the same as given for Case B in Section 2.3.2. Image pairs from each camera ($Cam2$ and $Cam3$) were cross-correlated separately and the $v_x -$, $v_y -$, and $v_z -$component velocities were reconstructed as described in [46] using the mapping function obtained from the calibration. Post-processing of the resulting velocity field to determine vortex core locations was performed as described in Section 2.3.2.

The uncertainty in stereoscopic PIV (stereo PIV) is a combination of the planar PIV uncertainty for each camera and the uncertainty in the stereo calibration function. We employed the framework proposed by [62] for stereo-PIV uncertainty estimation. In this framework, the individual camera image correlation uncertainty is combined with the angle uncertainty to get the uncertainty in the three velocity components. For each individual camera, uncertainties in the

displacement field were calculated using the Moment of Correlation method [57]. The angle uncertainty was obtained by propagating the elemental uncertainties (including the origin of calibration uncertainty, triangulation uncertainty, least-squares fit uncertainty, calibration mapping function coefficient uncertainty) through the mapping function gradient equation [62]. The estimated uncertainty of the velocity components at each Re for the 1σ and 2σ confidence intervals are presented in Table 2.2.

2.3.4. Case D: Background-Oriented Schlieren (BOS)

BOS images such as shown in Figure 2.5(b) were obtained using the setup described in Section 2.2.3.4. These BOS images were processed using RPC similar to the DPIV measurements (see Section 2.3.2). A total of four passes were used, with the window resolution varied from 64×64 pixels in the first pass to 16×16 pixels on the last pass. A window overlap of 50% was used for each pass for a final grid spacing of 8×8 pixels corresponding to a spatial resolution of 0.10 mm. This procedure yielded spatially and temporally resolved displacement fields such as the example shown in Figure 2.5(c).

As shown by Auliel et al. [24], a light ray traversing the soap film will experience refraction corresponding to the local thickness gradient, with a vector angular deflection of the light ray given by

$$\boldsymbol{\theta}(\boldsymbol{x}, t) = 2\left(\frac{n_{soap}}{n_{air}} - 1\right)\nabla\eta(\boldsymbol{x}, t), \qquad \text{Equation 2-4}$$

where $\eta = h - \bar{h}$ is the relative film thickness, with $\bar{h}$ the (constant) mean film thickness, and n_i is the refractive index of soap or air, respectively. This angular deflection can be related to the apparent displacement of the dot pattern obtained with BOS using the relationship [25]

$$\boldsymbol{\theta}(\boldsymbol{x}, t) = \frac{\boldsymbol{\xi}(\boldsymbol{x}, t)}{MZ_D}, \qquad \text{Equation 2-5}$$

where $\boldsymbol{\xi}(\boldsymbol{x}, t)$ is the displacement field of the dot pattern estimated from the cross-correlation analysis, M is the non-dimensional magnification of the dot pattern and Z_D is the perpendicular distance between the dot pattern and the soap film.

By combining Equation 2-4 and Equation 2-5, we obtain a relationship for calculating the local thickness gradient of the soap film from the image displacements of the dot pattern and the experimental parameters, including the optical layout and the refractive index of the soap film, namely

$$\nabla\eta(\boldsymbol{x}, t) = \frac{1}{2\left(\frac{n_{soap}}{n_{air}} - 1\right)} \frac{\boldsymbol{\xi}(\boldsymbol{x}, t)}{MZ_D}. \qquad \text{Equation 2-6}$$

Similar to what is done for standard BOS measurements [63], the equation for the thickness gradient field,

$$\frac{\partial^2\eta}{\partial x^2} + \frac{\partial^2\eta}{\partial y^2} = S(x, y), \qquad \text{Equation 2-7}$$

is then spatially integrated using a Weighted Least Squares [64] solver with Dirichlet boundary conditions on the left and right boundaries to obtain the thickness field η. $S(x, y)$ is a source term calculated from the divergence of the measured thickness gradient field, $S(x, y) = \nabla \cdot (\nabla\eta)$, where $\nabla\eta$ is determined empirically using Equation 2-6.

To solve Equation 2-7, the partial derivatives are discretized using a second-order central difference method and the system of linear equations are solved along with boundary conditions to obtain the thickness field,

$$\eta\,(\boldsymbol{x}, t) = (G^T W G)^{-1}(G^T W \nabla\eta). \qquad \text{Equation 2-8}$$

The weight matrix, W, assigned to each thickness gradient measurement is based on the inverse of the thickness gradient uncertainty, namely

$$W\ (\boldsymbol{x},t) = \left(\sigma_{\nabla\eta}\ (\boldsymbol{x},t)\right)^{-2} = \left(\frac{1}{2\left(\frac{n_{soap}}{n_{air}}-1\right)}\frac{\boldsymbol{\sigma_{\xi}}(\boldsymbol{x},t)}{MZ_D}\right)^2, \qquad \text{Equation 2-9}$$

where $\boldsymbol{\sigma_{\xi}}(\boldsymbol{x},t)$ is the displacement uncertainty associated with the cross-correlation analysis. Less reliable measurements are assigned a lower weight to improve the overall robustness of the integration procedure [64].

Dirichlet boundary conditions were imposed on the left and right boundaries of the flow domain, as they are six-cylinder diameters away from the axis of the cylinder along the horizontal and hence are assumed to be the free-stream. The thickness at these boundaries was set to zero, and therefore the thickness values in the field are the deviations with respect to these boundaries. That is, our solution approach results in determining the *relative* thickness field. Neumann boundary conditions were imposed on the top and bottom boundaries.

In this manner, BOS was used to determine a quantitative spatially and temporally resolved relative thickness field for the soap film, as shown in Figure 2.5(d). In this relative thickness field, each local minimum in the relative thickness was defined as a vortex center.

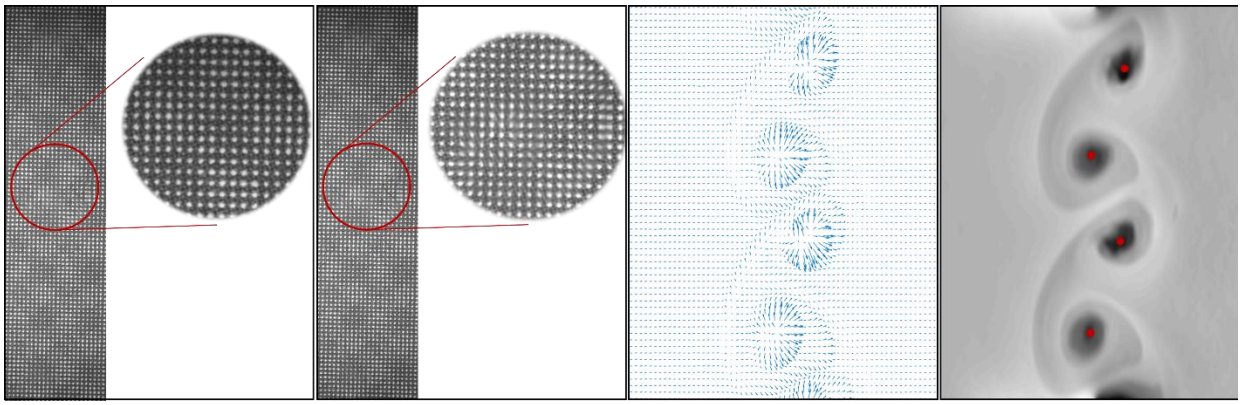

(a) (b) (c) (d)

Figure 2.5. (a) BOS grid dots in the absence of flow (reference image with no distorted dots), (b) example of raw data image (the pattern is visible in the magnified panel: see the distorted dots), (c) displacement field, and (d) relative thickness field with identified vortex centers (red markers).

Experimental uncertainties in the BOS measurements were propagated through the complete thickness integration procedure according to [65]. Uncertainties in the displacement field were calculated using the Moment of Correlation method [57] and then propagated through the optical layout followed by the WLS solver to obtain the uncertainty in the thickness field. Maximum uncertainties in the thickness field were approximately $0.02\ \mu m$, corresponding to 0.5% of the average thickness ($\bar{h} = 4.7\ \mu m$).

2.4.Results and discussion

Our experimental procedures and analysis enabled quantitative identification of the flow structures, specifically the vortex centers, in a cylinder wake using three different techniques and quantitative comparisons of the results from these different techniques. The ability of the interferometry and DPIV techniques to consistently quantify the same flow structures was determined through direct comparison of these techniques using Case C. The influence of varying experimental conditions on the interferometry and DPIV results was evaluated through various comparisons of Cases A–C. The interferometry and DPIV results were also compared with those obtained using BOS in Case D. Finally, the characteristics of the soap film wake structure were compared with published observations from low Reynolds number wakes to validate the use of a flowing soap film as an experimental platform for investigating two-dimensional flow phenomena.

2.4.1. Identifying flow structures in a flowing soap film

Figure 2.6 shows the wake of a stationary cylinder visualized simultaneously in Case C using interferometry (panel (a)) and using DPIV (panel (b)) at one particular instant in time. The vortex centers identified by each of these techniques are shown for this instant in Figure 2.6(c). Although this example shows one single instant, it illustrates the general trend: the discrepancy in vortex center identification is greatest in the near wake region, and this discrepancy decreases nearly monotonically with increasing streamwise location.

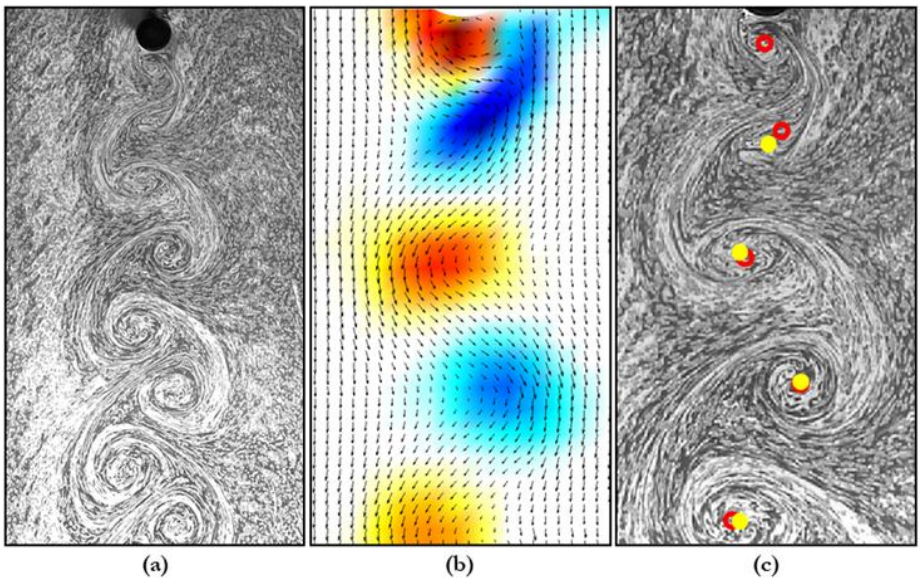

Figure 2.6. Wakes of a stationary cylinder from Case C at $Re \approx 200$: (a) soap film interferometry patterns in the presence of seeded particles and (b) velocity vector field from DPIV; both panels show the same wake at the same instant in time, but the magnification (field of view) is different. (c) Vortex centers superimposed on a magnified visualization image; red open markers are from DPIV and yellow solid markers are from interferometry. FOV of images: (a) $7d \times 13d$, (b, c) $4d \times 8d$.

To quantify this discrepancy, the vortex centers from the interferometry analysis, $\boldsymbol{x}_{\text{int}}$, at each instant of time are assigned to a bin location in the streamwise direction; for the purpose of this analysis, we used a bin size of $\Delta x = 0.025d$. For each of these centers, there is a corresponding center location determined using DPIV, $\boldsymbol{x}_{\text{DPIV}}$. For Case C, the simultaneous measurement techniques ensure that these locations were determined for the identical instant in time. The corresponding discrepancy, $\epsilon = |\boldsymbol{x}_{\text{int}} - \boldsymbol{x}_{\text{DPIV}}|$, is assigned to that bin location. The mean value of all discrepancies in a particular bin, $\overline{\epsilon}$, then represents the difference in the center locations identified by these methods at that streamwise position in the wake. Table 2.3 shows mean and maximum observed discrepancies for each Reynolds number tested; no dependence of these values on *Re* was observed.

Table 2.3. Observed mean and maximum discrepancies (with 95% confidence interval) between the vortex centers identified using interferometry and DPIV (Case C) or using interferometry and the minimum relative thickness (Cases A and D).

Nominal Re	Mean observed discrepancy ($\overline{\epsilon}$)		Maximum observed discrepancy, ($\epsilon_{\max}$)	
	DPIV vs. Int.	BOS vs. Int.	DPIV vs. Int.	BOS vs. Int.
100	$0.127d \pm 0.001d$	$0.032d \pm 0.001d$	$0.128d$	$0.034d$
200	$0.130d \pm 0.003d$	$0.033d \pm 0.002d$	$0.132d$	$0.036d$
300	$0.129d \pm 0.002d$	$0.032d \pm 0.001d$	$0.131d$	$0.033d$

In Figure 2.7(a) we show the combined $\overline{\epsilon}$ data for all three *Re* values as a function of streamwise position. The differences in the vortex locations are as large as $\epsilon_{\max} = 0.132d$. As shown in Section 2.4.2, the average streamwise spacing in our system was $\bar{a} \approx 4.7d$, with spacing dependent on *Re*, so that the observed discrepancy in the indentified vortex locations was $\epsilon/a \leq 3.2\%$ for $Re \lesssim 300$. The variation in the vortex center locations decreased with increasing distance downstream, becoming $\bar{\epsilon}/d \approx 0.02$ (or $\bar{\epsilon}/a \approx 0.4\%$) for $x/d \approx 9$. These results show that the interferometry and DPIV analyses obtained simultaneously in Case C both provide consistent quantitative identification of the same vortex structures in the wake of a stationary cylinder. That is, thickness variations in the film as identified using interferometry do provide an accurate representation of the vortex structures in a bluff body wake.

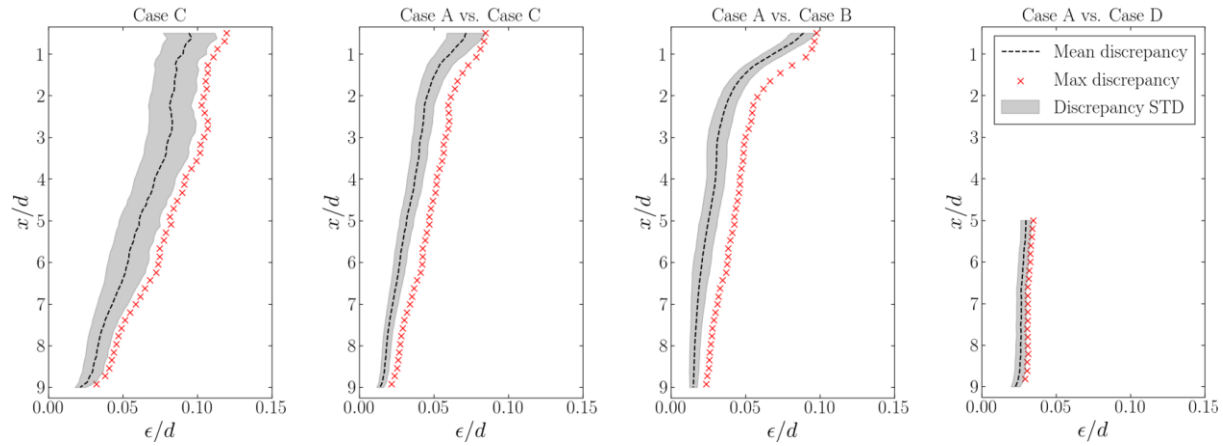

Figure 2.7. The discrepancy between the vortex centers as determined by (a) the simultaneous interferometry and DPIV measurements in Case C, (b) the interferometry measurements in Cases A and C, (c) the interferometry measurements in Case A and the DPIV measurements in Case B), and (d) the interferometry measurements in Case A and the BOS measurements in Case D. The origin of the streamwise direction (x/d) is located at the center of the cylinder.

The observed spatial developments of the wakes from both Cases A and C are shown in Figure 2.8. At each value of Re, the vortex centers from the 5 data sets in Case A were spatially averaged to determine the most probable path of a shed vortex in the cylinder's wake. For comparison, representative vortex centers from the particle-contaminated flow (Case C) are superimposed on these paths in Figure 2.8. The discrepancy in the vortex center locations in Case A and using interferometry in Case C is quantified in Figure 2.8(b). For this comparison, both methods used interferometry to identify the vortex centers, but for Case C the film contained seeding particles while for Case A it did not. These results suggest that the presence of particles in the film did have an adverse effect on the identification of vortex cores using interferometry, although the level of error was small.

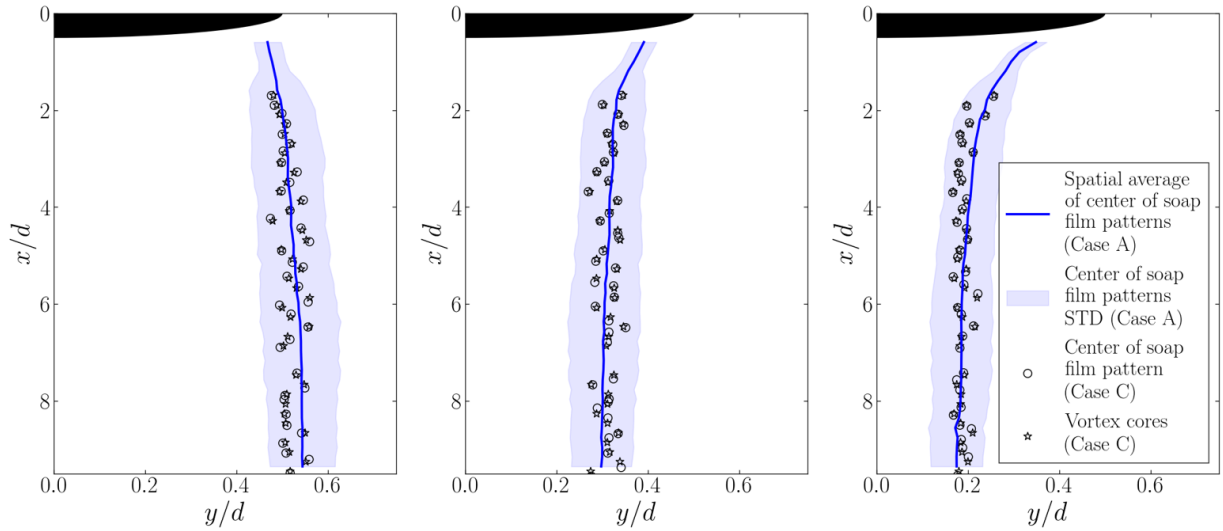

Figure 2.8. Comparison of vortex centers identified using interferometry and DPIV in the presence and absence of particles in the flow at (a) $Re \approx 100$, (b) $Re \approx 200$, and (c) $Re \approx 300$. The solid line is the spatial average of the vortex centers using interferometry with no particles (Case A); the shaded area shows the standard deviation. Markers show the vortex centers obtained from the concurrent experiment (Case C) using interferometry (circles) and DPIV (crosses).

Comparing vortex center locations between Case A and the other cases required phase-matching the wake structures. To do so, an interrogation window (IW) was defined based on the overlapped field of view of Case A and the other case; the size and location of the interrogation window used for each case are given in Table 2.4. Then, at each value of Re and for each of the 5 data sets in Case A, an arbitrary interferometry frame was selected to be cross-correlated with the

vorticity, thickness, or interferometry field of the other case. The phase-matched data was defined as that with the highest peak correlation score. Owing to the periodic nature of the cylinder wake, the remainder of the images were then phase-matched automatically by considering the sampling rate and shedding frequency of each set of data.

Table 2.4. The size and location of the interrogation window (IW) for phase-matching the wake structures defined based on the overlapped field of view of Case A and the other cases. The origin of the streamwise and spanwise directions is located at the center of the cylinder.

Overlapped field of view of Case A and	IW size (spanwise×streamwise)	IW expansion (spanwise)	IW expansion (streamwise)	Cross-correlated data
Case B	$5d \times 8.5d$	$-2.5d$ to $+2.5d$	$0.5d$ to $9d$	Vorticity field
Case C	$5d \times 8.5d$	$-2.5d$ to $+2.5d$	$0.5d$ to $9d$	Interferometry image
Case D	$5d \times 4d$	$-2.5d$ to $+2.5d$	$5d$ to $9d$	Thickness field

In all comparisons of vortex center locations determined using interferometry and DPIV across Cases A–C, the discrepancy in the locations was $\epsilon < 0.15d$, giving a relative error in the vortex locations of $\epsilon/a < 4\%$ over all cases. The discrepancy is largest for the near-wake region, $x/d \leq 2$. In this region of the wake, vortices are still forming and are not yet isolated circular structures, making them more difficult to consistently identify. It is possible that the identification of vortex centers in the interferometry data would be improved by the use of an elliptical Hough transform [66,67] instead of the circular Hough transform (CHT) employed here. For $x/d \geq 2$, the discrepancy is smallest when comparing the interferometry results from Case A (without seeding particles) with phase-matched DPIV results from Case B (using a standard single-camera technique). While the simultaneous measurements produced acceptable results, the most consistent identification came from the standard, independent methods. These results show that the presence of seeding particles in the film had a negligible effect on the fluid mechanics in the system, but that the effectiveness of the interferometry quantification technique was impacted (slightly) by the particles. Although Vorobieff et al. [31] recommended using submicron particles as a tracer in soap films to avoid any flow-tracking fidelity problems and interference with the physics of the flow, these results demonstrate that even particles with diameters the same order of magnitude as the film thickness do not interfere with the overall flow physics.

A representative example of the relative thickness field obtained using the BOS method in Case D is shown in Figure 2.9(a). In this approach, a vortex center is assumed to be located at a local minimum in the thickness field. Figure 2.9(b) shows these local minima superimposed on the corresponding phase-matched interferometry image from Case A. As one would expect, there is excellent agreement between the centers identified using these two thickness-based techniques. The discrepancy between phase-matched vortex center locations identified with these methods is quantified in Figure 2.8(d); for the streamwise range investigated with the BOS method, $5 \leq y/d \leq 9$, the observed discrepancy is $\epsilon/d \lesssim 0.036$ or $\epsilon/a \lesssim 0.8\%$ (see also Table 2.3).

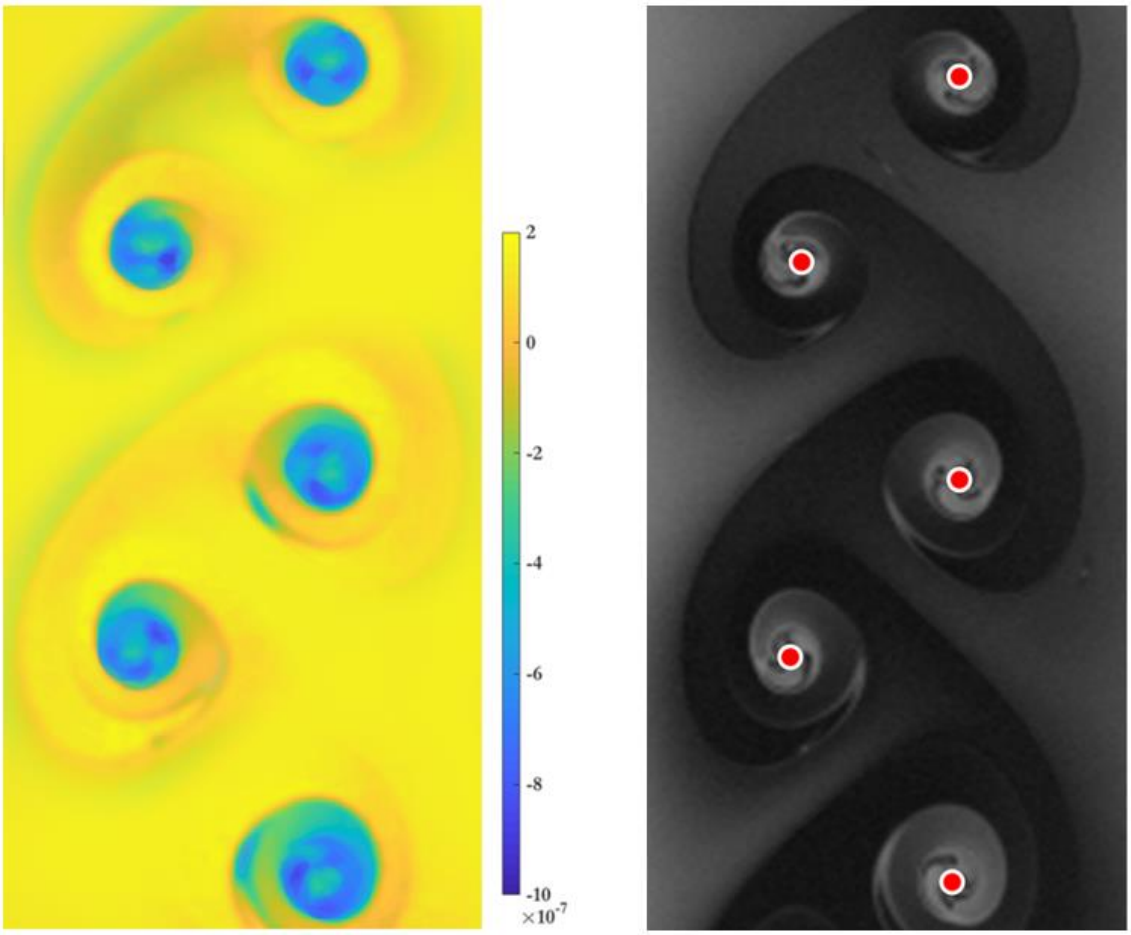

(a) (b)

Figure 2.9. (a) Relative thickness field, η, at one instant in time for $Re \approx 200$. Color scale indicates relative thickness value. (b) Comparison of the local minimum thickness locations (red markers) superimposed on the phase-matched interferometry image from Case A. The discrepancy between the interferometry and BOS vortex centers is quantified in Figure 2.7(d). FOV of images is $2.5d \times 4d$.

The BOS method allows us to quantify the relative film thickness in the cylinder wake. The thickness variations are crucial for flow visualization methods in soap films; however, large thickness variations may interfere with the physics of the flow, which is assumed to approximate that of an incompressible fluid [24]. Wu et al. [68] and Georgiev and Vorobieff [8] have demonstrated that a flowing soap film without obstructions produces an approximately uniform film thickness. However, the detailed thickness variation caused by the cylinder has not been previously quantified.

A representative example of the thickness field obtained using the BOS method in Case D is shown in Figure 2.10(a) together with the normalized thickness variations along two representative lines (AA and BB). We define the thickness variation percentage as the ratio of thickness range ($\Delta\eta = \eta_{max} - \eta_{min}$) at each snapshot over the average film thickness ($\bar{h}$). To find the film thickness variation at each Re, we averaged the instantaneous thickness variation over the time series. Figure 2.10(b) shows the thickness variation percentage as a function of Re.

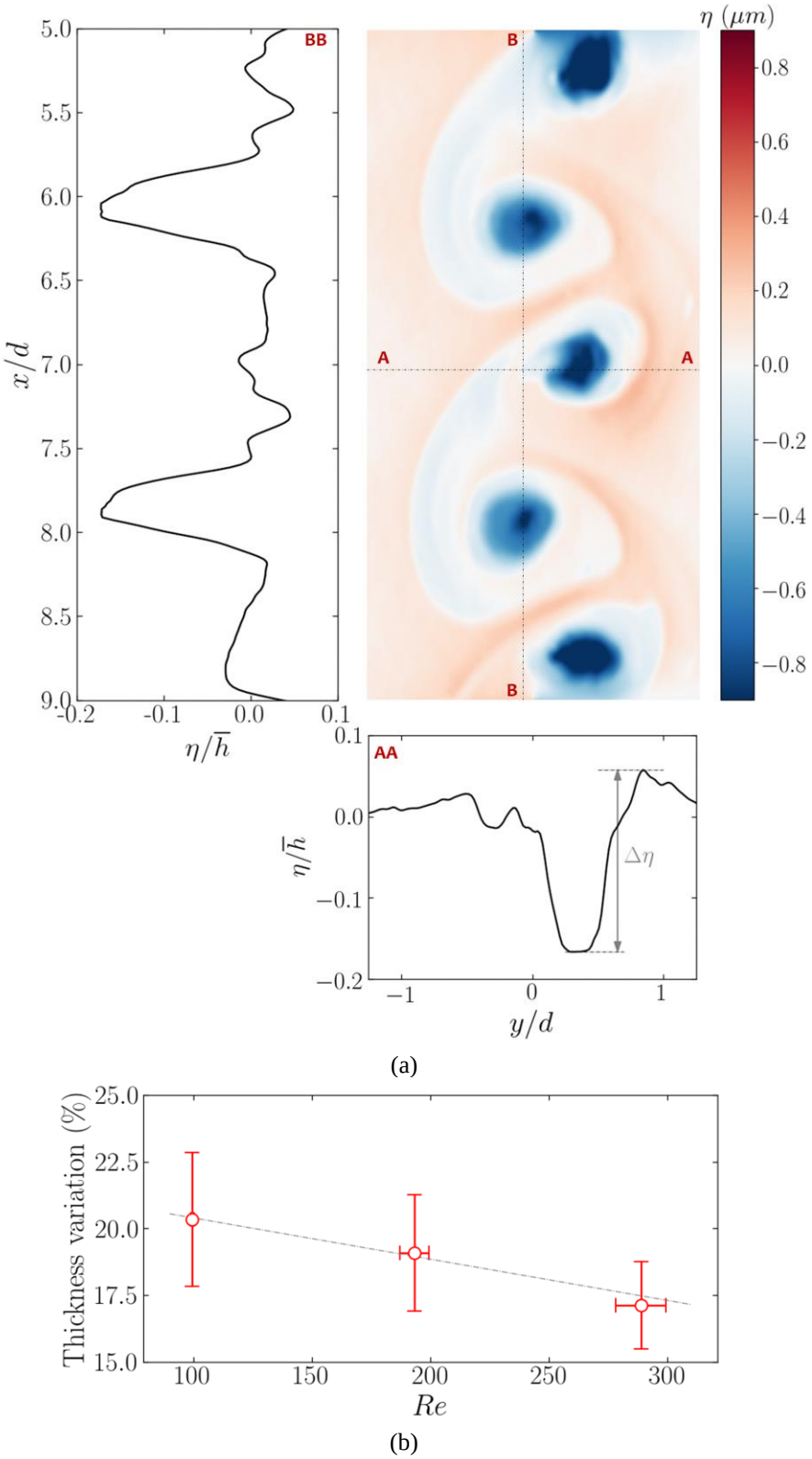

Figure 2.10. (a) Thickness field, η, and representative examples of thickness variation along the streamwise and spanwise directions at one instant in time for $Re \approx 300$. (b) Film thickness variation as a function of Re.

The maximum thickness variation observed in the wake of the cylinder was approximately 23%. In light of the favorable comparisons with incompressible, three-dimensional flows documented below, we consider this level of thickness variation to play a small role in the film dynamics except for how it represents the underlying flow structure.

2.4.2. Comparing soap film vortex wakes with existing results

Having established that the soap film interrogation approaches used in our study provide valid, interchangeable methods for identifying the vortex centers in a cylinder wake, we now address the question of whether the cylinder wake patterns in the soap film were consistent with other observations and models from the literature. To do so, we consider four quantities: (1) the streamwise distance between two consecutive vortices in the same row, a; (2) the spanwise distance between two consecutive vortices in parallel rows, b, which is typically reported in the literature as the dimensionless quantity b/a; (3) the eddy formation length, L_f, as defined by the streamwise location of the maximum velocity fluctuations, together with the magnitude of the velocity fluctuations; and (4) the circulation in the shed vortices.

Table 2.5. Wake characteristics (with 95% confidence interval) in the flowing soap film as a function of Reynolds number, consisting of the spanwise vortex spacing, a/d; the vortex formation length, L_f; and the normalized maximum streamwise velocity fluctuations along the centerline, $\sqrt{\overline{u'u'}}/U$.

Nominal Re	a/d	L_f	$\sqrt{\overline{u'u'}}/U$
100	5.29 ± 0.15	2.987 ± 0.25	0.24 ± 0.025
200	4.71 ± 0.12	2.13 ± 0.26	0.43 ± 0.045
300	4.11 ± 0.09	2.0199 ± 0.23	0.59 ± 0.050

In a laminar vortex street, the streamwise spacing, a, weakly depends on downstream location but is a strong function of Re [69–74], while the spacing ratio, b/a, depends on both downstream location and Re [69,73,75], with the observed widening due primarily to an increase in the spanwise spacing, b [76]. Table 2.5 lists the values of a from our experiments as determined using the DPIV data in Case B. Figure 2.11 depicts a and b/a for both the flowing soap film in the current study and for several three-dimensional systems reported in the literature. As shown in Figure 2.11(a), the variation of streamwise spacing with Re in a soap film agreed very well with

previously observed values [69,70,72,73]. For the transverse spacing ratio, b/a, there was more variation across all experiments, as shown in Figure 2.11(b), but the current soap film results were clearly consistent with the trends reported by the other studies. The constant spacing ratio predicted analytically by von Kármán [77] for an infinite, parallel vortex street is also shown for reference.

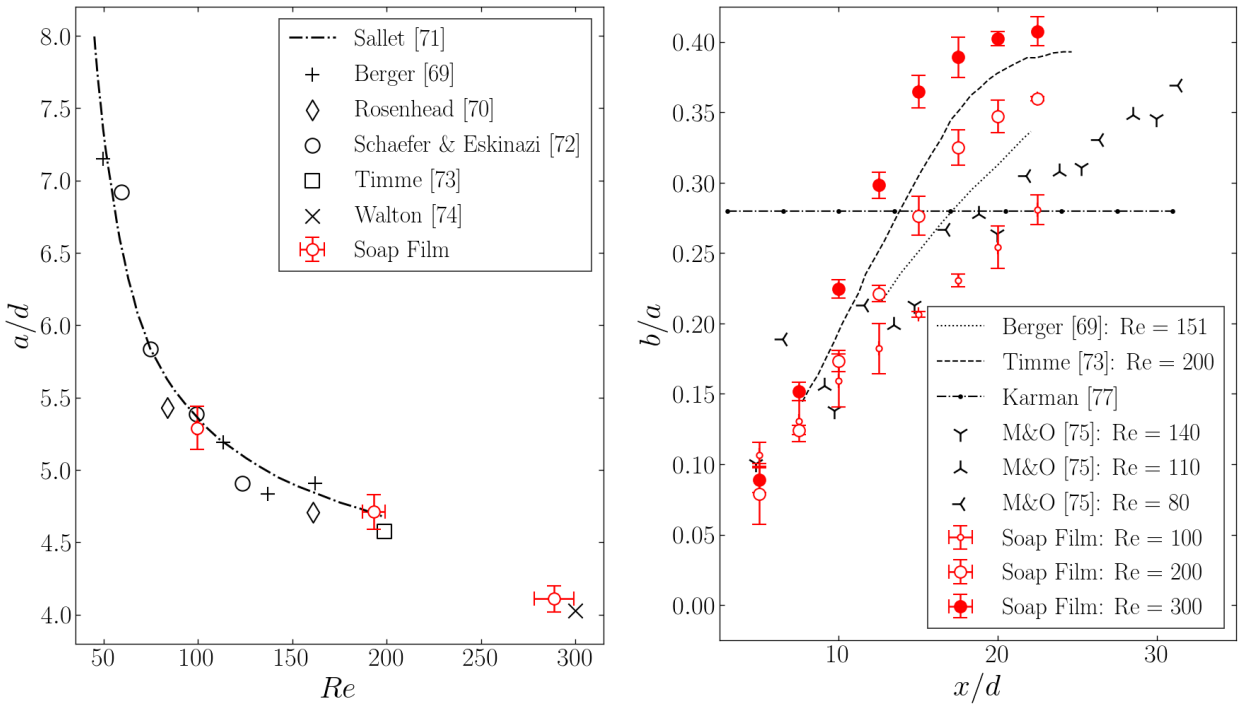

(a) (b)

Figure 2.11. Variation of (a) the average streamwise vortex spacing as a function of Re, and (b) the transverse spacing ratio with downstream distance and Re.

Another parameter that reflects the spacing and strength of passing vortices is the spatial variation in the magnitude of the time-averaged streamwise velocity fluctuations, $\overline{u'u'}$, in the wake [76]. The streamwise location of the maximum value of $\overline{u'u'}$ along the centerline has been defined as the eddy formation length, $L_f = (x/d)_{\max}$ [78], beyond which viscous dissipation gradually reduces the strength of vortices[1]. As shown in Figure 2.12(a), the values of L_f observed in the soap film were consistent with those measured in more traditional experimental systems [69,72,79–84]. Correspondingly, the normalized magnitudes of the instantaneous velocity

[1] A number of other definitions of vortex formation length have been introduced; see, e.g., Yang, Masroor & Stremler (in preparation).

fluctuation, $\sqrt{\overline{u'u'}}/U$, also compared favorably with published results [69,72,81–83], as illustrated in Figure 2.12(b), although the comparison is limited. The values of L_f and $\sqrt{\overline{u'u'}}/U$ from our experiments are listed in Table 2.5.

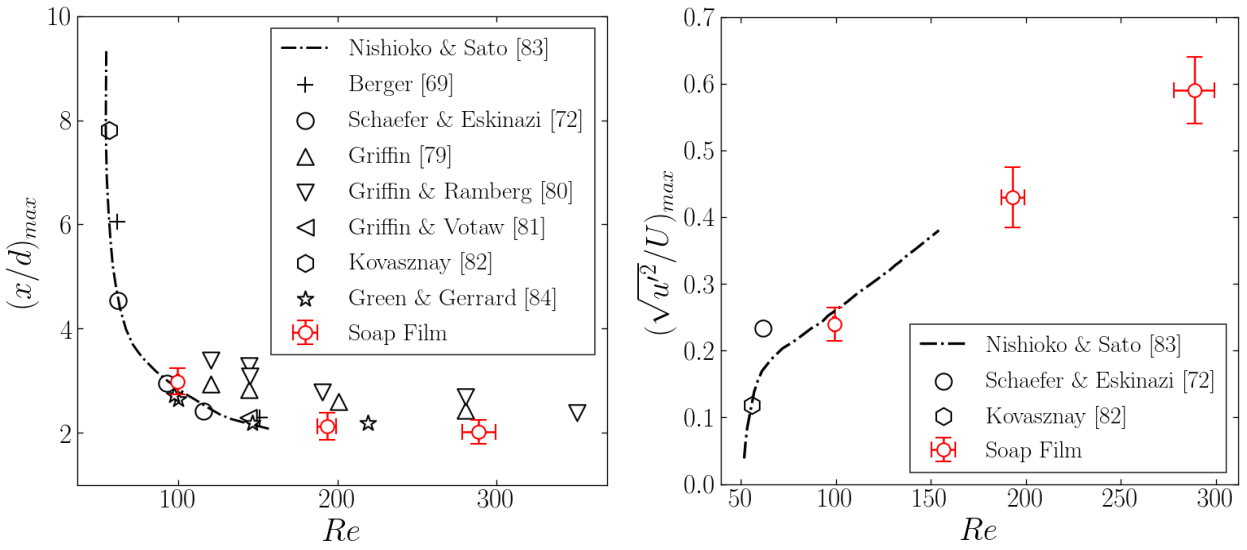

(a) (b)

Figure 2.12. Variation of (a) the length of the formation region and (b) normalized maximum velocity fluctuations as a function of Re.

The circulation of each vortex decreases with time through viscous dissipation. Using a procedure similar to that in Section 2.4.1 for determining the representative vortex locations, the individual vortex centers, $\boldsymbol{x}_\alpha(t)$, and corresponding circulations, $\Gamma_\alpha(t)$ in Equation 2-3, were assigned to bin locations in the streamwise direction with resolution $\Delta x = 0.012d$. The circulation values in each bin were averaged, giving the representative circulation in the wake as a function of (normalized) streamwise location, $\Gamma(x/d)$. The characteristic circulation for the wake was taken to be $\Gamma_0 = \Gamma(x/d = 2)$, the mean value of circulation at $x/d = 2$, which is the first location in the streamwise direction at which the circulation is determined. The mean and corresponding standard deviation of the normalized circulations, $\Gamma(x/d)/\Gamma_0$, are shown in Figure 2.13(a). For comparison with traditional measurements, the spatially dependent circulations were also averaged in the streamwise direction,

$$\bar{\Gamma} = \frac{1}{8}\int_{2}^{10} \Gamma(\chi) d\chi, \qquad \text{Equation 2-10}$$

where the integration variable is $\chi = x/d$. As shown in Figure 2.13(b), the values of $\bar{\Gamma}/\pi U d$ observed in the soap film were consistent with the majority of those measured in traditional experimental systems [69,72–74,85]; the result from Thom [86] is an outlier.

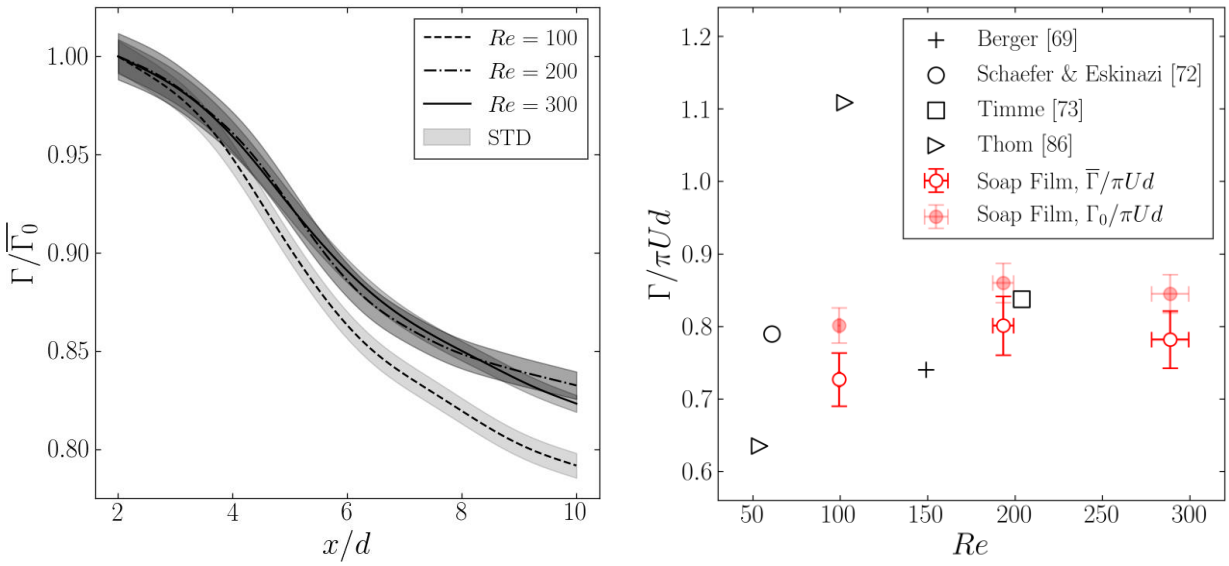

(a) (b)

Figure 2.13. Mean and standard deviation (STD) of the spatially-dependent representative circulation normalized by $\Gamma_0 = \Gamma(x/d = 2)$ at different Re. (b) Initial and averaged circulations compared with literature values as a function of Re.

For the range of Re values considered in this study, the characteristics of vortices in the flowing soap film correlated well with published results for three-dimensional flows in terms of streamwise spacing, transverse spacing ratio, length of the formation region, and vortex circulations. Also, the maximum velocity fluctuations obtained in the flowing soap film were consistent with previously reported results for three-dimensional flows. These results indicate that a flowing soap film is an appropriate tool for studying vortex wakes at low Re, an approach that overcomes a number of the challenges involved in conducting a well-controlled, low Reynolds number, three-dimensional flow experiment.

2.5.Summary

In this study, we have examined the correlations between classic and novel soap film interrogation techniques and the consistency of measurements in the wake of a stationary cylinder with results from studies in three-dimensional systems. To do so, we conducted a series of experiments designed for both simultaneous and independent collection of data using interferometry and digital particle image velocimetry (DPIV). We also introduced and validated a new background-oriented Schlieren (BOS) technique that can provide full-field quantitative measurements of the relative soap film thickness. Our results for $Re \approx 100, 200, 300$ show that these techniques provide interchangeable methods of identifying vortex centers in the wake of a stationary circular cylinder. The observed discrepancy in the vortex center locations as identified by both simultaneous and phase-matched interferometry and DPIV was $\epsilon/a < 4\%$ for all values of Reynolds number we considered, where a is the (average) streamwise spacing of like-signed vortices. Differences were greatest for $x/d \lesssim 2$ (or $x/a \lesssim 0.4$), which lies within the vortex formation region for every case. Vortices in this near-wake region do not consist of isolated, near-circular coherent structures, leading to greater discrepancies in the center locations identified by different experimental techniques. Differences were the greatest when comparing the interferometry and DPIV results obtained simultaneously in Case C; the high correlation of the other results suggests that some variation was introduced by the challenges associated with analyzing interferometry data from a particle-laden film. The observed discrepancy in the vortex center locations as identified by phase-matched interferometry and BOS was $\epsilon/a \lesssim 0.8\%$ in the far wake region for all values of Reynolds number we considered.

Comparisons of our results with those from prior experiments in three-dimensional systems demonstrate the validity of using a flowing soap film system as a two-dimensional laboratory model of the unsteady wake behind a circular cylinder at low Reynolds numbers. The streamwise vortex spacing, a, and the vortex formation length, L_f, two common metrics for quantifying the vortex wake structure, show excellent agreement with published results. Variations in the spanwise spacing ratio, b/a, and the magnitude of the maximum streamwise velocity fluctuation, $\sqrt{\overline{u'u'}}/U$, correlate well with prior observations. These results support the broader use of soap film studies for experimental investigations of low Reynolds number two-dimensional flow phenomena.

2.6.Authors contributions

Javad Eshraghi: Methodology, Software, Formal analysis, Data curation, Investigation, Visualization, Writing - original draft. Lalit K. Rajendran: Methodology, Software, Investigation, Writing - original draft. Wenchao Yang: Methodology, Writing - review & editing. Mark A. Stremler: Conceptualization, Methodology, Investigation, Supervision, Writing - original draft, review & editing. Pavlos P. Vlachos: Conceptualization, Methodology, Investigation, Supervision, Project administration, Funding acquisition, Writing - original draft, review & editing.

3. TO SEAL OR NOT TO SEAL: THE CLOSURE DYNAMICS OF A SPLASH CURTAIN

3.1.Background

Splashes are ubiquitous in nature and engineering as a result of an objects' impact on a free-surface (known as water entry) and govern processes form diving to ocean oxygenation. Work on water entry has been predominantly focused on the dynamics and fluid motion that occur below the surface [87–93], often not considering the dynamics of the splash curtain [88,94].

The study of splashes is dating back to 1908, where Worthington [95] published the results of his photographic investigations on crowns. Since then, two forces have been postulated as the driving factors for the closure of splashes: the cavity pressure difference with respect to the ambient, caused by the airflow rushing into the cavity behind the sphere, and the surface tension [96]. However, the interplay of these forces has been controversial, and some works selectively neglect one of the two and focus on the other as the governing parameter of the surface seal, in order to explain the closure of the splash curtain.

Gillbarg & Anderson [96] examined the splash evolution and closure under reduced pressure and assumed that the pressure drop across the splash curtain was equal to the dynamic pressure term from the Bernoulli equation, $1/2\rho V_0^2$, where ρ is air density and V_0 is the speed of the sphere at impact. In another study, Yakimov [97] who was investigating the effects of ambient pressure on the splash curtain, attributed the surface seal to the higher air drag experienced by the tip of the splash (referred to as rounded rim in our paper), which is responsible for the accumulation of liquid at the tip and relative thickening in comparison with splashes at lower ambient pressures. Furthermore, he estimated the pressure drop across the splash as $\Delta P = 1/2\rho(V_0^2 + 2V_0V_1)$, where V_0 is the airflow velocity, assumed to be the same as the projectile impact velocity, and V_1 is the velocity of the tip of the splash curtain ejecting upwards and outwards from the impact location.

However, Abelson [98] and Lee et al. [99] showed that the Bernoulli pressure drop is an underestimation of the actual pressure difference.

In addition to the studies that considered the pressure difference as the most significant factor in the surface seal, investigations of the interplay between inertia and surface tension at the length scale of the splash curtain thickness suggest that surface tension plays a significant role. Marston et al. [100] investigated splashes formed for different surface tension values and concluded that surface tension is not negligible in the surface sealing phenomena. Aristoff & Bush [101] presented an analysis of the water entry of small hydrophobic spheres, which also proposed a phenomenological model of the splash curtain shape at the time when it was assumed that the pressure differential was negligible, thus suggesting that the splash closure was primarily driven by surface tension. Also, these studies did not introduce any criteria for the transition from no surface-seal regime to surface-seal regime.

Hence, understanding what controls the occurrence of the surface-seal during water-entry remains elusive. As such, the principal aim of this study is to elucidate the role of the forces acting on the splash curtain and derive the physical mechanism that governs the surface seal. In doing so, we present the first detailed analysis and explanations of the splash curtain dynamics, supported by a new physical model and experimental observations, we show that the pressure difference is not negligible, and provide a scaling parameter that predicts the occurrence of the surface seal.

3.2.Experimental procedure

To study the dynamics of the splash curtain, we drop different spheres into a 25×40×50 cm^3 glass-sided aquarium tank filled with distilled water and record the phenomena using a high-speed digital video camera operating at 5000 fps. The tank does not interfere with cavity expansion or pinch-off for any of the experiments reported. The dropping mechanism is mounted above the tank to release spheres without imparting spin, which can strongly affect the cavity dynamics [93].

The projectiles used here include Acrylic ($\rho_s = 1.18$ g/cm^3), glass ($\rho_s = 2.40$ g/cm^3), alumina ($\rho_s = 3.96$ g/cm^3), steel ($\rho_s = 7.87$ g/cm^3), and tungsten ($\rho_s = 19.30$ g/cm^3) spheres of different diameters (d = 9.525–19.05 mm). In order to produce a cavity, the projectiles are coated with WX2100 [9,16], which creates a hydrophobic surface condition with a contact angle of 150 °–165 °. The sphere impact velocities ranged from 2.0 m/s to 6.0 m/s (by 0.5 m/s increments). The impact of a projectile of radius R_0 into a liquid at velocity U_0 is characterized by the non-

dimensional Froude number $Fr = U_0/\sqrt{gR_0}$, where g is the gravitational acceleration [17,18]. The Reynolds number (Re), the Weber number (We), and the Bond number (Bo), are also often used to provide insight into the interplay and relative importance of the physical forces governing free surface interaction in the water entry phenomenon; $Re = R_0U_0/\nu$ where ν is the kinematic viscosity of the liquid, $We = \rho U^2R_0/\gamma$ where ρ is the liquid density and γ is the surface tension, $Bo = \Delta\rho g R_0^2/\gamma$ where $\Delta\rho$ is the density difference.

3.3.Experimental observations

During the initial stages of impact, a splash curtain is ejected upwards and outwards, as seen in Figure 3.1 [105]. In addition, as the sphere descends into the fluid, an expanding air cavity is formed behind it [106].

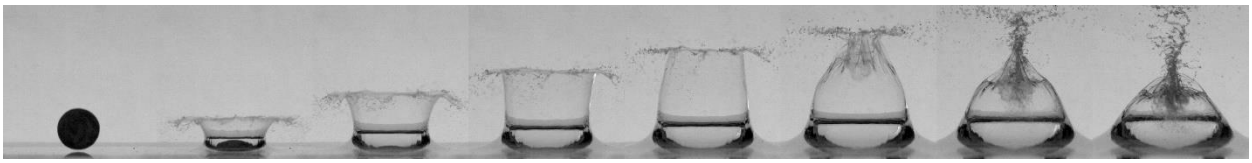

Figure 3.1. Splash curtain formed by a steel sphere, $R_0 = 0.95$ cm, $U_0 = 5.5$ m/s, $\Delta t = 3$ ms.

As the splash rises from the surface, it is subject to two main forces leading to its collapse: reduction in pressure caused by the airflow entrained into the cavity behind the sphere, and surface tension [13,21]. The air flowing into the expanding cavity induces pressure drag acting on the splash curtain and draws the splash radially inward. Surface closure is critical in the development of the cavity and influences the later cavity growth [16,22]. After surface closure, the cavity continues to expand due to the inertial effects of the sphere moving through the fluid, and the pressure inside the cavity decreases. The pressure governing the deep seal in the impact-produced cavities is the sum of the hydrostatic pressure due to the depth [13,17] and the pressure deficit in the cavity [21,23]. The higher the pressure difference between cavity and air above the surface, the closer the pinch-off location will be to the surface [10,23].

Our observations show that the cavity characteristics are highly dependent on the sphere density and do not scale linearly with Fr as had been observed experimentally by [110] for low Fr; The deviation is most pronounced for the cases with surface seal. Even though the modified

expressions for cavity characteristics developed by [94] agree with experimental observations in the regime without surface seal, they are not reliable in the surface seal regime, since the effect of surface seal on the cavity is ignored [111].

In the closure of the splash curtain, an intuitive interpretation might label an impact velocity as the primary cause in the occurrence of surface seal phenomenon. However, experimental observations imply dependency of the surface seal not only on the sphere impact velocity but also on the sphere size and density. To identify the surface closure mechanism, we will look at the interactions between the forces acting on the splash curtain, pulling it inward.

3.4.Splash curtain modeling

Shortly after the splash is ejected upon impact, surface tension causes the fluid at the tip of the splash to coalesce, forming a rounded rim. This rim is approximated as an axisymmetric circular ring about the z-axis, attached to a thin fluid film. In reality, the splash is very irregular, often forming a crown-like splash similar to those observed by [14,26].

The vector $\vec{x}(t) = r(t)\hat{r} + z(t)\hat{z}$, describes the position of the rim in the r-z plane. Figure 3.2(a) shows the splash geometry and coordinate system just after impact. Normal, $\hat{n}$, and tangential, $\hat{s}$, coordinates are also defined relative to the rim, in the direction of its instantaneous velocity. The angle θ is defined as the angle from the $\hat{r}$ unit vector to the $\hat{s}$ unit vector. Figure 3.2(b) shows the splash curtain at some later time as the trajectory of the splash has evolved. As the rim's trajectory evolves, the $\hat{n}$ and $\hat{s}$ coordinates remain fixed to the rim, and their orientation is described by the angle θ.

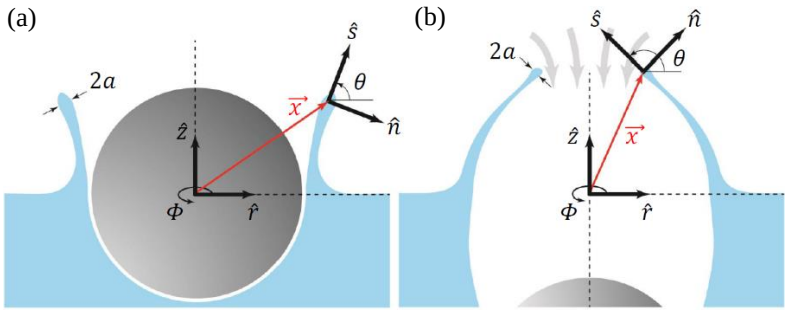

Figure 3.2. The coordinate system: (a) right after impact, (b) right before the surface seal.

The rounded rim is approximated by a finite mass, constant in time, with a circular profile in the r-z plane. The rim radius, a, is obtained from the experiment and assumed to be constant in time. With the assumed geometry and the coordinate system shown in Figure 3.2, a differential volume of the rim is given by $\rho\pi a^2 r d\phi$. This small mass is moving in a curved trajectory and has a centrifugal acceleration. This acceleration creates a force given by

$$\vec{F}_c(t) = \rho\pi a^2 r(t) d\phi \frac{|\dot{\vec{x}}(t)|^2}{R_c(t)} \hat{n}, \qquad \text{Equation 3-1}$$

where $R_c(t)$ is the instantaneous radius of curvature of the rim's trajectory given by

$$R_c(t) = \frac{d\theta(t)}{ds}. \qquad \text{Equation 3-2}$$

A drag force opposes the rim's motion, as the ejected fluid travels through the surrounding air. The drag force is given by

$$\vec{F}_d(t) = -\frac{1}{2}\rho_a C_d 2ar(t) d\phi |\dot{\vec{x}}(t)|^2 \hat{s}, \qquad \text{Equation 3-3}$$

where C_d is the drag coefficient. There have been many attempts to model the drag coefficient on drops and thin liquid sheets [113]. For simplicity, we have chosen to approximate the airflow around the rounded rim to be laminar, and the drag coefficient may be expressed as $C_d = 24/Re$.

Two surface tension forces need to be considered [28,29]. The first is a result of the thin fluid sheet attached to the rounded rim, given by

$$\vec{F}_{\gamma 1}(t) = -2\gamma r(t) d\phi \hat{s}. \qquad \text{Equation 3-4}$$

The sheet pulls the rim along the s direction, and we must account for both sides of the thin film (thus the factor of 2). The second surface tension force acts along the circumference of the rim, radially inward, given by

$$\vec{F}_{\gamma 2}(t) = -4\pi a \gamma d\phi \hat{r}. \qquad \text{Equation 3-5}$$

There is a gravitational force acting in the z direction [28,29], given by

$$\vec{F}_g(t) = -\rho g \pi a^2 r(t) d\phi \hat{z}. \qquad \text{Equation 3-6}$$

The expanding air cavity creates a pressure difference across the splash curtain. This pressure difference acts normal to the splash trajectory, collapsing it inward. This pressure difference creates a force given by

$$\vec{F}_{\Delta P}(t) = -2ar(t) d\phi \Delta P(t) \hat{n}, \qquad \text{Equation 3-7}$$

where $\Delta P(t)$ is the pressure difference across the splash. This pressure difference can be estimated by measuring the time rate of change of cavity volume, $dV_{cav}(t)/dt$. If the cavity is treated as a control volume, the rate of expansion (or collapse) can be thought of as the volumetric flow rate of air from the surrounding atmosphere into the cavity. If the area of the opening through which airflow is known, a mean air velocity, $U_{air}(t)$, can be estimated. With this mean air velocity, a pressure drop can be estimated using Bernoulli's principle.

The cavity was assumed to be axisymmetric about the z-axis (Figure 3.2(a)). Integrating the cavity radius, $R(z,t)$, over the length of the cavity, $Z(t)$, at each time step, yields the cavity volume history. An image processing routine was developed to determine the cavity profile from the captured image data and calculate the cavity volume, $V_{cav}(t)$.

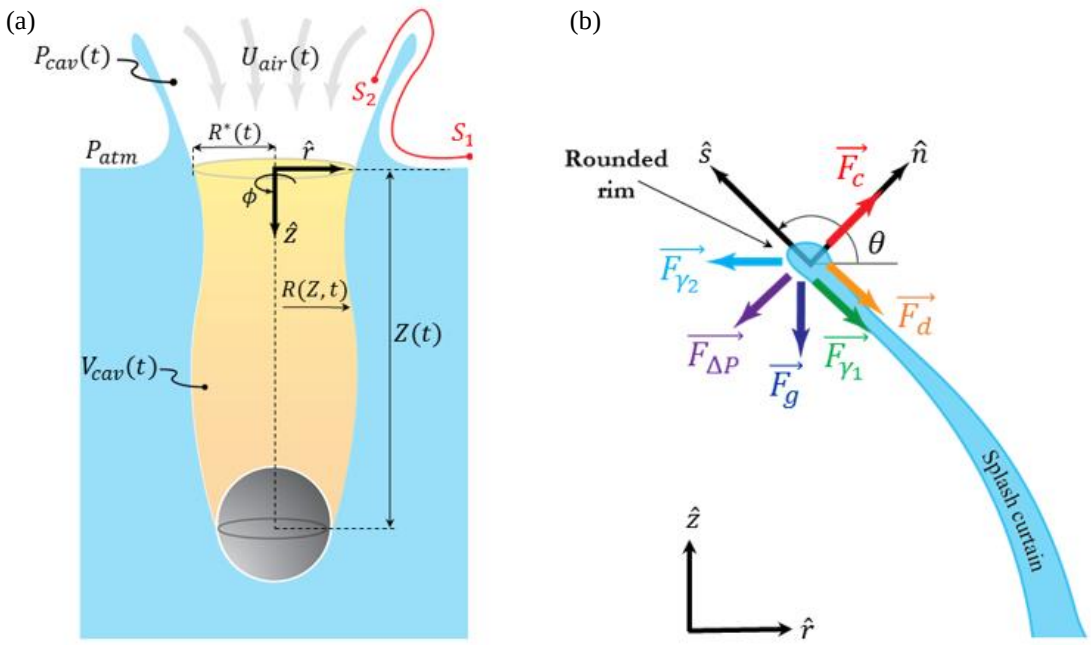

Figure 3.3. (a) Cavity behind the sphere. The cavity volume, $V_{cav}(t)$, can be approximated by integrating the cavity profile, $R(z,t)$, over the length of the cavity, $Z(t)$. (b) Forces acting on the rounded rim of the splash curtain.

As the sphere travels downward, it opens up and expanding the air cavity behind it. As the cavity expands, air is drawn into the cavity from the surrounding atmosphere. Neglecting compressibility effects, the time rate of change of cavity volume describes the volumetric flow rate of air into the cavity, given by

$$Q(t) = \frac{dV_{cav}(t)}{dt}, \qquad \text{Equation 3-8}$$

where $Q(t)$ is the volumetric flow rate. In order to suppress the amplification of noise, which can often be a problem for numerical derivatives, the cavity volume data was lightly smoothed using robust, locally weighted regression [116]. After the smoothing, a fourth-order central difference scheme was used to compute the derivative [117].

If the area of the opening through which the air flows is known, a mean air velocity, $U_{air}(t)$, can be estimated. We already found the cavity profile for cavity volume determination; thus, we consider the opening radius, R^*, at each time instant, t_i, as the $R^*(t = t_i) = R(z = 0, t_i)$, and the cavity opening area is $\approx \pi R^{*2}$. Hence, the mean airflow velocity can be estimated by

$$U_{air}(t) \approx \frac{Q(t)}{\pi R^{*2}}. \qquad \text{Equation 3-9}$$

This provides an estimate of the mean air velocity flowing from the surrounding atmosphere, past the splash curtain, into the air cavity. We can use this condition to estimate a cavity pressure using Bernoulli's principle. Picking two arbitrary points along a streamline, one outside the cavity and the other inside the cavity, we can write

$$\left[\rho g z + \frac{1}{2}\rho U^2 + P\right]_{S_1} = \left[\rho g z + \frac{1}{2}\rho U^2 + P\right]_{S_2}, \qquad \text{Equation 3-10}$$

where S_1 is some position far away from the cavity and S_2 is a position just inside the cavity, close to the rounded rim, as seen in Figure 3.3(a). Position S_1 was assumed to be at atmospheric pressure with no air motion. Position S_2 was assumed to be at cavity pressure, $P_{cav}(t)$, and have an airflow velocity of $U_{air}(t)$, given by Equation 3-9. Neglecting changes in elevation and assuming cavity conditions are constant throughout the cavity (not varying in space), the pressure difference across the splash can be estimated by

$$\Delta P(t) = P_{atm} - P_{cav}(t) = \frac{1}{2}\rho U_{air}^2(t), \qquad \text{Equation 3-11}$$

where $\Delta P(t)$ is the pressure difference across the splash. This assumes the air flowing into the cavity is incompressible, viscous effects are negligible and treats the cavity as a spatially uniform body. We will also assume that $P(t)$ is spatially uniform within the cavity. Figure 3.2(b) shows these forces and their directions relative to the splash curtain.

In this model, the force from the liquid sheet is ignored due to difficulty in measurement and estimation of fluid flow inside the thin sheet. Without experimental measurements, to estimate this force, we need to introduce several unknowns in the model, which will make the model complicated and more like a simple fitting. So, since the splash thickness is small, it is safe to ignore this effect.

Summing these forces results in an equation of motion for the rim, given by

$$\rho\pi a^2 r(t) d\phi \frac{d^2\ddot{\vec{x}}(t)}{dt^2} = \vec{F}_c + \vec{F}_{\gamma 1} + \vec{F}_{\gamma 2} + \vec{F}_g + \vec{F}_d + \vec{F}_{\Delta P}. \qquad \text{Equation 3-12}$$

Simplifying Equation 3-12 results in a second-order nonlinear ordinary differential equation describing the motion of the splash rim. The splash originates at a radial distance R_0 at the free surface ($z = 0$). The initial conditions in space are given by $\vec{x}(t = 0) = R_0\hat{r}$. The initial conditions for velocity are given by $\dot{\vec{x}}(t = 0)$, which is obtained from the experiment.

For a chosen set of system parameters and initial conditions, the trajectory of the splash curtain can be modeled by solving Equation 3-12. To validate the proposed model, we compare the rim trajectory predicted by the model with experimental observations in Figure 3.4 [32,33]. We define the first inflection point found in the splash curtain profile from the bottom of the curtain as the curtain rounded rim in the experimental videos (See Appendix 1).

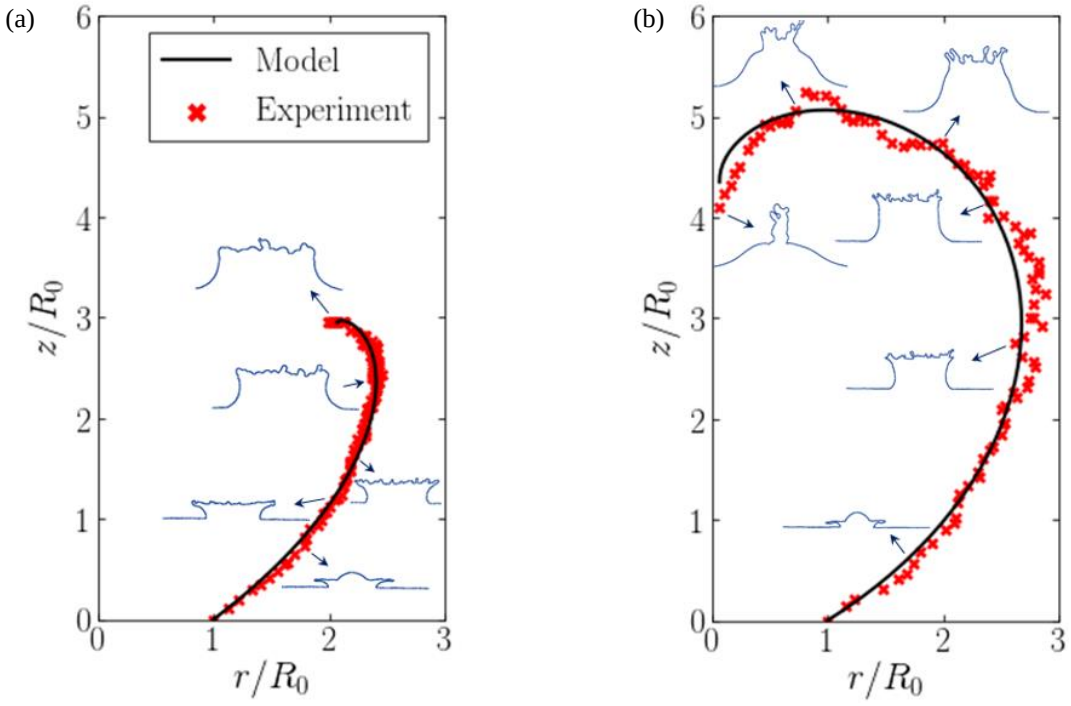

Figure 3.4. Splash curtain rounded rim trajectory: Experimental observation vs. Model prediction. (a) $We \approx 800$, $Bo \approx 12$, $DR = 7.87$, $U_{air,m}/U_0 \approx 0.1063$, (b) $We \approx 3950$, $Bo \approx 12$, $DR = 7.87$, $U_{air,m}/U_0 \approx 0.9474$ [118]. Density Ratio: $DR = \rho_s/\rho$, where ρ_s is sphere density.

Surface seal occurs when $r(t) = 0$. At this moment, the rounded rim has only one velocity component in the negative $\hat{z}$ direction. Thus, the occurrence of a surface seal, is defined by two criteria given by

$$t_{surf} \rightarrow \dot{r}(t) = 0 \;\&\; \dot{z}(t) < 0, \qquad \text{Equation 3-13}$$

where t_{surf} is the time elapsed between the initial impact of the sphere and the surface seal. The model predicts the surface seal as when the two criteria in Equation 3-13 are met. In the cases without surface seal, the time it takes for the splash to reach its maximum height is considered as the equivalent seal time, and the same criteria (Equation 3-13) are applied for modeling of these cases as well.

3.5.Discussion

The results of the model are susceptible to the pressure force. In the establishment of the pressure difference, we used the airflow velocity. Another approach for the formulation would be replacing the airflow velocity with the sphere impact velocity. Figure 3.5 shows a comparison between the surface seal time predicted by the model and the measured value from the experiment as well as the model performance sensitivity to the velocity selection in pressure difference formulation. Figure 3.5(a) indicates that the surface seal time predicted by the constant pressure difference, defined based on the sphere impact velocity, does not agree with the experimental measurements. On the other hand, by taking into account the instantaneous pressure difference across the splash curtain (Figure 3.5(b)), which is a representation of the cavity expansion history and airflow velocity, the maximum model error in the prediction of surface seal time is 5.6%.

Also, we report the dimensionless surface seal time as a function of We, defined based on sphere impact velocity, in Figure 3.6(a). Despite showing the general decaying trend with We, this scaling fails to identify a critical We for the transition from no surface seal regime to surface seal regime for all the spheres with different density and size [120].

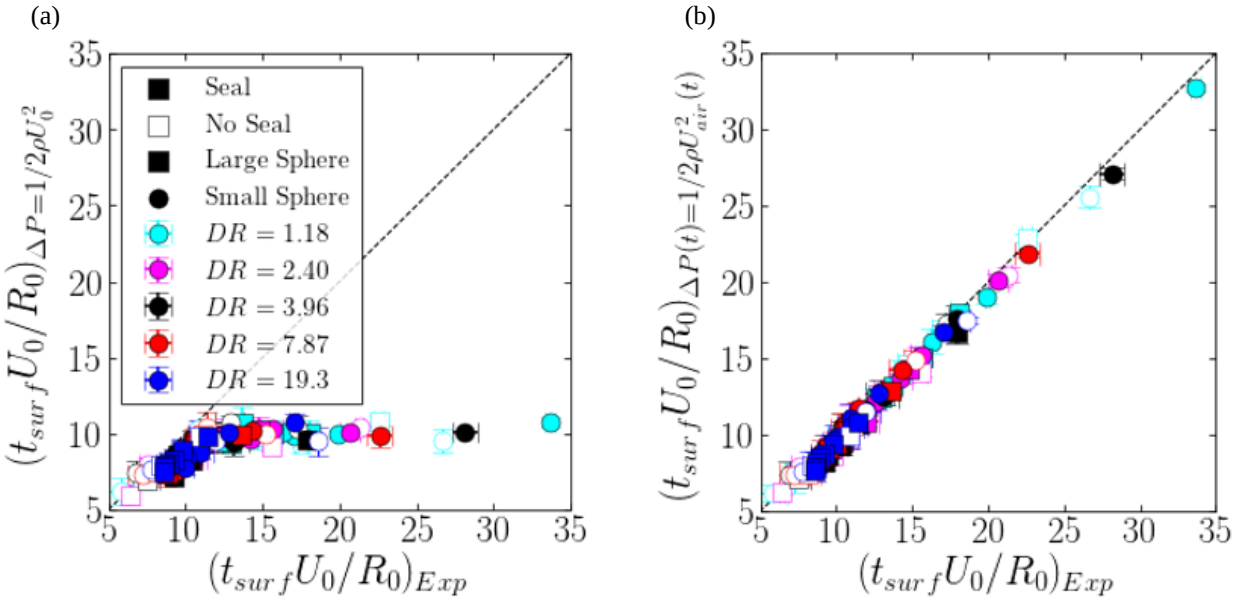

Figure 3.5. Model prediction for dimensionless surface seal time vs. measured value for two different approaches in pressure difference estimation. In (a), pressure difference was defined based on the sphere impact velocity, while in (b), the pressure difference was estimated using the cavity volume method. Cases without surface seal are shown with open markers.

Aristoff and Bush [15] scaled the dimensionless surface seal time with We and claimed that for $Bo \leq 3$ the surface seal occurs when the We exceeds ≈ 300. However, our observations show that this value has been underestimated, and how this value depends on the sphere density remained unexplored. For all the conditions tested, this surface seal criterion did not predict correctly the transition from no surface seal regime to surface seal regime and we observed no surface seal for $We < 850$ for the spheres with $Bo \approx 3$. Another proposed scaling for the surface seal time is based on the sphere impact velocity [10,13, 23] which also has the same limitation as We scaling. Namely, the impact velocity beyond which the surface seal occurs depends on sphere density and size. This limitation resulted in [10,13, 23] not proposing any criterion for the occurrence of surface seal based on the sphere impact velocity.

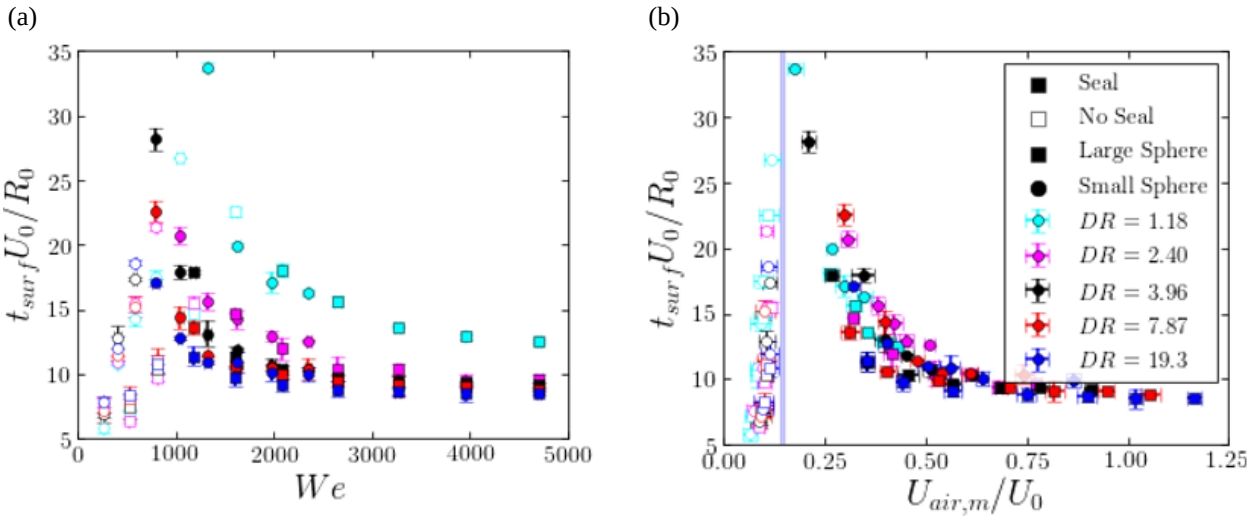

Figure 3.6. Dimensionless surface seal time as a function of (a) We defined based on sphere impact velocity, $We = \frac{\rho U_0^2 R_0}{\sigma}$, (b) ratio of air entrainment velocity to the sphere impact velocity, $U_{air,m}/U_0$. The predicted critical air entrainment velocity ratio from the mathematical model (Equation 3-21) is $U_{air,m}/U_0 \approx 0.146$ with an uncertainty of $\approx \pm 0.005$ (calculated based on the rounded rim radius, a, uncertainty).

These observations indicate that the sphere impact velocity is not the most significant parameter in the surface closure process. Based on the experiment, water entry cavities with quickly increasing volumes (high $dV_{cav}(t)/dt$ values) are associated with surface seal. In other words, surface seal cavities typically undergo a rapid increase in pressure difference (across the splash curtain) before dome closure, while a more gradual increase in pressure difference leads to a cavity without surface seal. Therefore, we can hypothesize that the closure dynamics of the splash is dominated by the pressure difference across it generated by cavity expansion and airflow into the cavity. Thus, to find the proper scaling for the dimensionless surface seal time, we only use pressure difference force to rewrite the equation of motion in the radial direction, $\hat{r}$, for the whole splash curtain

$$m\frac{d^2\vec{R}(t)}{dt^2} = \frac{1}{2}\rho A U_{air,m}^2, \qquad \text{Equation 3-14}$$

where m is the splash curtain mass and can be approximated as, $\rho A w$. Here, A and w are the splash curtain surface area and thickness, respectively. Also, $U_{air,m}$ is the temporal mean of

the air velocity averaged over the period of the sphere's impact to surface closure. Substitution leads to

$$\frac{d^2\vec{R}(t)}{dt^2} = \frac{1}{2w} U_{air,m}^2 \approx \text{const.} \qquad \text{Equation 3-15}$$

Solving Equation 3-15 for $\vec{R}(t)$ yeilds

$$\vec{R}(t) = R_0 - \frac{1}{4w} U_{air,m}^2 t^2. \qquad \text{Equation 3-16}$$

At the instant of the surface seal, $\vec{R}(t = t_{surf}) = 0$, and we find $t_{surf} = \sqrt{4wR_0}/U_{air,m}$. Assuming that the curtain thickness is a linear function of the sphere radius [101], $w \propto R_0$, surface seal time is deduced to be proportional to

$$t_{surf} \propto \frac{R_0}{U_{air,m}}. \qquad \text{Equation 3-17}$$

This suggests that the proper scaling for dimensionless surface seal time is defined based on the velocity of airflow into the cavity

$$\frac{t_{surf} U_0}{R_0} \propto \frac{1}{\frac{U_{air,m}}{U_0}}. \qquad \text{Equation 3-18}$$

Thus, we plot the dimensionless surface seal time as a function of air entrainment velocity to the impact velocity ratio in Figure 3.6(b). This plot indicates that this scaling enables us to obtain one single transition air velocity ratio from no surface seal regime to surface seal regime for all the spheres with different density and size. According to the experimental observations, the critical air velocity ratio for the occurrence of the surface seal is between 0.14 and 0.17.

Now, the model is used to find the critical airflow velocity beyond which the surface seal occurs. By revisiting Equation 3-12 and conducting a scaling analysis, this equation is reduced to

$$\frac{d^2R(t)}{dt^2} = -\frac{1}{\pi a}U_{air,m}^2 + \frac{2\gamma}{\rho\pi a^2}. \qquad \text{Equation 3-19}$$

To derive Equation 3-19 from Equation 3-12, we ignored the gravity, centrifugal acceleration, and air drag forces. Since the air density is low, $Fr >> 1$, and the mass of the rim is small, these forces should only exert a minor influence. To confirm that these forces are safely neglected, it would therefore be essential to compare the magnitude of the different contributions in Equation 3-12. Hence, we compare the contribution of each force ($\sqrt{\vec{F}_{\hat{r}} + \vec{F}_{\hat{z}}}$) in Equation 3-12:

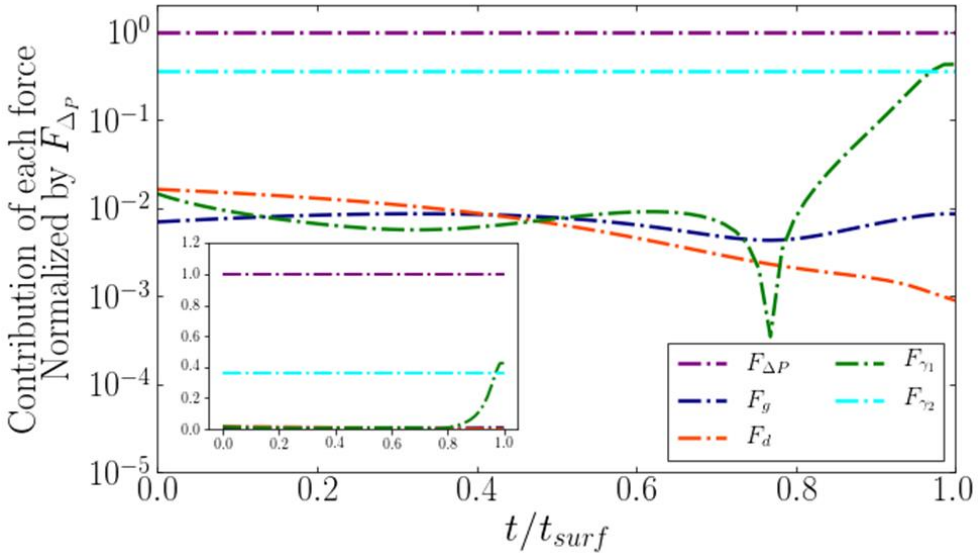

Figure 3.7. The mean contribution of each force in Equation 3-12 normalized by the magnitude of $F_{\Delta P}$.

Thus, Figure 3.7 indicates it is safe to ignore the centrifugal, gravity, and drag forces to derive Equation 3-19. It also demonstrates that a model developed to explain the dynamics of the splash curtain must account for both pressure difference and surface tension forces and the surface seal predominantly is governed by pressure difference force. Assuming that the pressure differential is negligible explains why the model by [15] does not predict the surface seal time accurately when compared with our experimental results (See Appendix 2).

We solve Equation 3-19 for $R(t)$ and set it equal to zero to find the surface seal time

$$t_{surf} = \sqrt{\frac{R_0}{[\frac{R_0}{\pi a U_0^2} U_{air,m}^2 - \frac{2\gamma R_0}{\rho \pi a^2 U_0^2}]}}. \qquad \text{Equation 3-20}$$

This equation has a real solution when the denominator is greater than zero, and, in that case, the occurrence of the surface seal is assured. Therefore, the singularity of Equation 3-20 corresponds to the transition from no seal regime to surface seal regime, and it is formulated as

$$\frac{U_{air,m}^2}{U_0^2} = \frac{2\gamma}{\rho a U_0^2} = \frac{2}{We_c}\frac{R_0}{a}, \qquad \text{Equation 3-21}$$

where We_c is the critical Weber number for the occurrence of the surface seal, defined based on sphere impact velocity. Experiments show that most of the cases with We greater than 1000 are associated with surface seal. Using experimental estimation for rounded rim radius, $a \approx 0.095 R_0$ ($a/R_0 \approx 0.095 \pm 0.007$), and choosing $We_c \approx 1000$, we can establish $U_{air,m}/U_0 \approx 0.146$ as a criterion for the occurrence of surface seal (Equation 3-21), which is consistent with experiments (see Figure 3.6(b)).

Rim radius, a, is a crucial input parameter for the model. Although we propagated the uncertainty in the measurement of the rim radius through the model to find the uncertainty on the predicted $U_{air,m}/U_0$ threshold by the model ($U_{air,m}/U_0 = 0.146 \pm 0.005$), it is also essential to study how much an error in a affects the predicted trajectory of the curtain's rim. Figure 3.8 shows the sensitivity of the model outputs (trajectory of the rim and prediction of transition threshold from no seal regime to surface seal regime) to the selection of rim radius.

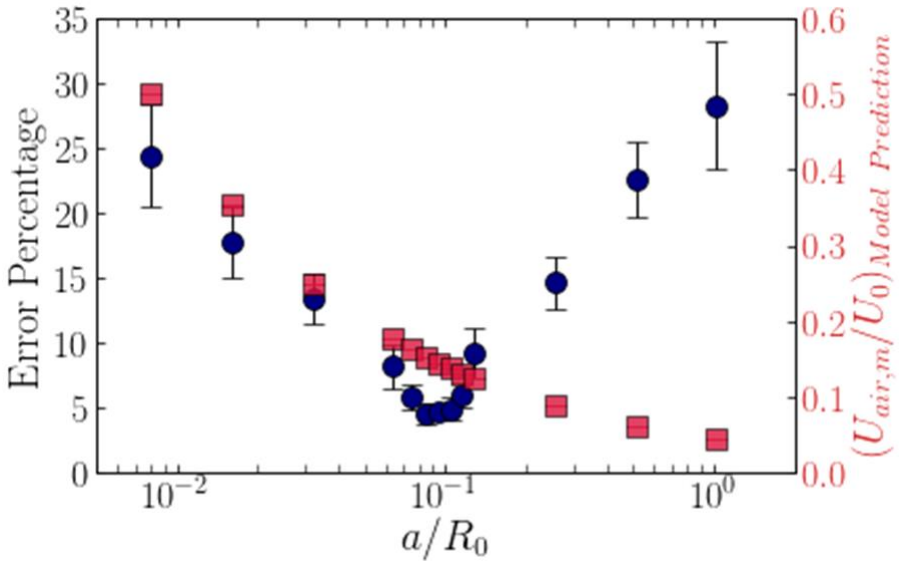

Figure 3.8. Model outputs sensitivity to the rim radius. The error percentage for each drop is calculated as: $\frac{\sum_{t=0}^{t_{surf}} (\frac{Observed\ rim's\ location - Predicted\ rim's\ location}{Observed\ rim's\ location})_t}{t_{surf}} \times 100$. The markers correspond to the mean value (of all the drops) and the error bars show the standard deviation. Circle markers represent the error percentage and the squares correspond to the predicted criterion for the occurrence of surface seal.

The results indicate that with a 50% error in the determination of rim's radius, less than 10% error is observed between the model's predictions and the observations.

Even though we focused on the dynamics of the splash curtain of the water-entering spheres, the model can be generalized to predict the splash curtain of projectiles with various geometries.

3.6.Summary

This work presented the first detailed analysis and physical understanding of why a splash does not always seal, supported by a developed theory and experimental observations. Contrary to current understanding, our observation showed projectile impact velocity is not the governing parameter determining the occurrence of surface seal and projectile density and size are also determinant factors in this phenomenon. We developed a physical model to predict the trajectory of the splash curtain. This model enabled us to discover the existence of a critical dimensionless number that predicts the occurrence of surface seal and revealed that the velocity of the airflow

rushing into the cavity is the determinant factor in the surface seal. Therefore, we determined the critical airflow velocity ratio beyond which the surface seal occurs in the water entry of hydrophobic spheres.

3.7.Appendix 1: Methods: Splash curtain imaging

Finding the experimental trajectory of the splash curtain from a typical shadowgraph video similar to [19] is difficult and can impose high error in the rounded rim determination. Instead, we developed a variation of shadowgraph imaging by capturing the shadow of the splash curtain on a transparent high quality paper. To do so, we used a point light source to make the shadow of the splash on the transparent paper (using the point light source is crucial in order to prevent the creation of any penumbra and antumbra in the shadow, i.e. creation of sharp edge images), and focused the camera on the transparent paper instead of real splash curtain [35]. These images are then converted to binary images, enabled us to determine the rounded rim location of the splash curtain in a robust way: we obtained the splash curtain boundary profile and found the first inflection point from the bottom of it as the location of rounded rim in each frame (Figure 3.9).

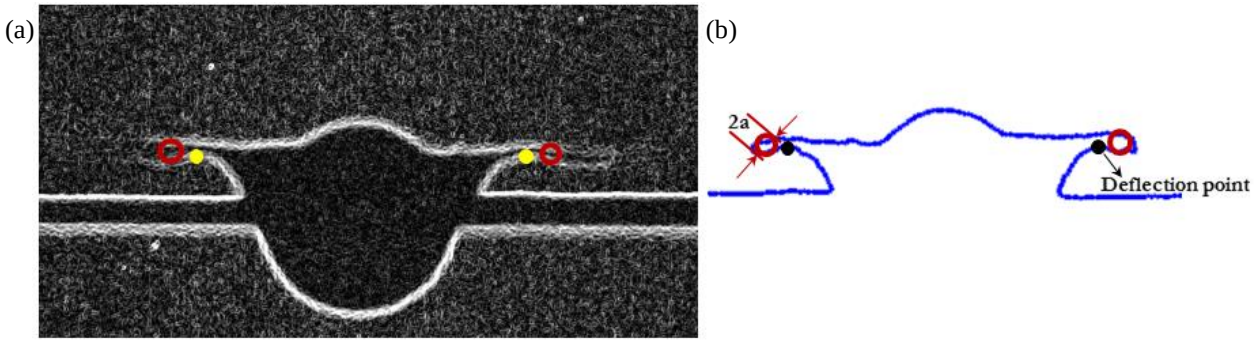

Figure 3.9. Locating splash curtain rounded rim by finding the splash curtain boundary profile from the shadow videos [121]: (a) Identified boundary profile of the splash curtain from binarized image, (b) Extracted boundary profile. The deflection point and identified rounded rim are shown by solid and open marker, respectively. The location of the rounded rim center is defined as the first inflection point (from the bottom) in the splash curtain boundary profile. The rounded rim radius is approximated as the radius of the closest identified circular object (in the splash curtain boundary profile) to the inflection point in a registered image around the inflection point.

We also found the rounded rim radius from the obtained curtain profile. This operation was performed for every frame of every case which resulted in a time history of rounded rim radius for

each case. We averaged it over time for each individual drop and then calculated the mean and standard deviation for all the drops (Figure 3.9).

3.8.Appendix 2: A comparison between our experimental observations and the predictions by Aristoff & Bush model

We use the obtained experimental parameters in the current study (impact velocity) into the Aristoff and Bush model [15] and compare the dimensionless surface seal predicted by this model with our experimental data.

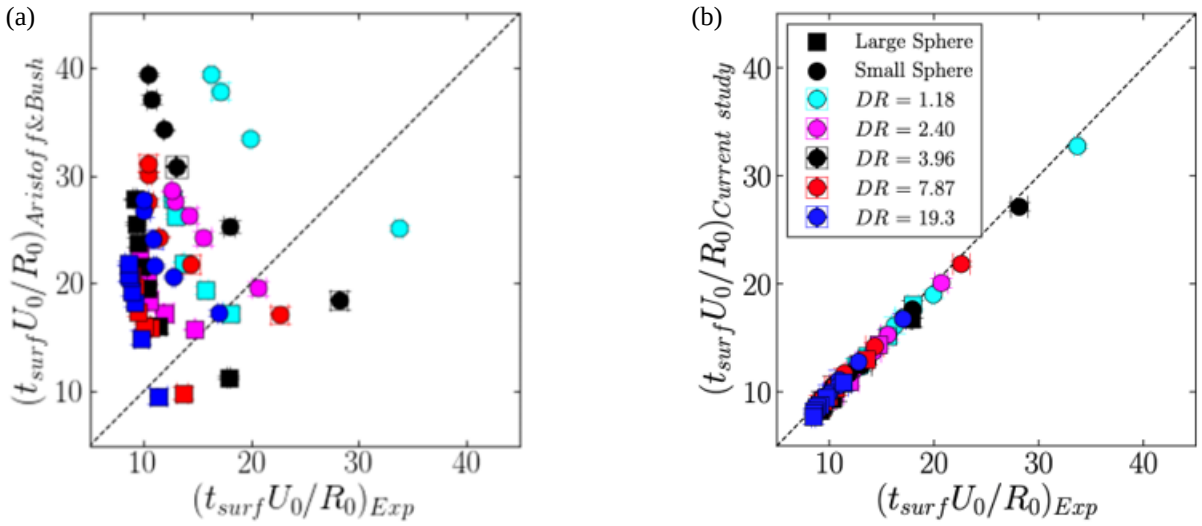

Figure 3.10. Prediction for dimensionless surface seal time vs. experimental data: (a) Aristoff and Bush model [15], (b) the proposed model in the current study.

Figure 3.10 shows the deviation of predictions by Aristoff and Bush model from the experimental data. To produce this plot, we employ the model of [15] with $\theta_c = 170^\circ$ and $\delta_0 = 0.02\ cm$. Note that the predictions of the model of [15] are sensitive to both initial film thickness, δ_0, and "cone angle", and both of these are not measurable quantities. Cone angle, θ_c, in [15] is defined as: "the angle that the cavity makes as it leaves the sphere with respect to the vertical tangent it is approximately constant as a function of depth and body speed for a given surface material". The maximum deviation of the predicted dimensionless surface seal time from the experiment is 278% for [15] and 5.6% for the model presented in this study.

Regarding the shape of the splash curtain, because our model predicts the trajectory of the splash curtain's rim, a direct comparison with the model prediction by [15] is not possible. However, a qualitative comparison with [15] shows deviation in the splash curtain prediction. The experimental observations show that the splash curtain ejects upwards and outwards, while in contrast, the predicted shape by [15] is an upwards and inwards splash curtain. To show this deviation, we performed image processing on the experimental images of Figure 18 in [15] and are superimposed with their model predictions in Figure 3.11, below.

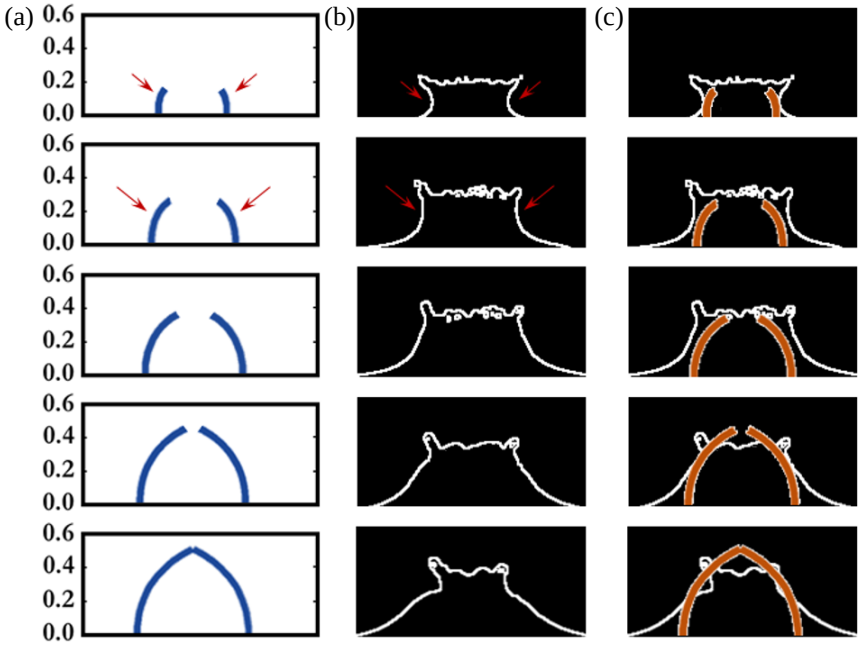

Figure 3.11. Comparison of the shape of splash curtain predicted by Aristoff and Bush model and their experimental observations: (a) model prediction by [15], (b) splash boundary of experimental observation by [15] detected by our imaging processing scheme, and (c) superimposition of experimental observation and model prediction. Red arrows show the deviation of splash curvature in model prediction from the experiment.

Figure 3.11 indicates that the model by [15] does not capture the curvature of the splash curtain, and how significantly this model prediction deviates from the experimental observation.

4. DATA ASSIMILATION FOR MODELING CAVITATION BUBBLE DYNAMICS

4.1.Background

Cavitation is a phenomenon in which rapid changes of pressure in a liquid could lead to the formation and growth of small vapor-filled cavities when the liquid's local pressure falls below its vapor pressure. These bubbles undergo several cycles of growth and collapse, and at the end of each cycle, at the moment of collapse, they generate pressure waves, heat, and sound. This process is important in engineering because of material damage to immersed bodies, alteration to the flow, and the noise created during the growth and collapse of cavitation bubbles. Despite considerable advances in the field, detailed knowledge about nuclei inception, bubble growth, and bubble dynamics is still lacking.

The growth of the cavitation bubble is relatively gentle, but the collapse is rapid, generating an intense shock wave and high shear stress to the surrounding liquid. Thus, capturing the collapsing of the bubble and induced pressure wave and shear stress upon collapse need high temporal resolution. Visualizing the cavitation bubble with high-speed imaging can help elucidate cavitation phenomena [122–125]. However, due to limited temporal resolution [126,127], the information obtained from this image-based technique is inadequate to analyze the collapse. Alternatively, cavitation modeling can predict the cavitation dynamics with the high temporal resolution, but these models' initial inputs' uncertainties can make the predictions unreliable. Therefore, a robust tool must be developed to overcome these challenges.

4.1.1. Cavitation modeling

Various cavitation models exist to describe the cavitation bubble dynamics. The model derived by Lord Rayleigh, dating back to 1917 (Rayleigh 1917), describes the change of a void in

water under constant external pressure. The Rayleigh equation was derived from the Navier-Stokes equation for a spherical bubble. Plesset modified the Rayleigh equation by including the effects of viscosity, surface tension, and a non-constant external pressure to the equation [129,130]. Therefore, the Rayleigh–Plesset equation describes the dynamics of a spherical bubble in an incompressible liquid. Lauterborn solved the equation for large oscillating bubbles, but he did not account for the viscosity, surface tension, incident sound wave, and acoustic radiation from the bubble [131]. These parameters were considered by Keller and Miksis to describe the oscillations of a trapped bubble in a sound field [132]. Since the liquid compressibility cannot be ignored when the bubble velocities reach to an appreciable order of magnitude compared with the speed of sound in liquid, Gilmore included the second-order compressibility terms of the liquid in his formulation to account for the energy loss of the bubble by the radiated pressure waves [133]. Fujikawa and Akamatsu [134] presented a detailed analysis of the laser-induced cavitation bubble, which takes the liquid compressibility, non-equilibrium evaporation and condensation, and thermal conduction into account. Their results indicate that evaporation and condensation strongly influence bubble dynamics. Yasui, in his mathematical description of the acoustic cavitation pulsation, accounted for the variation in liquid temperature at the bubble wall, non-equilibrium evaporation and condensation of water vapor at the bubble wall, the chemical reactions inside a bubble, and the gas diffusion (rectified diffusion) across the bubble wall [135]. Recently, Zhong et al. [136] modified Yasui's model that was initially derived for acoustic-induced cavitation bubbles to account for laser-induced cavitation bubbles by using a new approximation of the temperature gradient at the bubble surface.

Along with these well-known cavitation models, several other modifications to the RPE account for different physics [126,137]. A thorough review of cavitation modeling and simulation is presented by [127,138–140].

Coupling the RPE with other equations such as mass and heat transfers and accounting for physical parameters such as liquid compressibility and condensation-evaporation at bubble boundaries leads to more complex models. Although complex models offer improved accuracy of predictions, they need many input parameters, some of which are not easy to estimate or measure accurately. Nevertheless, the accuracy of these models' predictions is governed by the input parameters' initial values. However, due to the complicated physics of the cavitation and non-linearity in these equations, the initialization of input parameters is not trivial; parameters such as

the cavitation bubble's wall temperature, pressure and temperature of the bubble's gas content, the initial number of air molecules in the bubble, and the initial number of vapor molecules in the bubble are not measurable [134,135,140–142]. The current state of the art methods for estimation of these input parameters is using optimization [136]. However, this approach is not robust and accurate since (i) the uniqueness of the results is not guaranteed, (ii) there is no way to quantify uncertainties due to noisy measurements and model imperfections, (iii) there is no systematic way to account for prior knowledge, and (iv) the model may not be calibrated adequately due to insufficient data, measurement noise, and inherent model assumptions.

Hence, we propose a state-observer data assimilation approach for cavitation modeling to overcome the challenges mentioned above in property estimations, lack of physical knowledge, and underlying assumptions in cavitation models. This approach can overcome the deviation between the model predictions and experimental measurements by integrating the two.

4.1.2. Data assimilation: PID state observer controller

The concept of a state observer, or merely an observer, was proposed by Luenberger [143] and is essential in control theory. The state observer reconstructs a system's state by estimating the n-state variables from m-measurements, where $n > m$. In complex and nonlinear dynamical systems where it is difficult to measure all the state variables, the system's state is estimated from an incomplete set of measurements, and the system model predicts state variables.

In the state observer, a dynamical system is modeled as a set of differential equations. Combined with experimental measurements, time-resolved computations are needed to estimate the error between the modeled system output and the measurement. A feedback signal then uses the calculated error to modify the dynamical structure of the model. A properly designed feedback law is the key to an asymptotic reduction of the estimation error. Therefore, the mathematical model and the feedback law are the two essential elements in an observers' design.

Extensions of the state observer for applications to both linear [144] and nonlinear systems [145] have been studied extensively. The two most beneficial factors of the state observers are (1) simplicity and flexibility in determining the feedback gain, and (2) no need to model the measurement errors since they are constructed using deterministic models.

A state observer system can be written with a general equation:

$$\frac{\partial y_i}{\partial t} = A_{ij} y_i + B_{ik} x_k, \qquad \text{Equation 4-1}$$

where x_k and y_i contain the state variables and the experimental measurements, respectively. The system's dynamic model determines how the state variables evolve, and it is represented by the transition matrix, A_{ij}. B_{ik} is the distribution matrix, which is dependent on the observer system and the nature of the measurements. This matrix determines how the measurements are integrated into the dynamical system. The distribution matrix adjusts the influence the measurements have on the estimated state variables, using a multiplier. This multiplier is referred to as the feedback gain of the state observer system [146,147].

In fluid mechanics, data assimilation techniques include, but are not limited to, four-dimensional variational data assimilation [148] and Kalman filters [149]. State observers are also referred to as "measurement-integrated modeling" [150]. The state observer was initially introduced by treating the flow as a small degree-of-freedom dynamical system [151,152]. Later, it was used in reconstructing the structure of a flow field using the computational fluid dynamics (CFD) model for turbulent flow through a duct [150,153]. It was shown that an appropriate choice for the proportional feedback gain results in the acceleration in convergence and reduction in perturbation velocity estimation error, compared to the ordinary flow simulation without feedback. In all of these investigations, the flow field simulations' accuracy was improved by integrating experimental data into the numerical simulations.

In this work, we take advantage of the experimental measurements' reliability to predict the cavitation bubble dynamics more accurately and decrease the cavitation models' dependency on the input parameters and model assumptions. A PID controller will be employed to assimilate the experimental cavitation radius measurements with a cavitation model. This observer has the effect of making the system damped and stiffer and also allowing the steady-state error to converge to zero. The PID controller continuously calculates an error value, the difference between the desired set-point (experimental measurements), and a predicted process variable (model's predictions). Furthermore, the controller uses this error term to apply a correction based on the proportional term (proportional to the present error), the integral term (proportional to the integral of the error), and the derivative term (proportional to the derivative of the error) .

4.2.Data Assimilation Formulation

In this assimilated model, a PID controller continuously calculates an error value, $e(t)$, which is the difference between a measured cavitation bubble radius and an estimated value by the model, and applies a correction (control signal, u) based on proportional, integral, and derivative terms:

$$u = K_P(R(t) - R_d(t)) + K_I \int_0^t (R(\tau) - R_d(t))d\tau + K_D(\dot{R}(t) - \dot{R}_d(t)), \quad \text{Equation 4-2}$$

where K_P, K_I, and K_D are dimensionless proportionality, dimensionless integration, and dimensionless derivative constants, respectively. Also, R, R_d, $\dot{R}$, and $\dot{R}_d$ correspond to the estimated radius, desired radius (measured from the experiment), estimated radial velocity, and desired radial velocity, respectively. The first term in the control signal, u, is the proportional term which acts on the present value of the error, the second is the integral term representing an average of the past errors, and the last is the derivative term interpreted as a prediction for the future error. A flow chart diagram of the data assimilation technique is depicted in Figure 4.1.

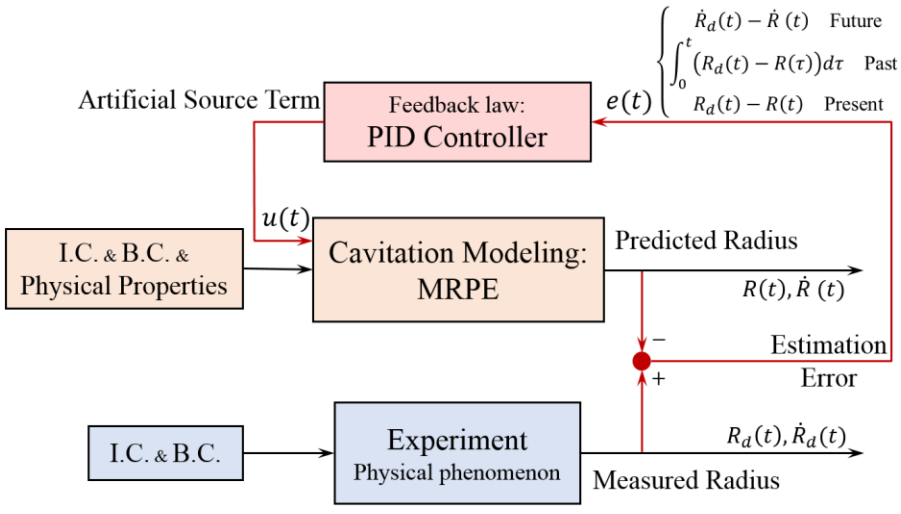

Figure 4.1. Algorithm flow chart for assimilated modeling of cavitation bubble dynamics.

The dimensionless constants in the control signal, u, are determined based on the Ziegler-Nichols method [154,155]. Here, we use $K_P = 6000000$, $K_I = 250000$, and $K_D = 25$ for all different conditions. Since the assimilated data correspond to the radius measurements, the observer is placed in the radius equation to fuse the measurements into the cavitation model.

The obtained equation and the additional equations from the cavitation model are solved for the cavitation bubble radius. At each time step, the experiment's measured value is used to calculate the error and activate the control signal, u, in the radius equation. This process iterates until the error reduces below a threshold value, and the control signal asymptotes towards zero before advancing to the next time step.

We selected to apply the PID controller on three cavitation models with different fidelity levels, namely, Rayleigh–Plesset [129], Yasui [135,140,141], and Zhong [136]. These models were selected due to the different fidelity levels, as the number of input parameters and the sensitivity of models' outputs to them increased to show the capability of the assimilated modeling in compensating for the models' underlying assumptions and decreasing the sensibility of the models' outputs to the uncertainty of the input parameters. However, the method is general and can apply similarly to any other cavitation bubble dynamics model.

Rayleigh–Plesset: This model governs the dynamics of a spherical bubble in an infinite body of incompressible fluid, written as

$$\ddot{R} = \frac{1}{R}\frac{p_{bubble} - p_\infty}{\rho_L} - \frac{3}{2}\frac{\dot{R}^2}{R} - 4\nu\frac{\dot{R}}{R^2} - \frac{2\sigma}{\rho_L R^2}, \qquad \text{Equation 4-3}$$

where $\ddot{R}$, $\dot{R}$, and R are the bubble radial acceleration, velocity, and radius, respectively. In this equation, ρ_L, ν, σ, P_{bubble}, and P_∞ denote liquid density, liquid viscosity, air-liquid surface tension, bubble contents pressure, and liquid pressure, respectively. We need two initial conditions to solve this ordinary differential equation (ODE): the cavitation bubble's size and its boundary expansion/contraction velocity. Liquid properties (ρ_L, ν, σ, and P_∞) are also prerequisites to predict the bubble dynamics using this model.

In the assimilated model, the observer, u, defined in Equation 4-2, is placed on the right-hand side of Equation 4-3 to fuse the measurements into the RPE:

$$\ddot{R} = \boldsymbol{u} + \frac{1}{R}\frac{p_{bubble} - p_{\infty}}{\rho_L} - \frac{3}{2}\frac{\dot{R}^2}{R} - 4\nu\frac{\dot{R}}{R^2} - \frac{2\sigma}{\rho_L R^2}. \qquad \text{Equation 4-4}$$

This ODE is solved using a Runge-Kutta fourth-order scheme (ODE45 in MATLAB) [156,157]. At each time step, the measured value is used to calculate the error and activate the control signal, u, in Equation 4-4. This process is iteratively performed until the error reduces below a relative tolerance of 10^{-6} and the control signal asymptotes towards zero before advancing to the next time step.

Yasui. Yasui model, Equation 4-5, is one of the most comprehensive cavitation models as it accounts for liquid compressibility, variation in liquid temperature at the bubble wall, non-equilibrium evaporation and condensation of water vapor at the bubble wall, and the gas diffusion across the bubble wall.

To solve the Yasui equation, we need to initialize the following inputs: cavitation bubble's size, cavitation bubble's wall expansion/contraction velocity, cavitation bubble's wall temperature, the temperature of bubble's gas content, the pressure of bubble's gas content, the initial number of air molecules in the bubble, initial number of vapor molecules in the bubble, the rate of mass transport at the bubble's wall, the diffusion coefficient of air in water, the ratio of the number of vapor molecules penetrating the interface to the number of vapor molecules striking at the interface. Besides, the physical properties such as density, viscosity, surface tension, speed of sound, air and vapor molecular masses, the intermolecular attraction of air and vapor, the volume occupied by air and vapor molecules, the gas constant of vapor, and water latent-heat are also prerequisites to obtain the bubble dynamics using this model. Several unknown physical parameters, such as the initial number of air and water vapor molecules present in the bubble, gas pressure inside the bubble, and gas diffusion coefficient, are not experimentally measurable and have to be estimated.

$$\ddot{R} = \frac{1}{\left(1 - \frac{\dot{R}}{c} + \frac{\dot{m}}{\rho_L c}\right)R + \frac{4\mu}{\rho_L c}}\left[\frac{1}{\rho_L}\left(1 + \frac{\dot{R}}{c}\right)\left[P - \frac{2\sigma}{R} - \frac{4\mu}{R}\left(\dot{R} - \frac{\dot{m}}{\rho_L}\right)\right.\right.$$
$$\left. - \dot{m}^2\left(\frac{1}{\rho_L} - \frac{1}{\rho_g}\right) - P_\infty\right] + \frac{d\dot{m}}{dt}\frac{R}{\rho_L}\left(1 - \frac{\dot{R}}{c} + \frac{\dot{m}}{\rho_L c}\right)$$
$$+ \frac{\dot{m}}{\rho_L}\left(\dot{R} + \frac{\dot{m}}{2\rho_L} + \frac{\dot{R}\dot{m}}{2c\rho_L}\right) - \frac{3}{2}\dot{R}^2\left(1 - \frac{\dot{R}}{3c} + \frac{2\dot{m}}{3\rho_L c}\right) \qquad \text{Equation 4-5}$$
$$+ \frac{R}{\rho_L c}\left[\frac{dP}{dt} + 2\sigma\frac{\dot{R}}{R^2} + 4\mu\left(\frac{\dot{R}^2}{R^2} + \frac{1}{\rho_L}\frac{R\frac{d\dot{m}}{dt} - \dot{R}\dot{m}}{R^2}\right)\right.$$
$$\left.\left. - 2\dot{m}\frac{d\dot{m}}{dt}\left(\frac{1}{\rho_L} - \frac{1}{\rho_g}\right) - \frac{\dot{m}^2}{\rho_g^2}\frac{d\rho_g}{dt}\right]\right].$$

In Equation 4-5, P corresponds to the bubble's internal pressure estimated from the Van der Waals equation of state, which is a function of the gas temperature inside the bubble and the bubble volume. The rate of mass transfer at the bubble boundaries is represented by $\dot{m}$ in this equation, and is a function of gas temperature at the bubble wall, the number of air and water vapor molecules, and internal bubble pressure. Further details on the rate of change of these variables and corresponding ODEs can be found in [135,140,141]. Also, t, c, μ, and ρ_g are time, the speed of sound in liquid, liquid viscosity, and air-water vapor mixture density, respectively.

To integrate the experimental measurements into this model, we place the control signal, u, in the Equation 4-5:

$$\ddot{R} = \frac{1}{\left(1 - \frac{\dot{R}}{c} + \frac{\dot{m}}{\rho_L c}\right)R + \frac{4\mu}{\rho_L c}} \Bigg[\boldsymbol{u}$$
$$+ \frac{1}{\rho_L}\left(1 + \frac{\dot{R}}{c}\right)\left[P - \frac{2\sigma}{R} - \frac{4\mu}{R}\left(\dot{R} - \frac{\dot{m}}{\rho_L}\right)\right.$$
$$\left. - \dot{m}^2\left(\frac{1}{\rho_L} - \frac{1}{\rho_g}\right) - P_\infty\right] + \frac{d\dot{m}}{dt}\frac{R}{\rho_L}\left(1 - \frac{\dot{R}}{c} + \frac{\dot{m}}{\rho_L c}\right)$$
$$+ \frac{\dot{m}}{\rho_L}\left(\dot{R} + \frac{\dot{m}}{2\rho_L} + \frac{\dot{R}\dot{m}}{2c\rho_L}\right) - \frac{3}{2}\dot{R}^2\left(1 - \frac{\dot{R}}{3c} + \frac{2\dot{m}}{3\rho_L c}\right)$$
$$+ \frac{R}{\rho_L c}\left[\frac{dP}{dt} + 2\sigma\frac{\dot{R}}{R^2} + 4\mu\left(\frac{\dot{R}^2}{R^2} + \frac{1}{\rho_L}\frac{R\frac{d\dot{m}}{dt} - \dot{R}\dot{m}}{R^2}\right)\right.$$
$$\left. - 2\dot{m}\frac{d\dot{m}}{dt}\left(\frac{1}{\rho_L} - \frac{1}{\rho_g}\right) - \frac{\dot{m}^2}{\rho_g^2}\frac{d\rho_g}{dt}\right]\Bigg].$$

Equation 4-6

This ODE is solved with the same algorithm that we explained for Equation 4-4. The thermal effects and mass transport in the assimilated model are modeled with a procedure identical to those in Yasui model (See Section 4.8).

Zhong et al., shown in Equation 4-7, is a modified version of Yasui's model that takes a different approach to model the heat transfer at the bubble boundaries. To predict bubble dynamics with the Zhong model, since the authors proposed a new model for the conduction in the thermal boundary layer around the cavitation bubble, in addition to Yasui's model input parameters, this model needs one more input to be initialized, namely, the initial thickness of thermal boundary layer. This parameter is not experimentally measurable and has to be estimated. Further details on this model can be found in [136].

$$\ddot{R} = \frac{1}{R\left[1-\frac{1}{c}\left(2\dot{R}-\frac{\dot{m}}{\rho_L}\right)+\frac{1}{c^2}\left(\frac{23\dot{R}^2}{10}-\frac{31\dot{m}\dot{R}}{10\rho_L}-\frac{\dot{m}^2}{5\rho_L^2}\right)\right]}\left[R\left(\frac{\frac{d\dot{m}}{dt}}{\rho_L}\right)\left[1\right.\right.$$
$$-\frac{1}{c}\left(2\dot{R}-\frac{\dot{m}}{\rho_L}\right)+\frac{1}{c^2}\left(\frac{23\dot{R}^2}{10}-\frac{31\dot{m}\dot{R}}{10\rho_L}-\frac{\dot{m}^2}{5\rho_L^2}\right)\Bigg]$$
$$-\frac{3}{2}\left(\dot{R}-\frac{\dot{m}}{\rho_L}\right)\left[\dot{R}+\frac{\dot{m}}{3\rho_L}-\frac{4\dot{R}^2}{3c}\right.$$
$$\left.+\frac{1}{c^2}\left(\frac{7\dot{R}^3}{5}-\frac{49\dot{m}\dot{R}^2}{30\rho_L}-\frac{14\dot{m}^2\dot{R}}{15\rho_L^2}-\frac{\dot{m}^3}{6\rho_L^3}\right)\right] \qquad \text{Equation 4-7}$$
$$-\frac{1}{\rho_L}\left[P_\infty - P_{B,2} - \frac{R\dot{p}_{B,1}}{c}\right.$$
$$+\frac{1}{c^2}\left\{\left(2\dot{R}-\frac{\dot{m}}{\rho_L}\right)R\dot{p}_{B,1}\right.$$
$$\left.\left.\left.+\left(P_\infty - P_{B,1}\right)\left[\frac{\dot{R}^2}{2}-\frac{3\dot{m}\dot{R}}{2\rho_L}-\frac{\dot{m}^2}{\rho_L^2}+\frac{3\left(P_\infty - P_{B,1}\right)}{2\rho_L}\right]\right\}\right]\right],$$

where

$$p_{B,1} = p - \frac{2\sigma}{R} - \frac{4\mu}{R}\left(\dot{R}-\frac{\dot{m}}{\rho_L}\right) - \dot{m}^2\left(\frac{1}{\rho_L}-\frac{1}{\rho_g}\right), \qquad \text{Equation 4-8}$$

and

$$p_{B,2} = p_{B,1} + \frac{4\mu}{3c^2}\left[\frac{3\dot{m}}{2\rho_L R}\left(\dot{R}-\frac{\dot{m}}{\rho_L}\right)^2 - \frac{\dot{p}_{B,1}}{\rho_L} + \frac{\dot{m}\left(p_\infty - p_{B,1}\right)}{\rho_L^2 R}\right]. \qquad \text{Equation 4-9}$$

To conduct assimilation and predict bubble dynamics, we place the control signal, u, in Equation 4-7, and employ the same algorithm used for solving Equation 4-4 and Equation 4-6:

$$\ddot{R} = \frac{1}{R\left[1-\frac{1}{c}\left(2\dot{R}-\frac{\dot{m}}{\rho_L}\right)+\frac{1}{c^2}\left(\frac{23\dot{R}^2}{10}-\frac{31\dot{m}\dot{R}}{10\rho_L}-\frac{\dot{m}^2}{5\rho_L^2}\right)\right]}\Bigg[\boldsymbol{u}$$
$$+R\left(\frac{\frac{d\dot{m}}{dt}}{\rho_L}\right)\left[1-\frac{1}{c}\left(2\dot{R}-\frac{\dot{m}}{\rho_L}\right)\right.$$
$$\left.+\frac{1}{c^2}\left(\frac{23\dot{R}^2}{10}-\frac{31\dot{m}\dot{R}}{10\rho_L}-\frac{\dot{m}^2}{5\rho_L^2}\right)\right]$$
$$-\frac{3}{2}\left(\dot{R}-\frac{\dot{m}}{\rho_L}\right)\left[\dot{R}+\frac{\dot{m}}{3\rho_L}-\frac{4\dot{R}^2}{3c}\right.$$
$$\left.+\frac{1}{c^2}\left(\frac{7\dot{R}^3}{5}-\frac{49\dot{m}\dot{R}^2}{30\rho_L}-\frac{14\dot{m}^2\dot{R}}{15\rho_L^2}-\frac{\dot{m}^3}{6\rho_L^3}\right)\right]$$
$$-\frac{1}{\rho_L}\left[P_\infty-P_{B,2}-\frac{R\dot{p}_{B,1}}{c}\right.$$
$$+\frac{1}{c^2}\left\{\left(2\dot{R}-\frac{\dot{m}}{\rho_L}\right)R\dot{p}_{B,1}\right.$$
$$\left.\left.\left.+\left(P_\infty-P_{B,1}\right)\left[\frac{\dot{R}^2}{2}-\frac{3\dot{m}\dot{R}}{2\rho_L}-\frac{\dot{m}^2}{\rho_L^2}+\frac{3\left(P_\infty-P_{B,1}\right)}{2\rho_L}\right]\right\}\right]\Bigg]. \qquad \text{Equation 4-10}$$

In the Equation 4-10, the procedure to model the thermal effects and obtain the rate of mass transfer are identical to those Zhong model (See Section 4.8).

A series of controlled experiments to validate the assimilated models for laser-induced cavitation is described in Section 4.3.1.

4.3.Experiment and Analysis Methodology

4.3.1. Experimental setup

The laser-induced cavitation was generated under stagnant flow conditions at the center of an acrylic chamber filled with distilled water. The chamber had a cross-section of $5\ cm$ by $5\ cm$ and a height of $10\ cm$. Water temperature and dissolved oxygen level were measured using Dissolved Oxygen Meter Kit (Extech, 407510, Accuracy: $\pm 0.4\ mg/L$ for dissolved oxygen level

and $\pm 0.8°C$ for temperature) and found to be $23°C$ and 8.7 mg/L, respectively. The chamber was closed on top, eliminating the free surface to provide symmetric boundary conditions. The acrylic chamber provided optical access for illumination and imaging. A schematic of the experimental setup is presented in Figure 4.2.

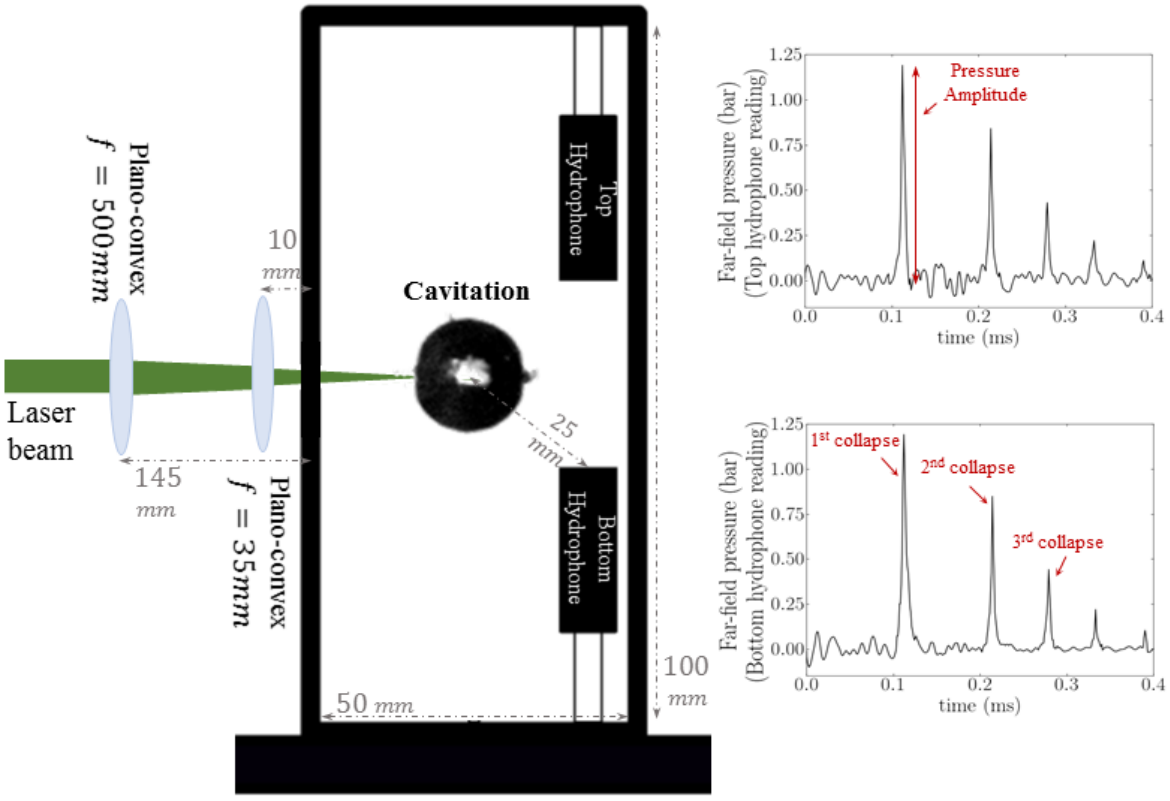

Figure 4.2. Schematic of the experimental setup for the laser-induced cavitation and sample pressure readings from hydrophones.

We employed a $532nm$ Nd:YAG laser (New Wave Research, SOLO 120) with a series of optics to produce a laser-induced cavitation bubble. The laser passed through two converging lenses ($f = 500\ mm$ and $f = 35\ mm$ plano-convex lenses) and focused at the acrylic chamber center. The lenses were located $145\ mm$ and $10\ mm$ away from the chamber's wall, respectively. The cavitation was induced at seven different laser powers ranging from $13\ \mu J$ to $81\ \mu J$ ($13.1 \pm 0.9\ \mu J$, $24.3 \pm 1.1\ \mu J$, $35.5 \pm 2.6\ \mu J$, $46.7 \pm 1.2\ \mu J$, $56.9 \pm 1.3\ \mu J$, $69.2 \pm 1.6\ \mu J$, and $80.4 \pm 2.1\ \mu J$) to obtain a variety of bubble sizes. Due to changes in laser power from pulse to pulse, we

evaluated the repeatability and sphericity of the generated laser-induced cavitation bubbles in Figure 4.3.

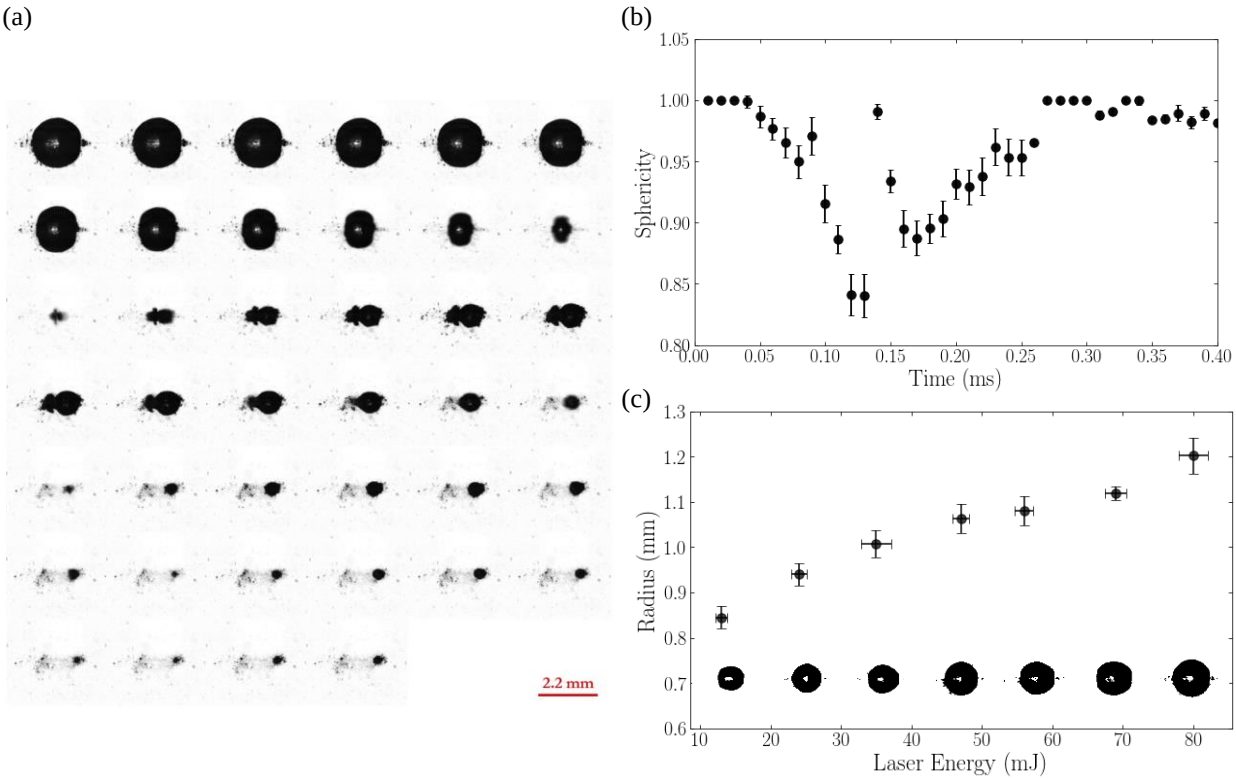

Figure 4.3. (a) A sequence of the growth and collapse of a laser-induced cavitation bubble. The laser energy is $69.15 \pm 1.55\ mJ$, and the time interval between frames is $t = 10\ \mu s$. The first frame is when the bubble reaches the maximum size. (b) Sphericity of the bubbles shown in (a). The error bars represent the standard deviation of the generated cavitation bubbles sphericty at the laser energy of $69.15 \pm 1.55\ mJ$. (c) Bubbles initial radius variation from pulse to pulse at different laser energy. The markers and error bars are the mean and standard deviation of 5 runs, respectively.

We defined bubble's sphericity as the ratio of the circumference of an equal-surface area bubble to the actual circumference of the bubble (See **Fig. S1** and **Movie S1** for the sequence of the growth and collapse of a laser-induced cavitation bubble and videos of cavitation oscillations at different laser powers).

A 1-megapixel camera (Photron, FASTCAM SA-Z) with a $105mm$ Nikon lens was placed at a working distance of $25\ cm$ from the chamber's wall for the time-resolved cavitation bubble image size measurements. A bellow (Nikon, PB-4) was employed to zoom in at the region of interest, yielding a magnification of $15.5\ \mu m/px$ and a field of view of $10\ mm$ height and $4\ mm$

width (650×256 pixels). The cavitation bubbles were back-lit by a white LED source (LaVision, LED-Flashlight 300) synchronized with the laser and the camera, set at the maximum current in constant illumination mode. Since the LED provided non-uniform illumination, a diffuser plane was used between the LED and the chamber. This allowed us to capture high-quality shadowgraph images to determine the bubble diameter at $100k$ fps with sufficient illumination at the focal ratio $f-16$. Five sets of 1000 time-resolved images were collected for each one of the seven different laser powers. The captured images were processed in MATLAB to obtain the equivalent bubble diameter in each frame. To accurately locate and track the cavitation bubble dynamics, image processing algorithms were developed in MATLAB that automatically detect the cavitation bubble boundaries and its equivalent bubble diameter. The bubble detection scheme consists of four steps: pixel intensity thresholding, median filtering, image dilation, and edge detection. The threshold pixel intensity algorithm filters all signals below a given brightness thus rendering the cavitation position. Median filtering compares pixels with others in their neighborhood and thus high frequency signal components are removed. The resulting mask isolates the cavitation bubble for detecting its boundaries, by locating the discontinuity in the brightness signal, and thus finding the equivalent bubble diameter. These measurements are then assimilated into the cavitation model with the PID feedback controller.

We used two hydrophones (Bruel & Kjaer) sampling at $1\ MS/s$ placed $25\ mm$ away from the cavitation site, on top of each other, with a separation distance of $\sim 15\ mm$. The upper bound for the rise time, horizontal directivity (radial, xy plane) and vertical directivity (axial, xz plane) of the hydrophone are reported as $55.3\ ns$, ± 2 dB at $100\ kHz$, and ± 4 dB at $100\ kHz$, respectively. It is shown that a hydrophone with such features is able to capture the bubble collapse shock wave [158]. The pressure data were recorded using a NI DAQ board (NI, USB 6363). The pressure signal was used to obtain the collapse pressure wave amplitude for the first three collapses to compare model predictions and experimental readings.

4.3.2. Analysis methodology

We processed 100 experimental images to obtain the time series of the cavitation bubble radius for each experimental condition. The cavitation bubble characteristics extracted from these signals are referred to as the results of the image-based analysis. According to the Nyquist's Theorem, for an accurate representation of a signal, the sampling rate must be at least two times

faster than the highest frequency to be resolved. Since the bubbles' oscillation instantaneous frequency increases with time and reaches $\approx 25000\ Hz$, after the 7^{th} cycle, we discard the signal after this cycle and keep the first 50 data points. Thus, we have at least nine measurements per cycle. We select the maximum value of the first rebound as the initial radius for all the cavitation models in each signal. At the cavitation bubble's maximum radius, the radial velocity of the bubble's wall and mass transfer at the bubble's wall can be safely assumed to be zero. We set these initial values, and through optimization (following the optimization procedure explained in [136,159,160]) estimate the rest of the initial inputs and solve Equation 4-3, Equation 4-5, and Equation 4-7 for cavitation bubble radius. Then, we calculate the root mean squared error (RMSE) between the predicted bubble radius by these models and the experimental measurements. Although the assimilated model does not need accurate initial inputs or any trial and error or optimization to estimate these inputs, for an impartial comparison between the original cavitation models and assimilated versions, we use the same initial inputs for the assimilated models.

One crucial parameter in the assimilated modeling is the level of assimilation, i.e., the number of measurements fused with the model. In this study, our experimental signal has 50 data points. So, we can fuse up to a maximum of 50 measurements with the cavitation models. But the question is, what is the minimum number of measurements that must be assimilated into the model for an accurate prediction? To find out, we investigate the dependence of the assimilated model performance on the number of measured data points integrated into the model and quantify the error between the experimentally measured radius and assimilated models' predictions for different assimilation levels in terms of root mean squared error.

For each experimentally measured radius signal that contains 50 data points, before assimilation, we subsample the signal from 10% to 100% with increments of 10%. Also, at each level of downsampling, we create 100 sub-collections (of different combinations of data points) from the original signal. So, we would have 100 distinct sub-collections for measurement integration at each level of assimilation. Next, for each sub-collection, the assimilated models (Equation 4-4, Equation 4-6, and Equation 4-10) are employed to predict the cavitation bubble radius and compare it with the experimental measurements. Then, the RMSE is quantified between the predictions and experimental observations. Note that, for the 100% assimilation level, we can only have one sub-collection to fuse the measurements with the model.

In this paper, we report the assimilation level in terms of the *equivalent number of oscillation cycles* defined as the multiplication of the number of frames assimilated into the cavitation models (frames), the multiplicative inverse of the sampling rate (second per frame), and average oscillation frequency (cycles per second). The sampling rate is $100k$ fps, and our measurements show that the mean oscillation frequency for laser-induced cavitation for the first ten oscillation cycles is $\approx 15000\ Hz$.

4.4.Results

4.4.1. Performances of models with no assimilation

We first discuss the cavitation models' predictions for bubble radius, the amplitude of induced pressure upon the collapse of cavitation, and the time of collapse incidence without assimilation.

Cavitation bubble radius. Sample bubble radius predictions by the three cavitation models are presented in Figure 4.4. The experimental measurements are shown with the black markers in this figure. Predictions by all three models agree with the experiment for the first oscillation cycle as the underlying assumptions of bubble's sphericity and no chemical reactions within the bubble in these models are still valid. Predictions by R–P and Yasui start deviating from the measurements after the first collapse, which is expected since R–P does not account for the evaporation and condensation, and the approximation of the vapor thermal layer thickness by Yasui does not sufficiently capture the thermal conduction and non-equilibrium evaporation. Although the Zhong model has the best agreement between the tested models, a phase-shift of predictions after the first collapse is observed when compared with the experiments. We remark that this may be caused by ignoring the chemical reactions, which occur near the collapse moment and the number of air molecules decreases after the first collapse. The observed deviations between measurements and the models' predictions are too caused by the sensitivity of the models' predictions to the uncertainty of the initial inputs. The deviation for each model is quantified in terms of RMS error between the predictions and the measurements in Figure 4.4(b). Predictions by R-P have the most significant deviations from the measurements due to the inherent model assumptions. This figure implies that by accounting for mass and heat transfer at the boundaries of the bubble, the RMSE is decreased by up to 80%; such that the mean RMSE for R-P is 0.58 mm

and it drops to 0.16 mm and 0.11 mm for the predictions by Yasui and Zhong, respectively. In addition, we observe a 31% improvement in RMSE of predictions by Zhong as a result of the proposed new conduction model in the thermal boundary layer around the cavitation bubble.

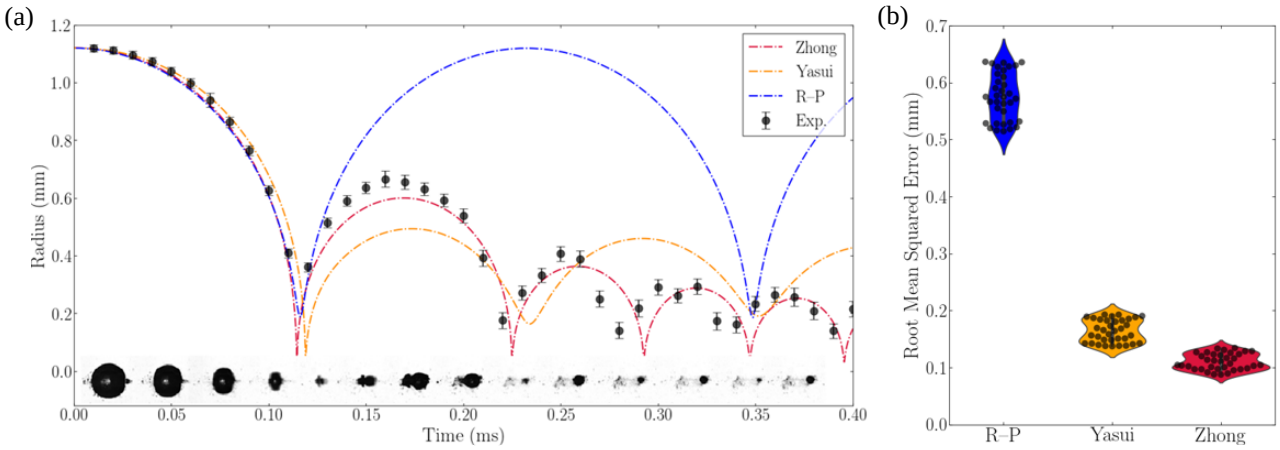

Figure 4.4. (a) Cavitation bubble radius predicted by R–P, Yasui, and Zhong models with $c = 1483\ m/s$, $\rho_L = 1000\ kg/m^3$, $\mu = 1e-3\ m^2/s$, $\sigma = 0.072\ kg/s^2$, $P_\infty = 1.01e+05\ Pa$, $\alpha_M = 0.039$, $T_0 = T_{B_0} = 293.15K$, $n_{air_0} = 4.2e+13$, $n_{water_0} = 3.7e+16$, $P_0 = 50\ kPa$, $\dot{m}_0 = 0\ kg/s$, $R_0 = 1.12\ mm$, $\dot{R}_0 = 0\ m/s$, and $\delta_{l_0} = 0.38\ \mu m$. (b) RMS error between predictions and measurements for different cavitation models. In the Rayleigh-Plesset equation, the gas in the bubble is assumed to follow adiabatic process. The values of the physical properties are estimated at 1 atm and 25℃.

Collapse-induced pressure. We calculate the far-field pressure at the hydrophones' location with outputs from the three cavitation models to estimate the collapse-induced pressure. The far-field pressure, P_{FF}, at distance r from bubble's center can be written as

$$P_{FF} = \frac{\rho_L R}{r}\left(2\dot{R}^2 + R\ddot{R} - \frac{R^3\dot{R}^2}{2r^3}\right) + P_\infty, \qquad \text{Equation 4-11}$$

which is valid for all three models. It must be noted that for a one-on-one comparison between the predictions of the three models, the delay due to wave propagation has not been included in Equation 4-11, as the liquid compressibility is not modeled in the R-P. Also, these effects were found to be negligible since the far-field pressure is calculated at a distance $\sim 20D$ from the bubble's nucleation site.

The cavitation collapse is distinguishable by its high amplitude in the signal (see Figure 4.2(b)). Thus, the pressure amplitude is picked as a comparison parameter between the hydrophone measurements and predicted pressure by the cavitation models. Therefore, the agreement between the predicted far-field pressure and the hydrophones' data is investigated for the first three collapses. Figure 4.5 illustrates the difference between the models' estimation and hydrophone data for each model. Columns in this figure are allocated to different models, and rows represent the collapse.

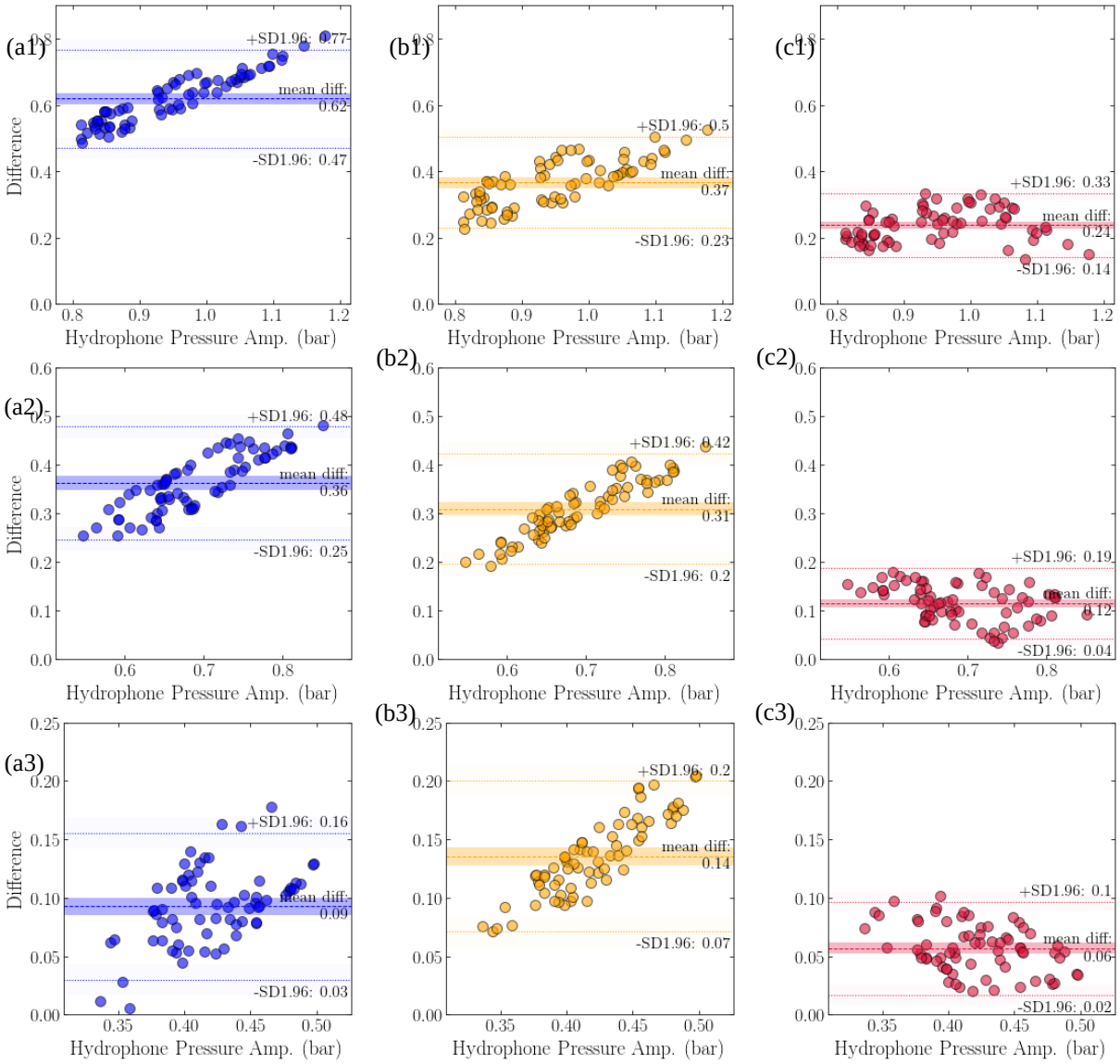

Figure 4.5. Amplitude of collapse-induced pressure for the first three collapses: the difference between hydrophones readings and models' predictions. (a1) R–P, first collapse, (a2) R–P, second collapse, (a3) R–P, third collapse, (b1) Yasui, first collapse, (b2) Yasui, second collapse, (b3) Yasui, third collapse, (c1) Zhong, first collapse, (c2) Zhong, second collapse, and (c3) Zhong, third collapse.

Figure 4.5 shows that R–P underpredicts the far-field pressure, for the first collapse, with a 60% error compared to the measurements, and this deviation is 25% for the Zhong's model, implying the significant role of the evaporation rate and the bubble's non-condensable gas contents in the bubble dynamics [136]. R–P neglects the evaporation and condensation, and therefore the air and vapor molecules within the bubble remain constant, and the amplitude of rebounds and induced pressure remain unchanged after the collapse. Also, increasing the amount of air in the bubble helps to resist the bubble collapse and decreases the induced pressure amplitude. Since the initial number of air molecules in the bubble and the evaporation rate are inputs of both Yasui and Zhong models, even a small uncertainty in their estimation may lead to significant error in predicting bubble dynamics. Zhong et al. [136], in their parametric study, showed that 20% error in the estimation of initial values of either of these two parameters could lead to 60% difference in the cavitation-induced pressure and shear stress predictions by their model. Besides, they showed that the cavitation dynamics are also subject to change as the maximum induced pressure and shear stress could occur at not necessarily the first, but second, or third collapse instead, determined by changes to the evaporation rate within the range of $\alpha_M = 0.036$ to $\alpha_M = 0.050$.

Time of collapse incidence. The measured or predicted local minimum radius at the end of each oscillation cycle is defined as the cavitation collapse. Due to low temporal resolution, experimental data are not able to pick the exact collapse time. However, we are confident that the collapse is occurring in an interval of $2 \times fps^{-1}$ (collapse interval) around the local minimum value at the end of each rebound (shaded area in Figure 4.6), and the interval is centered at the local minimum. Figure 4.6 shows the predicted time of the cavitation bubble collapse for each model's first three collapses. The markers represent the mean value of all conditions we tested (seven different laser powers and five runs per each).

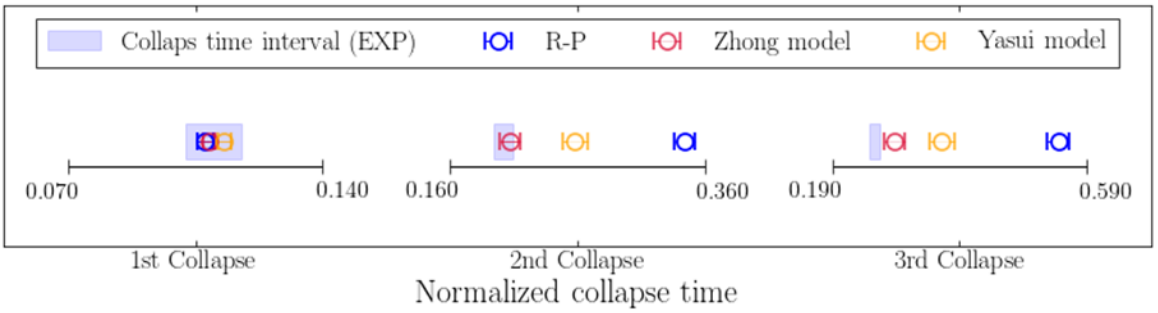

Figure 4.6. Predicted time (normalized by the cavitation duration) for the occurrence of cavitation collapse by different models for the first three collapses. The shaded area represents the time interval for the occurrence of collapse based on the experimental observations and sampling rate.

The models and the experiment agree if the predictions fall within the collapse interval. Note that the experimental measurements can only provide a collapse interval for the incident of cavitation collapse and not the exact time. Although all the models' predictions agree with the first collapse observations, they deviate significantly from the collapse interval in the second and third collapses. As mentioned earlier, ignoring the evaporation and condensation by R–P, and poor approximation for the vapor thermal layer thickness, and ignoring the decrease in the number of air molecules after Yasui's first collapse, cause this significant phase-shift. Ignoring the chemical reactions within the bubble near the collapse moment by Zhong does not result in any significant phase-shift for the first three collapses, and it starts deviating after the third collapse for this model.

4.4.2. Performances of assimilated models

Cavitation bubble size. We integrate the cavitation models with the experimental measurements and illustrate the effects of increasing the number of assimilated data points into these models on the bubble's size prediction in Figure 4.7. We quantify the deviation from the experimental measurements for the different levels of assimilation for each model. In Figure 4.8, we plot the quantified error between measurements and the predictions to investigate how accuracy is improved for each model by increasing the assimilation level. For each model, the ratio of RMSE at each assimilation level to RMSE for the non-assimilated model is defined as the error-ratio. The markers and the error bars represent the mean and the standard deviation at each assimilation level, respectively. Results in Figure 4.7 and Figure 4.8 indicate that for R-P (low fidelity model), we

need to assimilate the captured information of at least three equivalent cycles to get the same error as Zhong (high fidelaty model). This value is approximately 0.75 for Yasui. This implies that to compensate for ignoring the liquid compressibility, variation in liquid temperature at the bubble wall, non-equilibrium evaporation and condensation of water vapor at the bubble wall, and the gas diffusion across the bubble wall ignored in R-P, experimental information of three equivalent cycles must be assimilated into this model. In addition, to reach the RMSE of below 0.05 mm, we need to integrate the information of 5.25 equivalent cycles into R-P. However, assimilating the information of ~3 and ~1.5 equivalent cycles with Yasui and Zhong, respectively, yields the RMSE of 0.05 mm.

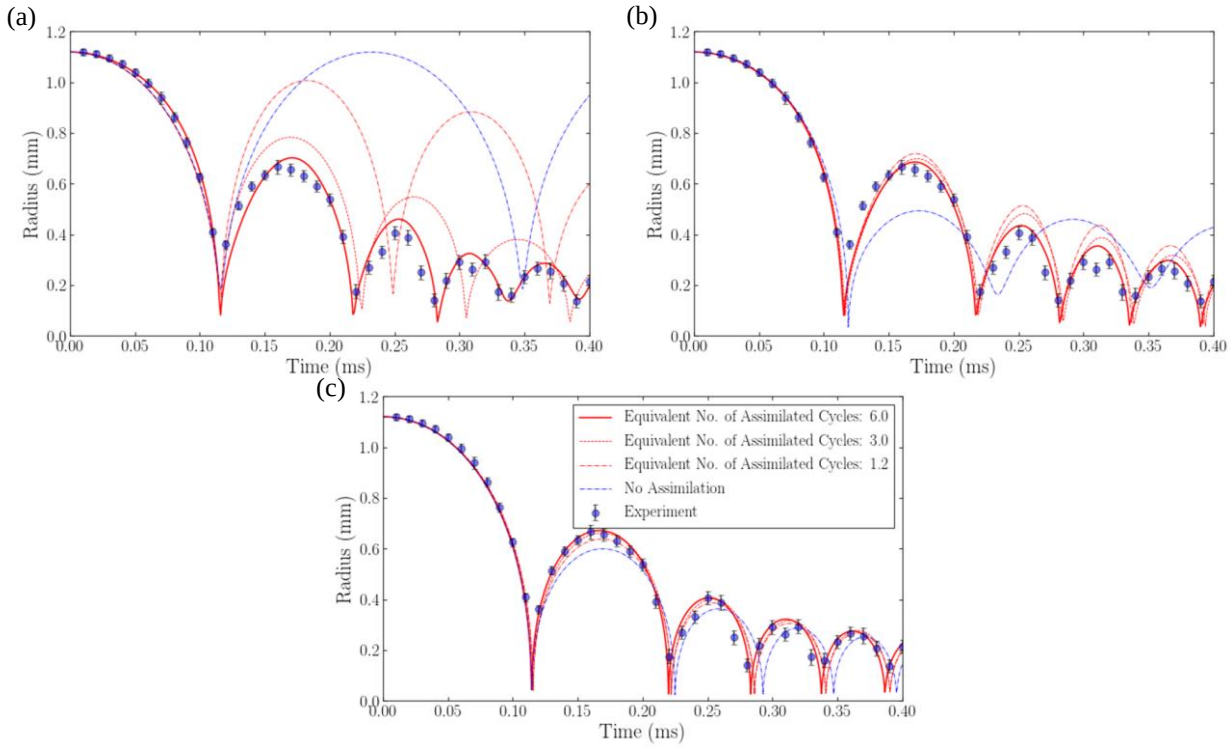

Figure 4.7. The assimilated models' performance at different levels of assimilation for a sample case with $c = 1483\ \ m/s$, $\rho_L = 1000\ \ kg/m^3$, $\mu = 1e-3\ \ m^2/s$, $\sigma = 0.072\ \ kg/s^2$, $P_\infty = 1.01e+05\ \ Pa$, $\alpha_M = 0.039$, $T_0 = T_{B_0} = 293.15K$, $n_{air_0} = 4.2e+13$, $n_{water_0} = 3.7e+16$, $P_0 = 50\ \ kPa$, $\dot{m}_0 = 0\ \ kg/s$, $R_0 = 1.12\ \ mm$, $\dot{R}_0 = 0\ \ m/s$, and $\delta_{I_0} = 0.38\ \ \mu m$: (a) R–P, (b) Yasui, and (c) Zhong. See **Fig. S2** for a comparison between the predicted bubble radius by assimilated Zhong model and the experimental data at different laser powers.

The sensitivity of the models to increasing the assimilation level is also different, such that low fidelity models result in faster measurement integration response; further the error percentage

decreaces more rapidly. Although, by increasing the level of assimilation, the assimilated models predict the cavitation bubble's size more accurately, for each cavitation model, there is an assimilation level beyond which the estimations accuracy does not increase significantly. For R-P and Yasui, after assimilating the information of six equivalent cycles, the error-ratio remains unchanged. And the estimation accuracy does not improve after integrating the information of 4.5 equivalent cycles with Zhong.

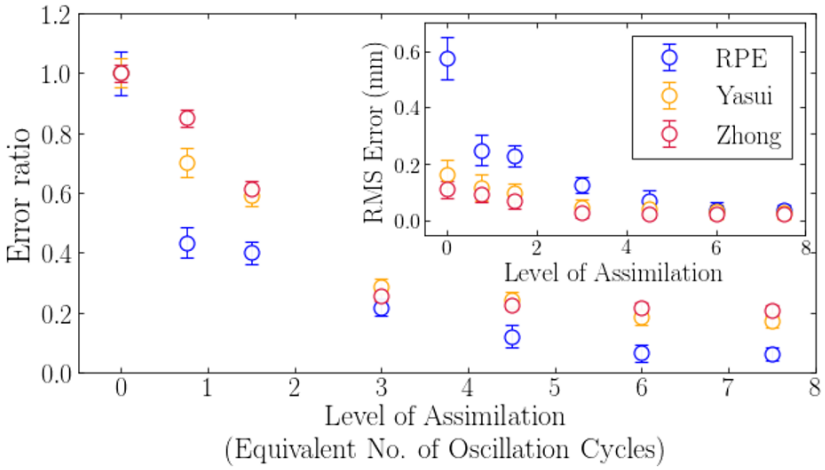

Figure 4.8. Assimilated models' error ratio at different assimilation levels.

Results in Figure 4.7 and Figure 4.8 indicate that lower levels of data assimilation for low fidelity models yield higher error than assimilation with higher fidelity models. This is expected due to the inherent physical limitations of the low fidelity models. Also, assimilation with lower fidelity models takes longer to converge. Therefore, in the assimilation with R–P, we still can predict the cavitation bubble characteristics with the same error as the assimilated model with the Zhong model but only by using a relatively larger number of assimilated data points and allowing longer convergence time.

Although in the assimilated model using R–P, the error for higher levels of data assimilation eventually falls in the range of assimilated model with the Zhong model, further observations show that this assimilated model is not able to capture any collapses after the third one. Moreover, from there on, due to underlying assumptions in the original equation, it practically interpolates between the experimental measurements (See Figure 4.7(a)). Contrarily, data assimilation with higher fidelity models captures all collapses in the same conditions, which rely

on the consideration of liquid compressibility, heat transfer, and mass transport at the cavitation boundaries in the original equation. This implies that the assimilated model eventually fails to characterize the collapses and cavitation bubble dynamics if it is applied to a model not physically compatible with the problem.

We remark that although increasing the number of assimilated data points improves the agreement between predictions and the experimental measurements, it also significantly escalates the convergence time.

Collapse-induced pressure. Next, we compare the estimated collapse-induced pressure amplitude computed by original cavitation models and assimilated versions. Figure 4.9 shows the error between hydrophones measurements and predictions by original and assimilated models for the first three collapses. Each panel in this figure corresponds to one model.

The most significant deviation between models' predictions and measurements is observed at the first collapse where R-P predicts the pressure amplitude with 65% error in average. The mean error decreases for the subsequent collapses to such extent that the mean error falls below 22% for the third collapse. Nevertheless, assimilation of measurements with R-P, results in 81%, 85%, and 66% average improvements in the estimation of the far-field pressure amplitude for the first three collapses, respectively. In this regard, by fusing experimental measurements with Yasui, the accuracy of the far-field pressure estimations are improved by 82% in average. And even though Zhong has the best performance in the prediction of the far-field pressure amplitude, integration of measurements into this model can improve the estimations by 70% in average.

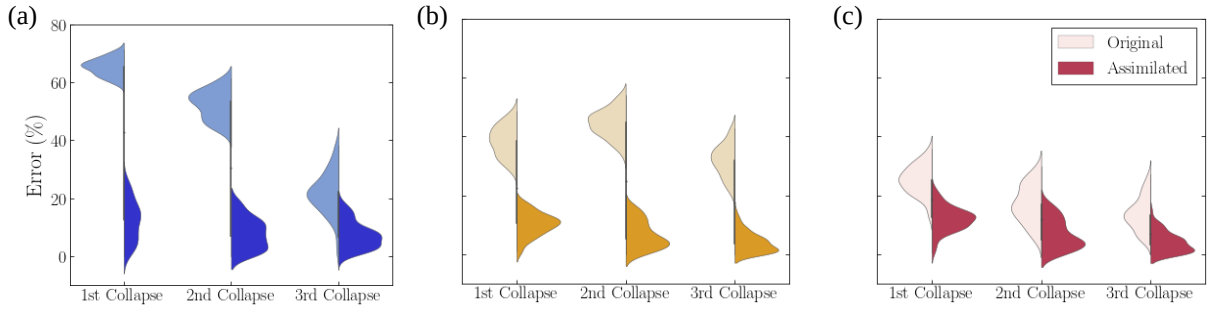

Figure 4.9. Percentage error in prediction of collapse-induced pressure amplitude by cavitation models: original models versus assimilated models. (a) R–P, (b) Yasui, and (c) Zhong.

Time of collapse incidence. We investigate the assimilated models' performance in predicting collapse occurrence time and compare it with predictions from cavitation models with no assimilation. In Figure 4.10, we depict the predicted time for cavitation collapse by three assimilated models for the first three collapses. In this figure, colors correspond to different models, and markers distinguish between assimilated and original models.

As discussed in Section 4.4.1, ignoring or inaccurate modeling of the non-equilibrium evaporation and condensation at the bubble boundaries in cavitation models result in a phase shift in the prediction of collapse incidence time after the first collapse. However, assimilated modeling can compensate for the lack of evaporation and condensation modeling in R-P and inaccurate modeling of the thermal boundary layer in Yasui, and adjust the time of collapse incidence within the collapse interval for the second and third collapses. Such that the 70% and 128% phase shifts occurred in the predictions by R-P for the second and third collapses, respectively, are adjusted after measurements fusion. In this regard, the assimilated Yasui corrects the 34% and 53% phase shifts of the second and third collapses. In spite that the phase shift in the predictions by Zhong starts at the third collapse, integration of measurements with this model results in the correction of the 7% phase shift for the third collapse.

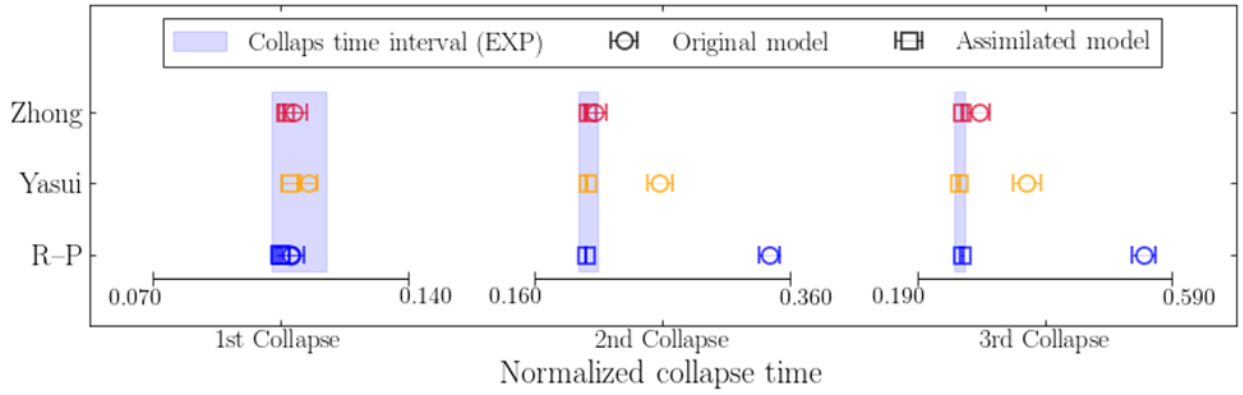

Figure 4.10. Predicted time (normalized by the cavitation duration) for the occurrence of cavitation collapse: original models versus assimilated models. Markers represent the mean values.

The assimilated model's sensitivity to the initial inputs is presented in the Appendix A. Also see **Fig. S3** for a study on the dynamic behavior of the laser-induced cavitation bubble at different laser powers.

4.5.Summary

A novel state-observer data assimilation technique, specifically designed to assimilate the measured cavitation bubble diameter, was described and then verified with a series of experiments. Thorough error analysis on this assimilated model was conducted, and the effects of different levels of assimilation were investigated. This method most accurately predicted the cavitation size and collapse-induced pressure in the liquid.

The results showed significant improvements in the bubble radius and far-field pressure estimations by assimilated models compared to cavitation models with no assimilation. For the time of collapse incidence, contrary to the original cavitation models, the assimilated models agree with the experimental measurements and predict the collapse time in the collapse interval for all three investigated collapses.

In the results section, we used the optimized inputs for the original and assimilated models for a one-on-one comparison. However, using non-optimized inputs for the assimilated model resulted in less than 2% discrepancy between the predicted cavitation bubble radius by optimized-inputs assimilated model and the non-optimized-inputs version (See Appendix A). In contrast to cavitation models, this technique made predictions of the cavitation bubble dynamics that were robust and not sensitive to the input parameters.

We applied this technique on three cavitation models with different fidelity levels. However, this assimilation technique can be integrated with other cavitation models. The results indicate that if a high fidelity model is not available, the assimilated model compensates for the lack of physical knowledge and underlying assumptions in the models. Even if a high fidelity model is available, the assimilated modeling can be employed to yield enhanced Spatiotemporal prediction of the cavitation bubble dynamics to characterize the collapse of the cavitation bubble more accurately.

This assimilated model is a tool to yield enhanced spatiotemporal prediction of the cavitation bubble dynamics with the existing models to overcome the models' limitations, including underlying assumptions and uncertainty of the initial inputs. We remark that the data assimilation is not a substitute for a model, and the most compatible model available should always be used. But subjected to model and other constraints, the data assimilation helps to overcome both minor and even more major model assumptions and limitations.

Since the factors like bubble non-sphericity, bubble cloud interaction, and the effect of stiffness of the material boundary are not well established in the existing models, the assimilated modeling is a viable tool to discover the significance of these factors in the dynamics of cavitation bubble.

4.6.Authors contributions

Javad Eshraghi: Methodology, Software, Formal analysis, Data curation, Investigation, Visualization, Writing - original draft. Arezoo M. Ardekani: Methodology, Writing - review & editing, Funding acquisition. Pavlos P. Vlachos: Conceptualization, Methodology, Investigation, Supervision, Project administration, Funding acquisition, Writing - original draft, review & editing.

4.7.Appendix A

In the results section, we used the optimized inputs for the original and assimilated models for a one-on-one comparison. However, the assimilated models are not sensitive to the models' initialization. In this Appendix, we investigate the effects of models' initialization with non-optimized inputs on assimilated models' performance. For each laser power, we found a set of optimized inputs. To set the non-optimized inputs, for each initial input, we average the optimized values for all the laser powers and add ten standard deviations to the mean. Then, we run the assimilated models with the same inputs for all the cases: $\alpha_M = 0.095$, $n_{air_0} = 3.3e + 14$, $n_{water_0} = 1.5e + 17$, and $\delta_{I_0} = 1.05\ \mu m$.

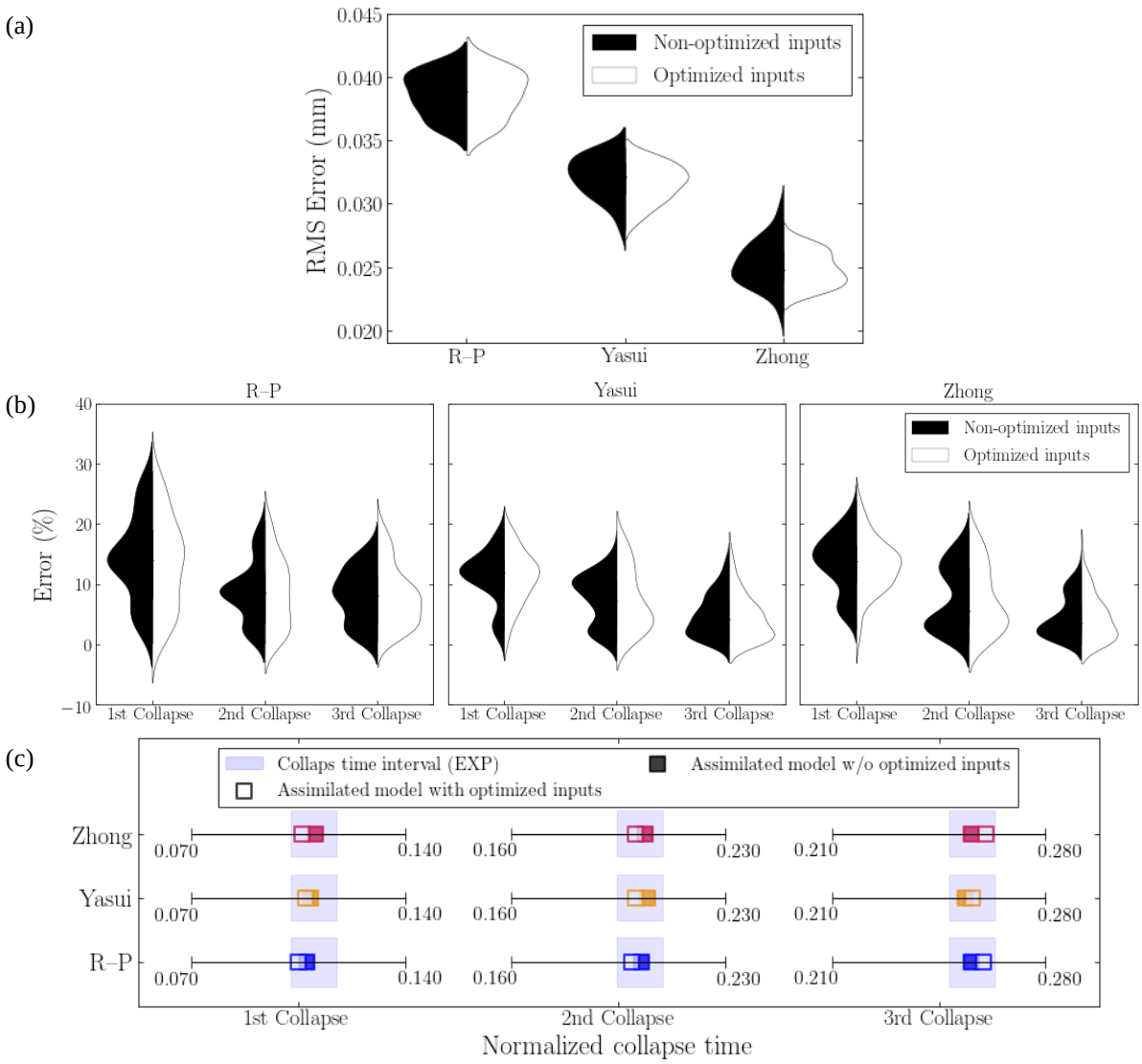

Figure 4.11. Assimilated models performances: with optimized inputs vs. without optimized inputs. (a) RMSE of predicted bubble radius, (b) percentage error in prediction of collapse-induced pressure amplitude, (c) predicted time (normalized by the cavitation duration) for the occurrence of cavitation collapse.

Figure 4.11 indicates that contrary to cavitation models, assimilated models' predictions are not sensitive to the input parameters. Significant effects of the input parameters on the bubble dynamics predicted by existing models can be found in the parametric study section of the paper by Zhong [136].

4.8.Appendix B

In this appendix, we summarize the governing equations of Yasui and Zhong models. In the assimilated models, the procedure to model the thermal effects and obtain the rate of mass transfer are identical to those for Yasui and Zhong models.

Yasui. In the Yasui model, the Van der Waals equation, $(p + a/v^2)(v - b) = R_g T$, was applied for the mixture of air and vapor inside the bubble. a and b are the coefficient of the intermolecular attraction of air and the volume occupied by vapor molecules, respectively. The changes of the number of vapor and air molecules were:

$$\frac{dn_{air}}{dt} = 4\pi R \frac{D10^3 \rho_L N_A}{18K_B}\left(0.1P_\infty - \frac{n_{air}}{n_t}P\right), \qquad \text{Equation 4-12}$$

$$\frac{dn_{H_2O}}{dt} = 4\pi R^2 \frac{10^3 N_A}{18}\frac{\alpha_M}{\sqrt{2\pi R_v}}\left[\frac{P_v^*(T_\infty)}{\sqrt{T_\infty}} - \Gamma\left(\frac{\dot{m}n_t}{n_{H_2O}P}\sqrt{\frac{R_v T_B}{2}}\right)\frac{n_{H_2O}P}{n_t\sqrt{T_B}}\right], \qquad \text{Equation 4-13}$$

and

$$\frac{dn_t}{dt} = \frac{dn_{air}}{dt} + \frac{dn_{H_2O}}{dt}. \qquad \text{Equation 4-14}$$

The changes in bubble internal pressure and mass transfer were obtained with the following ODEs:

$$\frac{dP}{dt} = \frac{R_g \frac{dT}{dt} - \left(P + \frac{a}{\left(\frac{N_A V}{n_t}\right)^2}\right)\left(\frac{4\pi}{3} N_A \frac{1}{n_t^2}\left(3R^2 \dot{R} n_t - R^3 \frac{dn_t}{dt}\right) - \frac{db}{dt}\right)}{\frac{N_A V}{n_t} - b} + \frac{2a}{\left(\frac{N_A V}{n_t}\right)^3}\left(\frac{4\pi}{3} N_A \frac{1}{n_t^2}\left(3R^2 \dot{R} n_t - R^3 \frac{dn_t}{dt}\right)\right) - \frac{1}{\left(\frac{N_A V}{n_t}\right)^2}\frac{da}{dt}, \quad \text{Equation 4-15}$$

$$\frac{d\dot{m}}{dt} = -\frac{\alpha_M}{\sqrt{2\pi R_v}}\Gamma\left(\frac{\dot{m} n_t}{n_{H_2O} P}\sqrt{\frac{R_v T_B}{2}}\right)\left[\frac{P}{\sqrt{T_B}}\frac{1}{n_t^2}\left(n_t \frac{dn_{H_2O}}{dt} - n_{H_2O}\frac{dn_t}{dt}\right) + \frac{n_{H_2O}}{n_t}\left(\frac{1}{\sqrt{T_B}}\frac{dP}{dt} - \frac{1}{2}P\frac{1}{T_B^{1.5}}\frac{dT_B}{dt}\right)\right], \quad \text{Equation 4-16}$$

where

$$\frac{dT_B}{dt} = G\frac{-\frac{dT}{dt}\sqrt{\frac{M}{T_B}} + (T_B - T)\frac{1}{2T_B}\sqrt{\frac{T_B}{M}}\frac{dM}{dt}}{1 - G\sqrt{\frac{M}{T_B}} + \frac{M}{2T_B^2}\sqrt{\frac{T_B}{M}}(T_B - T)}. \quad \text{Equation 4-17}$$

In this ODE, $M = \frac{10^{-3}}{N_A n_t}\left(18 n_{H_2O} + 28.97 n_{air}\right)$, $G = -\frac{1}{2\times 1.38\times 10^{-23}}\sqrt{\frac{\pi}{1.38\times 10^{-23}}}\,1.173\kappa\,\frac{4\times 10^{-19}}{n}$, and $n = 3$.

The temperature inside the bubble was expressed as

$$\frac{dT}{dt} = \frac{1}{4.40808\times10^{-23}n_{air} + 6.2721\times10^{-23}n_{H_2O}}\Bigg[-P\,4\pi R^2\dot{R} + 4\pi R^2\kappa\frac{T_B - T}{n\lambda} + 4\pi R^2\frac{10^3 N_A}{18}\frac{\alpha_M}{\sqrt{2\pi R_v}}\Bigg(\frac{P_v^*(T_\infty)}{\sqrt{T_\infty}}e_{H_2O}(T_\infty) - \Gamma\left(\frac{\dot{m}n_t}{n_{H_2O}P}\sqrt{\frac{R_v T_B}{2}}\right)\frac{n_{H_2O}P}{n_t\sqrt{T_B}}e_{H_2O}(T_B)\Bigg) + 4\pi R\frac{D10^3\rho_L N_A}{18K_B}\left(0.1P_\infty - \frac{n_{air}}{n_t}P\right)e_{air}(Z) - \frac{n_t^2 a}{N_A^2}\frac{1}{V^2}4\pi R^2\dot{R} + \frac{1}{N_A^2 V}\left(2n_t\frac{dn_t}{dt}a + n_t^2\frac{da}{dt}\right) - \frac{dn_{air}}{dt}e_{air}(T) - \frac{dn_{H_2O}}{dt}e_{H_2O}(T)\Bigg], \quad \text{Equation 4-18}$$

where $e_{air}(T)$ and $e_{vapor}(T)$ are the energy carried by one air molecule and one vapor molecule at temperature T, respectively, and $Z = \begin{cases} T_B, & 0.1P_\infty - \frac{n_{air}}{n_t}P < 0 \\ T_0, & 0.1P_\infty - \frac{n_{air}}{n_t}P > 0 \end{cases}$, $\lambda = \frac{V}{0.4\times10^{-18}\sqrt{2}n_t}$, $K_B = 6.737\times10^9$. Also, $\kappa = \frac{b}{\frac{N_A V}{n_t}}\left(\frac{1}{Y} + 1.2 + 0.755Y\right)\kappa_{0,mix}$, where $Y = \frac{b}{\frac{N_A V}{n_t}} + 0.625\left(\frac{b}{\frac{N_A V}{n_t}}\right)^2 + 0.2869\left(\frac{b}{\frac{N_A V}{n_t}}\right)^3 + 0.115\left(\frac{b}{\frac{N_A V}{n_t}}\right)^4$, $\kappa_{0,mix} = 0.5\left[\frac{n_{H_2O}}{n_t}\kappa_{0,H_2O} + \frac{n_{air}}{n_t}\kappa_{0,air} + \frac{1}{\frac{n_{H_2O}}{n_t}\frac{1}{\kappa_{0,H_2O}} + \frac{n_{air}}{n_t}\frac{1}{\kappa_{0,air}}}\right]$, $\kappa_{0,H_2O} = 9.98\times10^{-5}T_B - 0.0119$, and $\kappa_{0,air} = 5.39\times10^{-5}T_B + 0.0108$.

Finally, the equation of motion of the bubble could be defined as

$$\ddot{R} = \frac{1}{\left(1-\frac{\dot{R}}{c}+\frac{\dot{m}}{c\rho_L}\right)R+\frac{4\mu}{\rho_L c}}\left[\frac{1}{\rho_L}\left(1+\frac{\dot{R}}{c}\right)\left[P-\frac{2\sigma}{R}-\frac{4\mu}{R}\left(\dot{R}-\frac{\dot{m}}{\rho_L}\right)\right.\right.$$
$$\left.-\dot{m}^2\left(\frac{1}{\rho_L}-\frac{1}{\rho_g}\right)-P_\infty\right]+\frac{d\dot{m}}{dt}\frac{R}{\rho_L}\left(1-\frac{\dot{R}}{c}+\frac{\dot{m}}{c\rho_L}\right)$$
$$+\frac{\dot{m}}{\rho_L}\left(\dot{R}+\frac{\dot{m}}{2\rho_L}+\frac{\dot{R}\dot{m}}{2c\rho_L}\right)-\frac{3}{2}\dot{R}^2\left(1-\frac{\dot{R}}{3c}+\frac{2\dot{m}}{3c\rho_L}\right) \qquad \text{Equation 4-19}$$
$$+\frac{R}{\rho_L c}\left[\frac{dP}{dt}+2\sigma\frac{\dot{R}}{R^2}+4\mu\left(\frac{\dot{R}^2}{R^2}+\frac{1}{\rho_L}\frac{\left(R\frac{d\dot{m}}{dt}-\dot{R}\dot{m}\right)}{R^2}\right)\right.$$
$$\left.\left.-2\dot{m}\frac{d\dot{m}}{dt}\left(\frac{1}{\rho_L}-\frac{1}{\rho_g}\right)-\frac{\dot{m}^2}{\rho_g^2}\frac{d\rho_g}{dt}\right]\right],$$

where $\rho_g = \frac{10^{-3}}{N_A V}\left(18n_{H_2O}+28.97n_{air}\right)$.

Zhong. The bubble was assumed to be spherical with a uniform pressure inside. There were two thermal layers around the bubble surface. Thermal conduction, evaporation, and condensation occured in the thermal layer I with a thickness δ_I, which was inside the bubble; Thermal conduction occured in the thermal layer II with a thickness δ_{II}, which was in the liquid; There was a temperature discontinuity at the bubble surface. The temperature profile in the thermal layer II was a parabolic curve; and the thickness of the thermal layer II was inversely proportional to the square of the bubble radius.

They used the modified Rayleigh-Plesset equation

$$
\begin{aligned}
R\left(\ddot{R}-\frac{\dot{m}}{\rho_l}\right)\left[1-\frac{1}{c}\left(2\dot{R}-\frac{\dot{m}}{\rho_l}\right)+\frac{1}{c^2}\left(\frac{23\dot{R}^2}{10}-\frac{31\dot{m}\dot{\rho}}{10\rho_l}-\frac{\dot{m}^2}{5\rho_l^2}\right)\right] \\
+\frac{3}{2}\left(\dot{R}-\frac{\dot{m}}{\rho_l}\right)\left[\dot{R}+\frac{\dot{m}}{3\rho_l}-\frac{4\dot{R}^2}{3c}\right. \\
\left.+\frac{1}{c^2}\left(\frac{7\dot{R}^3}{5}-\frac{49\dot{m}\dot{R}^2}{30\rho_l}-\frac{14\dot{m}^2\dot{R}}{15\rho_l^2}-\frac{\dot{m}^3}{6\rho_l^3}\right)\right]+\frac{p_\infty-p_{B,2}}{\rho_l} \\
-\frac{R\dot{p}_{B,1}}{\rho_l c} \\
+\frac{1}{\rho_l c^2}\left[R\dot{p}_{B,1}\left(2\dot{R}-\frac{\dot{m}}{\rho_l}\right)\right. \\
\left.+\left(p_\infty-p_{B,1}\right)\left(\frac{\dot{R}^2}{2}-\frac{3\dot{m}\dot{R}}{2\rho_l}-\frac{\dot{m}^2}{\rho_l^2}+\frac{3p_\infty-3p_{B,2}}{2\rho_l}\right)\right] \\
=0,
\end{aligned}
\qquad \text{Equation 4-20}
$$

In which

$$p_{B,1}=p-\frac{2\sigma}{R}-\frac{4\mu}{R}\left(\dot{R}-\frac{\dot{m}}{\rho_l}\right)-\dot{m}^2\left(\frac{1}{\rho_l}-\frac{1}{\rho_g}\right), \qquad \text{Equation 4-21}$$

$$p_{B,2}=p_{B,1}+\frac{4\mu}{3c^2}\left[\frac{3\dot{m}}{2\rho_l R}\left(\dot{R}-\frac{\dot{m}}{\rho_l}\right)^2-\frac{\dot{p}_{B,1}}{\rho_l}+\frac{\dot{m}\left(p_\infty-p_{B,1}\right)}{\rho_l^2 R}\right]. \qquad \text{Equation 4-22}$$

For the mixture of air and vapor inside the bubble, the Van der Waals equation, $(p+a/v^2)(v-b)=R_gT$ was applied.

The net evaporation rate, $\dot{m}$, was expressed by the modified Hertz-Knudsen-Langmuir relation, $\dot{m}=\dot{m}_{eva}-\dot{m}_{con}$, where the evaporation rate $\dot{m}_{eva}=\alpha_M p_v^*(T_l)/\sqrt{2\pi R_v T_l}$, and the condensation rate $\dot{m}_{con}=\alpha_M \Gamma p_v/\sqrt{2\pi R_v T_B}$. Γ was a correction factor for the non-equilibrium evaporation and condensation process. The changes of the number of vapor and air molecules were

$$\dot{n}_{vapor}=4\pi R^2\dot{m}N_A/M_{vapor}, \qquad \text{Equation 4-23}$$

$$\dot{n}_{air}=4\pi RD(c_0-c_s), \qquad \text{Equation 4-24}$$

where M_{vapor} was the molar weight of vapor, D was the diffusion coefficient of air in the liquid, c_0 was the number concentration of air in the liquid at infinity, and c_s was the saturated air concentration at the bubble surface. The temperature discontinuity at the bubble surface was approximated as $T_B - T_l = \Lambda(\partial T_I/\partial r)|_{r=R}$, in which $(\partial T_I/\partial r)|_{r=R}$ was the temperature gradient at the bubble surface in the thermal layer I. They approximated $(\partial T_I/\partial r)|_{r=R}$ as $(T_B - T)R^2/\left(\delta_I^{(0)} R_0^2\right)$, where $\delta_I^{(0)}$ represented the thickness of the thermal layer I at the initial moment.

The internal energy of the bubble was $E = n_{air}e_{air}(T) + n_{vapor}e_{vapor}(T) - a(n_t/N_A)^2/V$. $e_{air}(T)$ and $e_{vapor}(T)$ are the energy carried by one air molecule and one vapor molecule at temperature T, respectively. The change of the energy inside the bubble was

$$\dot{E} = -4\pi R^2 \dot{R} p + 4\pi R^2 \left[\dot{m}_{eva} e_{vapor}(T_l) - \dot{m}_{con} e_{vapor}(T_B)\right] \frac{N_A}{M_{vapor}} + \dot{n}_{air} e_{air}(T'') + 4\pi R^2 \kappa \left.\frac{\partial T_I}{\partial r}\right|_{r=R} + \sigma_r 4\pi R^2 (T_B^4 - T^4), \quad \text{Equation 4-25}$$

where σ_r was the Stefan-Boltzmann constant. $T'' = T_l$ if $\dot{n}_{air} > 0$, otherwise $T'' = T$.

5. THE ROLE OF ABSORBED ENERGY ON OSCILLATION MODE OF AN AIR BUBBLE IN A CAVITATION-INDUCED ACOUSTIC FIELD

5.1.Background

The mechanism underlying bubble surface oscillations is similar to the Faraday instability creating waves on the surface of a vertically oscillating liquid layer [161]. In the specific case of a bubble, the volume oscillations act as a source for the parametric excitation of shape modes. Compared with volume oscillation, shape oscillation can cause more severe effects on the surrounding [162–169]. Further, more energy is required to trigger the shape oscillation on the bubble surface. Thus, a proper characterization of the shape oscillation and energy absorption at different oscillation regimes is required to understand the effects on the bubble's surroundings when sustained in the acoustic field. Theoretical research discussed the excitation of volume and shape oscillations as well as oscillation-mode-transition problems in a single bubble system under finite-amplitude external force [170–173]. However, less knowledge has been accumulated by experimental approaches [174]. Moreover, to date, we do not have a physical understanding of the role of absorbed energy by the acoustically excited gas bubble in the shape taken by the fluid-fluid interface and transition from volume oscillation to shape oscillation to breakup. This paper presents a detailed analysis of a single air bubble dynamics exposed to a cavitation-induced acoustic field in water from an energy absorption perspective.

To study the interactions of a single air bubble with an acoustic field induced by a cavitation bubble, we inject air bubbles with five different sizes ($D_g = 1.30 \pm 0.01\ mm$, $1.48 \pm 0.01\ mm$, $1.75 \pm 0.01\ mm$, $2.00 \pm 0.01\ mm$, and $2.25 \pm 0.02\ mm$) under stagnant flow conditions at the bottom of a $5 \times 5 \times 10\ cm^3$ acrylic-sided container filled with distilled water. To control the acoustic field intensity, the cavitation bubbles are generated on top of the air bubble at the center of the container (see Fig. S1 [175]) using a laser at three different laser powers ($29.9 \pm 1.6\ \mu J$, $51.8 \pm 1.5\ \mu J$, and $80.4 \pm 2.1\ \mu J$). We record the dynamics of both cavitation and air bubbles using a high-speed digital video camera operating at 66,000 fps. The far-field pressure is also recorded using two hydrophones sampling at $1\ MS/s$ placed $25\ mm$ away from the cavitation nucleation site, on top of each other, with a separation distance of $\sim 15\ mm$. We vary the relative distance between the gas bubble and the cavitation bubble, L/D_g (ranged from 4.75 to 10), by

delaying the cavitation inception using a photodiode detector. All the tests are performed after the gas bubble reaches a terminal velocity of $0.16 - 0.24\ m/s$ at $L/D_g \sim 15 - 20$.

5.2.Observations

Once the cavitation bubble is generated, the air bubble starts oscillating in the volume oscillation regime. The volume oscillation means the radial expansion and contraction of the bubble without varying its shape. As soon as the incident acoustic wave is sufficiently intense [171,176–183], the oscillating surface of the acoustically active air bubble becomes unstable through the forcing of large amplitude purely radial volume oscillations. This instability leads to the onset of shape oscillations corresponding to zonal harmonics of the initially spherical bubble (see Figure 5.1, Fig. S2 [184]). That is, the volume oscillations act as a source for the parametric excitation of shape modes (see Movie S1 [185]). Representative images of the air bubble oscillations at different oscillation regimes are illustrated in Figure 5.1 and Fig. S2 [184]. In addition, the effects of air bubble size, D_g, and relative distance between the gas bubble and the cavitation bubble, L/D_g, on the air bubble oscillation regimes are shown in Movie S1 [185].

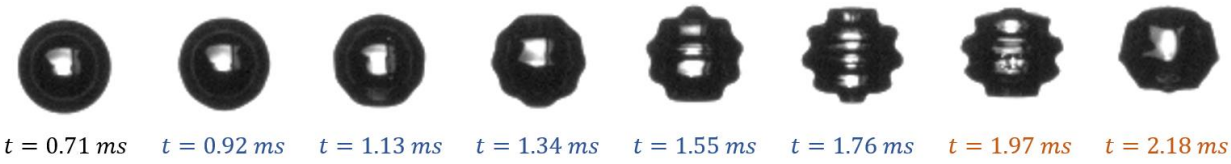

Figure 5.1. Representative images of oscillation-mode-transition of a gas bubble. The bubble's final oscillation regime is multi-mode shape oscillation. $D_g = 1.48\ mm$, $L/D_g = 8.25$, and $E_{cav} = 0.82\ mJ$. The time instant of cavitation onset is considered as $t = 0$.

In general, under acoustic pressure forcing, if the acoustic wavelength is much larger than the bubble size, the initial bubble response is spherical oscillations of the radius. However, as the amplitude of forcing increases, the spherical shape of the bubble becomes unstable. This instability leads to the onset of shape oscillations. When the spherical volume oscillation becomes unstable, linear stability theory predicts exponential growth of the shape oscillation amplitude that is ultimately controlled by nonlinearity [172].

5.3.Methodology

Currently, no single approach can define different oscillation regimes and automatically detect the regime's transition from one to another. Here, we propose a robust frequency-based approach to define different oscillation regimes. In this approach, the air bubble volume variation over time signal obtained from the high-speed imaging (Figure 5.2(a)) is analyzed with the continuous wavelet transform to find the dominant frequency of size variations over time (Figure 5.2(b)). Next, the air bubble boundary at each instant is transformed into $r-\theta$ coordinate. The obtained signal is denoised with a discrete wavelet transform [186,187] by performing multilevel wavelet decomposition [188] using Daubechies wavelets (db6) (Figure 5.2(c) inset). Then, the dominant wavenumber of the denoised signal is determined by performing Fast Fourier transform (FFT) and finding the maximum amplitude wavenumber (Figure 5.2(c) inset). Thus, the time history of the dominant wavenumber of air bubble boundary is obtained (Figure 5.2(c)). Lastly, the air bubble oscillation modes are achieved by plotting the time history of boundary wave number against the dominant frequency of size variations over time (Figure 5.2(d)). Thus, the air bubble undergoes volume oscillation regime if one mode is observed in the air bubble oscillation mode map (Figure 5.2(e-1)); if exactly two modes are observed in the map, the final oscillation regime that the air bubble undergoes is single-mode shape oscillation (Figure 5.2(e-2)); and if the map shows multiple modes of oscillation, the bubble final oscillation regime is multi-mode shape oscillation (Figure 5.2(e-3)). Moreover, in more intense acoustic fields and when the air bubble is closer to the acoustic source, the air bubble may break into single/multiple small bubbles while undergoing multi-mode shape oscillation. Hence, we define a new regime as a *breakup* for such cases. This regime is automatically detected during the image processing step as detecting more than one bubble in any of the frames indicates that the bubble has broken up. The detailed methodology framework for different air bubble oscillation regimes can be found in Fig. S3 [189]. Effects of induced energy and relative air bubble-cavitation bubble distance on the instantaneous dominant frequency of air bubble volume variation (obtained from continuous wavelet transform of the air bubble volume variation signal), dominant wave number of air bubble boundary, and the air bubble oscillation mode map are also shown in Fig. S5 [190].

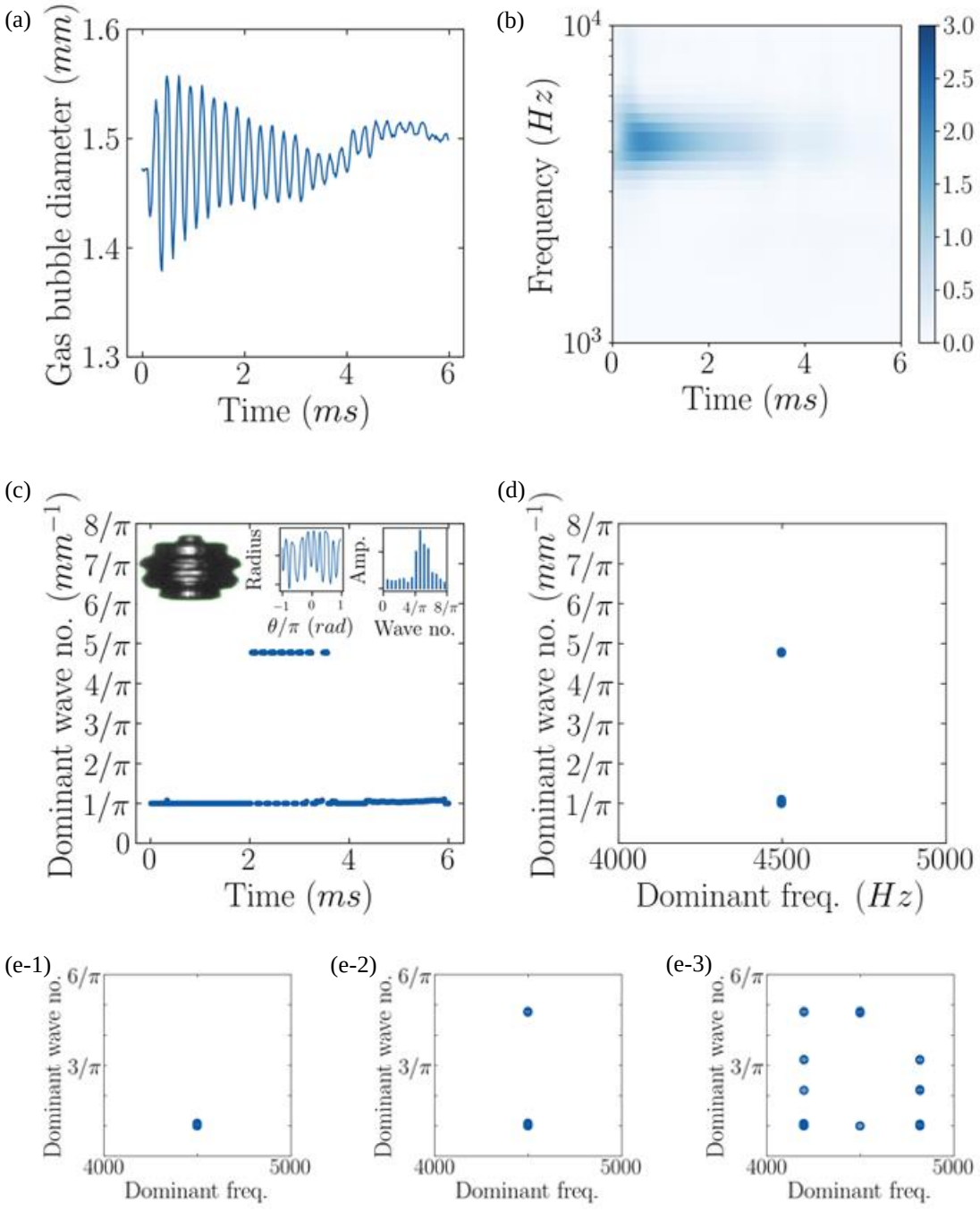

Figure 5.2. Methodology framework for the analysis of gas bubble dynamics. Representative analysis for a single-mode shape oscillation gas bubble: (a) Gas bubble equivalent diameter variation in time, (b) Continuous wavelet transform of the gas bubble diameter signal shown in panel (a), (c) Dominant wave number of gas bubble boundary at each frame (Insets show the gas bubble detected boundary, radius, and boundary wave number at $t = 2.3\ ms$), and (d) the gas bubble oscillation mode map (gas bubble boundary wavenumber as a function of gas bubble diameter oscillation frequency). See Fig S3 for the representative methodology of gas bubble analysis at different oscillation regimes. $D_g = 1.48\ mm$, $L/D_g = 9.5$, and $E_{cav} = 0.58\ mJ$. (e) Sample oscillation mode map for (e-1) volume oscillation, (e-2) single-mode shape oscillation, and (e-3) multi-mode shape oscillation. It's worth mentioning we have multiple points overtopping for each mode that correspond to different times..

The characteristic wave number of volume oscillation is $1/\pi$ due to pure radial oscillation; the presence of this wavenumber in all the oscillation regimes implies that the shape oscillation is superimposed on top of the volume oscillation when it is triggered.

In the absence of an air bubble, we can quantify the induced energy by the cavitation bubble oscillations using the obtained pressure signal by the hydrophone. The energy of the pressure signal at the hydrophone location is calculated as $E_S = 4\pi r^2/(\rho c) \int p^2 dt$, where ρ, c, and t are water density, speed of sound in water, and time, respectively. Also, r and p represent the hydrophone distance from the cavitation nucleation site and hydrophone reading (bottom one), respectively. When the air bubble is injected into the container, part of the induced energy by the cavitation bubble is absorbed by the air bubble. To calculate the amount of absorbed energy by the air bubble (E_{Abs}), we predict the far-field pressure, P_{FF}, induced by the cavitation bubble in the absence of the air bubble using the assimilated Zhong model [191,192] (Figure 5.3(a)), compute the induced energy by this predicted signal, and compare it with the energy of the pressure signal obtained by the hydrophone that is captured in the presence of the air bubble (Figure 5.3(b)). Both P_{FF} and E_{Abs} are time dependent parameters. In this work, we use the maximum value of P_{FF} and the value of E_{Abs} at the end of the 10th oscillation cycle of cavitation bubble where we see no time variation anymore.

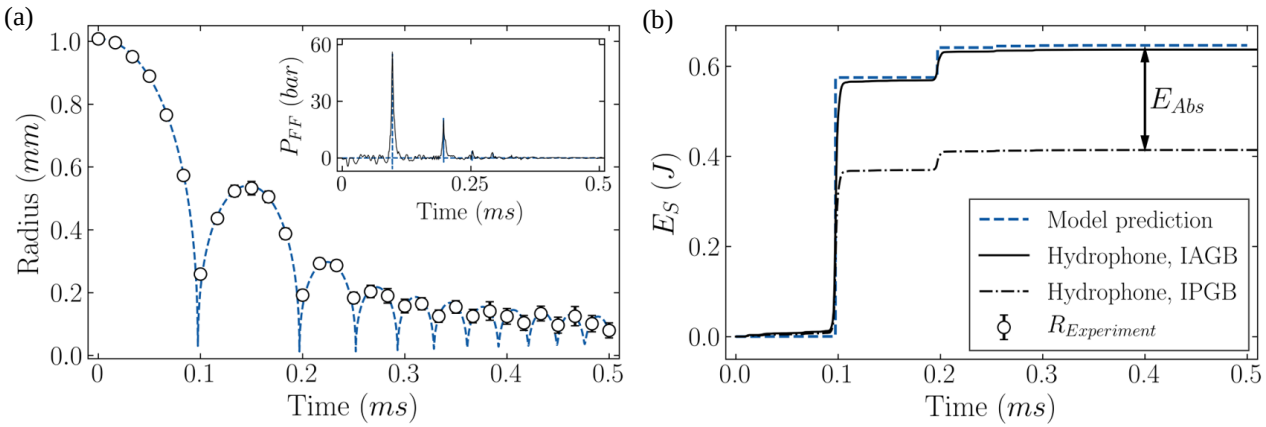

Figure 5.3. (a) Cavitation bubble radius measured from the experiment (black circle markers) vs. the predicted radius with the assimilated model. Inset: Time variation of the induced pressure at the hydrophone location measured with the hydrophone and predicted with the model, P_{FF}. (b) Cavitation-induced far-field pressure signal energy in the gas bubble's absence (IAGB) and presence (IPGB). $D_g = 1.48\ mm$, $L/D_g = 8.25$, and $E_{cav} = 0.82\ mJ$ (see Figure S4 [193]).

Furthermore, the available energy in the field, which is induced by the cavitation bubble and known as cavitation energy, can be written as, $E_{Cav} = 4\pi/3(p_{stat} - p_v)\int_{t_0}^{t_f} R^3 dt$, where p_{stat} and p_v are the hydrostatic pressure and water vapor pressure, t_0 is the time instant that the cavitation bubble reaches its maximum radius, t_f is the time instant at the end of the 10th oscillation cycle, and the and R represents the instantaneous radius of the cavitation bubble.

5.4.Discussion

We conducted a parameter study by varying the air bubble size, cavitation generation delay, and laser power, thus elucidating the influence of cavitation energy, L/D_g, and $Bo = \rho g D_g^2/\sigma$ on the air bubble final oscillation regime (see Figure 5.4). Figure 5.4 illustrates the air bubble oscillations regimes map based on the cavitation energy and a modified Bo ($\widetilde{Bo} = \rho g D_g L/\sigma$) that includes the distance between air bubble and cavitation bubble. At high $\widetilde{Bo} > 4.2$, the air bubble is stiffer, that is, the bubble needs more energy for deformation and transition to another oscillation regime. Also, the air bubble is further from the acoustic source; thus, the excitation energy at the air bubble location is not high enough to cause a transition to shape oscillation. In contrast, at low $\widetilde{Bo} < 2$, the air bubble is smaller and closer to the cavitation nucleation site. Thus, the induced energy exceeds the energy absorption capacity of the air bubble leading to its break up. Contrary to these two extremes, for a $\widetilde{Bo}$ in the range of 2 to 4.2, the air bubble oscillation regime is found to be also a function of the cavitation energy, as shown in Figure 5.4. In this range, the air bubble oscillation regime transitions from volume oscillation to single-mode shape oscillation to multi-mode shape oscillation to finally break up as the cavitation energy, E_{Cav}, is increased. The transitions between the multi-mode shape oscillation and breakup are determined based on the presence of tiny ($\sim 25\,\mu m$) bubbles in the vicinity of the air bubble detected in the image processing step. The distinction between the volume, single-mode shape, and multi-mode shape oscillation regimes is made based on the air bubble oscillation mode map (Figure 5.2(d) and Fig. S3(c-1-3) [189]): for air bubble oscillating at one mode, it is considered as volume oscillation, for the bubble oscillating at exactly two modes as single-mode shape oscillation, and for the air bubble oscillating at more than two modes as multi-mode shape oscillation.

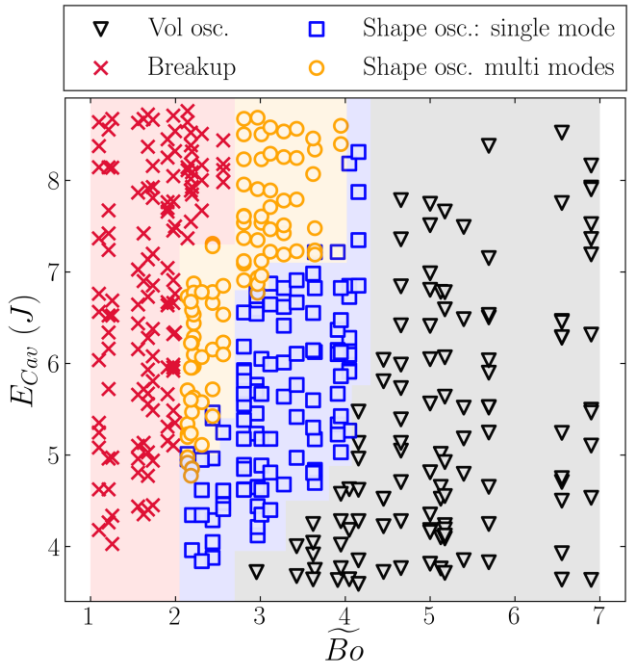

Figure 5.4. Air bubble oscillation regime map: The influence of E_{Cav} and $\widetilde{Bo}$ on the air bubble final oscillation regime.

In the case of shape oscillation, our observations show that the transition from volume oscillation to shape oscillation is a function of cavitation energy, L, and air bubble size. Hence, we hypothesize that the acoustic energy absorbed by the air bubble controls the ripples' onset on the air bubble surface. To investigate the correlation between the shape oscillation onset time and the air bubble absorbed energy, we first nondimensionalize the shape oscillation onset time and the absorbed energy.

The dynamics of an air bubble in an external acoustic field is expressed in terms of the Rayleigh-Plesset (R-P) equation [128,194]:

$$\frac{P_B - P_\infty}{\rho} = R\frac{d^2R}{dt^2} + \frac{3}{2}\left(\frac{dR}{dt}\right)^2 + \frac{4\nu}{R}\frac{dR}{dt} + \frac{2\sigma}{\rho R}, \qquad \text{Equation 5-1}$$

where R, P_B, and P_∞ represent the air bubble radius, air bubble internal pressure, and the external pressure field, respectively. Also, ρ, ν, and σ are the surrounding liquid density, kinematic viscosity, and surface tension, respectively. To evaluate the relative importance of different terms in R-P, we nondimensionalize Equation 5-1 by defining $P^* = P/(\sigma/L_c)$, $R^* = R/L_c$, and $t^* = tf$

as non-dimensional variables, where L_c and f are characteristic length and frequency, respectively. The nondimensionalization leads to

$$P_B^* - P_\infty^* = \boldsymbol{St}^2.\boldsymbol{Re}.\boldsymbol{Ca}\, R^*\ddot{R}^* + \boldsymbol{St}^2.\boldsymbol{Re}.\boldsymbol{Ca}\,\frac{3}{2}\,\dot{R}^{*2} + \boldsymbol{Ca}\frac{4\dot{R}^*}{R^*} + \frac{2}{R^*}, \qquad \text{Equation 5-2}$$

where $\boldsymbol{Re} = \frac{\rho L_c V}{\mu}$, $\boldsymbol{St} = \frac{f L_c}{V}$, $\boldsymbol{Ca} = \frac{\mu V}{\sigma}$, and $V = f L_c$ is the characteristic velocity. The scaling analysis ($St^2.Re \gg 1$) yields to

$$\frac{P_B^* - P_\infty^*}{L/\sigma} = \rho L^2 f^2 \left(R^* \frac{d^2 R^*}{dt^{*2}} + \frac{3}{2}\left(\frac{dR^*}{dt^*}\right)^2 \right). \qquad \text{Equation 5-3}$$

Equation 5-3 implies that the dimensionless pressure ($P_B^* - P_\infty^*$) is correlated with the nondimensionalized energy per unit mass $\left(R^* \frac{d^2 R^*}{dt^{*2}} + \frac{3}{2}\left(\frac{dR^*}{dt^*}\right)^2 \right)$. Thus, the bubble's internal energy is scaled with $\rho {L_c}^5 f^2 \equiv \rho D_g^5 f^2$, where f is the dominant frequency of the air bubble volume variations. We also nondimensionalize ripples onset time (t_{ripp}) by ν/D_g^2 and then plot it against dimensionless absorbed energy ($E_{Abs}/(\rho D_g^5 f^2)$).

Figure 5.5 shows a linear relationship (in log-log scale) between the dimensionless absorbed energy and shape oscillation onset time. The results demonstrate that the more energy absorbed by the air bubble, the sooner the ripples appear on the bubble surface. In addition, such bubbles are more likely to break into smaller bubbles. Figure 5.5 also indicates the feasibility of employing the nondimensionalized absorbed energy to define transition thresholds between different oscillation regimes. The results point out that if the nondimensionalized acoustic energy absorbed by an air bubble exceeds 4500, the bubble breaks into smaller bubbles. Also, the transition from single-mode shape oscillation to multi-mode shape oscillation occurs when the dimensionless air bubble absorbed energy goes beyond 3400.

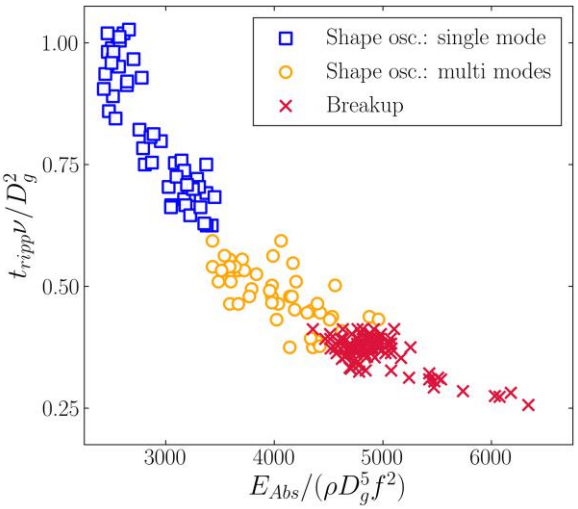

Figure 5.5. Air bubble shape oscillation onset as a function of absorbed energy. The time instant of cavitation onset is considered as $t = 0$.

Results shown in Figure 5.4 and Figure 5.5 imply that the local acoustic intensity and air bubble size are determinant factors in the air bubble energy absorption. Absorbed energy by the air bubble over a finite time interval (t_i, t_f) increases the bubble internal energy that can be written as

$$E_{Abs} \sim P\Delta V + \sigma\Delta S + \Delta \mathrm{K}, \qquad \text{Equation 5-4}$$

where $P\Delta V$ is the work done on the surrounding liquid by the changes in the air bubble's volume ($\Delta V = 0.5\pi D_g^2 \Delta D_g$), $\sigma\Delta S$ represents the changes in the surface energy due to changes in the surface area ($\Delta S = 2\pi D_g \Delta D_g$), and ΔK is the changes in the kinetic energy ($\mathrm{K}|_{t_i} = 0$) of the bubble formulated as $\Delta \mathrm{K} = \mathrm{K} = \pi\rho D_g^3 \left(\Delta D_g f\right)^2/16$. Substitution in Equation 5-4 and keeping only the most dominant term lead to

$$\frac{E_{Abs}}{\rho D_g^5 f^2} \sim \frac{2\pi\Delta D_g^2}{32 D_g^2} \frac{8P}{\rho D_g \Delta D_g f^2} = \frac{\pi\sigma\Delta D_g}{2\rho D_g^4 f^2} \frac{P D_g}{\sigma}. \qquad \text{Equation 5-5}$$

This suggests a linear relationship between the dimensionless absorbed energy and a modified $We = P_{FF} D_g/\sigma$, that measures the relative importance of the acoustic intensity, in terms of

induced pressure at the air bubble location, P_{FF}, compared to the surface tension, σ. In Figure 5.6, we illustrate the correlation of dimensionless absorbed energy with modified We. Figure 5.6 indicates that the air bubble energy absorption increases linearly with We that agrees with our analytical solution presented in Equation 5-5. The scaling constant in Equation 5-5 is assumed to be the number of oscillation cycles of the air bubble before the oscillations fade, which is $n = 37 \pm 3$, according to the experimental data. The dot-dashed line in Figure 5.6 is the predicted absorbed energy by the analytical solution at different We, which is consistent with experiments.

Figure 5.6 also shows that the modified We can also be employed to determine critical thresholds for oscillation regime transitions. That is, a bubble present in an acoustic field oscillates in the volume oscillation regime if $We < 2.3 \times 10^5$. The bubble undergoes single-mode shape oscillation if $2.3 \times 10^5 < We < 3.2 \times 10^5$, and multi-mode shape oscillation occurs when $3.2 \times 10^5 < We < 4.7 \times 10^5$. Lastly, $We > 4.7 \times 10^5$ causes high-amplitude oscillations that lead to bubble breakup.

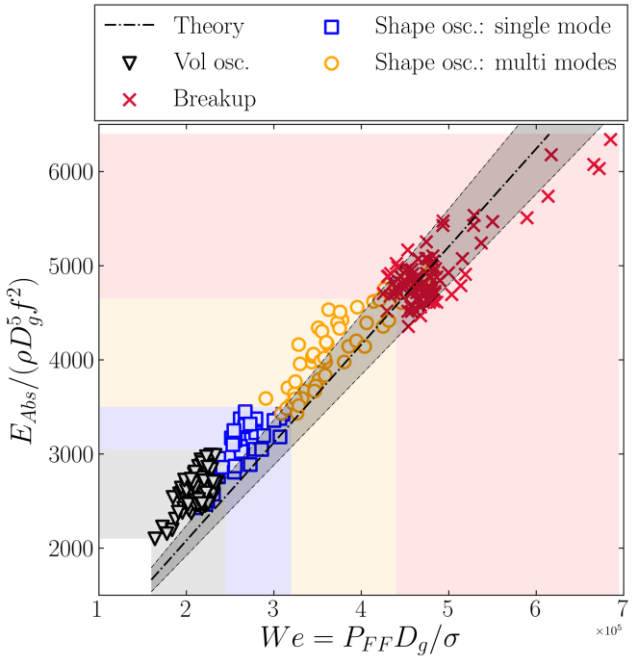

Figure 5.6. Dimensionless absorbed energy as a function of modified We at different air bubble oscillation regimes. The slope of the dot-dashed line (theory) is 0.0010 ± 0.0001 (The uncertainty was calculated by propagating the uncertainty in the measurement of n, f, and D_g), and the slope of the line of best fit to the experimental data (not shown here) is 0.0011 with $R^2 = 0.89$. The shaded area around the dot-dashed line shows the lower and upper bounds at a 95% confidence interval.

We point out that the distinction of volume oscillation from single-mode shape oscillation has the most uncertainty where we observe a 15% overlap between these two oscillation regimes. This uncertainty is caused by the low amplitude ripples that may not be fully captured due to the spatial resolution of the images.

5.5.Summary

The frequency-based analysis of an air bubble oscillating in a cavitation-induced acoustic field revealed that different regimes could be defined robustly based on the wavenumber of the air bubble boundary. It was also shown that the transition between different regimes was controlled by the air bubble absorbed energy and that the absorbed energy was a linear function of We defined based on the induced acoustic pressure.

Even though we focused on the interactions of a single bubble with an acoustic source, it can be expanded to investigate the energy absorbance of bubble curtains used to contain oil spills, reduce shock wave propagation, and analyze other environmental and industrial problems.

5.6.Authors contributions

Javad Eshraghi: Methodology, Software, Formal analysis, Data curation, Investigation, Visualization, Writing - original draft. Sayantan Bhattacharya: Methodology, Software, Formal analysis, Investigation, Writing - review & editing. Lalit K Rajendran: Methodology, Investigation, Writing - review & editing. Hector Gomez: Conceptualization, Analytical modeling, Investigation, Supervision, Writing - Review & editing, Pavlos P. Vlachos: Conceptualization, Methodology, Investigation, Supervision, Project administration, Funding acquisition, Writing - Review & editing.

6. ASSESSMENT OF CAVITATION INTENSITY IN SPRING-DRIVEN AUTOINJECTORS

6.1.Background

Autoinjectors (AIs) are medical devices designed for delivering a bolus dose, typically no more than 2 mL, of a drug product solution to patients via subcutaneous and intramuscular injections. Self-administering subcutaneous (SQ) and intramuscular injections using AIs are used to treat many indications, such as anaphylaxis, multiple sclerosis, and rheumatoid arthritis [195]. The global autoinjectors (AIs) market size is estimated to hit around US$3.2 billion by 2026 and is expected to grow at CAGR (compound annual growth rate) above 19.6% over the forecast time frame [196]. Most of the drugs delivered by AIs are proteins and amino acid derivatives, i.e., monoclonal antibodies (mAb), interferon, and epinephrine [197]. A schematic of a spring-driven autoinjector is shown in Figure 6.1(a). The administration process can be divided into three stages:(i) activation, (ii) insertion, and (iii) injection [198]. However, for some devices, activation and insertion stages can coincide. The insertion process in spring-driven AIs can generate abrupt acceleration and deceleration of the syringe, inducing violent motion of the air-fluid interface [199] and can potentially cause cavitation [200].

Cavitation occurs in a liquid when the local pressure suddenly drops at or below the vapor pressure, resulting in small vapor cavities. These small cavities undergo several cycles of growth and collapse, and each collapse generates extreme heat and pressure. In an AI, cavitation can occur as the fluid is impulsively set into motion during insertion (See Figure 6.1(b)) [201,202]. The motion generates pressure waves propagating inside the drug column reflected by the air–drug interface and the bottom wall resulting in multiple reverberations of pressure waves and yielding to cavitation onset [202,203]. The collapse of the cavitation bubbles may damage the container - syringe, and inside syringe, it may impose mechanical and hydrodynamic stresses on drug biomolecules. The therapeutic protein molecules are susceptible to loss of bioactivity and aggregation. The therapeutic protein aggregates are a potential concern to product quality and patient safety because the particles can evoke immunogenic responses [204–207]. It is, thus, essential to evaluate the intensity of cavitation formed upon autoinjector activation and investigate the effects of AI design parameters on the cavitation intensity formed in AIs [202]. In the current work, we perform a series of physical experiments to capture the dynamics of cavitation using

high-speed photography. Additionally, we employ a data assimilation approach to quantify the cavitation collapse-induced extension rate in syringes during the insertion stage of the AI administration.

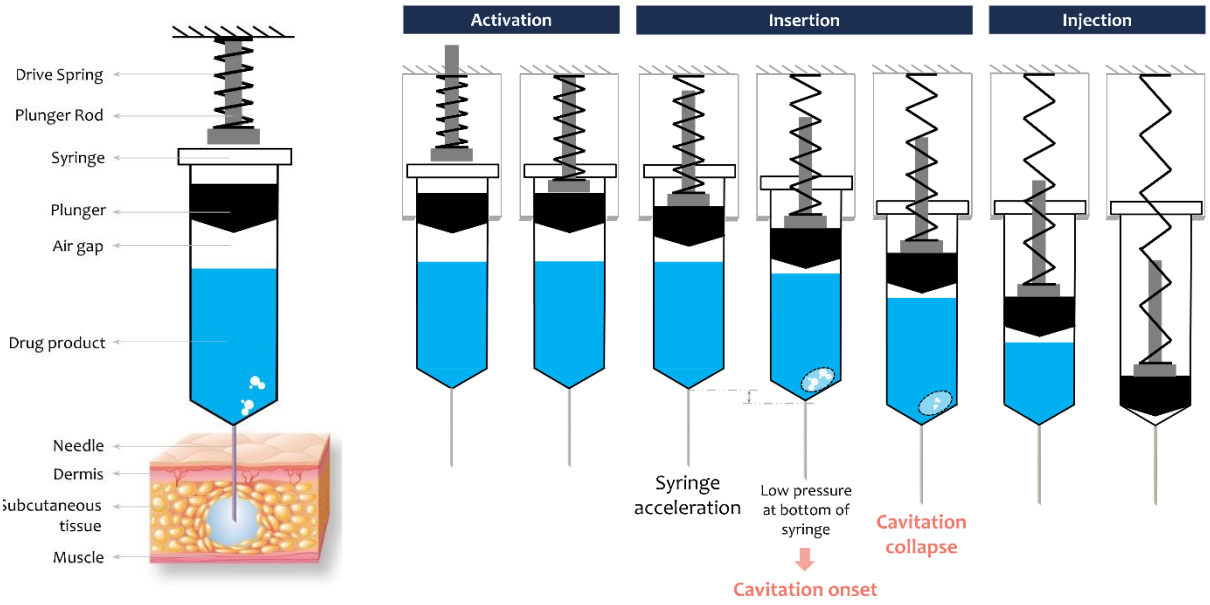

Figure 6.1. (a) Schematic of a spring-driven autoinjector. (b) The administration process of a spring-driven autoinjector and occurrence of cavitation due to sudden acceleration during needle insertion stage. Cavitation in AI happens due to the high acceleration of the syringe and the subsequent relative displacement between the drug product and the syringe. This relative displacement causes a pressure drop at the bottom of the container, and if the local pressure goes below the vapor pressure, cavitation is formed.

The moment that yields the most considerable pressures, temperatures, strains, and stresses during the growth and collapse of the cavitation bubble is the end of the collapse when the bubble radius is close to its minimum, which happens within less than a microsecond, and has the largest impact. An accurate characterization of the collapse is needed to assess the effects of cavitation. One approach for quantifying collapse-induced shear stress and pressure wave is the direct measurement by placing a pressure transducer and a strain gauge inside the syringe [201]. However, this invasive measurement requires modifications of the autoinjector device, which is not desired. Moreover, since only a small portion of the drug is exposed to the high shear stress and the cavitation location is unpredictable, determining a spot in the syringe to place the sensors for a reliable measurement is challenging. In addition, the temporal resolution of the measurement

tools is another limitation for directly measuring the collapse-induced shear stress and pressure wave. Quantitative flow visualization is a non-invasive technique that can investigate cavitation collapse. However, the insufficient temporal resolution makes it impractical to measure the cavitation intensity (induced extension rate upon collapse, pressure upon collapse, and etc...). Therefore, we propose employing a data assimilation approach that combines the experimentally captured cavitation dynamics from the visualization and cavitation dynamics models to achieve high spatiotemporal resolution predictions for cavitation collapse characterization [208]. This technique takes advantage of the reliability of the experimental measurements and high temporal resolution of cavitation dynamics models and can overcome the modeling limitations.

Due to the abovementioned limitations, no study to date has focused on quantifying cavitation intensity in the AIs with a non-invasive approach. This manuscript presents the first detailed analysis of cavitation dynamics that occurs in autoinjectors to address this gap. We investigate the effects of drive spring force, air gap size, fluid column height, and fluid viscosity on the severity of cavitation that occurs in AI.

6.2.Methods

6.2.1. Experimental setup

The experimental setup was described in detail in [4], and only a summary is given here. To replicate the operating procedures of a single-spring actuated AI, a simplified AI platform was implemented to study the cavitation phenomenon due to the sudden acceleration of the syringe in the AI device. The plunger rods, drive springs, and syringes were mounted on a 3D-printed fixture and imaged using a high-speed camera (Phantom V2640, Vision Research Inc). An LED light source (Flashlight300, LaVision) accompanied by a light diffuser (DG100X100–1500, ThorLabs, Inc.) was used to achieve uniform background illumination of the prefilled syringe. For each experimental run, we collected images at 20000 fps with a spatial resolution of $15.6\ \mu m/pixel$.

Three separate test matrices were designed to study the effects of drive spring force, air gap size, and filling volume on cavitation intensity. The detail of each test matrix is shown in Table 6.1. For the air gap size study, the drive spring force of the autoinjector devices was kept constant at $2.25X\ N$, and for the filling volume and drive spring force studies, the air gap height was constant at $2\ mm$.

Table 6.1. Experimental test matrices for drive spring force, air gap size, and filling volume studies. (The numbers under the viscosity columns represent the number of the tested autoinjector devices at that configuration).

Case A: Drive spring force study

Syringe fill volume (mL)	Drive spring force (N)	Viscosity				
		1 cP (sample counts)	5 cP (sample counts)	10 cP (sample counts)	18 cP (sample counts)	25 cP (sample counts)
~1.0	X	3	0	3	3	3
	2.25X	3	0	3	3	3
	3.375X	3	0	3	3	3
~2.0	1.50X	3	3	3	3	0
	2.125X	3	3	3	3	0
	3.75X	3	3	3	3	0

Case B: Air gap size study

Syringe fill volume (mL)	Air gap size (mm)	Viscosity	
		1 cP (sample counts)	18 cP (sample counts)
~1.0	4	4	4
	3	4	4
	2	4	4
	1	4	4
~2.0	4	4	4
	3	4	4
	2	4	4
	1	4	4

Case C: Fill volume study

Syringe volume (mL)	Fill volume (mL)	Drive spring force (N)	Viscosity
			1 cP (sample counts)
1.0	~ 0.2	X	4
		1.5X	4
		2X	4
	~ 0.4	X	4
		1.5X	4
		2X	4

All syringes used in the experiments were prefillable glass syringes (BD Neopak^{TM}) with an inner diameter of 8.5 *mm* for the 2.25 mL syringes (~2.0 mL liquid fill) and 6.35 *mm* for the 1 mL syringes (~1.0 mL liquid fill).

Each high-speed video recording was analyzed using an in-house image processing code implemented in MATLAB. The method automatically detected the cavitation bubble boundaries and calculated the equivalent bubble diameter to locate and track the cavitation bubble dynamics.

The bubble detection scheme consists of three steps: (1) noise reduction and image contrast enhancement, (2) binarization, and (3) boundary detection and bubble size computation. First, an isotropic Gaussian smoothing kernel filters the original image (Figure 6.2(a)) to reduce noise (see Figure 6.2(b)). Next, we enhance the image contrast by saturating the bottom 1% and the top 1%

of all image pixel values (see Figure 6.2(c)). Then, median filtering removes high-frequency signal components (also known as impulse noise and salt-and-pepper noise). In the binarization step, the pixel intensity thresholding filters all signals below a given brightness by replacing all pixels in the image with luminance greater than the specified threshold with white pixels and replacing all the other pixels with black pixels. However, to smooth rough edges along the binary image, we blur the image (see Figure 6.2(e)) and then re-threshold the blurred one to convert it to binary (see Figure 6.2(f)). In the last step, the bubble boundary is detected by calculating the image gradient and locating the discontinuity in the brightness signal (see Figure 6.2(g)). Next, the detected boundary is smoothed with a Savitzky-Golay sliding polynomial filter [209] (see Figure 6.2 (h)). Lastly, the area (A) of the detected boundary is determined and then the equivalent diameter, D, is obtained using $D = \sqrt{4A/\pi}$. These measurements were then assimilated into the cavitation model using the PID feedback controller to estimate the cavitation intensity.

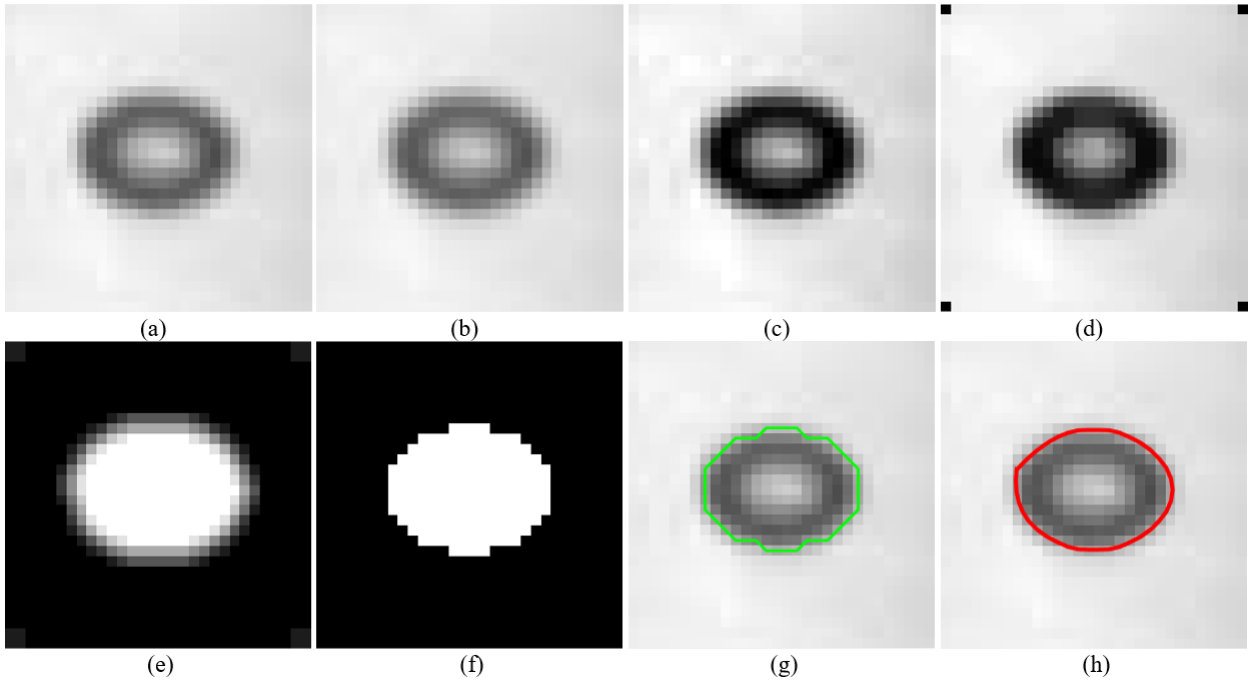

Figure 6.2. Image processing steps: (a) Original image, (b) Gaussian filtered image, (c) contrast-enhanced image, (d) median filtered image, (e) blurry image, (f) binarized image, (g) detected bubble boundary on top of the original image, and (h) smoothed bubble boundary on top of the original image.

6.2.2. Cavitation intensity estimation

We measure the cavitation intensity in terms of cavitation collapse-induced extension rate. The extension rate measures the amount of fluid compression or elongation when it is forced to extend in the flow direction and is calculated from invariants of the rate of strain tensor (six times the ratio of the third to the second invariant) [210]. For cavitation, the extension rate, $\dot{\gamma}$, along the radial direction in the distance r from the center of the cavitation bubble is computed as

$$\dot{\gamma}(\boldsymbol{r},t)=\frac{-2}{r^3}\left[R^2\left(\dot{R}-\frac{\dot{m}}{\rho_L}\right)-\frac{R^2}{c}\left[2\dot{R}\left(\dot{R}-\frac{\dot{m}}{\rho_L}\right)+R\left(\ddot{R}-\frac{\ddot{m}}{\rho_L}\right)\right]\right]. \qquad \text{Equation 6-1}$$

In Equation 6-1, c and ρ_L are the speed of sound in the liquid and liquid density, respectively. To obtain the time-resolved bubble radius, R , and the net evaporation rate, $\dot{m}$, and $\ddot{m}$, we model the cavitation bubble dynamics. To do so, we employ a non-invasive measurement technique that takes advantage of the reliability of the experimental measurements and high temporal resolution of modeling simultaneously by assimilating experimental measurements into the existing cavitation models. In this technique, when the predicted bubble diameter by the model and experimentally measured value have a discrepancy, an error term is calculated and is fed to a proportional–integral–derivative (PID) controller. The controller generates a source term, u, in the original model equations and iterates until the error goes below a threshold value. As shown in [208], the data-assimilated modeling most accurately estimates the bubble diameter and far-field pressure. Since this technique overcomes the inherent model assumptions and makes the model's outputs more robust for the physical parameters' initial values, it would estimate the most reliable collapse characteristics.

Cavitation bubble dynamics are described by the Rayleigh–Plesset equation (RPE). A typical cavitation bubble is filled with vapor and non-condensable gas such as air, and the pressure inside a bubble is higher than the liquid pressure at the bubble wall due to surface tension. In RPE derivation, a spherical liquid volume with radius R_L surrounding a spherical bubble with radius R is considered with the center of a liquid volume at the center of a spherical bubble. The radius of the liquid volume is much smaller than the wavelength of pressure waves in the liquid. When a bubble expands or collapses, the liquid volume also correspondingly expands or contracts, respectively. When the bubble expands, it does work on the surrounding liquid, and when it

collapses, the surrounding liquid does work on the bubble. In addition, when the bubble expands, the liquid volume also expands. In other words, the liquid volume does work to the surrounding liquid. The conservation of energy is satisfied when the summation of the kinetic energy of the liquid volume and the work done by the liquid volume is equal to the work done by the bubble to the surrounding liquid.

Rayleigh–Plesset equation is derived by differentiation of conservation of energy with respect to R. In the derivation of RPE, the liquid is assumed to be incompressible. However, the equation is no longer valid when a bubble collapses with speed comparable to sound velocity in the liquid; that is the case for most cavitation bubbles. Thus, the effects of liquid compressibility should be considered for modeling the cavitation bubble dynamics. In addition, during the cavitation oscillations, the mass transfer occurs at the bubble wall. The two types of mass transfer across the bubble wall are 1) non-equilibrium evaporation and condensation of (water) vapor and 2) the diffusion of non-condensable gases. Thus, an essential modification to RPE is modeling the non-equilibrium evaporation and condensation of water vapor. Another significant effect not considered in RPE is the temperature increase at the bubble interface that is sometimes assumed to be identical to the ambient liquid temperature. However, experimental works show a substantial increase in liquid temperature at the bubble wall [126]. Therefore, another modification to RPE is modeling the interface temperature at the bubble wall. Gas diffusion across the bubble surface should also be considered for modeling cavitation bubbles as the gas concentration in the liquid adjacent to the bubble wall changes during expansion and collapse. The gas diffuses into a bubble during expansion as the pressure inside a bubble is lower than the ambient pressure. In contrast, the gas diffuses out of the bubble during the collapse as the pressure inside the bubble is higher than the surrounding liquid pressure.

Yasui model [135,140,141,211] is a high fidelity cavitation model that accounts for the abovementioned parameters. However, a discrepancy between the estimations and experimental measurements is observed due to inherent model assumptions, such as the spherical shape of the bubble, and uncertainties of initial inputs. Thus, we employ a PID controller that continuously calculates an error value, $e(t)$, which is the difference between a measured radius of the cavitation bubble and an estimated value by the model, and applies a correction (control signal, u) based on proportional, integral, and derivative terms:

$$u = K_P\big(R(t) - R_d(t)\big) + K_I \int_0^t \big(R(\tau) - R_d(t)\big)d\tau + K_D\left(\dot{R}(t) - \dot{R}_d(t)\right), \quad \text{Equation 6-2}$$

where K_P, K_I, and K_D are dimensionless proportionality, dimensionless integration, and dimensionless derivative constants, respectively. Also, R, R_d, $\dot{R}$, and $\dot{R}_d$ correspond to the estimated radius, desired radius (measured from the experiment), estimated radial velocity, and desired radial velocity, respectively.

To integrate the experimental measurements into the Yasui model [135,140,141,211], we place the control signal, u, in the equation of motion:

$$\begin{aligned}\ddot{R} = \frac{1}{\left(1 - \frac{\dot{R}}{c} + \frac{\dot{m}}{\rho_L c}\right)R + \frac{4\mu}{\rho_L c}}\Bigg[& \boldsymbol{u} \\ & + \frac{1}{\rho_L}\left(1 + \frac{\dot{R}}{c}\right)\left[P - \frac{2\sigma}{R} - \frac{4\mu}{R}\left(\dot{R} - \frac{\dot{m}}{\rho_L}\right)\right. \\ & \left. - \dot{m}^2\left(\frac{1}{\rho_L} - \frac{1}{\rho_g}\right) - P_\infty\right] + \frac{d\dot{m}}{dt}\frac{R}{\rho_L}\left(1 - \frac{\dot{R}}{c} + \frac{\dot{m}}{\rho_L c}\right) \\ & + \frac{\dot{m}}{\rho_L}\left(\dot{R} + \frac{\dot{m}}{2\rho_L} + \frac{\dot{R}\dot{m}}{2c\rho_L}\right) - \frac{3}{2}\dot{R}^2\left(1 - \frac{\dot{R}}{3c} + \frac{2\dot{m}}{3\rho_L c}\right) \\ & + \frac{R}{\rho_L c}\left[\frac{dP}{dt} + 2\sigma\frac{\dot{R}}{R^2} + 4\mu\left(\frac{\dot{R}^2}{R^2} + \frac{1}{\rho_L}\frac{R\frac{d\dot{m}}{dt} - \dot{R}\dot{m}}{R^2}\right)\right. \\ & \left. - 2\dot{m}\frac{d\dot{m}}{dt}\left(\frac{1}{\rho_L} - \frac{1}{\rho_g}\right) - \frac{\dot{m}^2}{\rho_g^2}\frac{d\rho_g}{dt}\right]\Bigg],\end{aligned} \quad \text{Equation 6-3}$$

where P, $\dot{m}$, t, c, μ, ρ_L and ρ_g are the bubble's internal pressure, the rate of mass transfer at the bubble boundaries, time, the speed of sound in liquid, liquid viscosity, liquid density, and air-water vapor mixture density, respectively.

This ODE is solved using a Runge-Kutta fourth-order scheme (ODE45 in MATLAB) [156,157]. The experimentally measured value is used at each time step to calculate the error and activate the control signal, u, in Equation 6-3. This process is iteratively performed until the error reduces below a relative tolerance of 10^{-6}. Moreover, the control signal asymptotes towards zero before advancing to the next time step. The assimilated model's thermal effects and mass transport are modeled with a procedure identical to those in the Yasui model. The details of Yasui and assimilated Yasui models can be found in [208].

6.2.3. Methodology

To estimate the severity of cavitation, we first modeled the dynamics of this phenomenon using the assimilated model introduced in [208]. We manually checked the video frame-by-frame for each captured video of the tested autoinjectors and determined if cavitation happened during the syringe acceleration. The frames with cavitation were extracted from the videos, and the equivalent diameter of the cavitation bubble was determined automatically by an in-house image processing code described above. Then, the obtained equivalent diameter of the cavitation bubble was fed to the assimilated Yasui model to characterize the cavitation dynamics.

We estimated the Yasui model's unknown physical parameters using a Bayesian approach and obtained the unknown parameters' probability distributions rather than point estimates [212]. Next, the assimilated model was solved for the radius, radial velocity, radial acceleration, mass transfer at the boundaries, and internal pressure of the cavitation bubble. Finally, the time variation of the maximum collapse-induced extension rate, at $r = R$, was computed with Equation 6-1, and the maximum extension rate was reported. In addition, we reported maximum radius of the cavitation bubble, R_{max}, and corresponding cavitation energy computed as

$$E_{Cav} = \frac{4}{3}\pi(P_{stat} - P_v)R_{max}^3, \qquad \text{Equation 6-4}$$

where P_{stat} corresponds to the static pressure.

6.3.Results and discussion

We investigated the effects of drive spring force, air gap size, fluid column height, fluid viscosity, and preexisting air bubble size on the cavitation intensity in the autoinjectors in terms of maximum induced extension rate. In addition, we quantified the maximum induced pressure amplitude, the maximum radius of the cavitation bubble, and cavitation energy to explore cavitation characteristics under various conditions.

Figure 6.3 shows the first three oscillation (growth and contraction) cycles of a cavitation bubble in the autoinjector due to the sudden acceleration of the syringe. This cavitation bubble was characterized by the described methodology in the previous section, and the intensity of cavitation was quantified in terms of induced extension rate.

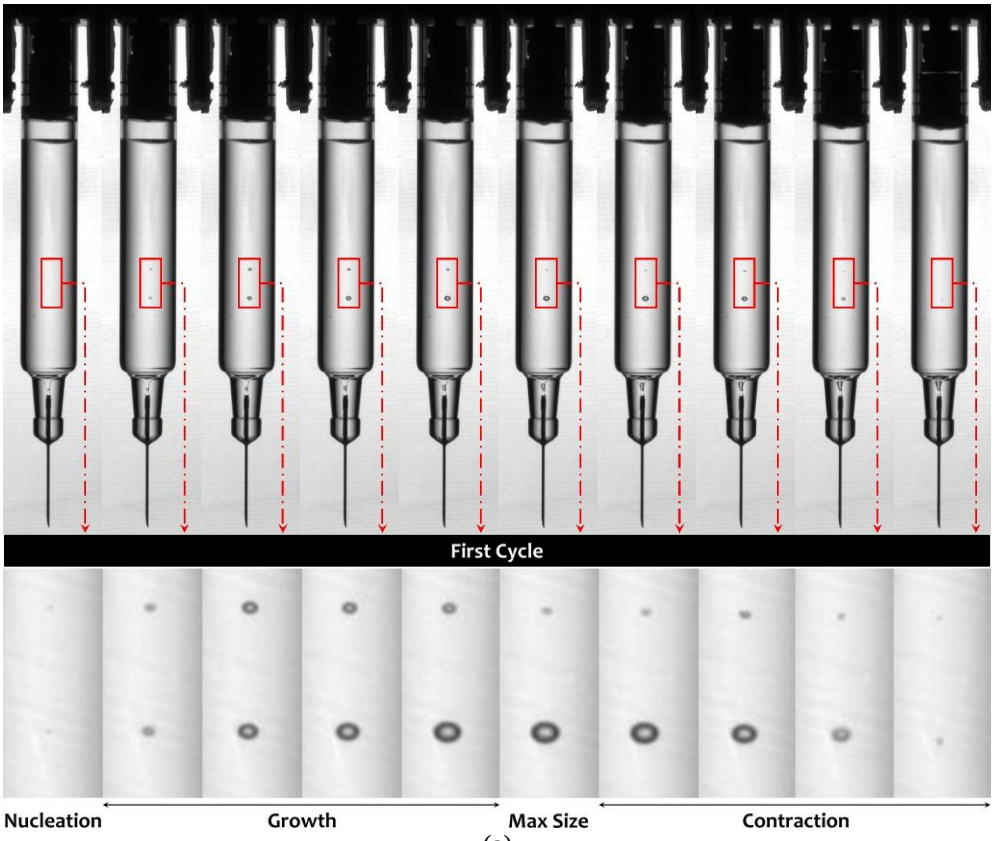

(a)

Figure 6.3. Representative images of cavitation that occurs due to the sudden acceleration of the syringe: (a) first cycle, (b) second cycle, and (c) third cycle of cavitation growth and collapse ($\Delta t = 20\ \mu s$, Bottom row: zoom-in view). The marked domain shows the nucleation and growth site of the cavitation bubble

Figure 6.3 continued

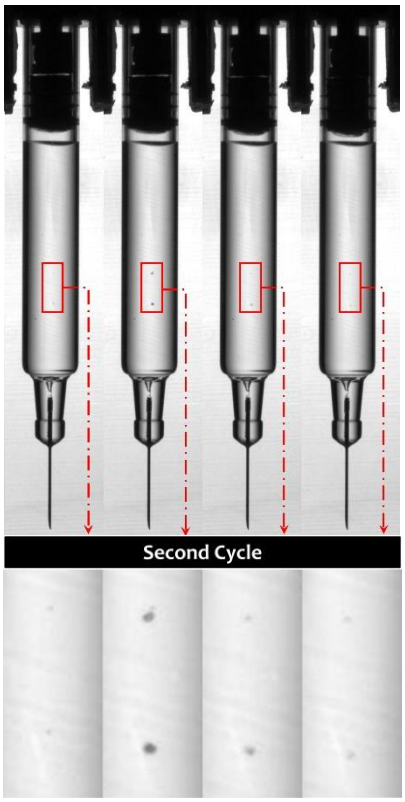

(b)

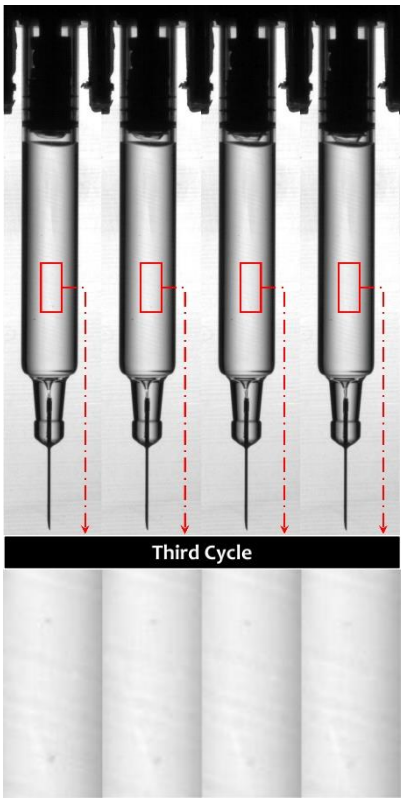

(c)

.

Figure 6.4 shows the variation of cavitation bubble radius, cavitation wall velocity, and cavitation-induced extension rate predicted by the assimilated model for the cavitation shown in Figure 6.3.

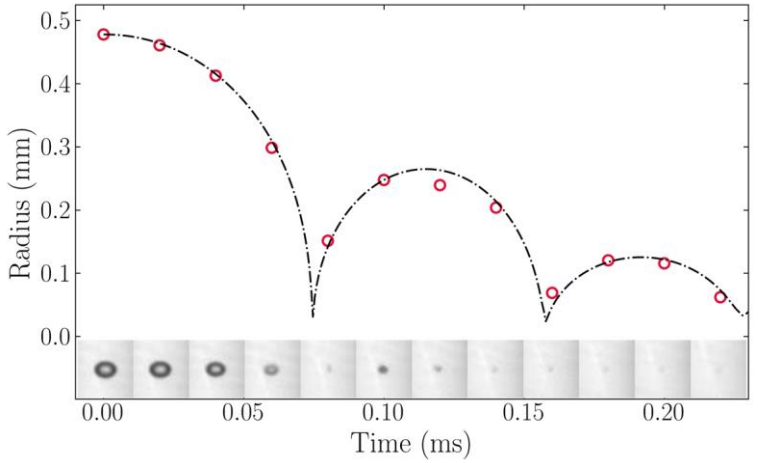

(a)

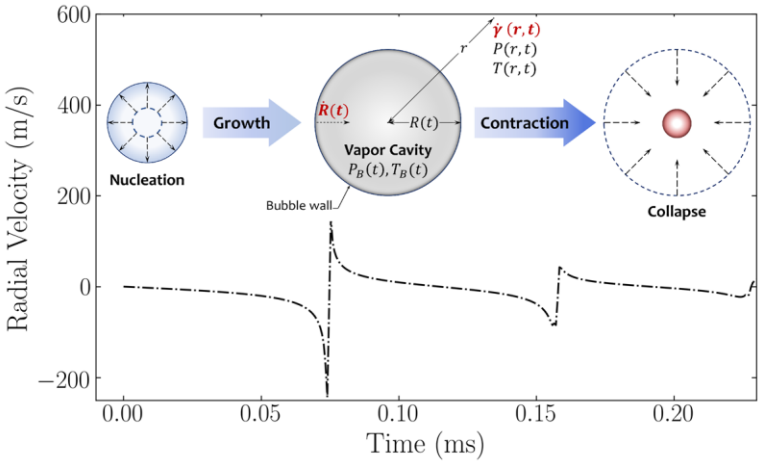

(b)

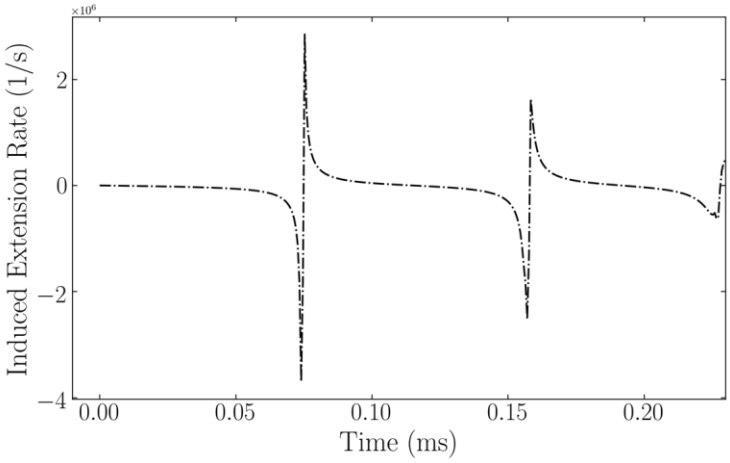

(c)

Figure 6.4. (a) Radius of the cavitation bubble measured from the experiment (red circle markers) vs. the predicted radius with the assimilated model. (b) Cavitation wall radial velocity, $\dot{R}(t)$, and (c) Cavitation-induced extension rate, ($\dot{\gamma}(\boldsymbol{r},t)$), predicted by the assimilated model (Equation 6-1).

6.3.1. Effects of spring force

Figure 6.5 shows the cavitation characteristics as a drive spring force and viscosity function for 1 mL and 2 mL syringe fills individually. The results indicate the significant roles of drive spring force and viscosity on the cavitation intensity in autoinjectors. Increasing the drive spring force results in more severe cavitations in autoinjectors. However, higher fluid viscosities attenuate the cavitation intensity. The same trend is observed for the maximum pressure, radius, and cavitation energy.

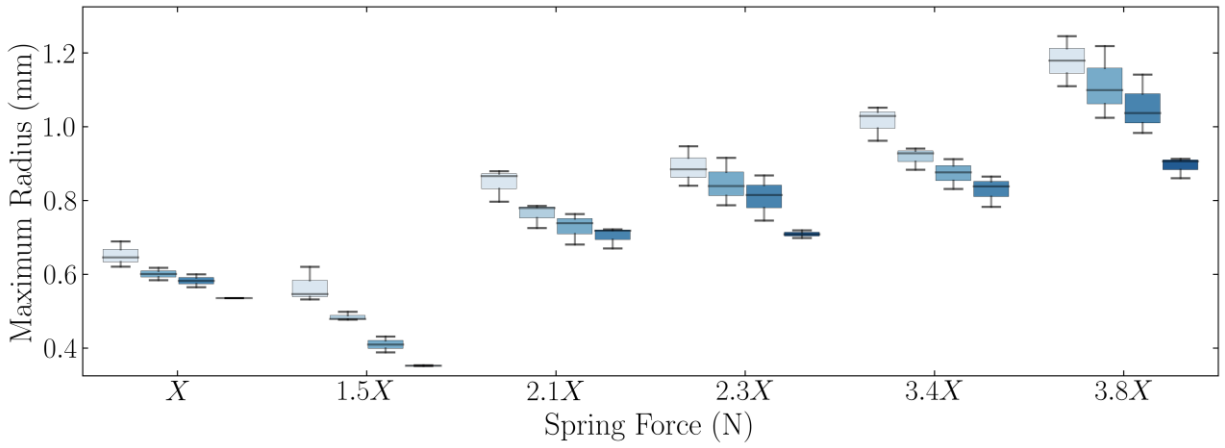

(a)

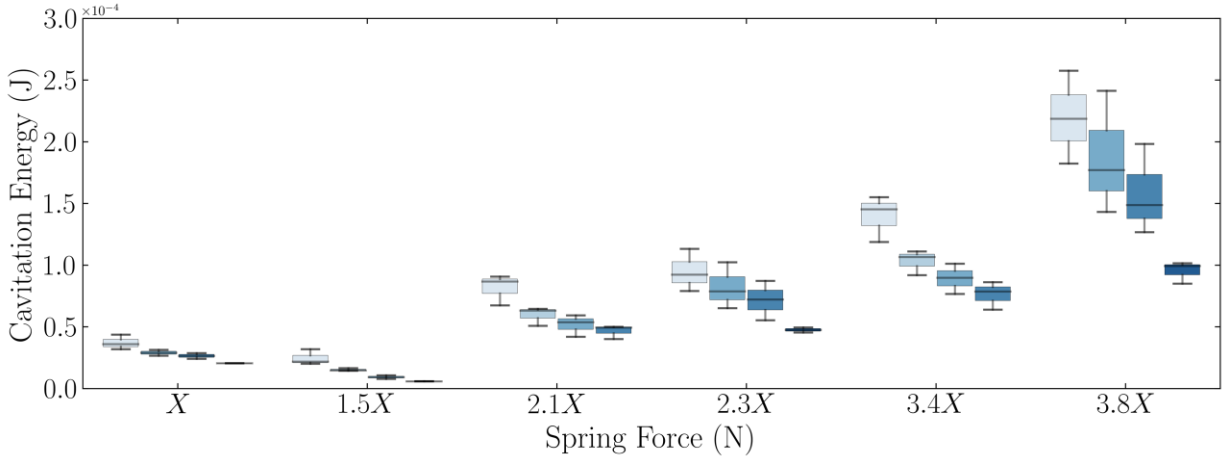

(b)

Figure 6.5. Drive spring force effects on the (a) maximum radius of the cavitation bubble, (b) cavitation energy, (c) cavitation collapse-induced pressure, and (d) cavitation collapse-induced extension rate.

Figure 6.5 continued

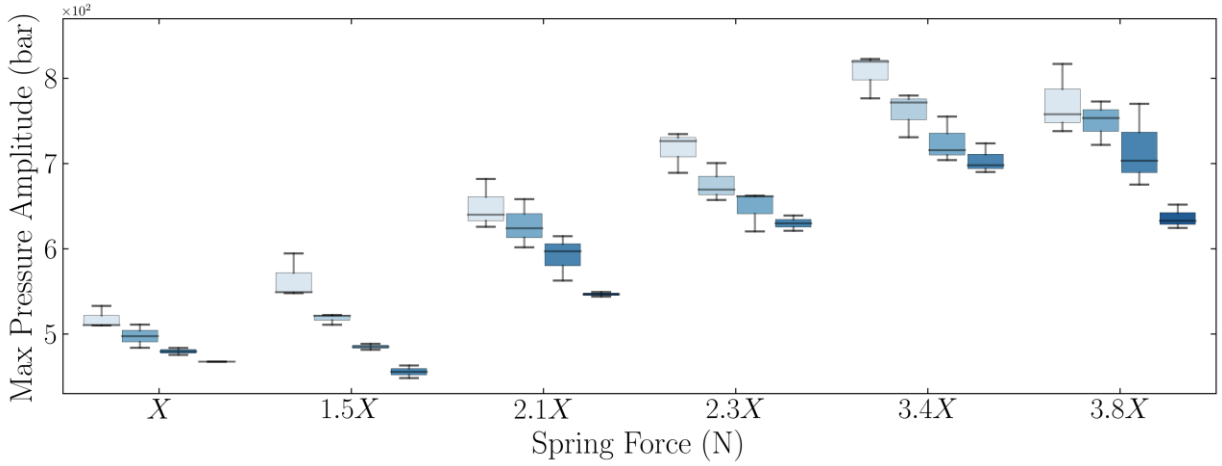

(c)

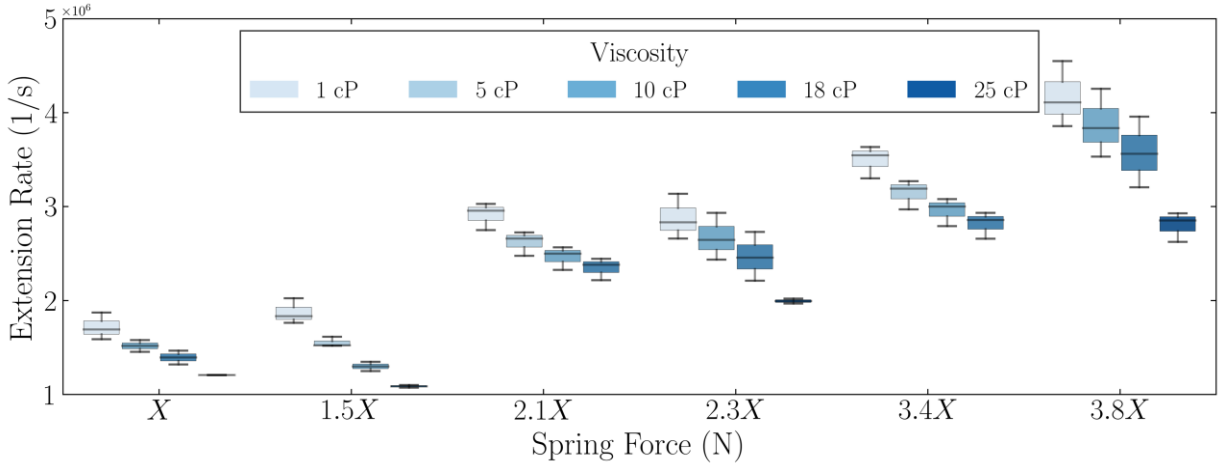

(d)

Higher drive spring force corresponds to the higher acceleration of the syringe during the insertion stage. Thus, to clarify the effects of drive spring force on the cavitation intensity, we explored the characteristics of the cavitation as a function of the syringe's maximum acceleration. To do so, the syringe displacement was first obtained using a cross-correlation-based image registration technique [213]. Then a second-order central difference method was used to compute the syringe acceleration (see [198] for more detail). Figure 6.6 shows the cavitation intensity as a function of syringe acceleration and fluid viscosity. In this figure, we consolidated the cavitations that occurred in both 1 mL and 2 mL syringe fills. The results indicate that the most severe cavitation occurs in an autoinjector with the highest drive spring force filled with the least viscous fluid. It also shows a linear relationship between maximum syringe acceleration and maximum

cavitation-induced extension rate. Although this linear relationship is not observed for the cavitation size and energy, these parameters increase with the syringe's maximum acceleration.

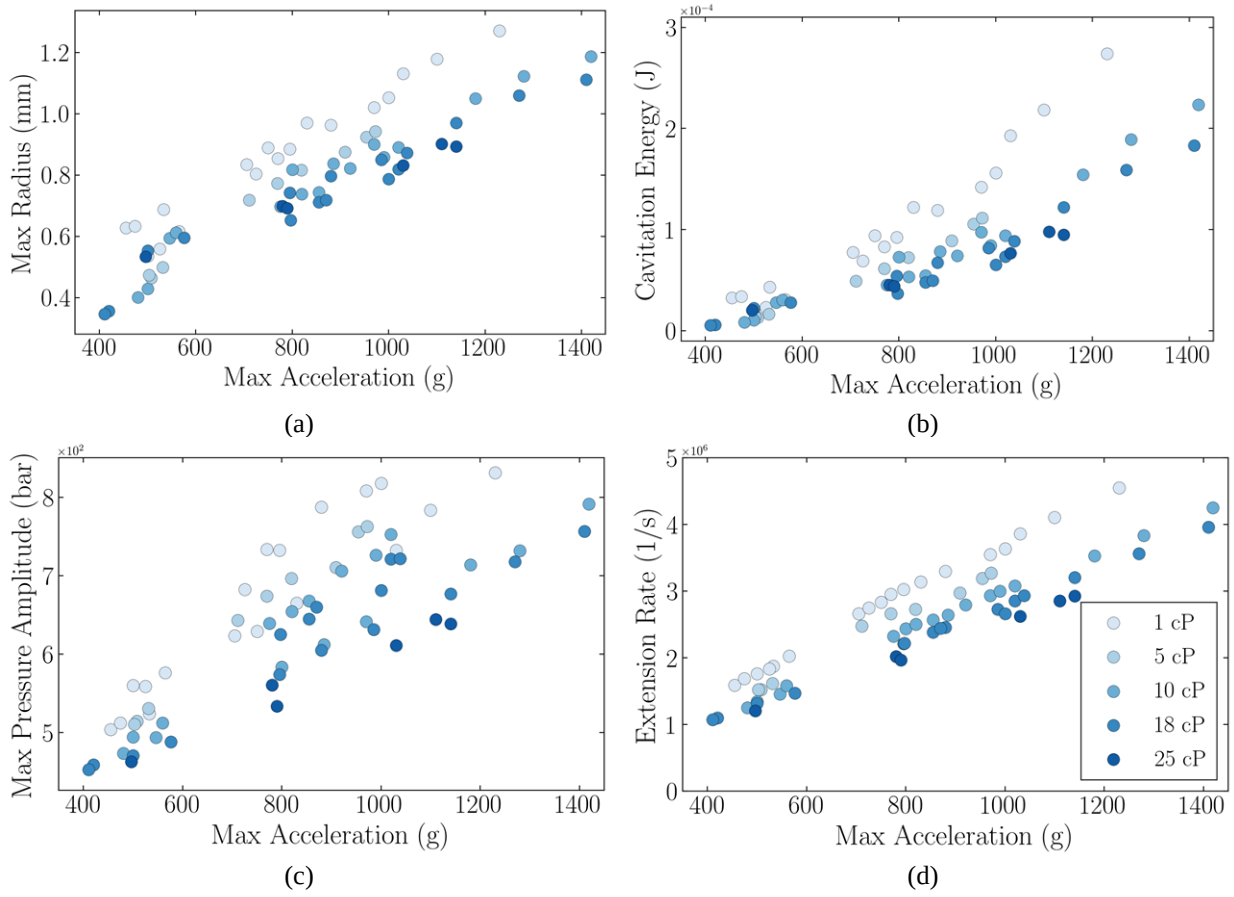

Figure 6.6. Cavitation characteristics as a function of maximum acceleration of the syringes: (a) Maximum radius of the cavitation bubble, (b) Cavitation energy, (c) Maximum cavitation collapse-induced pressure, and (d) Maximum induced extension rate. Data points from 1 mL and 2 mL syringe fills were consolidated in this figure.

To explain this, we consider a vertical, cylindrical column of liquid undergoing a sudden acceleration in the vertical direction, as shown in Figure 6.1(b). Based on the assumption that the liquid is inviscid and incompressible and has a velocity magnitude significantly smaller than the acceleration ($\partial v/\partial t$), as is commonly known [214–217], only the pressure gradient and acceleration remain [214], and the Navier–Stokes equations are reduced to

$$\frac{\partial v}{\partial t} = -\frac{1}{\rho}\nabla p. \qquad \text{Equation 6-5}$$

Integrating Equation 6-5 along the centerline of the liquid from the free surface to the bottom of the column (assuming the depth of the liquid is h), denoting the magnitude of the vertical component of $\partial v/\partial t$ as a, and solving for the pressure difference in the liquid column yields

$$p_r - p_b = \rho a h, \qquad \text{Equation 6-6}$$

where p_r is the reference pressure at the free surface and p_b is the pressure at the bottom of the column. Cavitation is likely to occur when $p_b < p_v$ [218]. Thus, increasing the acceleration increases the probability of observing cavitation and intensity of cavitation bubbles in AI devices.

6.3.2. Effects of air gap size

Another important design parameter of an autoinjector is the air gap size or the distance between the initial plunger position and the fluid interface. Here, we investigated the effect of this parameter on the severity of cavitation in the autoinjectors by changing the air gap height between 1 mm to 4 mm for two syringes with 1 mL and 2 mL fills. Besides, the fluid's viscosity was varied to study the effect of this parameter on the cavitation intensity. Figure 6.7 illustrates the cavitation characteristics as a function of air gap height and fluid viscosity. It indicates that the least severe cavitations are observed in the autoinjector with the largest air gap filled with the more viscous fluid.

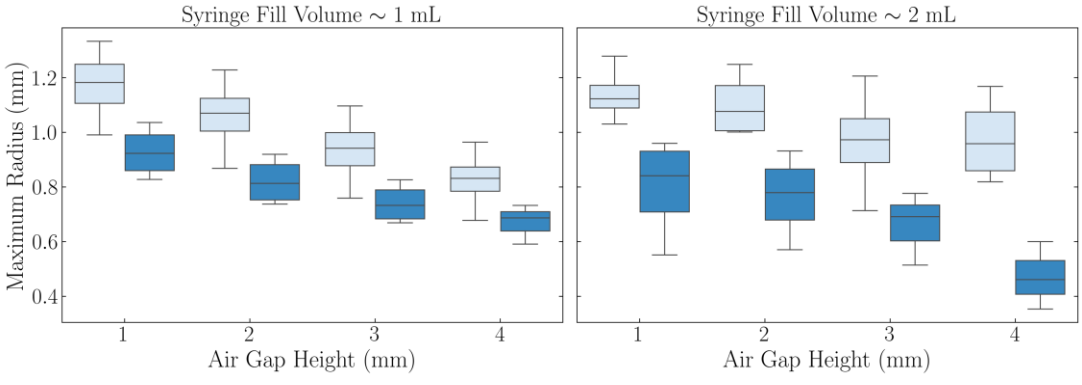

Figure 6.7. Air gap size effects on the (a, b) maximum radius of the cavitation bubble, (c, d) cavitation energy, (e, f) cavitation collapse-induced pressure, and (g, h) cavitation collapse-induced extension rate. Panels a, c, e, and g correspond to the syringe with 1 mL fill, and panels b, d, f, and h represent the data for the syringe with 2 mL fill.

Figure 6.7 continued

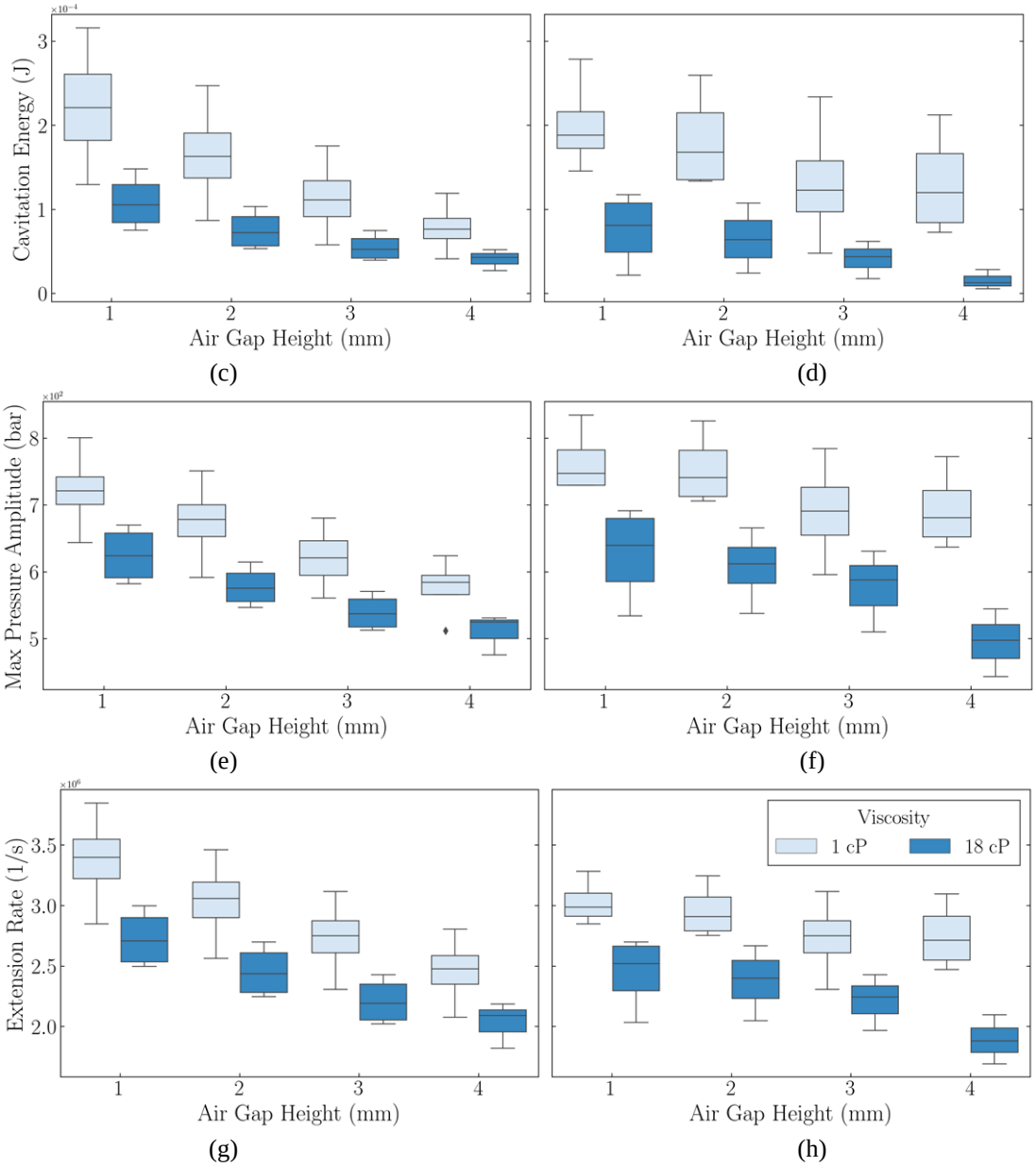

As it is shown in Figure 6.7, increasing the air gap size results in less severe cavitation. One explanation for this observation could be the higher dampening effects of larger air gaps on propagated pressure waves inside the syringe. The cavitation occurs when the inertial force, which is a function of liquid column acceleration, exceeds the maximum force that the pressure difference can provide, which is proportional to the $P_r - P_v$ [218], where P_r and P_v are the reference pressure (air gap pressure) and liquid vapor pressure, respectively. Thus, the most severe cavitation is observed when the $P_r - P_v$, becomes insignificant, or according to Equation 6-6, $P_b = P_r - \rho a h$,

air gap pressure, P_r, becomes smaller. Once the plunger rod hits the plunger, the air gap is pressurized due to the air compressibility. This pressurization would be more significant for the larger air gaps. Thus, cavitation effects are more prominent if the initial air gap size decreases or the air gap is less compressed during the rod impact. The other explanation could be the reduction in impact velocity due to the reduced plunger rod to plunger separation, thus generating a weaker acoustic wave inside the syringe.

Although increasing the air gap size reduces the cavitation-induced extension rate, it also increases the interactions of air-fluid interfaces during handling, shipping, and administration of the drug, resulting in potential drug inefficiency due to aggregation [199,219–224]. Therefore, careful consideration should be given to the air gap size determination in developing autoinjectors and plunger motion during the transportation of AIs.

6.3.3. Effects of drug column height

Another significant parameter in cavitation onset in an accelerating syringe is the height of the fluid column inside the syringe. To investigate the effect of this parameter on cavitation intensity, we filled the 1 mL syringe with two fill volume targets: 0.2 mL and 0.4 mL. Since the syringe diameter was constant, the fluid column in the 0.4 mL filling target was two times higher than the 0.2 mL filling target. We also varied the drive spring force of the autoinjector and kept the fluid viscosity at 1 cP. We compare the probability of observing cavitation in various filling targets and the corresponding cavitation-induced extension rate in Figure 6.8.

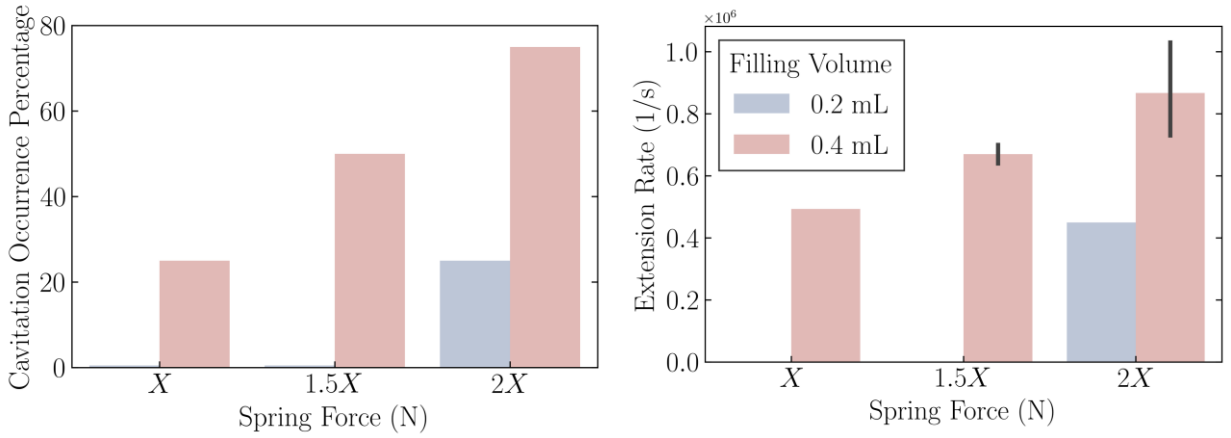

Figure 6.8. (a) Percentage of cavitation occurrence in syringes with different fill volumes at different drive spring forces. (b) Cavitation intensity in syringes with different fill volumes.

As shown in Figure 6.8(a), cavitation was observed only in one autoinjector with the 0.2 mL filling volume actuated with a $2X\ N$ drive spring force. The cavitation intensity in terms of the induced extension rate was also smaller than that of the 0.4 mL filling volume. Figure 6.8(b) also indicates that cavitation in smaller filling volumes only occurs when higher sudden acceleration is applied. Recent computational results suggest that the pressure drop at the syringe bottom is $\rho c \Delta V$, where ΔV was the velocity change of the syringe bottom in a half period $2L/c$ [225]. When the liquid column height increases, more time is required for pressure waves to travel inside the liquid column before returning to the bottom wall and being reflected. During this time, the syringe bottom obtains a larger ΔV and thus experiences a larger pressure drop that increases the risk of cavitation occurrence. Besides, Equation 6-6 also implies that increasing the fluid column height in the autoinjectors increases the probability of observing cavitation due to sudden acceleration in these devices.

6.3.4. Spatial intensity of cavitation in syringe

Based on our observations, cavitation was more likely to occur at the bottom of the syringes. This is in accordance with the theory that demonstrates the lowest pressure at the bottom of an accelerating liquid column (Equation 6-6) that increases the risk of cavitation occurrence. Besides, the most severe cavitations also occurred at the bottom and corners of the tested syringes where the lowest pressures occurred. To investigate this observation further, we provide a heat map

showing the most probable spots for cavitation with the corresponding intensity. To create the cavitation intensity heat map in the syringes, we used the existing data from the drive spring force effects (Case A in Table 6.1) and air gap size effects (Case B in Table 6.1) studies and consolidated the data points from these two studies. So, for each one of the 1 mL and 2 mL syringe fills, we first superimposed the induced extension rate field, $\dot{\Gamma}(\boldsymbol{r})$, of all observed cavitations in a single plot created based on the dimensions of each syringe with a spatial resolution of $\Delta\boldsymbol{x} = 15.6\ \mu m$. Then, the highest cavitation-induced extension rate at each spatial location was picked as the corresponding cavitation intensity at that spot. Figure 6.9 shows the cavitation intensity heat maps for 1 mL and 2 mL syringe fills. These intensity maps indicate that the cavitation intensity at the bottom of the syringes is higher than that of the bulk fluid. Also, cavitation mainly occurs near the syringe wall due to the abundance of nuclei, and the corresponding intensity decreases as it gets closer to the air-fluid interface.

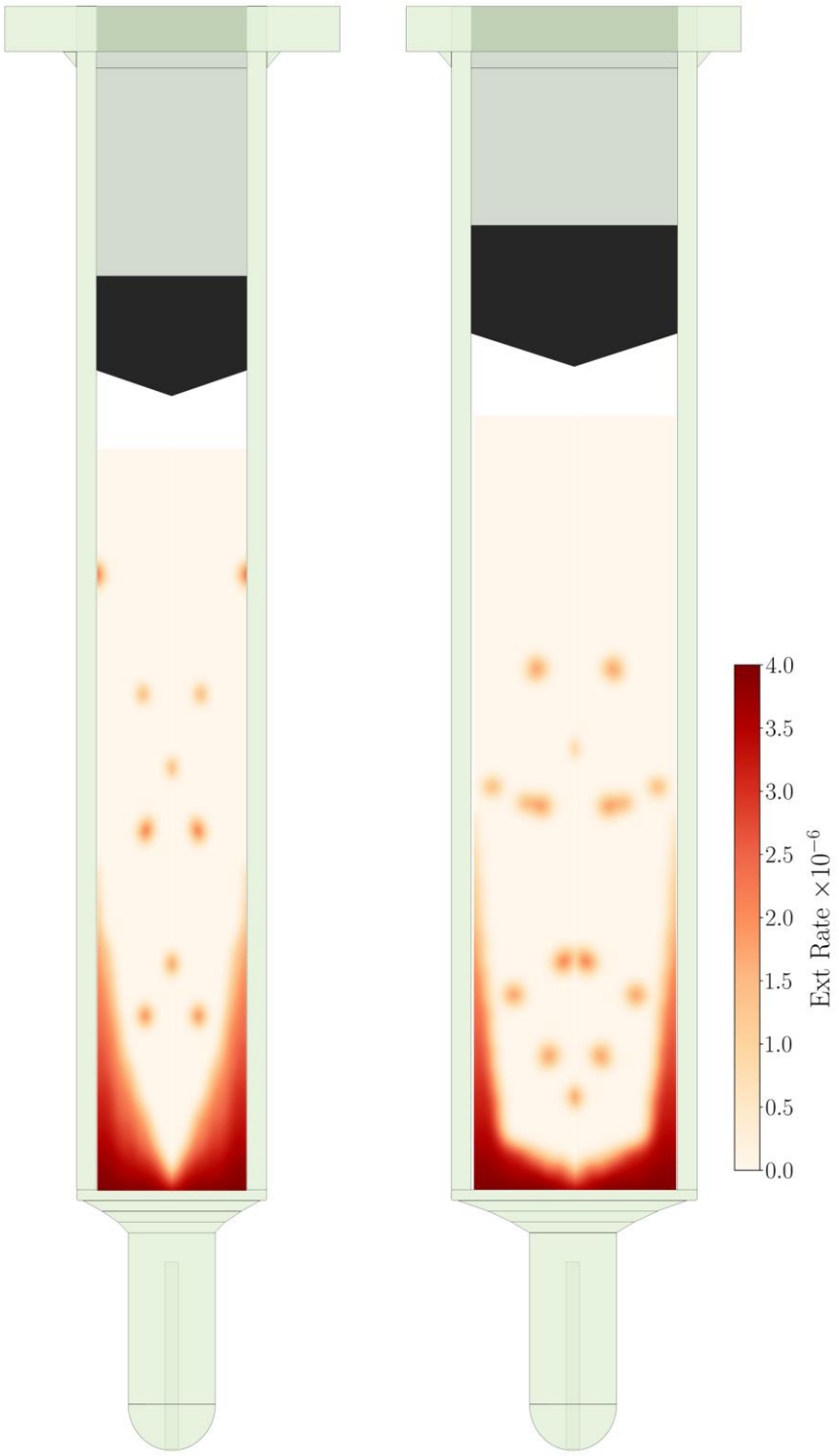

(a) (b)

Figure 6.9. Cavitation intensity map in the syringe: (a) 1 mL syringe fill, (b) 2 mL syringe fill. The observed cavitations in tested autoinjectors of Case A and Case B were used to generate these maps.

Note that the cavitations that occur in the bulk of the fluid are primarily the result of the preexisting air bubbles' collapse.

6.3.5. Effects of preexisting air bubbles

Our observations show that the existence of an air bubble inside the syringes increases the risk of occurrence of cavitation upon actuating the autoinjectors. These micron-sized air bubbles can be formed during transportation due to the mixing of the air gap with the drug and/or during the filling process. Either way, they act as a nucleation site for the cavitation and increase the probability of observing the cavitation bubble. Thus, another parameter that we study is the size of these preexisting air bubbles inside the syringe. For this investigation, we used the existing data from the drive spring force effects (Case A), air gap size effects (Case B), and fluid column height (Case C) effects studies. To do so, before actuating the autoinjector, we manually inspected all the syringes for the preexisting air bubbles, and those cases with an air bubble were selected for this investigation. Due to the limited spatial resolution of the images, we could only detect the preexisting air bubbles larger than $10\ \mu m$. Figure 6.10 illustrates the correlation between the size of preexisting air bubbles and their induced extension rate upon collapse.

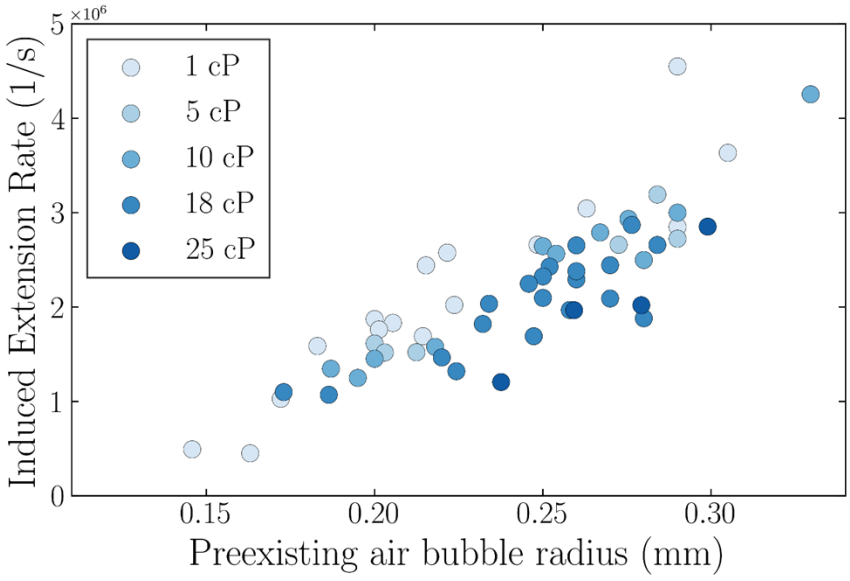

Figure 6.10. Cavitation intensity as a function of preexisting air bubble size.

The results indicate that as the preexisting air bubbles become larger, they generate a larger extension rate upon collapse. Recently, Zhang et al. [202] also showed that increasing the nucleus size results in a larger cavitation bubble and higher collapse-induced pressure wave in the liquid column. Therefore, the risk of occurrence of cavitation and the adverse effects of this phenomenon in autoinjectors can be suppressed by (i) controlling the formation of air bubbles during transportation and filling processes, and (ii) giving proper instructions to patients for handling the AIs.

6.3.6. Potential effects of cavitation on the drug

The literature is unclear about the characteristics of irreversible mechanical stretching of proteins due to shear stress and the resulting aggregation behavior. Moreover, neither the influence of high shear rates nor the impact of cavitation on protein aggregation is fully understood. It has been hypothesized that in the presence of shear stress the effect of cavitation may be overlooked and the possible impact is misattributed to shear stress [224,226]. Duerkop et al. [227] observed human serum albumin (HSA) aggregation when cavitation occurred. They found that shear stress (maximum and average shear rates of up to $10^8\ s^{-1}$ and $1.6 \times 10^6\ s^{-1}$) by itself did not alter protein structural properties and the increase in vapor-solution interface due to bubble growth generated by cavitation caused protein aggregation in HSA. Thus, they concluded the impact of cavitation on protein aggregation to be similar to air-solution-mediated protein aggregation and that cavitation-associated protein aggregation is driven by vapor-solution interfaces.

The maximum estimated extension rate of the observed cavitation bubbles in this study is in the order of $10^7\ 1/s$, which is beyond the protein inactivation limit ($\sim 10^4 - 10^5\ 1/s$) reported in the literature [228–231]. Nevertheless, note that the therapeutic protein type and the time it is exposed to the shear stress are also the determinant factors in protein aggregation. In particular, no protein aggregation was observed for short exposure durations (<1 sec) in the abovementioned studies, while for the cavitation, the high values of shear rates occur during the cavitation collapse, which only lasts $\sim 10\ \mu s$. Thus, the duration of the large shear seems to be potentially too short to damage the proteins. Also, the average cavitation-induced shear rate is far from those reported in literature [228–231]. Thus, it is inconclusive if the cavitation-induced stress field causes the therapeutic protein aggregation in AI. Therefore, the authors suggest conducting controlled experiments to resemble the cavitation-induced shear in the protein solution to investigate if the

cavitation in AI harms the therapeutic proteins. It is noteworthy that the syringes in this study were filled with water-based solutions at different viscosities, as mentioned in Table 6.1, and the solution did not contain any proteins.

6.4.Summary

This paper presented the first detailed analysis of cavitation occurrence in AIs due to the sudden syringe acceleration. Effects of syringe and autoinjectors design parameters such as drive spring force, air gap size, fluid column height, and fluid viscosity on the cavitation intensity were investigated. In addition, the effects of preexisting air bubbles in the syringes on the severity of cavitation were analyzed and a cavitation intensity map was presented to show the most probable locations for severe cavitation in an autoinjector. The results indicated that larger drive spring force generated stronger cavitation, and the most severe cavitation occurred in a syringe with a smaller air gap size. Moreover, the severity of cavitation in the smaller fill volume compared to the larger column height was one order of magnitude smaller, and the probability of cavitation occurrence in smaller fluid column height was significantly smaller with each configuration of the autoinjector, and less severe cavitation occurred in a more viscous fluid.

6.5.Authors contributions

Javad Eshraghi: Methodology, Software, Formal analysis, Data curation, Investigation, Visualization, Writing - original draft. Jean-Christophe Veilleux: Methodology, Writing - review & editing. Galen Shi: Methodology, Writing - review & editing. David Collins: Methodology, Writing - review & editing. Arezoo M. Ardekani: Conceptualization, Methodology, Interpretation of the results, Writing - review & editing, Funding acquisition. Pavlos P. Vlachos: Conceptualization, Methodology, Investigation, Supervision, Project administration, Funding acquisition, Writing - original draft, review & editing.

7. THE AIR ENTRAINMENT AND HYDRODYNAMIC SHEAR OF THE LIQUID SLOSH IN SYRINGES

7.1.Background

Autoinjectors (AIs) are pen-like devices designed to deliver a bolus dose of a drug to patients via subcutaneous (SQ) injection. AIs are used for both emergency purposes (e.g., epinephrine) and long-term treatments requiring a frequent injection of biopharmaceuticals (e.g., etanercept, adalimumab, and darbepoetin alfa) [232]. The volume of subcutaneous injection with an autoinjector is limited to approximately $0.5-2.0\ mL$ [233–235] because subcutaneous tissues can only absorb a finite quantity of liquid at the high injection speed of AIs.

Although the specific designs of autoinjector devices differ, most devices currently available on the market are spring actuated [235–237]. Activation of such devices results in mechanical impacts between the moving components of the AI mechanism and large accelerations/decelerations of the moving parts. When very viscous drug solutions are injected, stiff springs must power the autoinjector [238] causing impact velocities and accelerations/decelerations large enough to cause device failure [239,240].

Drug administration using most of the single-spring-driven autoinjectors is completed in two main processes: (1) insertion of the needle into the patient and (2) delivery of the drug product to the patient. In this study, only the sequence of events depicted in Figure 7.1 corresponding to the insertion process is considered.

Figure 7.1 is a simplified schematic of a single-spring-driven autoinjector's internal components and actuation sequence. The compressed drive spring is released upon device actuation, propelling the plunger rod to hit the plunger. The syringe and the plunger are accelerated forward by the plunger rod, thus inserting the needle into the patient. Once the needle reaches the target depth for injection (SQ tissue), the syringe is decelerated to a complete stop (insertion process). The force exerted by the spring-actuated plunger rod on the plunger-stopper pressurizes the syringe, and the medicament is extruded through the needle into the SQ tissue (delivery process). More details on these processes can be found in [241].

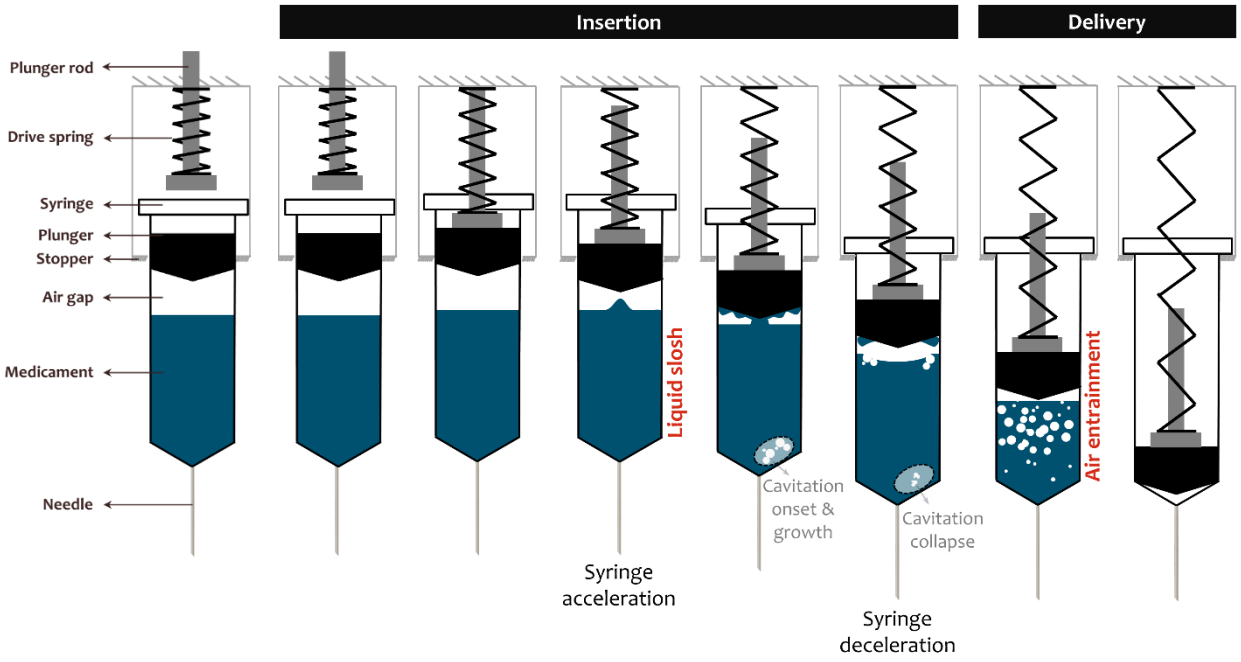

Figure 7.1. (a) Schematic of a single-spring-driven autoinjector's internal components and (b) actuation sequence.

The acceleration of the syringe during the insertion process can be substantial, as high as 10^3 to 10^4 m/s^2. Although the syringe is impulsively accelerated as soon as the insertion mechanism is released, the liquid inside the syringe is not. The liquid‘s acceleration lags behind the acceleration of the syringe, and cavitation may occur at the bottom of the syringe [242–244]. In addition, syringe acceleration at the beginning of the insertion process and its deceleration upon reaching the proper penetration depth for the needle can induce intense motion of the air-liquid interface and may impose mechanical and hydrodynamic stresses on drug molecules [245–248]. Thus, it is essential to understand the role of the liquid sloshing upon AI actuation on the mechanical and hydrodynamic stresses acting on the drug molecules and the air entrainment. Although the potential issues associated with the liquid sloshing in AIs have been acknowledged in the literature, no experimental study has been performed to investigate the induced air entrainment and hydrodynamic stress upon actuation. Additionally, there is a lack of detailed understanding of how design parameters affect liquid sloshing in AI devices.

Experimentally measuring the air-liquid interface area and hydrodynamic stress for the liquid slosh inside an AI presents many challenges [249]. We developed and employed novel non-invasive techniques using shadowgraphs and PIV measurements to simultaneously quantify the

air-liquid interface area and hydrodynamic stress during AI actuation. The interface area and hydrodynamic shear are quantified experimentally, and their dependences on the syringe kinematics, solution type (water and silicon oil at $1\ cP$), and air gap size in the syringe are revealed. This research aims to understand the impact of liquid sloshing to improve the current designs and make AIs more robust and reliable.

The effects of hydrodynamic shear on protein molecules depend on the concentration and structure of the proteins and the type and duration of the shear and strain applied. Recent works demonstrated that the air-liquid interface is detrimental to protein denaturation, while the hydrodynamic shear alone is rarely the leading cause of damage for therapeutic proteins [250–252]. On the other hand, some argue that the protein aggregation and unfolding may occur at relatively low shear rates ($10^2 \sim 10^5\ s^{-1}$) [253].

This paper will first describe the experimental methods used to quantify air entrainment and hydrodynamic stress, followed by results and discussion. Lastly, the findings will be summarized.

7.2.Experiment and methodology

7.2.1. Experimental procedure

An operational replication of an autoinjector was designed and 3D-printed to house the drive spring, plunger rod, and pre-filled syringes [241]. The system was mounted vertically on an optical post and submerged in a small water tank to account for optical distortions. A schematic of the experimental setup as well as the camera and light sources configuration are illustrated in Figure 7.2(a).

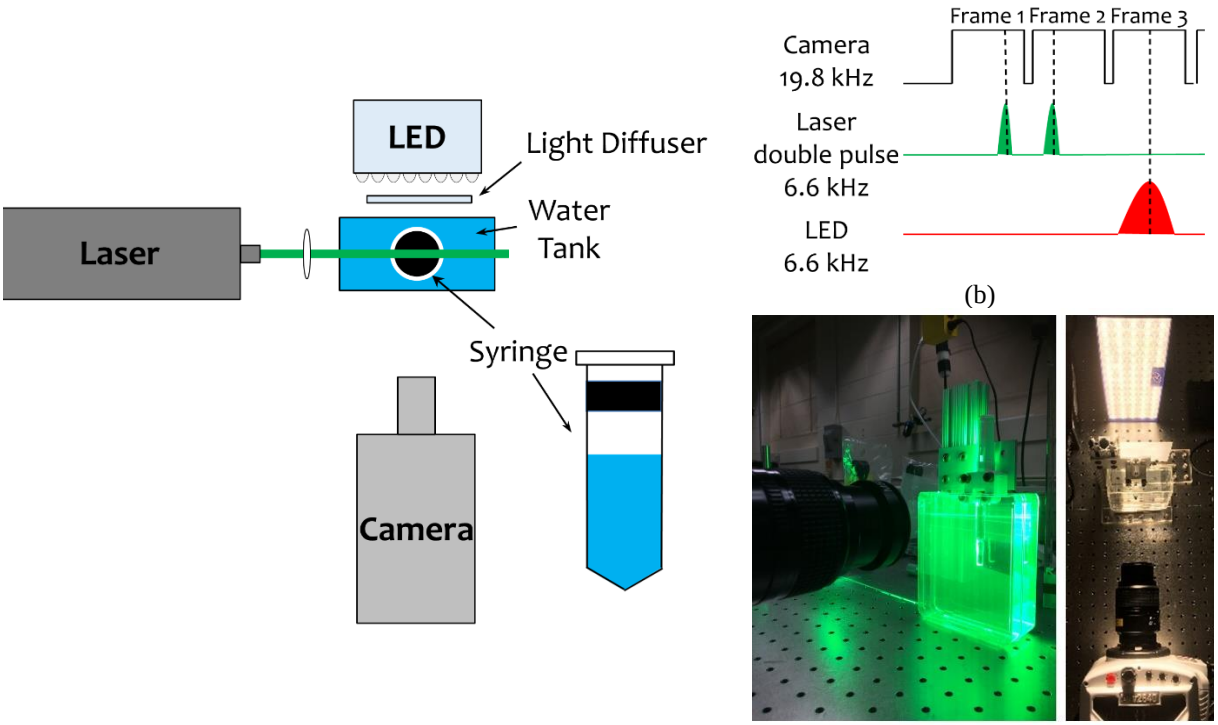

Figure 7.2. (a) Schematic of the experimental setup (top view). (b) The operating frequency of Laser, camera, and LED and pulses synchronization. (c) Snapshots from PIV and shadowgraph experiments.

The syringes used in the experiments were 2.25 mL pre-fillable glass syringes (BD Neopak) with an inner diameter of 8.5 mm (~2.0 mL syringe fill). The syringes were filled with two fluids: water and silicon oil at 1 cP and actuated with two different drive springs of 1.0X N (acceleration: 150g, deceleration: 400g) and 1.5X N (acceleration: 200g, deceleration: 700g) drive spring force. For 1.0X N drive spring, we varied the air gap height from 2 mm to 6 mm with an increment of 2 mm, and for 1.5X N drive spring force, we only tested one air gap. For DPIV measurements, we added 10 μm diameter fluorescent particles (PS-FluoRed-10.0, Ex/Em 530 nm/607 nm, mean diameter: 9.89 μm, standard deviation: 0.1 μm, density: 1.05 g/cm^3, microParticles GmbH) to the fluid in the syringe as flow tracers. The detail of the test matrix is shown in Table 7.1. For repeatability purposes, we repeated the tests five times per condition.

Table 7.1. Experimental test matrix (number of the tested syringes at each configuration: 5).

Solution			**Glass tube**		**Actuation**	**Air gap height, h_a (mm)**		
Name	Viscosity (cP)	Surface tension (mN/m)	Surface coating	Contact angle[1], θ_c	Drive spring force (N)			
Water	1	72.0	Silicone	$90° \pm 1°$	$1.0X$	2	4	6
					$1.5X$	4		
Silicone Oil	1	17.4	Silicone	$30° \pm 2°$	$1.0X$	2	4	6
					$1.5X$	2		

[1] *Average of 10 measurements.*

The contact angle between the air-liquid interface and the syringe wall was measured by extracting the interface profile from the captured images when the free-surface interface was at rest and found to be $\theta_c = 90° \pm 1°$ and $\theta_c = 30° \pm 2°$ for water and silicone oil, respectively.

We conducted simultaneous time-resolved Digitial Particle Image Velocimetry (TR-DPIV) and shadowgraph visualization. DPIV is an optical quantitative flow visualization method used to obtain instantaneous velocity measurements. The fluid is seeded with micron-sized tracer particles assumed to accurately follow the flow, and the fluid is illuminated so that particles are visible. The motion of the seeding particles is used to calculate the velocity field of the flow being studied [254,255]. DPIV measurements give the quantitative description of the velocity field, and from this field, the strain and shear rates were computed. Shadowgraph visualization was also used to identify the air bubbles formed upon the entrainment of the air and quantify the interfacial area by the formed bubbles.

For the time-resolved DPIV measurements, a Continuum Terra PIV DM 527-100M Nd:YLF laser operating at 6.6 kHz at double-pulsed mode was employed. The laser beam was passed through light-forming optics to form a vertical sheet with a nominal thickness of $4\ mm$ centered in the midplane of the syringe. One high-speed 4-megapixel CMOS camera (The Phantom v2640) was synchronized with the laser and oriented normal to the laser sheet plane. The camera was situated $13\ cm$ from the light sheet and mounted a 105 mm Nikon lens (f#11), yielding a field of view of $10.5\ mm$ along the horizontal direction *x* and $35.0\ mm$ along the vertical direction *y* with a magnification of $17\ \mu m/pixel$. For DPIV measurements with fluorescent particles, an OD4 long-pass filter (Edmund Optics) with a cut-on wavelength of 575 nm was also attached to the lens, blocking out all the incident laser light and only allowing particle-emitted fluorescent light to be captured by the camera.

For shadowgraph imaging, an LED array (LaVision LED Flashlight 300) operating at 6.6 kHz illuminated the field of view, and a light diffuser (DG100X100-1500, ThorLabs, Inc.) between the LED and the experimental setup was used to achieve uniform background illumination. The LED was synchronized with the camera and the double-pulsed laser to capture the shadowgraph images with the same camera used for DPIV. The camera was operated at 19.8 kHz and in every three frames, the first two frames captured the particle images for DPIV where the third captured the shadowgraph. Thus, in every three frames, the LED was switched off while capturing the first two frames and then switched on for the last frame while the laser was switched off. The operating frequency of the laser, camera, and LED and pulses synchronization details are depicted in Figure 7.2(b).

In addition, the shadowgraph images were employed to obtain the syringe displacement using the cross-correlation method described in [256]. Later, the velocity and acceleration were calculated from the first and second-time derivatives of the spline fit of the displacement.

For each condition in the test matrix, 5 sets of 3300 images (2200 particle images and 1100 shadowgraphs) were collected. Two sample videos of the raw data can be found in the supplementary materials for demonstration purposes.

7.2.2. Data analysis

The objectives of the post-processing were to 1) quantify the air entrainment from the shadowgraph images and 2) compute the shear and strain fields from the DPIV images.

7.2.2.1.Air entrainment quantification

The shadowgraphs are used for 1) quantifying the instantaneous size distribution of the entrained air bubbles and 2) creating a dynamic mask for processing the particle images with the PIV processing toolbox. For processing the DPIV images, we are interested only in the liquid phase regions with the seeded particles, so we need to mask out the autoinjector components, syringe wall, and the air gap. Since these unwanted objects are not stationary, we need to mask the particle images dynamically. Thus, shadowgraphs are employed to detect those components and mask them out from the particle images. In every three frames of each high-speed video recording,

we have one shadowgraph and two particle images, and this shadowgraph is used for mask creation for the two particle images.

Each shadowgraph image was analyzed using MATLAB's in-house image processing code. The code automatically detected the AI components, syringe wall, and air gap boundaries along with the entrained air bubbles. It also calculated the equivalent diameter of the entrained bubbles to find the instantaneous size distribution of the air entrainment and interfacial area of the gas phase.

Each shadowgraph image was analyzed using MATLAB's in-house image processing code. The code automatically detected the AI components, syringe wall, air gap boundaries, and entrained air bubbles. It also calculated the equivalent diameter of the entrained bubbles to find the instantaneous size distribution of the air entrainment and interfacial area of the gas phase.

The image processing was completed in two steps: 1) mask creation and 2) entrained bubble detection and sizing. In the mask creation step, we first cropped the syringe wall from the original image and then enhanced the image contrast. Next, a Gaussian smoothing filter was applied to reduce the image noise and a median filter removed the high-frequency signal components. Thereupon, pixel intensity thresholding filtered all signals below a given brightness followed by an image dilation to enhance the features of the image; thus, detecting features more accurately. Lastly, the small objects were removed from the binary image and the mask was generated based on the remaining features for processing the PIV particle images. A more detailed description of the image processing steps and the effect of each filtering on the image can be found in [244]. Figure 7.3 summarizes all the image processing steps.

The bubble detection step included isolated bubbles (bubbles with no overlapping) detection and overlapping bubbles detection. To detect the isolated bubbles, we first computed the roundness of each detected feature from the mask generation step. The roundness was defined as the ratio of the object's surface area to the area of the circle whose diameter is equal to the maximum diameter of the object. Then, the objects with a circularity of greater than 0.89 were registered as isolated bubbles and masked out for the overlapping bubbles detection step. Thus, those objects with a circularity smaller than 0.89 were considered overlapping bubbles and were detected in the following step. Lastly, the area (A) of the isolated bubbles was determined and then the equivalent diameter, D, was obtained using $D = \sqrt{4A/\pi}$.

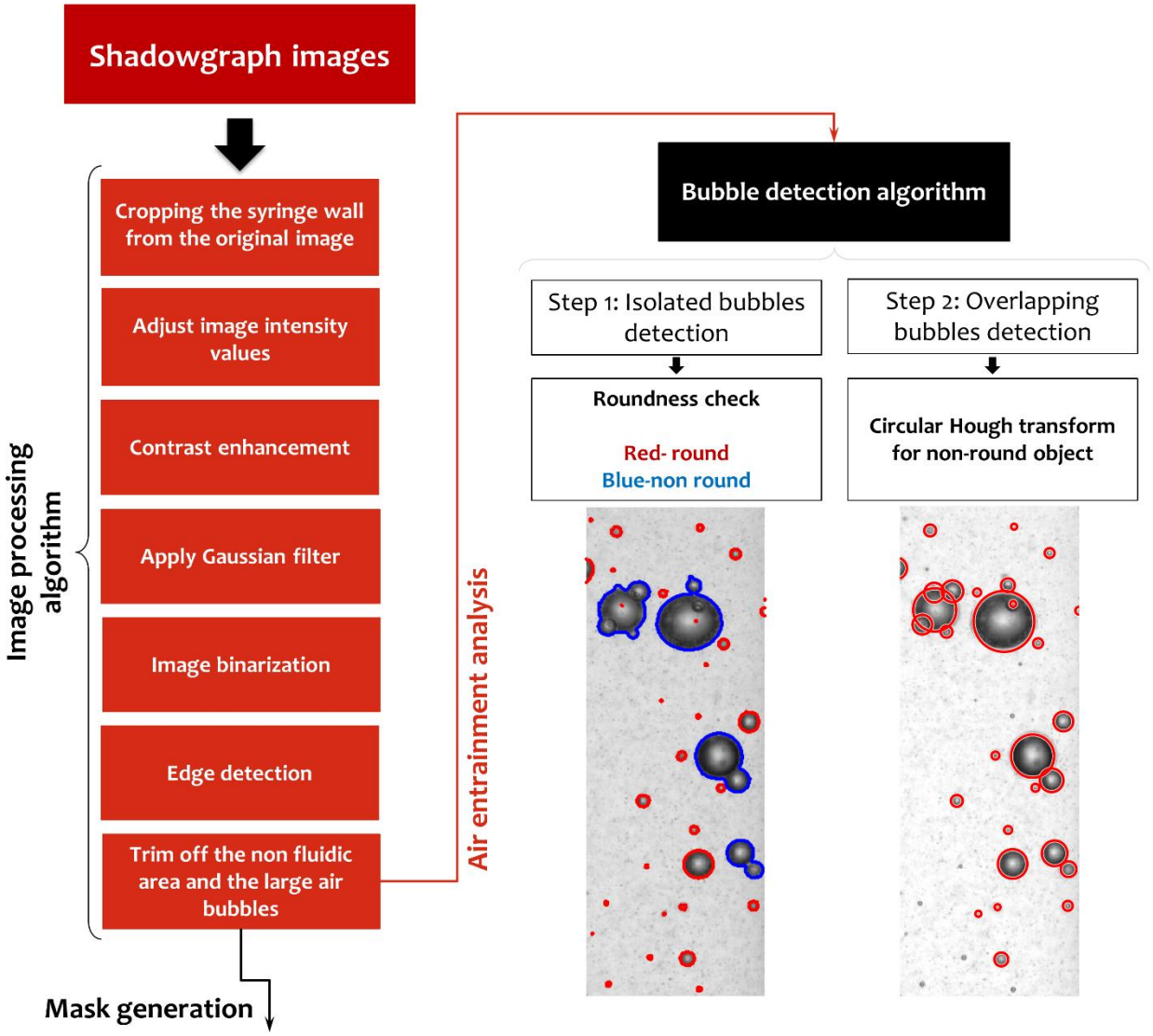

Figure 7.3. Image processing algorithm and sample images with the two-step bubble detection algorithm applied.

In the overlapping bubbles detection step, we employed the modified Circle Hough transform (CHT) [48–50] to identify the overlapping bubbles. The CHT aims to find circular patterns of a specified radius R within an image. The CHT is formulated as a convolution whose binary mask coefficients are set on the circle boundary and are zero elsewhere. This convolution is applied to an edge magnitude image (after suitable edge detection). A separate circle filter is used for each circle radius to be detected for the CHT calculation. For the overlapping bubbles, we used the magnitude of the image gradient to detect the edges and defined the radius range in the circle filter from $0.1\ mm$ to $5\ mm$. Thus, the overlapping bubbles were detected automatically

and the corresponding size was obtained. Figure 7.3 shows the detected bubbles for a sample frame after applying our two-step bubble detection methodology. A sample video of the generated mask for the PIV processing and the detected bubbles from the shadowgraphy can be found in Supplementary Materials.

7.2.2.2.Strain-shear quantification (PIV processing)

For the obtained DPIV images, our in-house DPIV processing software was employed to determine the velocity field in the liquid phase of the syringe. After applying the generated PIV mask from the shadowgraph images, we used Robust Phase Correlation (RPC), which improves accuracy and spatial resolution compared to conventional methods when processing images with a low signal-to-noise ratio. RPC builds upon our earlier work [51,52] and recent advancements [53–55] by incorporating a series of optimized filters to the Fourier-based cross-correlation. The particle images were processed using RPC in a multi-grid window deformation framework with intermediate passes smoothed and validated using Universal Outlier Detection [52,54–56]. A total of four passes were used with the window resolution varying from 64×64 pixels on the first pass to 16×16 pixels on the last pass. Additionally, a window overlap varied from 87.5% on the first pass to 50% on the last pass to provide a final grid spacing of 8×8 pixels corresponding to a spatial resolution of $0.16\ mm$.

Even though PIV is a robust and accurate method for non-invasive fluid velocity measurements, like other measurement techniques, PIV measurements involve instrument and algorithm chains with coupled uncertainty sources [257,258]. In contrast to the error, which is the difference between the measured quantity and the true value, uncertainties are qualified by a confidence level (a percentage). Given an uncertainty, we can expect the true value to be within that range this percentage of the time. Uncertainty in the velocity fields was quantified using a Moment of Correlation method [57]. Uncertainty was computed using 2σ (95%) confidence intervals, excluding the outliers. The estimated uncertainty of the velocity components (u, v) was $0.21\ px$ and $0.25\ px$ for u and v components, respectively.

We then employed a fourth-order Richardson gradient scheme [259] to compute the instantaneous shear ($\frac{\partial v}{\partial x} + \frac{\partial u}{\partial y}$) and strain ($\frac{\partial u}{\partial x} + \frac{\partial v}{\partial y}$) fields from the velocity field obtained from DPIV processing.

7.3.Results and discussion

7.3.1. Air-solution interface observations

Figure 7.4 shows the air-solution interface evolution in the syringes filled with water and silicone oil. The motion of the air-solution interface in the syringes filled with water is different from that in silicone oil-filled syringes at a constant acceleration, viscosity, and air gap height (also see supplementary materials). The equilibrium shape of the air-solution interface is governed by the balance between the pressure excess inside the bubble, ΔP, and a combination of gravitational and capillary forces that is a function of surface tension [260]. For water, the air-solution interface starts with a flat surface ($\theta_c \sim 90°$). When the syringe accelerates, the center of the interface gains a vertical speed and rises relative to the syringe wall (Figure 7.4 ($t = 0 - 2.7\, ms$) and Figure 7.5(a-1)). Then, the syringe hits the stopper and decelerates and the interface near the wall rises along the syringe wall, reaches the plunger (Figure 7.4 ($t = 3.6 - 5.4\, ms$)), and focuses at the center (Figure 7.4 ($t = 3.6 - 5.4\, ms$) and Figure 7.5(a-2)). The air gap deforms into a toroidal shape, increasing the strain rate (Figure 7.4 ($t = 8.1 - 9.0\, ms$) and also see supplementary materials). Next, the air-solution interface deforms and may rupture into micron-sized air bubbles. While for silicone oil, the air-solution interface starts with a concave meniscus ($\theta_c \sim 30°$) where the interface at the center is lower than the interface near the wall (Figure 7.4 ($t = 0$)). The interface near the wall rises along the syringe wall during the syringe acceleration because of interfacial instability caused by the Rayleigh-Taylor instability (Figure 7.4 ($t = 0 - 3.6$) and Figure 7.5(b-1)). The syringe's deceleration causes the center of the interface to move upwards, leading the interface to become flatter due to its stabilizing effect (Figure 7.4 ($t = 4.5 - 8.1$) and Figure 7.5(b-2)). The final air gap is trapped near the plunger and fewer micron-sized bubbles are formed in the solution (Figure 7.4 ($t = 8.1 - 9.0$) and see supplementary materials).

Figure 7.5 provides a quantitative description of air-solution interface evolution during acceleration and deceleration for water and silicone oil in the cases presented in Figure 7.4. Figure 7.5(a-3,a-4) and Figure 7.5(b-3,b-4) illustrate the time history of velocity components along the red line for water and silicone oil. During the acceleration, water flows upwards and towards the center with a maximum velocity of $(U/U_0)_{max} \sim 0.14$, and during deceleration, solution flows downwards and towards the wall with a maximum velocity of $(U/U_0)_{max} \sim 0.71$. While for silicone oil, when the syringe accelerates, the solution flows downwards ad towards the wall at a

maximum velocity of $(U/U_0)_{max}$~0.14, and during the deceleration, solution flows upwards and towards the center with a maximum velocity of $(U/U_0)_{max}$~0.82.

Considering that the viscosity, syringe acceleration, and air gap height are kept constant, this substantial difference can be the effect of either surface tension or interface-wall contact angle. In this regard, Zhang et al. [249] showed numerically that the surface tension has a less significant impact on the air-solution interface dynamics. They showed that the sloshing intensity in terms of induced hydrodynamic stress and interfacial increases with the syringe wall hydrophobicity and hardly changes with the surface tension. Thus, the different behavior during acceleration and deceleration phases is primarily due to differences in the wettability of the syringe wall.

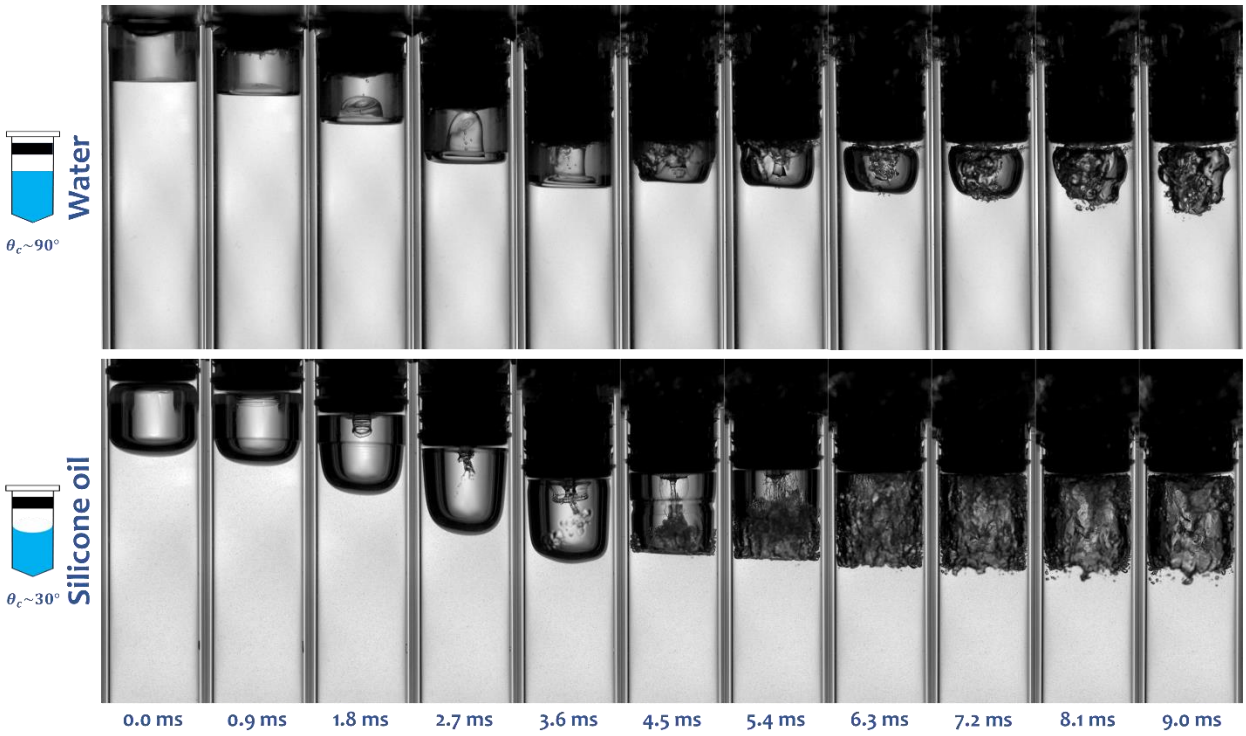

Figure 7.4. Representative images of the air-solution interface evolution in the syringes filled with water and silicone oil. The syringes were actuated with a 12 N drive spring, and the air gap height was 2 mm.

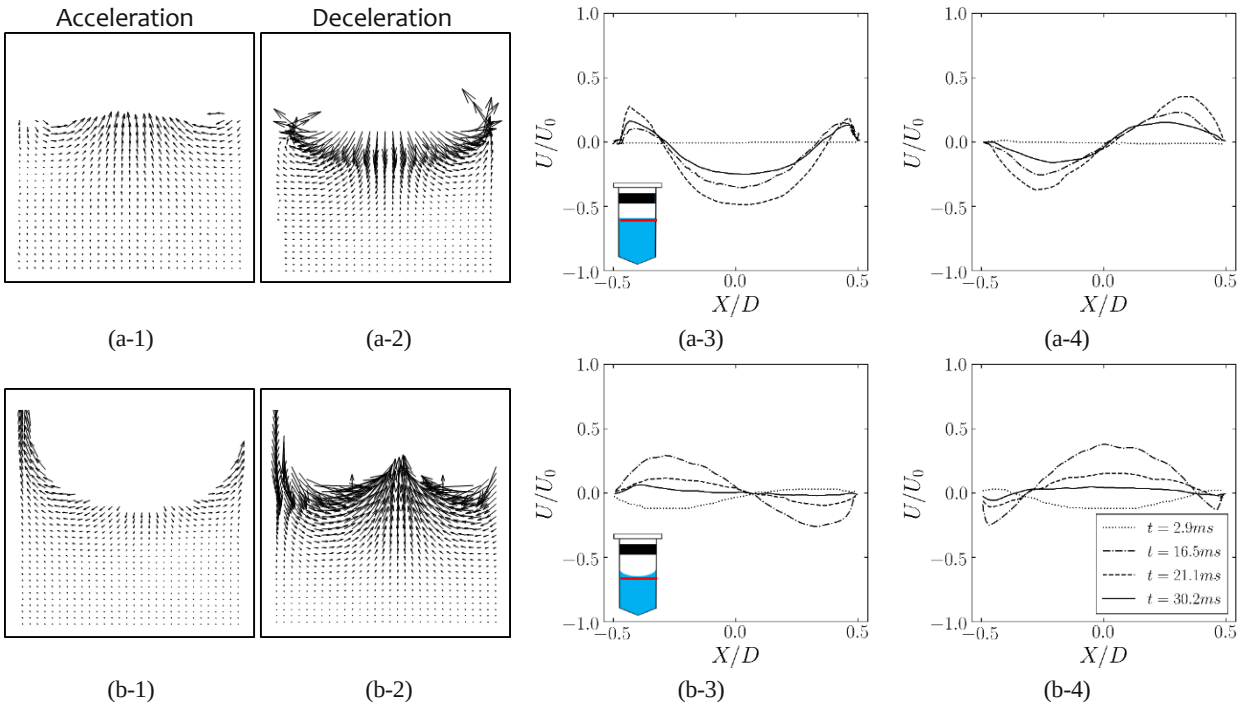

Figure 7.5. A sample snapshot from the solution velocity field in the vicinity of the air-solution interface during acceleration (a-1 and b-1) and deceleration (a-2 and b-2) for (a) water and (b) silicone oil. Velocity components profiles for an arbitrary cross-section (50 μm below the interface, red line in the syringe schematic) in (a) water and (b) silicone oil. (a-3) and (b-3) correspond to the u component (velocity in the horizontal direction). (a-4) and (b-4) correspond to the v component (velocity in the vertical direction). The motion of the air-solution interface in the syringes filled with water and silicone oil. In the shown cases, the syringes were actuated with a 1.0X N drive spring, and the air gap height was 2 mm. U and U_0 are the velocity components and the characteristic velocity, respectively. Characteristic velocity is defined as the ratio of syringe diameter to travel time (5 ms).

This substantial difference in sloshing dynamics between water and silicone oil leads to dissimilarity in the formation of micron-sized bubbles upon the air gap bubble collapse. The intense motion of the air-solution interface may result in air gap bubble collapse and air entrainment in the form of micron-sized bubbles. For both water and silicone oil, after a transient phase ($t < 30\ ms$), the mean diameter variation of these micron-sized bubbles over time reaches a steady-state distribution. However, the size distribution of micron-sized bubbles formed in water and silicone oil at different air gap heights does not follow the same patterns. Figure 7.6 shows the ensemble-averaged size distribution of micron-sized bubbles at different air gap heights for water and silicone oil. The results suggest that most of the formed micron-sized bubbles are less than $100\ \mu m$. For water (Figure 7.6(a)), the smaller air gap collapses more easily and produces more micron-sized bubbles, while for the larger air gaps, more air volume will be trapped inside the water. The toroidal interface is elongated, increasing the interfacial area. That is why the number of micron-sized bubbles due to the air gap bubble collapse decreases with the air gap size. In contrast, the variation of the bubble size distribution for different air gap heights is not significant for silicone oil (Figure 7.6(b)). The smaller contact angle between the silicone oil and syringe wall causes the final air entrainment to be trapped near the plunger for all different air gaps, and fewer small bubbles form in the solution.

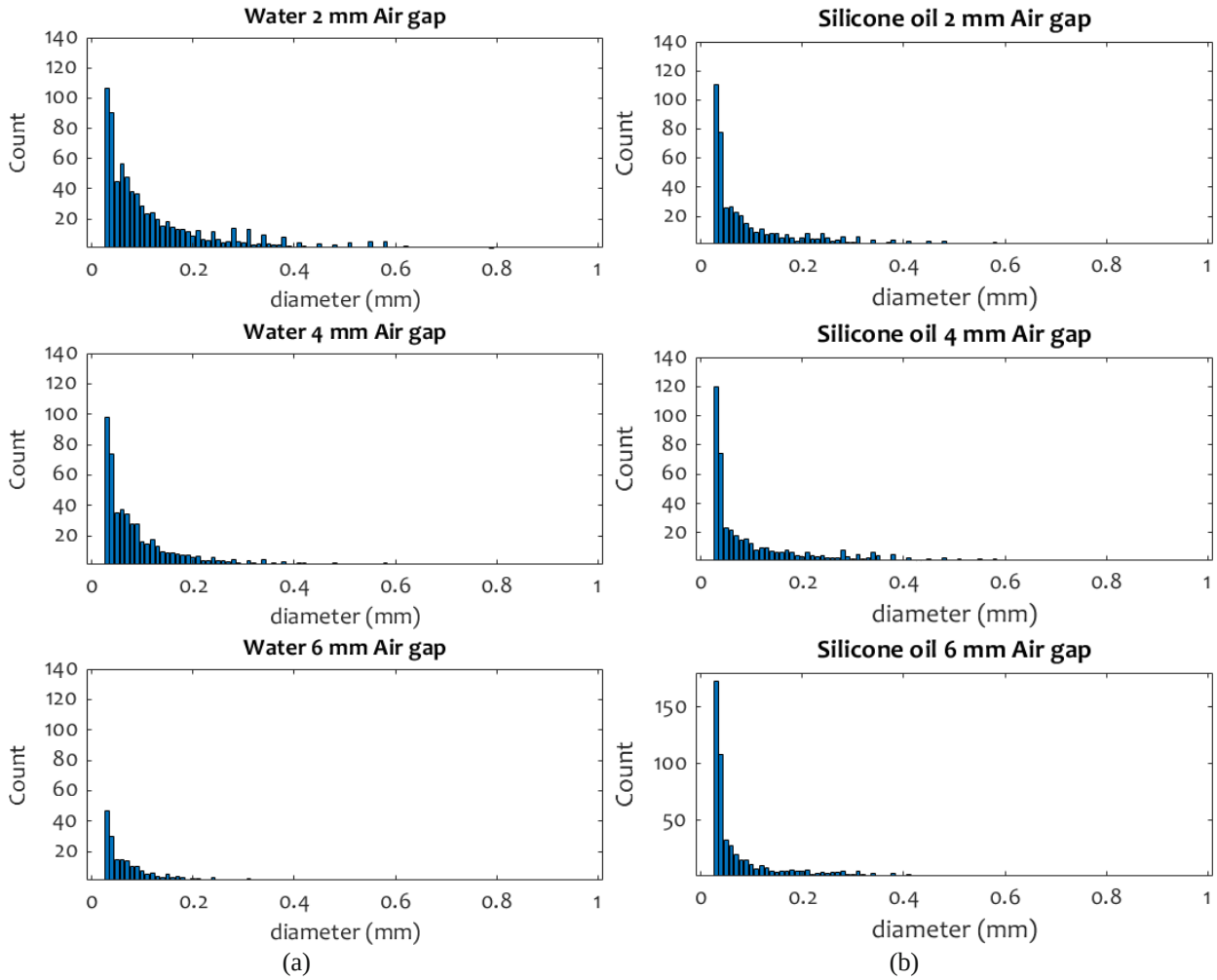

Figure 7.6. Ensemble averaged size distribution of micron-sized bubbles formed in syringes filled with (a-1) water and (b-1) silicone oil at different air gap heights. For these plots, we show the cases in which the syringes were actuated with a $1.0X\ N$ drive spring.

7.3.2. Induced strain rate during autoinjector's insertion

During the insertion of the autoinjector, the syringe accelerates due to the collision of the plunger rod with the plunger and then decelerates by a mechanical stop. This process induces an abrupt change in the kinetic energy of the syringe and the solution inside. Thus, the fluid experiences deformation that can be quantified in terms of shear and strain rate. To explore the correlation between the syringe acceleration and the induced strain rate, we plot the maximum strain rate observed during syringe acceleration and deceleration for water and silicone oil, as well as the corresponding velocity and acceleration profiles in Figure 7.7.

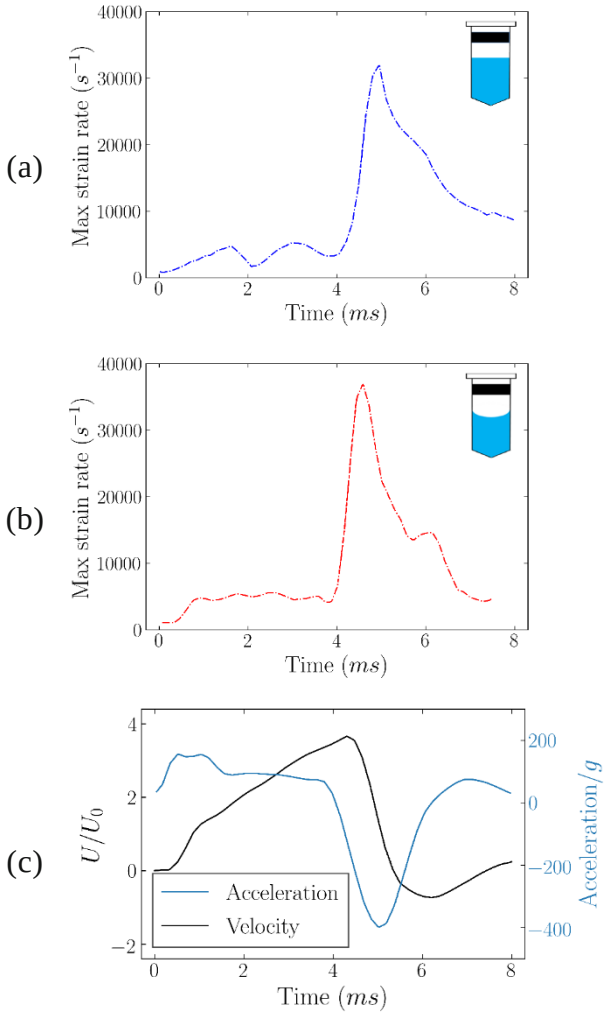

Figure 7.7. Maximum strain rate observed during syringe acceleration and deceleration for (a) water and (b) silicone oil. (c) Velocity and acceleration profiles of the syringe. The plots show the ensemble average of strain rates and velocity/acceleration profiles for the cases where the syringes were actuated with a 1.0X N drive spring, and the air gap height was 2 mm. U and U_0 are the syringe maximum velocity and the characteristic velocity, respectively. Characteristic velocity is defined as the ratio of syringe diameter to travel time (5 ms). Each line represents the ensemble average of 5 trials for that condition.

Figure 7.7 indicates that as the syringe is set into motion upon autoinjector actuation, the strain rate in the solution starts increasing. The strain rate keeps increasing during the acceleration, it sharply increases during deceleration, and the maximum strain rate occurs at the end of the deceleration phase. Thus, the moment that yields the most considerable hydrodynamic stress is the end of the insertion phase of autoinjector actuation and has the largest impact on the surrounding solution. The results also indicate that the maximum induced strain rate has the same orders of

magnitude for water and silicone oil. Our observations show that the hydrodynamic shear mainly occurs near the syringe wall and entrained bubbles.

7.3.3. Air entrainment-induced strain rate and interfacial area

In this section, we discuss the effects of air gap height, syringe acceleration, and solution on the time evolution of the air entrainment-induced interfacial area due to the solution sloshing. We compute the strain-rate tensor in the liquid phase $\frac{1}{2}(\nabla v + \nabla v^T)$ using the obtained velocity field, v, from the PIV measurements. The magnitude of the strain rate $|D| = \left|\frac{\partial u}{\partial x} + \frac{\partial v}{\partial y}\right|$ quantifies the rate of extensional deformation of fluid particles. We use the strain rate threshold of $D_0 = 10^4\ s^{-1}$ as a representative value above which the strain rate can affect the drug product and we quantify the volume fraction of the solution at which $|D| > D_0$ in the syringe.

When the air gap height increases, more air volume is trapped inside the liquid (Figure 7.8). The toroidal interface is elongated, increasing the interfacial area for $t > 8\ ms$. In syringes filled with water, for $h_a = 2$, the interfacial area does not change significantly for $t > 10\ ms$. However, the interfacial area monotonically increases with time for air gap heights of $4\ mm$ and $6\ mm$. For silicone oil-filled syringes, the interfacial area does not change significantly for $t > 10\ ms$ at different air gap heights (see supplementary materials).

In syringes with larger air gaps, more fluids are also subject to high strain rates and the volume fraction of solution with $|D| > D_0$ increases with the air gap height. The maximum volume fraction of solution with $|D| > D_0$ occurs in the first $10\ ms$ of the device actuation and for $t > 10\ mm$ the volume fraction of solution with $|D| > D_0$ approaches zero for all air gap heights.

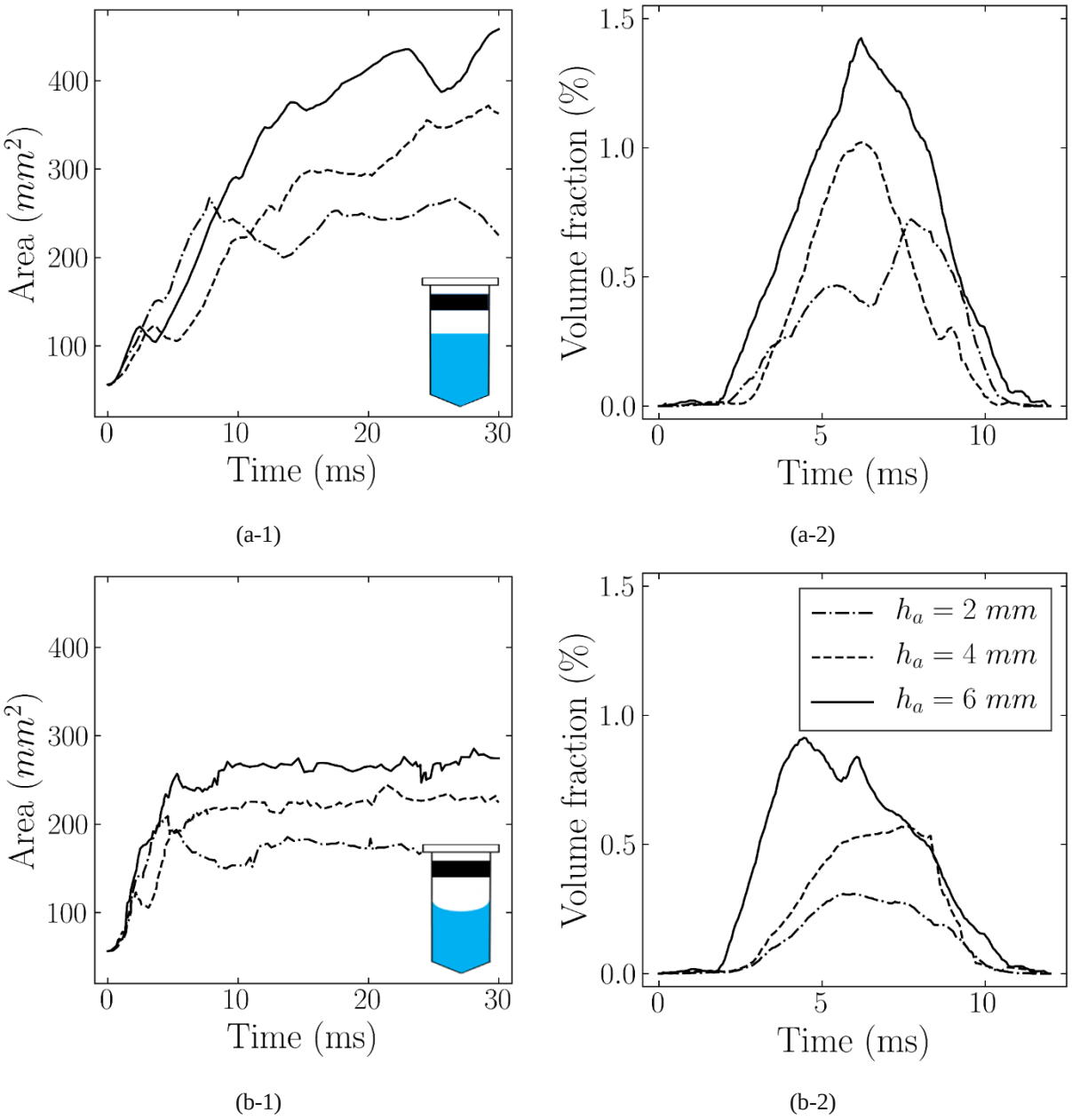

Figure 7.8. Effect of air gap height on the interfacial area for (a-1) water and (b-1) silicone oil. Air gap height effect on the volume fraction for the solution with strain rate> D_0 in syringes filled with (a-2) water and (b-2) silicone oil. In these plots, the syringes were actuated with a 1.0X N drive spring. Each line represents the ensemble average of 5 trials for that condition.

The interfacial area in the syringes filled with water and silicone oil increases at the same rate for $t < 5\ ms$ (Figure 7.9). For silicone oil, the interfacial area stops growing and remains constant for $t > 5\ ms$, however, the interfacial area in water-filled syringes increases for $t > 5\ ms$. Thus, for a fixed air gap height, the interfacial area in the water solution is higher than in silicone

oil and the water solution is subject to higher strain rates. It implies that the sloshing dynamics are dependent on the contact angle between the wall and the solution (see supplementary materials).

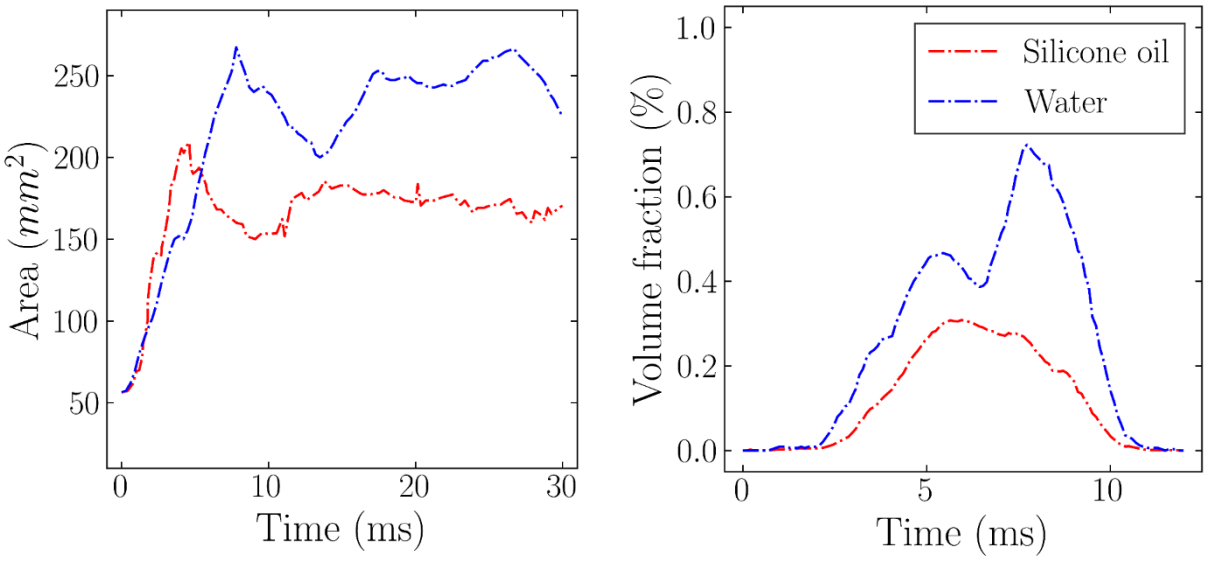

Figure 7.9. Effect of solution on the (a) interfacial area and (b) volume fraction for the solution with strain rate$>$ D_0. For the shown cases in these plots, the syringes were actuated with a 1.0X N drive spring and the air gap height was 2 mm. Each line represents the ensemble average of 5 trials for that condition.

When the drive spring force increases, more kinetic energy is induced in the syringe. Thus, the solution gains more kinetic energy during the sloshing motion (Figure 7.10), enhancing bubble formation, and the solution is also subject to a higher strain rate. The interfacial area increases with drive spring force for both water and silicone oil. However, for silicone oil, the interfacial area does not change significantly for $t > 8\,ms$ for both $1.0X\ N$ and $1.5X\ N$ drive springs. The volume fraction of fluids with $|D| > D_0$ also increases when the syringe is actuated with a stronger drive spring. The time instant at which the maximum volume fraction of fluids with $|D| > D_0$ occurs does not change with changing the actuation force (see supplementary materials).

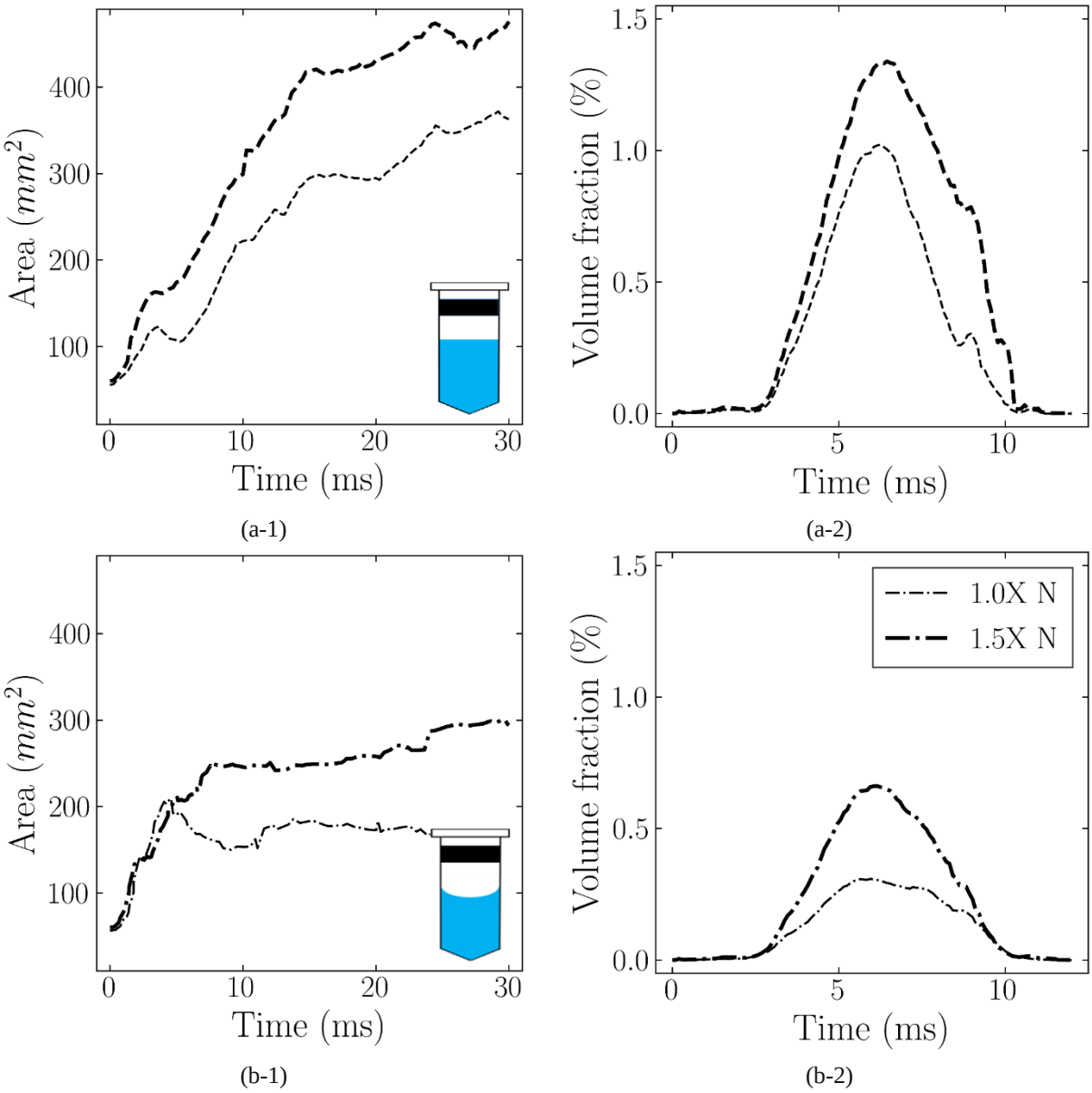

Figure 7.10. Effect of drive spring force on the interfacial area for (a-1) water and (b-1) silicone oil. Drive spring force effect on the volume fraction for the solution with strain rate$>$ D_0 in syringes filled with (a-2) water and (b-2) silicone oil. These plots show only the cases with an air gap height of 2 mm for silicone oil and 4 mm for water. Each line represents the ensemble average of 5 trials for that condition.

Higher drive spring force corresponds to the higher acceleration of the syringe during the insertion stage. Thus, to delineate the effects of drive spring force on the sloshing dynamics, we explored the maximum interfacial area after the liquid sloshing and volume fraction for the solution with a strain rate greater than D_0 as a function of a dimensionless number defined based

on the syringe's maximum acceleration. The Froude number, $Fr = U/\sqrt{aD}$, is a dimensionless number defined as the ratio of the flow inertia to the acceleration force. Here, we define U as the interface maximum relative velocity, a as the syringe max acceleration, and D as the syringe diameter.

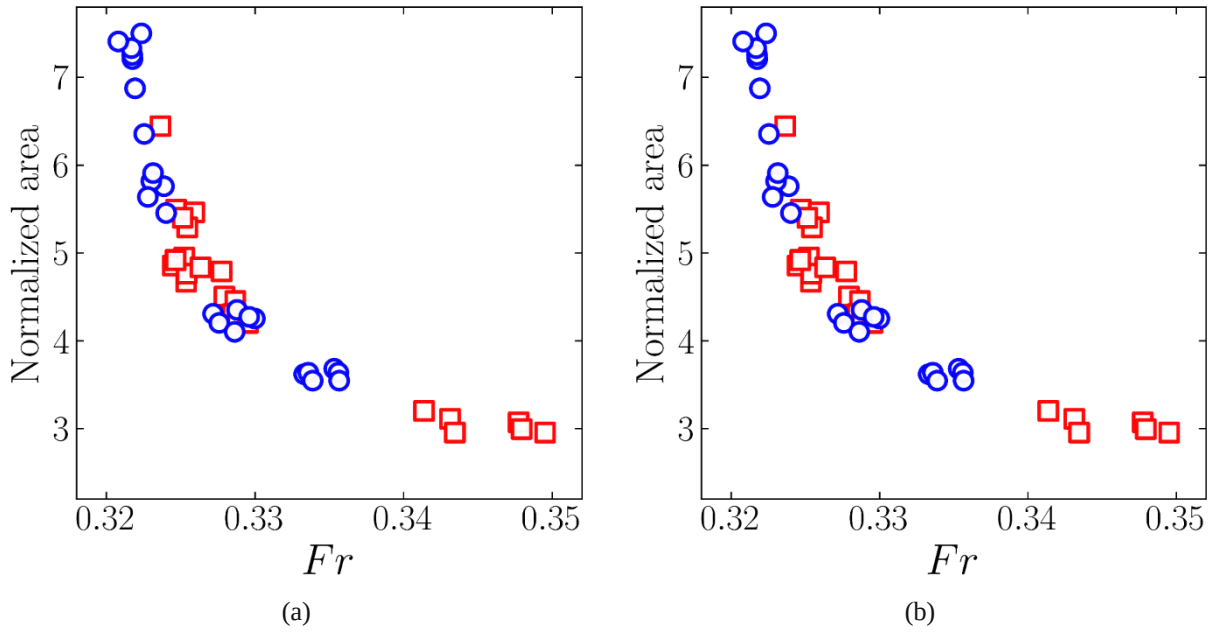

Figure 7.11. (a) Maximum interfacial area after the liquid slosh normalized with the initial air-solution interface area as a function of Fr. (b) Maximum volume fraction for the solution with strain rate$> D_0$ as a function of Fr.

Figure 7.11 shows the maximum interfacial area after the liquid sloshing normalized with the initial air-solution interface area (before the actuation of the autoinjector) and volume fraction for the solution with a strain rate greater than D_0 as a function of Fr. The results indicate that the induced interfacial area and the volume fraction of solution with $|D| > D_0$ decrease with the Fr. It also shows that the most severe sloshing occurs in an autoinjector with the lowest Fr.

To compute Fr, we used the maximum relative velocity of the interface as the characteristic velocity. However, we are interested in obtaining the induced interfacial area as a function of autoinjector design parameters. Thus, we follow a dimensional analysis to find the maximum interface-relative-velocity as a function of autoinjector design parameters. The interface velocity is a function of solution surface tension, σ, solution density, ρ, syringe acceleration/deceleration, a, and syringe diameter, D [261]. These parameters can be grouped into

one dimensionless number as $\rho a D^2/\sigma$ that can be interpreted as the multiplication of the Weber number, $We = \rho U^2 D/\sigma$, and the Strouhal number, $St = fD/U$. We measures the relative importance of the fluid's inertia compared to its surface tension, and St is used to describe the oscillating flow, where $f = a/U$ is the characteristic frequency [200,202]. Figure 7.12 illustrates the correlation of the maximum relative velocity of the air-solution interface with $We.St$. Therefore, by having the syringe acceleration and diameter, the interface velocity is obtained from Figure 7.12 that can be used to compute the Fr.

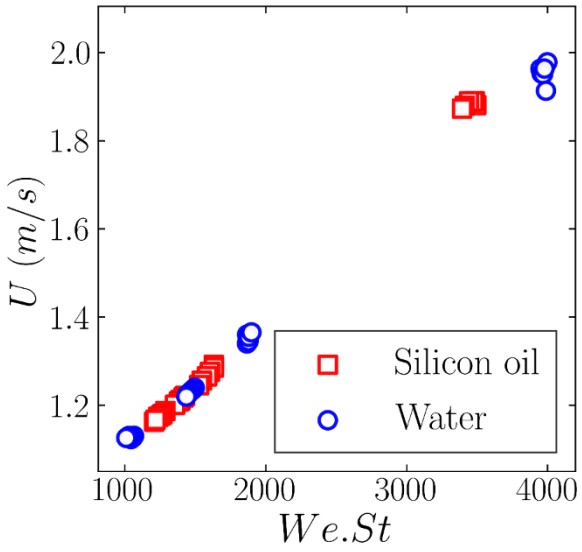

Figure 7.12. Maximum relative velocity of the air-solution interface as a function of autoinjector design parameters.

7.3.4. Potential effects of sloshing on the protein molecules

Liquid sloshing induces hydrodynamic shear and increases the air-solution interfaces in the AI that can impact the therapeutic protein. Our results show that during the liquid sloshing, only a small volume ($< 5\%$) of the liquid inside the syringe is subject to the shear and strain rates up to $10^4\ s^{-1}$. The therapeutic proteins experience the same magnitude of strain rate during the pumping and filtration processes [262,263], where shear forces on the protein molecules are on the order of $10^{-1}\ pN$. It has been shown that the required shear force to unfold proteins is between 20 to $150\ pN$ [262,263]. Thus, shear forces alone may not cause any protein aggregation during the liquid sloshing in the syringes. In this regard, the air-liquid interface could be more harmful to

therapeutic proteins, where forces on protein molecules can be as high as $140\,pN$ at the interface [262,263]. Thus, it has been hypothesized that, in the presence of shear stress, the effect of the air-liquid interface may be overlooked, and the possible impact is misattributed to shear stress [224,226]. Lin et al. showed that the protein aggregation and subvisible particles (SVPs) formation at the air-liquid interface are controlled by the change in the interface area [264]. They observed SVPs formation for a $\Delta A/A_0$ of 0.7 and the protein was exposed to that interfacial area change for $70\,s$, where ΔA is the change in the interfacial area and A_0 is the initial interfacial area. During the liquid sloshing, although the $\Delta A/A_0$ is $\sim 3-8$, the exposure is $\sim 50\,ms$. This is a relatively short time period for the protein molecules to be absorbed by the interface. However, in the sloshing phenomenon, the advective transport is dominant when it is compared to diffusive transport (Péclet number$\sim 10^8$ [249]). That is, the protein molecules are transported by the liquid bulk motion and, additionally, some of the entrained bubbles may last long after the insertion process. Thus, the protein molecules are likely to be absorbed by the air-liquid interface while advection and may form aggregates. Therefore, further investigation is needed to explore if the sloshing in AI harms the therapeutic proteins and increases the number of SVPs in the drug products. Note that we studied sloshing phenomenon in syringes filled with water and silicone oil and not the therapeutic proteins.

7.4.Summary

Interface motion and hydrodynamic shear induced by the liquid sloshing during the needle insertion upon autoinjector actuation were investigated experimentally, generating insights that may help assess the potential impact on therapeutic protein molecules inside the syringe during autoinjector activation. The air-liquid interface and the air entrainment area were quantified using high-speed shadowgraph visualization. The strain and shear rate experienced by the liquid during the liquid sloshing was also computed from the velocity field obtained from PIV measurements. The interfacial area and the volume of the fluid subject to high strain and shear rates increased with the air gap height and syringe acceleration. The interfacial area decreased with the Fr. The hydrodynamic shear mainly occurred near the syringe wall and entrained bubbles. Strain and shear rates sharply increased during deceleration, and the maximum strain and shear rates occurred at the end of the deceleration phase. Future experiments under similar hydrodynamic stresses, shear, and exposure time would help understand whether these conditions can lead to protein aggregation.

7.5.Authors contributions

Javad Eshraghi: Methodology, Software, Formal analysis, Data curation, Investigation, Visualization, Writing - original draft. Zhongwang Dou: Data acquisition. Jean-Christophe Veilleux: Methodology, Interpretation of the results, Writing - review & editing. Galen Shi: Methodology, Interpretation of the results, Writing - review & editing. David Collins: Methodology, Writing - review & editing. Arezoo M. Ardekani: Conceptualization, Methodology, Interpretation of the results, Writing - review & editing, Funding acquisition. Pavlos P. Vlachos: Conceptualization, Methodology, Investigation, Interpretation of the results, Supervision, Project administration, Funding acquisition, Writing - original draft, review & editing.

8. CONCLUSIONS AND FUTURE WORK

Several multidisciplinary problems pertaining to water entry, cavitation, and the wake of stationary cylinders were investigated in this dissertation. The principal idea behind the dissertation is justified by the need to quantify the intensity of cavitation and liquid slosh to evaluate their impacts in different disciplines such as medical device development, as well as the need to explain some ubiquitous physical phenomena.

The surface seal in the water entry of hydrophobic spheres was shown to be mainly governed by the velocity of the airflow rushing into the cavity, which was in contrast to the current understanding that considered the impact velocity as the determinant parameter. Therefore, this work presented the first detailed analysis and physical understanding of why a splash does not always seal, supported by a developed theory and experimental observations. We developed a physical model to predict the trajectory of the splash curtain and determined the critical airflow velocity ratio beyond which the surface seal occurs in the water entry. Even though we focused on the dynamics of the splash curtain of the water-entering spheres, the model can be generalized to predict the splash curtain of projectiles with various geometries.

The data-assimilated modeling most accurately estimated the bubble diameter and far-field pressure as the deviation of bubble diameter and far-field pressure predictions from measurements decrease by up to 90% and 60%, respectively. Although the assimilated model is not a substitute for high fidelity models, this technique overcomes the inherent model assumptions and makes the model's outputs more robust with respect to the physical parameters' initial values. Also, since the factors like bubble non-sphericity, bubble cloud interaction, and the effect of stiffness of the material boundary are not well established in the existing models, assimilated modeling is a viable tool to discover the significance of these factors in the dynamics of the cavitation bubble.

The frequency-based analysis of an air bubble oscillating in a cavitation-induced acoustic field revealed that different regimes could be defined robustly based on the wavenumber of the air bubble boundary. It was also shown that the transition between different regimes was controlled by the air bubble absorbed energy and that the absorbed energy was a linear function of We defined based on the induced acoustic pressure. Even though we focused on the interactions of a single bubble with an acoustic source, it can be expanded to investigate the energy absorbance of bubble curtains used to contain oil spills, reduce shock wave propagation, and analyze other

environmental and industrial problems. This work will enable the physics community to explain fundamental bubble-bubble and cavitation-bubble interactions.

Analyzing the effects of autoinjectors' design parameters on the intensity of cavitation that occurred in these medical devices, using the data assimilated modeling, revealed the generation of an intense shock wave and a high extension rate upon cavitation collapse. The cavitation collapse-induced extension rate increased with syringe acceleration and filling volume (fluid column height in the syringe) and decreased with the fluid viscosity and air gap size. Therefore, the most severe cavitation occurred in an AI device with the larger spring force and smaller air gap size filled with less viscous fluid and larger filling volume.

Analyzing sloshing in autoinjectors revealed that reducing the air gap volume and syringe acceleration/deceleration for a given dose of drug solution during the actuation of these devices mitigates the interface area and effective shear. We showed that strain and shear rates sharply increased during deceleration, and the maximum strain and shear rates occurred at the end of the deceleration phase. The hydrodynamic shear mainly occurred near the syringe wall and entrained bubbles.

Even though high values of shear rates occur during the sloshing and cavitation, the time duration is relatively short ($\sim 40\ ms$). Future experiments using methods such as dynamic light scattering under similar hydrodynamic stresses, shear conditions, and time duration would help to understand whether the proteins aggregate under these conditions. Furthermore, in biotherapeutic drug manufacturing processes where the occurrence of shear stress, interfacial stress, and cavitation are reasonable, determination of the driving mechanism for protein aggregation is crucial to properly design the bioprocesses, drug handling, and administration of the drugs. For instance, determining the shear rate threshold beyond which the protein aggregation occurs will significantly impact the design of auto-injectors.

We also demonstrated the validity of using a flowing soap film system as a two-dimensional laboratory model of the unsteady wake behind a circular cylinder at low Reynolds numbers. We introduced a quantitative soap film thickness measurement method using Background Oriented Schlieren (BOS) to provide a spatially resolved (relative) thickness field. Vortex cores in the cylinder wake appeared as low thickness zones, and the minimum thickness regions identified with BOS were shown to coincide with the vortex centers identified in phase-matched interferograms.

REFERENCES

[1] K. J. Mysels, S. Frankel, and K. Shinoda, *Soap Films: Studies of Their Thinning and a Bibliography* (Pergamon press, 1959).

[2] Y. Couder, *Two-Dimensional Grid Turbulence in a Thin Liquid Film*, J. Phys. Lettres **45**, 353 (1984).

[3] Y. Couder, J. M. Chomaz, and M. Rabaud, *On the Hydrodynamics of Soap Films*, Phys. D Nonlinear Phenom. **37**, 384 (1989).

[4] Y. Couder and C. Basdevant, *Experimental and Numerical Study of Vortex Couples in Two-Dimensional Flows*, J. Fluid Mech. **173**, 225 (1986).

[5] M. Gharib and P. Derango, *A Liquid Film (Soap Film) Tunnel to Study Two-Dimensional Laminar and Turbulent Shear Flows*, Phys. D **37**, 406 (1989).

[6] H. Kellay, X. L. Wu, and W. I. Goldburg, *Experiments with Turbulent Soap Films*, Phys. Rev. Lett. **74**, 3975 (1995).

[7] M. A. Rutgers, X. Wu, R. Bhagavatula, A. A. Petersen, and W. I. Goldburg, *Two-dimensional Velocity Profiles and Laminar Boundary Layers in Flowing Soap Films*, Phys. Fluids **8**, 2847 (1996).

[8] D. Georgiev and P. Vorobieff, *The Slowest Soap-Film Tunnel in the Southwest*, Rev. Sci. Instrum. **73**, 1177 (2002).

[9] P. Vorobieff, M. Rivera, and R. E. Ecke, *Soap Film Flows: Statistics of Two-Dimensional Turbulence*, Phys. Fluids **11**, 2167 (1999).

[10] M. Rivera, P. Vorobeiff, and R. Ecke, *Turbulence in Flowing Soap Films: Velocity, Vorticity, and Thickness Fields*, Phys. Rev. Lett. **81**, 1417 (1998).

[11] H. Kellay, *Hydrodynamics Experiments with Soap Films and Soap Bubbles: A Short Review of Recent Experiments*, Phys. Fluids **29**, 111113 (2017).

[12] M. Rivera and X. L. Wu, *External Dissipation in Driven Two-Dimensional Turbulence*, Phys. Rev. Lett. **85**, 976 (2000).

[13] P. Vorobieff and R. E. Ecke, *Cylinder Wakes in Flowing Soap Films*, Phys. Rev. E **60**, 2953 (1999).

[14] W. Yang and M. A. Stremler, *Critical Spacing of Stationary Tandem Circular Cylinders at $Re \approx 100$*, J. Fluids Struct. (2019).

[15] T. Schnipper, A. Andersen, and T. Bohr, *Vortex Wakes of a Flapping Foil*, J. Fluid Mech. **633**, 411 (2009).

[16] Y. Chen and E. Fried, *Stability and Bifurcation of a Soap Film Spanning an Elastic Loop*, (2013).

[17] M. M. Bandi, A. Concha, R. Wood, and L. Mahadevan, *A Pendulum in a Flowing Soap Film*, Phys. Fluids **25**, 41702 (2013).

[18] L. B. Jia and X. Z. Yin, *Passive Oscillations of Two Tandem Flexible Filaments in a Flowing Soap Film*, Phys. Rev. Lett. **100**, 228104 (2008).

[19] L. Jia, Q. Xiao, H. Wu, Y. Wu, and X. Yin, *Response of a Flexible Filament in a Flowing Soap Film Subject to a Forced Vibration*, Phys. Fluids **27**, 17101 (2015).

[20] J. Zhang, S. Childress, A. Libchaber, and M. Shelley, *Flexible Filaments in a Flowing Soap Film as a Model for One-Dimensional Flags in a Two-Dimensional Wind*, Nature **408**, 835 (2000).

[21] L.-B. Jia and X.-Z. Yin, *Response Modes of a Flexible Filament in the Wake of a Cylinder in a Flowing Soap Film*, Phys. Fluids **21**, 101704 (2009).

[22] H. Fujiwara, *Spectroscopic Ellipsometry: Principles and Applications* (John Wiley & Sons, 2007).

[23] P. Rai-Choudhury, J. L. Benton, D. K. Shroder, and T. F. Shaffner, *Diagnostic Techniques for Semiconductor Materials and Devices*, in *Diagnostic Techniques for Semiconductor Materials and Devices*, Vol. 3322 (1997).

[24] M. I. Auliel, C. F. Hebrero, R. Sosa, and G. Artana, *Schlieren Technique in Soap Film Flows*, **58**, (2017).

[25] M. Raffel, *Background-Oriented Schlieren (BOS) Techniques*, Exp. Fluids **56**, 60 (2015).

[26] M. Raffel, C. E. Willert, S. T. Wereley, J. Kompenhans, S. Willert, S. T. Wereley, and J. Kompenhans, *Particle Image Velocimetry: A Practical Guide*, Vol. 2nd (Springer, 2007).

[27] R. J. Adrian, *Twenty Years of Particle Image Velocimetry*, in *Experiments in Fluids*, Vol. 39 (Springer, 2005), pp. 159–169.

[28] J. M. Chomaz and B. Cathalau, *Soap Films as Two-Dimensional Classical Fluids*, Phys. Rev. A **41**, 2243 (1990).

[29] J. M. Chomaz and M. Costa, *Thin Film Dynamics*, in *Free Surface Flows* (Springer Vienna, 1998), pp. 45–99.

[30] J. M. Chomaz, *The Dynamics of a Viscous Soap Film with Soluble Surfactant*, J. Fluid Mech. **442**, 387 (2001).

[31] P. Vorobieff, M. Rivera, and R. E. Ecke, *Imaging 2D Turbulence*, J. Vis. **3**, 323 (2001).

[32] M. S. Chong, A. E. Perry, and B. J. Cantwell, *A General Classification of Three-Dimensional Flow Fields*, Phys. Fluids A **2**, 765 (1990).

[33] T. S. Yang, C. Y. Wen, and C. Y. Lin, *Interpretation of Color Fringes in Flowing Soap Films*, Exp. Therm. Fluid Sci. **25**, 141 (2001).

[34] M. H. Wu, C. Y. Wen, R. H. Yen, M. C. Weng, and A. B. Wang, *Experimental and Numerical Study of the Separation Angle for Flow around a Circular Cylinder at Low Reynolds Number*, J. Fluid Mech. **515**, 233 (2004).

[35] E. C. Maskell, *A Theory of the Blockage Effects on, Bluff Bodies and Stalled Wings in a Closed Wind Tunnel*, Reports Memo. 1 (1963).

[36] G. S. West and C. J. Apelt, *The Effects of Tunnel Blockage and Aspect Ratio on the Mean Flow Past a Circular Cylinder with Reynolds Numbers between 104 and 105*, J. Fluid Mech. **114**, 361 (1982).

[37] I. Kim and S. Mandre, *Marangoni Elasticity of Flowing Soap Films*, Phys. Rev. Fluids **2**, 082001 (2017).

[38] N. Jaensson and J. Vermant, *Tensiometry and Rheology of Complex Interfaces*, Current Opinion in Colloid and Interface Science.

[39] P. Tchoukov, F. Yang, Z. Xu, T. Dabros, J. Czarnecki, and J. Sjöblom, *Role of Asphaltenes in Stabilizing Thin Liquid Emulsion Films*, Langmuir **30**, 3024 (2014).

[40] C.-Y. Wen and C.-Y. Lin, *Two-Dimensional Vortex Shedding of a Circular Cylinder*, Phys. Fluids **13**, 557 (2001).

[41] P. Roushan and X. L. Wu, *Structure-Based Interpretation of the Strouhal-Reynolds Number Relationship*, Phys. Rev. Lett. **94**, 54504 (2005).

[42] C. H. K. Williamson and G. L. Brown, *A Series in 1/√ Re to Represent the Strouhal--Reynolds Number Relationship of the Cylinder Wake*, J. Fluids Struct. **12**, 1073 (1998).

[43] V. K. Horváth, J. R. Cressman, W. I. Goldburg, and X. L. Wu, *Hysteresis at Low Reynolds Number: Onset of Two-Dimensional Vortex Shedding*, Phys. Rev. E **61**, R4702 (2000).

[44] Y. C. Hum, K. W. Lai, and M. I. Mohamad Salim, *Multiobjectives Bihistogram Equalization for Image Contrast Enhancement*, Complexity **20**, 22 (2014).

[45] T. Acharya and A. K. Ray, *Image Processing: Principles and Applications* (John Wiley & Sons, 2005).

[46] S. M. Soloff, R. J. Adrian, and Z.-C. Liu, Distortion Compensation for Generalized Stereoscopic Particle Image Velocimetry, 1997.

[47] B. Wieneke, *Stereo-PIV Using Self-Calibration on Particle Images*, Exp. Fluids **39**, 267 (2005).

[48] J. Illingworth and J. Kittler, *A Survey of the Hough Transform*, Comput. Vision, Graph. Image Process. **44**, 87 (1988).

[49] V. F. Leavers, *Which Hough Transform?*, CVGIP Image Underst. **58**, 250 (1993).

[50] H. K. Yuen, J. Princen, J. Illingworth, and J. Kittler, *Comparative Study of Hough Transform Methods for Circle Finding*, Image Vis. Comput. **8**, 71 (1990).

[51] C. Abiven and P. P. Vlachos, *Super Spatio-Temporal Resolution, Digital PIV System for Multi-Phase Flows with Phase Differentiation and Simultaneous Shape and Size Quantification*, in *2002 Proceedings of the ASME IMECE* (ASME, 2002), pp. 635–644.

[52] C. Abiven, P. P. Vlachos, and G. Papadopoulos, *DPIV Strategies for Resolving High Shear and Vortical Flows*, in *2002 Proceedings of the ASME IMECE* (ASME, n.d.).

[53] A. C. Eckstein, J. Charonko, and P. Vlachos, *Phase Correlation Processing for DPIV Measurements*, Exp. Fluids **45**, 485 (2008).

[54] A. Eckstein and P. P. Vlachos, *Assessment of Advanced Windowing Techniques for Digital Particle Image Velocimetry (DPIV)*, Meas. Sci. Technol. **20**, 75402 (2009).

[55] A. Eckstein and P. P. Vlachos, *Digital Particle Image Velocimetry (DPIV) Robust Phase Correlation*, Meas. Sci. Technol. **20**, 055401 (2009).

[56] J. Westerweel and F. Scarano, *Universal Outlier Detection for PIV Data*, Exp. Fluids **39**, 1096 (2005).

[57] S. Bhattacharya, J. J. Charonko, and P. P. Vlachos, *Particle Image Velocimetry (PIV) Uncertainty Quantification Using Moment of Correlation (MC) Plane*, Meas. Sci. Technol. **29**, 115301 (2018).

[58] M. C. Brindise and P. P. Vlachos, *Proper Orthogonal Decomposition Truncation Method for Data Denoising and Order Reduction*, Exp. Fluids **58**, 28 (2017).

[59] A. Etebari and P. P. Vlachos, *Improvements on the Accuracy of Derivative Estimation from DPIV Velocity Measurements*, Exp. Fluids **39**, 1040 (2005).

[60] J. Jeong and F. Hussain, *On the Identification of a Vortex*, J. Fluid Mech. **285**, 69 (1995).

[61] J. C. R. Hunt, *VORTICITY AND VORTEX DYNAMICS IN COMPLEX TURBULENT FLOWS.*, Trans. Can. Soc. Mech. Eng. **11**, 21 (1987).

[62] S. Bhattacharya, J. J. Charonko, and P. P. Vlachos, *Stereo-Particle Image Velocimetry Uncertainty Quantification*, Meas. Sci. Technol. **28**, 015301 (2017).

[63] L. Venkatakrishnan and G. E. A. Meier, *Density Measurements Using the Background Oriented Schlieren Technique*, Exp. Fluids **37**, 237 (2004).

[64] L. Rajendran, J. Zhang, S. Bane, and P. Vlachos, *Uncertainty-Based Weighted Least Squares Density Integration for Background-Oriented Schlieren*, Exp. Fluids **61**, 239 (2020).

[65] L. K. Rajendran, J. Zhang, S. Bhattacharya, S. P. M. Bane, and P. P. Vlachos, *Uncertainty Quantification in Density Estimation from Background-Oriented Schlieren Measurements*, Meas. Sci. Technol. **31**, 054002 (2020).

[66] X. Yonghong and J. Qiang, *A New Efficient Ellipse Detection Method*, in *Proceedings - International Conference on Pattern Recognition*, Vol. 16 (2002), pp. 957–960.

[67] C. A. Başca, M. Takş, and R. Brad, *Randomized Hough Transform for Ellipse Detection with Result Clustering*, in *EUROCON 2005 - The International Conference on Computer as a Tool*, Vol. II (IEEE Computer Society, 2005), pp. 1397–1400.

[68] X. L. Wu, R. Levine, M. Rutgers, H. Kellay, and W. I. Goldburg, *Infrared Technique for Measuring Thickness of a Flowing Soap Film*, Rev. Sci. Instrum. **72**, 2467 (2001).

[69] E. Berger, *The Determination of Hydrodynamic Parameters of a Karman Eddy Street from Hot-Wire Measurements at Low Reynolds Numbers*, Zeitschrift Fiir Flugwissenschaften **12**, 41 (1964).

[70] L. Rosenhead, *An Experimental Investigation of the Flow behind Circular Cylinders in Channels of Different Breadths*, Proc. R. Soc. London. Ser. A, Contain. Pap. a Math. Phys. Character **129**, 115 (1930).

[71] D. W. Sallet, *On the Spacing of Karman Vortices*, (1969).

[72] J. W. Schaefer and S. Eskinazi, *An Analysis of the Vortex Street Generated in a Viscous Fluid*, J. Fluid Mech. **6**, 241 (1959).

[73] A. Timme, *On the Velocity Distribution in Eddies*, Fundamentals **25**, 205 (1957).

[74] E. T. S. Walton, *The Formation of Vortices Behind a Cylinder Moving Through a Fluid*, in *Scientific Proceedings of the Royal Dublin Society*, Vol. 18 (1928), pp. 521–534.

[75] T. Matsui and M. Okude, *Rearrangement of Kármán Vortex Street at Low Reynolds Numbers*, in *XVth International Congress of Theoretical and Applied Mechanics, University of Toronto, August* (1980), pp. 1–27.

[76] M. M. Zdravkovich, *Flow around Circular Cylinders*, Fundamentals **1**, 566 (1997).

[77] T. Von Kármán, *On the Mechanism of Resistance Produced by Moving Body in Liquid*, Nachrichtungen Des Gesellschaft Wiss. **19**, (1912).

[78] O. M. Griffin, *A Note on Bluff Body Vortex Formation*, J. Fluid Mech. **284**, 217 (1995).

[79] O. M. Griffin, *The Unsteady Wake of an Oscillating Cylinder at Low Reynolds Number*, J. Appl. Mech. Trans. ASME **38**, 729 (1971).

[80] O. M. Griffin and S. E. Ramberg, *The Vortex-Street Wakes of Vibrating Cylinders*, J. Fluid Mech. **66**, 553 (1974).

[81] O. M. Griffin and C. W. Votaw, *The Vortex Street in the Wake of a Vibrating Cylinder*, J. Fluid Mech. **55**, 31 (1972).

[82] L. S. G. Kovasznay, *Hot-Wire Investigation of the Wake behind Cylinders at Low Reynolds Numbers*, Proc. R. Soc. London. Ser. A. Math. Phys. Sci. **198**, 174 (1949).

[83] M. Nishioka and H. Sato, *Mechanism of Determination of the Shedding Frequency of Vortices behind a Cylinder at Low Reynolds Numbers*, J. Fluid Mech. **89**, 49 (1978).

[84] R. B. Green and J. H. Gerrard, *Vorticity Measurements in the near Wake of a Circular Cylinder at Low Reynolds Numbers*, J. Fluid Mech. **246**, 675 (1993).

[85] Y. N. Chen, *Fluctuating Lift Forces of the Karman Vortex Streets on Single Circular Cylinders and in Tube Bundles: Part 1—the Vertex Street Geometry of the Single Circular Cylinder*, J. Manuf. Sci. Eng. Trans. ASME **94**, 603 (1972).

[86] A. Thom, *The Flow Past Circular Cylinders at Low Speeds*, Proc. R. Soc. A Math. Phys. Eng. Sci. **141**, 651 (1933).

[87] R. Bergmann, D. Van Der Meer, M. Stijnman, M. Sandtke, A. Prosperetti, and D. Lohse, *Giant Bubble Pinch-Off*, Phys. Rev. Lett. **96**, 154505 (2006).

[88] V. Duclaux, F. Caillé, C. Duez, C. Ybert, L. Bocquet, and C. Clanet, *Dynamics of Transient Cavities*, J. Fluid Mech. **591**, 1 (2007).

[89] S. Gekle, J. M. Gordillo, D. der Meer, and D. Lohse, *High-Speed Jet Formation after Solid Object Impact*, Phys. Rev. Lett. **102**, 34502 (2009).

[90] S. Gekle, J. H. Snoeijer, D. Lohse, and D. der Meer, *Approach to Universality in Axisymmetric Bubble Pinch-Off*, Phys. Rev. E **80**, 36305 (2009).

[91] J.-F. Louf, B. Chang, J. Eshraghi, A. Mituniewicz, P. P. Vlachos, and S. Jung, *Cavity Ripple Dynamics after Pinch-Off*, J. Fluid Mech. **850**, 611 (2018).

[92] T. T. Truscott, B. P. Epps, and A. H. Techet, *Unsteady Forces on Spheres during Free Surface Water Entry*, J. Fluid Mech. **704**, 173 (2012).

[93] T. T. Truscott and A. H. Techet, *Water Entry of Spinning Spheres*, J. Fluid Mech. **625**, 135 (2009).

[94] J. M. Aristoff, T. T. Truscott, A. H. Techet, and J. W. M. Bush, *The Water Entry of Decelerating Spheres*, Phys. Fluids **22**, (2010).

[95] A. M. Worthington, *A Study of Splashes* (Longmans, Green, and Company, 1908).

[96] D. Gilbarg and R. A. Anderson, *Influence of Atmospheric Pressure on the Phenomena Accompanying the Entry of Spheres into Water*, J. Appl. Phys. **19**, 127 (1948).

[97] Y. L. Yakimov, *Effect of the Atmosphere with the Fall of Bodies into Water*, Fluid Dyn. **8**, 679 (1973).

[98] H. I. Abelson, *Pressure Measurements in the Water-Entry Cavity*, J. Fluid Mech. **44**, 129 (1970).

[99] M. Lee, R. G. Longoria, and D. E. WIlson, *Cavity Dynamics in High-Speed Water Entry*, Phys. Fluids **9**, (1997).

[100] J. O. Marston, T. T. Truscott, N. B. Speirs, M. M. Mansoor, and S. T. Thoroddsen, *Crown Sealing and Buckling Instability during Water Entry of Spheres*, J. Fluid Mech. **794**, 506 (2016).

[101] J. M. Aristoff and J. W. M. Bush, *Water Entry of Small Hydrophobic Spheres*, J. Fluid Mech. **619**, (2009).

[102] A. May, *Effect of Surface Condition of a Sphere on Its Water-Entry Cavity*, J. Appl. Phys. **22**, 1219 (1951).

[103] E. G. Richardson, *The Impact of a Solid on a Liquid Surface*, Proc. Phys. Soc. **61**, 352 (1948).

[104] G. Birkhoff and E. H. Zarantonello, *Jets, Wakesand Cavities*.

[105] *See Supplemental Material at Movie S1(a) for a Video of Splash Curtain Evolution*, (n.d.).

[106] *See Supplemental Material at Movie S1(b) for a Video of Cavity Evolution*, (n.d.).

[107] G. Birkhoff and R. Isaacs, *Transient Cavities in Air--Water Entry*, Navord Rep. **1490**, (1951).

[108] M. M. Mansoor, J. O. Marston, I. U. Vakarelski, and S. T. Thoroddsen, *Water Entry without Surface Seal: Extended Cavity Formation*, J. Fluid Mech. **743**, 295 (2014).

[109] A. May, *Vertical Entry of Missiles into Water*, J. Appl. Phys. **23**, 1362 (1952).

[110] J. W. Glasheen and T. A. McMahon, *Vertical Water Entry of Disks at Low Froude Numbers*, Phys. Fluids **8**, (1996).

[111] *See Supplemental Material at Fig. S1 for Cavity Characteristics Plots*, (n.d.).

[112] A. L. Yarin, *Drop Impact Dynamics: Splashing, Spreading, Receding, Bouncing…*, Annu. Rev. Fluid Mech. **38**, 159 (2006).

[113] R. Clift, J. R. Grace, and M. E. Weber, *Bubbles, Drops, and Particles* (Courier Corporation, 2005).

[114] S. Gart, B. Chang, B. Slama, R. Goodnight, S. H. Um, and S. Jung, *Dynamics of Squeezing Fluids: Clapping Wet Hands*, Phys. Rev. E **88**, 23007 (2013).

[115] L. Vincent, T. Xiao, D. Yohann, S. Jung, and E. Kanso, *Dynamics of Water Entry*, J. Fluid Mech. **846**, 508 (2018).

[116] W. S. Cleveland, *Robust Locally Weighted Regression and Smoothing Scatterplots*, J. Am. Stat. Assoc. **74**, 829 (1979).

[117] A. Etebari and P. P. Vlachos, *Improvements on the Accuracy of Derivative Estimation from DPIV Velocity Measurements*, Exp. Fluids **39**, 1040 (2005).

[118] *See Supplemental Material at Movie S2 for Splash Curtain Rounded Rim Trajectory: Experimental Observation vs. Model Prediction*, (n.d.).

[119] *See Supplemental Material at Fig. S2 for the Effects of Sphere Density and Impact Velocity on the Rim Trajectory*, (n.d.).

[120] *See Supplemental Material at Movie S3 for We Scaling Failure to Identify a Critical We for Transition from No Surface Seal Regime to Surface Seal Regime for All the Spheres with Different Density and Size*, (n.d.).

[121] *See Supplemental Material at Movie S4 for Splash Curtain Imaging*, (n.d.).

[122] D. Kröninger, K. Köhler, T. Kurz, and W. Lauterborn, *Particle Tracking Velocimetry of the Flow Field around a Collapsing Cavitation Bubble*, Exp. Fluids **48**, 395 (2010).

[123] H. Lee, A. B. Gojani, T. H. Han, and J. J. Yoh, *Dynamics of Laser-Induced Bubble Collapse Visualized by Time-Resolved Optical Shadowgraph*, J. Vis. **14**, 331 (2011).

[124] G. Sinibaldi, A. Occhicone, F. Alves Pereira, D. Caprini, L. Marino, F. Michelotti, and C. M. Casciola, *Laser Induced Cavitation: Plasma Generation and Breakdown Shockwave*, Phys. Fluids **31**, 103302 (2019).

[125] G. N. Sankin, W. N. Simmons, S. L. Zhu, and P. Zhong, *Shock Wave Interaction with Laser-Generated Single Bubbles*, Phys. Rev. Lett. **95**, (2005).

[126] I. Akhatov, O. Lindau, A. Topolnikov, R. Mettin, N. Vakhitova, and W. Lauterborn, *Collapse and Rebound of a Laser-Induced Cavitation Bubble*, Phys. Fluids **13**, 2805 (2001).

[127] W. Lauterborn and R. Mettin, *Acoustic Cavitation: Bubble Dynamics in High-Power Ultrasonic Fields*, in *Power Ultrasonics* (Elsevier, 2015), pp. 37–78.

[128] Lord Rayleigh, *On the Pressure Developed in a Liquid during the Collapse of a Spherical Cavity*, Philos. Mag. **34**, 94 (1917).

[129] M. S. Plesset, *The Dynamics of Cavitation Bubbles*, J. Appl. Mech. **16**, 277 (1949).

[130] M. S. Plesset and A. Prosperetti, *Bubble Dynamics and Cavitation*, Annu. Rev. Fluid Mech. **9**, 145 (1977).

[131] W. Lauterborn and C.-D. Ohl, *Cavitation Bubble Dynamics*, Ultrason. Sonochem. **4**, 65 (1997).

[132] J. B. Keller and M. Miksis, *Bubble Oscillations of Large Amplitude*, J. Acoust. Soc. Am. **68**, 628 (1980).

[133] F. R. Gilmore, *The Growth or Collapse of a Spherical Bubble in a Viscous Compressible Liquid*, Calif. Inst. Technol. Hydrodyn. Lab. Rep. No. 26 **4**, (1952).

[134] S. Fujikawa and T. Akamatsu, *Effects of the Non-Equilibrium Condensation of Vapour on the Pressure Wave Produced by the Collapse of a Bubble in a Liquid*, J. Fluid Mech. **97**, 481 (1980).

[135] K. Yasui, *Variation of Liquid Temperature at Bubble Wall near the Sonoluminescence Threshold*, J. Phys. Soc. Japan **65**, 2830 (1996).

[136] X. Zhong, J. Eshraghi, P. Vlachos, S. Dabiri, and A. M. Ardekani, *A Model for a Laser-Induced Cavitation Bubble*, Int. J. Multiph. Flow 103433 (2020).

[137] A. Prosperetti and A. Lezzi, *Bubble Dynamics in a Compressible Liquid. Part 1. First-Order Theory*, J. Fluid Mech. **168**, 457 (1986).

[138] A. Prosperetti, *Bubble Dynamics: A Review and Some Recent Results*, Applied Scientific Research.

[139] A. Prosperetti, *Vapor Bubbles*, Annu. Rev. Fluid Mech. **49**, 221 (2017).

[140] K. Yasui, *Acoustic Cavitation and Bubble Dynamics*, 1st Ed (Springer, 2018).

[141] K. Yasui, *Effect of Liquid Temperature on Sonoluminescence*, Phys. Rev. E - Stat. Physics, Plasmas, Fluids, Relat. Interdiscip. Top. **64**, 10 (2001).

[142] T. Alty and C. A. M. Ackay, *The Accommodation Coefficient and the Evaporation Coefficient of Water*, Proc. R. Soc. London. Ser. A - Math. Phys. Sci. **149**, 104 (1935).

[143] D. G. Luenberger, *Observing the State of a Linear System*, IEEE Trans. Mil. Electron. **8**, 74 (1964).

[144] R. E. Skelton, *Dynamic Systems Control: Linear Systems Analysis and Synthesis* (John Wiley & Sons, Inc., 1988).

[145] E. A. Misawa and J. K. Hedrick, *Nonlinear Observers—a State-of-the-Art Survey*, J. Dyn. Syst. Meas. Control **111**, 344 (1989).

[146] N. J. Neeteson and D. E. Rival, *State Observer-Based Data Assimilation: A PID Control-Inspired Observer in the Pressure Equation*, Meas. Sci. Technol. **31**, 14003 (2019).

[147] T. Hayase, *Numerical Simulation of Real-World Flows*, Fluid Dyn. Res. **47**, 51201 (2015).

[148] T. Misaka, S. Obayashi, and E. Endo, *Measurement-Integrated Simulation of Clear Air Turbulence Using a Four-Dimensional Variational Method*, J. Aircr. **45**, 1217 (2008).

[149] Y. Ishikawa, T. Awaji, K. Akitomo, and B. Qiu, *Successive Correction of the Mean Sea Surface Height by the Simultaneous Assimilation of Drifting Buoy and Altimetric Data*, J. Phys. Oceanogr. **26**, 2381 (1996).

[150] T. Hayase and S. Hayashi, *State Estimator of Flow as an Integrated Computational Method with the Feedback of Online Experimental Measurement*, J. Fluids Eng. **119**, 814 (1997).

[151] O. O. Badmus, S. Chowdhury, and C. N. Nett, *Nonlinear Control of Surge in Axial Compression Systems*, Automatica **32**, 59 (1996).

[152] C.-H. Yau, A. K. Bajaj, and O. D. I. Nwokah, *Active Control of Chaotic Vibration in a Constrained Flexible Pipe Conveying Fluid*, J. Fluids Struct. **9**, 99 (1995).

[153] K. Imagawa and T. Hayase, *Numerical Experiment of Measurement-Integrated Simulation to Reproduce Turbulent Flows with Feedback Loop to Dynamically Compensate the Solution Using Real Flow Information*, Comput. Fluids **39**, 1439 (2010).

[154] C. C. Hang, K. J. Åström, and W. K. Ho, *Refinements of the Ziegler--Nichols Tuning Formula*, IEE Proc. D - Control Theory Appl. **138**, 111 (1991).

[155] J. G. Ziegler and N. B. Nichols, *Optimum Settings for Automatic Controllers*, J. Dyn. Syst. Meas. Control **115**, (1993).

[156] L. F. Shampine and M. W. Reichelt, *The MATLAB Ode Suite*, SIAM J. Sci. Comput. **18**, 1 (1997).

[157] J. R. Dormand and P. J. Prince, *A Family of Embedded Runge-Kutta Formulae*, J. Comput. Appl. Math. **6**, 19 (1980).

[158] J. H. Song, K. Johansen, and P. Prentice, *An Analysis of the Acoustic Cavitation Noise Spectrum: The Role of Periodic Shock Waves*, J. Acoust. Soc. Am. **140**, 2494 (2016).

[159] P. Knysh and Y. Korkolis, *Blackbox: A Procedure for Parallel Optimization of Expensive Black-Box Functions*, (2016).

[160] R. G. Regis and C. A. Shoemaker, *Constrained Global Optimization of Expensive Black Box Functions Using Radial Basis Functions*, J. Glob. Optim. **31**, 153 (2005).

[161] T. B. Benjamin and F. J. Ursell, *The Stability of the Plane Free Surface of a Liquid in Vertical Periodic Motion*, Proc. R. Soc. London. Ser. A. Math. Phys. Sci. **225**, 505 (1954).

[162] B. Dollet, S. M. van der Meer, V. Garbin, N. de Jong, D. Lohse, and M. Versluis, *Nonspherical Oscillations of Ultrasound Contrast Agent Microbubbles*, Ultrasound Med. Biol. **34**, 1465 (2008).

[163] V. Poulichet and V. Garbin, *Ultrafast Desorption of Colloidal Particles from Fluid Interfaces*, Proc. Natl. Acad. Sci. U. S. A. **112**, 5932 (2015).

[164] V. Poulichet, A. Huerre, and V. Garbin, *Shape Oscillations of Particle-Coated Bubbles and Directional Particle Expulsion*, Soft Matter **13**, 125 (2017).

[165] J. E. Chômas, P. Dayton, J. Alien, K. Morgan, and K. W. Ferrara, *Mechanisms of Contrast Agent Destruction*, IEEE Trans. Ultrason. Ferroelectr. Freq. Control **48**, 232 (2001).

[166] M. Postema, A. Van Wamel, C. T. Lancée, and N. De Jong, *Ultrasound-Induced Encapsulated Microbubble Phenomena*, Ultrasound Med. Biol. **30**, 827 (2004).

[167] P. Tho, R. Manasseh, and A. Ioo, *Cavitation Microstreaming Patterns in Single and Multiple Bubble Systems*, J. Fluid Mech. **576**, 191 (2007).

[168] D. Ahmed, X. Mao, B. K. Juluri, and T. J. Huang, *A Fast Microfluidic Mixer Based on Acoustically Driven Sidewall-Trapped Microbubbles*, Microfluid. Nanofluidics **7**, 727 (2009).

[169] P. Marmottant, T. Biben, and S. Hilgenfeldt, *Deformation and Rupture of Lipid Vesicles in the Strong Shear Flow Generated by Ultrasound-Driven Microbubbles*, Proc. R. Soc. A Math. Phys. Eng. Sci. **464**, 1781 (2008).

[170] M. S. Plesset and A. Prosperetti, *Bubble Dynamics and Cavitation*, Ann. Rev. Fluid Mech **9**, 145 (1977).

[171] Z. C. Feng and L. G. Leal, *Nonlinear Bubble Dynamics*, Annu. Rev. Fluid Mech. **29**, 201 (1997).

[172] Z. C. Feng and L. G. Leal, *Bifürcation and Chaos in Shape and Volume Oscillations of a Periodically Driven Bubble with Two-to-One Internal Resonance*, J. Fluid Mech. **266**, 209 (1994).

[173] A. O. Maksimov and T. G. Leighton, *Pattern Formation on the Surface of a Bubble Driven by an Acoustic Field*, in *Proceedings of the Royal Society A: Mathematical, Physical and Engineering Sciences*, Vol. 468 (2012), pp. 57–75.

[174] I. Ueno, K. Matsumoto, A. Machida, and T. Hanyu, *Shape Oscillation of Bubble(S) in Acoustic Field*, in *14th International Heat Transfer Conference, IHTC 14*, Vol. 3 (2010), pp. 923–927.

[175] Supplementary Information, *See Supplemental Material in Figure S1 for Representative Images of Cavitation Bubble Dynamics*, (2022).

[176] T. G. Leighton, *From Seas to Surgeries, from Babbling Brooks to Baby Scans: The Acoustics of Gas Bubbles in Liquids*, Int. J. Mod. Phys. B **18**, 3267 (2004).

[177] T. G. Leighton, *The Acoustic Bubble* (Elsevier, 1994).

[178] M. S. Longuet-Higgins, *Nonlinear Damping Of Bubble Oscillations By Resonant Interaction*, J. Acoust. Soc. Am. **91**, 1414 (1992).

[179] M. S. Longuet-Higgins, *Monopole Emission of Sound by Asymmetric Bubble Oscillations. Part 1. Normal Modes*, J. Fluid Mech. **201**, 525 (1989).

[180] M. S. Longuet-higgins, *Monopole Emission of Sound by Asymmetric Bubble Oscillations. Part 2. An Initial-Value Problem*, J. Fluid Mech. **201**, 543 (1989).

[181] E. H. Trinh, D. B. Thiessen, and R. G. Holt, *Driven and Freely Decaying Nonlinear Shape Oscillations of Drops and Bubbles Immersed in a Liquid: Experimental Results*, J. Fluid Mech. **364**, 253 (1998).

[182] T. J. Asaki, P. L. Marston, and E. H. Trinh, *Shape Oscillations of Bubbles in Water Driven by Modulated Ultrasonic Radiation Pressure: Observations and Detection with Scattered Laser Light*, J. Acoust. Soc. Am. **93**, 706 (1993).

[183] C. C. Mei and X. Zhou, *Parametric Resonance of a Spherical Bubble*, J. Fluid Mech. **229**, 29 (1991).

[184] Supplementary Information, *See Supplemental Material in Figure S2 for Representative Images of the Air Bubble Oscillations at Different Oscillation Regimes*, (2022).

[185] Supplementary Information, *See Supplemental Material in Movie S1 for Effects of Air Bubble Size and Relative Distance between an Air Bubble and Cavitation Bubble on Air Bubble Oscillations in a Cavitation-Induced Acoustic Field*, (2022).

[186] M. J. Sathe, I. H. Thaker, T. E. Strand, and J. B. Joshi, *Advanced PIV/LIF and Shadowgraphy System to Visualize Flow Structure in Two-Phase Bubbly Flows*, Chem. Eng. Sci. **65**, 2431 (2010).

[187] Y. Tian, H. Qian, and Q. H. Ke, *A Bubble Detection Algorithm Based on Wavelet Transform and Canny Operator for Deinked Pulp Flotation Column*, Appl. Mech. Mater. **278**–**280**, 1162 (2013).

[188] S. G. Mallat, *A Theory for Multiresolution Signal Decomposition: The Wavelet Representation*, IEEE Trans. Pattern Anal. Mach. Intell. **11**, 674 (1989).

[189] Supplementary Information, *See Supplemental Material in Figure S3 for the Methodology Framework to Analyze Air Bubble Dynamics at Volume Oscillation, Single-Mode Shape Oscillation, and Multi-Mode Shape Oscillation Regimes*, (2022).

[190] Supplementary Information, *See Supplemental Material in Figure S5 for Effects of Induced Energy and Air Bubble-Cavitation Distance on the Dominant Frequency of Air Bubble Size Oscillations, Dominant Wave Number of Air Bubble Boundary, and the Air Bubble Oscillation Mode Map*, (2022).

[191] J. Eshraghi, A. M. Ardekani, and P. P. Vlachos, *Data Assimilation for Modeling Cavitation Bubble Dynamics*, Exp. Fluids **62**, 90 (2021).

[192] X. Zhong, J. Eshraghi, P. Vlachos, S. Dabiri, and A. M. Ardekani, *A Model for a Laser-Induced Cavitation Bubble*, Int. J. Multiph. Flow **132**, 103433 (2020).

[193] Supplementary Information, *See Supplemental Material in Figure S4 for a Detailed Analysis of Cavitation Bubble Dynamics*, (2022).

[194] M. S. Plesset, *The Dynamics of Cavitation Bubbles*, J. Appl. Mech. **16**, 277 (1949).

[195] R. Mathaes, A. Koulov, S. Joerg, and H. C. Mahler, *Subcutaneous Injection Volume of Biopharmaceuticals—Pushing the Boundaries*, J. Pharm. Sci. **105**, 2255 (2016).

[196] Market Analysis Report: Auto-Injectors Market Size, Share, & Trends Analysis, 2019-2026, 2019.

[197] M. X. Yang, B. Shenoy, M. Disttler, R. Patel, M. McGrath, S. Pechenov, and A. L. Margolin, *Crystalline Monoclonal Antibodies for Subcutaneous Delivery*, Proc. Natl. Acad. Sci. U. S. A. **100**, 6934 (2003).

[198] X. Zhong, T. Guo, P. Vlachos, J. C. Veilleux, G. H. Shi, D. S. Collins, and A. M. Ardekani, *An Experimentally Validated Dynamic Model for Spring-Driven Autoinjectors*, Int. J. Pharm. **594**, 120008 (2021).

[199] Y. Zhang, D. Han, Z. Dou, J. C. Veilleux, G. H. Shi, D. S. Collins, P. P. Vlachos, and A. M. Ardekani, *The Interface Motion and Hydrodynamic Shear of the Liquid Slosh in Syringes*, Pharm. Res. **38**, 257 (2021).

[200] J. C. Veilleux and J. E. Shepherd, *Impulsive Motion in a Cylindrical Fluid-Filled Tube Terminated by a Converging Section*, J. Press. Vessel Technol. Trans. ASME **141**, (2019).

[201] J. C. Veilleux and J. E. Shepherd, *Pressure and Stress Transients in Autoinjector Devices*, Drug Deliv. Transl. Res. **8**, 1238 (2018).

[202] Y. Zhang, Z. Dou, J. C. Veilleux, G. H. Shi, D. S. Collins, P. P. Vlachos, S. Dabiri, and A. M. Ardekani, *Modeling Cavitation Bubble Dynamics in an Autoinjector and Its Implications on Drug Molecules*, Int. J. Pharm. **608**, 121062 (2021).

[203] M. H. Chaudhry, *Applied Hydraulic Transients*, 3rd Ed. (Springer, New York, NY, 2014).

[204] A. Braun, L. Kwee, M. A. Labow, and J. Alsenz, *Protein Aggregates Seem to Play a Key Role among the Parameters Influencing the Antigenicity of Interferon Alpha (IFN-α) in Normal and Transgenic Mice*, Pharm. Res. **14**, 1472 (1997).

[205] E. M. Moussa, J. P. Panchal, B. S. Moorthy, J. S. Blum, M. K. Joubert, L. O. Narhi, and E. M. Topp, *Immunogenicity of Therapeutic Protein Aggregates*, J. Pharm. Sci. **105**, 417 (2016).

[206] A. S. Rosenberg, *Effects of Protein Aggregates: An Immunologic Perspective*, AAPS J. **8**, E501 (2006).

[207] P. C. Frei, B. Benacerraf, and G. J. Thorbecke, *Phagocytosis of the Antigen, A Crucial Step in the Induction of the Primary Response*, Proc. Natl. Acad. Sci. U. S. A. **53**, 20 (1965).

[208] J. Eshraghi, A. M. Ardekani, and P. P. Vlachos, *Data Assimilation for Modeling Cavitation Bubble Dynamics*, Exp. Fluids **62**, 90 (2021).

[209] A. Savitzky and M. J. E. Golay, *Smoothing and Differentiation of Data by Simplified Least Squares Procedures.*, Anal. Chem. **36**, 1627 (2002).

[210] B. Debbaut and M. J. Crochet, *Extensional Effects in Complex Flows*, J. Nonnewton. Fluid Mech. **30**, 169 (1988).

[211] K. Yasui, *Alternative Model of Single-Bubble Sonoluminescence*, Phys. Rev. E - Stat. Physics, Plasmas, Fluids, Relat. Interdiscip. Top. **56**, 6750 (1997).

[212] A. M. Zhong, Xiaoxu; Eshraghi, Javad; Vlachos, Pavlos P.; Dabiri, Sadegh; Ardekani, *A Model for a Laser-Induced Cavitation Bubble*, in *11th International Symposium on Cavitation* (Daejeon, Korea, 2021).

[213] B. Srinivasa Reddy and B. N. Chatterji, *An FFT-Based Technique for Translation, Rotation, and Scale-Invariant Image Registration*, IEEE Trans. Image Process. **5**, 1266 (1996).

[214] G. K. Batchelor, *An Introduction to Fluid Dynamics* (Cambridge University Press, 1967).

[215] M. J. Cooker and D. H. Peregrine, *Pressure-Impulse Theory for Liquid Impact Problems*, J. Fluid Mech. **297**, 193 (1995).

[216] R. Krechetnikov, *Flow around a Corner in the Water Impact Problem*, Phys. Fluids **26**, 72107 (2014).

[217] A. Antkowiak, N. Bremond, S. Le Dizès, and E. Villermaux, *Short-Term Dynamics of a Density Interface Following an Impact*, J. Fluid Mech. **577**, 241 (2007).

[218] Z. Pan, A. Kiyama, Y. Tagawa, D. J. Daily, S. L. Thomson, R. Hurd, and T. T. Truscott, *Cavitation Onset Caused by Acceleration*, Proc. Natl. Acad. Sci. U. S. A. **114**, 8470 (2017).

[219] C. Vaclaw, K. Merritt, V. Pringle, N. Whitaker, M. Gokhale, T. Carvalho, D. Pan, Z. Liu, D. Bindra, M. Khossravi, M. Bolgar, D. B. Volkin, M. O. Ogunyankin, and P. Dhar, *Impact of Polysorbate 80 Grade on the Interfacial Properties and Interfacial Stress Induced Subvisible Particle Formation in Monoclonal Antibodies*, J. Pharm. Sci. **110**, 746 (2021).

[220] M. Rodríguez-Hakim, S. Anand, J. Tajuelo, Z. Yao, A. Kannan, and G. G. Fuller, *Asphaltene-Induced Spontaneous Emulsification: Effects of Interfacial Co-Adsorption and Viscoelasticity*, J. Rheol. (N. Y. N. Y). **64**, 799 (2020).

[221] P. Hollowell, Z. Li, X. Hu, S. Ruane, C. Kalonia, C. F. van der Walle, and J. R. Lu, *Recent Advances in Studying Interfacial Adsorption of Bioengineered Monoclonal Antibodies*, Molecules **25**, 2047 (2020).

[222] V. Chandran Suja, A. Kar, W. Cates, S. M. Remmert, and G. G. Fuller, *Foam Stability in Filtered Lubricants Containing Antifoams*, J. Colloid Interface Sci. **567**, 1 (2020).

[223] E. Chatzigiannakis and J. Vermant, *Breakup of Thin Liquid Films: From Stochastic to Deterministic*, Phys. Rev. Lett. **125**, 158001 (2020).

[224] J. S. Bee, J. L. Stevenson, B. Mehta, J. Svitel, J. Pollastrini, R. Platz, E. Freund, J. F. Carpenter, and T. W. Randolph, *Response of a Concentrated Monoclonal Antibody Formulation to High Shear*, Biotechnol. Bioeng. **103**, 936 (2009).

[225] Y. Zhang, Z. Dou, J. C. Veilleux, G. H. Shi, D. S. Collins, P. P. Vlachos, S. Dabiri, and A. M. Ardekani, *Modeling Cavitation Bubble Dynamics in an Autoinjector and Its Implications on Drug Molecules*, Int. J. Pharm. **608**, 121062 (2021).

[226] A. Nayak, J. Colandene, V. Bradford, and M. Perkins, *Characterization of Subvisible Particle Formation during the Filling Pump Operation of a Monoclonal Antibody Solution*, J. Pharm. Sci. **100**, 4198 (2011).

[227] M. Duerkop, E. Berger, A. Dürauer, and A. Jungbauer, *Impact of Cavitation, High Shear Stress and Air/Liquid Interfaces on Protein Aggregation*, Biotechnol. J. **13**, 1800062 (2018).

[228] J. Jaspe and S. J. Hagen, *Do Protein Molecules Unfold in a Simple Shear Flow?*, Biophys. J. **91**, 3415 (2006).

[229] Y. F. Maa and C. Hsu, *Liquid-Liquid Emulsification by Rotor/Stator Homogenization*, J. Control. Release **38**, 219 (1996).

[230] J. S. Bee, J. L. Stevenson, B. Mehta, J. Svitel, J. Pollastrini, R. Platz, E. Freund, J. F. Carpenter, and T. W. Randolph, *Response of a Concentrated Monoclonal Antibody Formulation to High Shear*, Biotechnol. Bioeng. **103**, 936 (2009).

[231] J. Dobson, A. Kumar, L. F. Willis, R. Tuma, D. R. Higazi, R. Turner, D. C. Lowe, A. E. Ashcroft, S. E. Radford, N. Kapur, and D. J. Brockwell, *Inducing Protein Aggregation by Extensional Flow*, Proc. Natl. Acad. Sci. U. S. A. **114**, 4673 (2017).

[232] M. J. Akers, *Sterile Drug Products: Formulation, Packaging, Manufacturing and Quality*, 1st ed. (CRC Press, 2016).

[233] M. Adler, *Challenges in the Development of Pre-Filled Syringes for Biologics from a Formulation Scientist's Point of View*, Am. Pharm. Rev. (2012).

[234] S. J. Shire, Z. Shahrokh, and J. Liu, *Challenges in the Development of High Protein Concentration Formulations*, J. Pharm. Sci. **93**, 1390 (2004).

[235] D. L. French and J. J. Collins, *Advances in Parenteral Injection Devices and Aids*, in *Pharmaceutical Dosage Forms - Parenteral Medications*, edited by S. Nema and J. Ludwig, 3rd ed., Vol. 3 (CRC Press, New York, 2010), pp. 71–85.

[236] I. Thompson, *Self-Injection Technology and Trends*, J. Innov. Pharm. Technol. **20**, 60 (2006).

[237] I. Thompson and J. Lange, *Pen and Autoinjector Drug Delivery Devices*, in *Sterile Product Development: Formulation, Process, Quality and Regulatory Considerations*, edited by P. Kolhe, M. Shah, and N. Rathore (Springer, New York, 2013), pp. 331–356.

[238] J. C. Veilleux and J. E. Shepherd, *Pressure and Stress Transients in Autoinjector Devices*, Drug Deliv. Transl. Res. **8**, 1238 (2018).

[239] A. Fry, *Injecting Highly Viscous Drugs*, Pharm. Technol. **38**, (2014).

[240] D. Stout and V. Vilivalam, *Plastic Prefilled Syringes: A Better Fit for Autoinjector Systems*, Pharm. Technol. **2009**, (2009).

[241] Z. Dou, J. Eshraghi, T. Guo, J. C. Veilleux, K. H. Duffy, G. H. Shi, D. S. Collins, A. M. Ardekani, and P. P. Vlachos, *Performance Characterization of Spring Actuated Autoinjector Devices for Emgality and Aimovig*, Curr. Med. Res. Opin. **36**, 1343 (2020).

[242] Franc J and Michel J., *Fundamentals of Cavitation*, 1st ed. (Springer, Dordrecht, 2006).

[243] C. Brennen, *Cavitation and Bubble Dynamics* (Cambridge University Press, Cambridge, 2013).

[244] J. Eshraghi, J.-C. Veilleux, G. Shi, D. Collins, A. M. Ardekani, and P. P. Vlachos, *Assessment of Cavitation Intensity in Spring-Driven Autoinjectors*, Pharm. Res. (2022).

[245] A. S. Rosenberg, *Effects of Protein Aggregates: An Immunologic Perspective*, AAPS J. **8**, E501 (2006).

[246] P. C. Frei, B. Benacerraf, and G. J. Thorbecke, *Phagocytosis of the Antigen, A Crucial Step in the Induction of the Primary Response*, Proc. Natl. Acad. Sci. U. S. A. **53**, 20 (1965).

[247] E. M. Moussa, J. P. Panchal, B. S. Moorthy, J. S. Blum, M. K. Joubert, L. O. Narhi, and E. M. Topp, *Immunogenicity of Therapeutic Protein Aggregates*, J. Pharm. Sci. **105**, 417 (2016).

[248] A. Braun, L. Kwee, M. A. Labow, and J. Alsenz, *Protein Aggregates Seem to Play a Key Role among the Parameters Influencing the Antigenicity of Interferon Alpha (IFN-Alpha) in Normal and Transgenic Mice*, Pharm. Res. **14**, 1472 (1997).

[249] Y. Zhang, D. Han, Z. Dou, J. C. Veilleux, G. H. Shi, D. S. Collins, P. P. Vlachos, and A. M. Ardekani, *The Interface Motion and Hydrodynamic Shear of the Liquid Slosh in Syringes*, Pharm. Res. **38**, 257 (2021).

[250] H. C. Mahler, R. Müller, W. Frieß, A. Delille, and S. Matheus, *Induction and Analysis of Aggregates in a Liquid IgG1-Antibody Formulation*, Eur. J. Pharm. Biopharm. **59**, 407 (2005).

[251] C. R. Thomas and D. Geer, *Effects of Shear on Proteins in Solution*, Biotechnol. Lett. **33**, 443 (2011).

[252] J. S. Bee, J. L. Stevenson, B. Mehta, J. Svitel, J. Pollastrini, R. Platz, E. Freund, J. F. Carpenter, and T. W. Randolph, *Response of a Concentrated Monoclonal Antibody Formulation to High Shear*, Biotechnol. Bioeng. **103**, 936 (2009).

[253] I. B. Bekard, P. Asimakis, J. Bertolini, and D. E. Dunstan, *The Effects of Shear Flow on Protein Structure and Function*, Biopolymers **95**, 733 (2011).

[254] R. J. Adrian, *Twenty Years of Particle Image Velocimetry*, Exp. Fluids **39**, 159 (2005).

[255] R. J. Adrian, *Particle-Imaging Techniques for Experimental Fluid Mechanics*, Annu. Rev. Fluid Mech. **23**, 261 (1991).

[256] X. Zhong, T. Guo, P. Vlachos, J. C. Veilleux, G. H. Shi, D. S. Collins, and A. M. Ardekani, *An Experimentally Validated Dynamic Model for Spring-Driven Autoinjectors*, Int. J. Pharm. **594**, 120008 (2021).

[257] Z. Xue, J. J. Charonko, and P. P. Vlachos, *Particle Image Pattern Mutual Information and Uncertainty Estimation for Particle Image Velocimetry*, Meas. Sci. Technol. **26**, 074001 (2015).

[258] J. J. Charonko and P. P. Vlachos, *Estimation of Uncertainty Bounds for Individual Particle Image Velocimetry Measurements from Cross-Correlation Peak Ratio*, Meas. Sci. Technol. **24**, 065301 (2013).

[259] L. F. Richardson, *IX. The Approximate Arithmetical Solution by Finite Differences of Physical Problems Involving Differential Equations, with an Application to the Stresses in a Masonry Dam*, Philos. Trans. R. Soc. London. Ser. A **210**, 307 (1911).

[260] Y. Toba, *Drop Production by Bursting of Air Bubbles on the Sea Surface (II) Theoretical Study on the Shape of Floating Bubbles*, J. Oceanogr. Soc. Japan **15**, 121 (1959).

[261] Y. Zhang, T. Guo, P. Vlachos, and A. M. Ardekani, *Velocity Scaling and Breakup Criteria for Jets Formed Due to Acceleration and Deceleration Process*, Phys. Rev. Fluids **5**, 74003 (2020).

[262] A. Hawe, M. Wiggenhorn, M. van de Weert, J. H. O. Garbe, H. C. Mahler, and W. Jiskoot, *Forced Degradation of Therapeutic Proteins*, J. Pharm. Sci. **101**, 895 (2012).

[263] J. S. Bee, J. L. Stevenson, B. Mehta, J. Svitel, J. Pollastrini, R. Platz, E. Freund, J. F. Carpenter, and T. W. Randolph, *Response of a Concentrated Monoclonal Antibody Formulation to High Shear*, Biotechnol. Bioeng. **103**, 936 (2009).

[264] G. L. Lin, J. A. Pathak, D. H. Kim, M. Carlson, V. Riguero, Y. J. Kim, J. S. Buff, and G. G. Fuller, *Interfacial Dilatational Deformation Accelerates Particle Formation in Monoclonal Antibody Solutions*, Soft Matter **12**, 3293 (2016).